Development of Photocatalytic Materials and Systems for the Removal of Selenium from Industrially Impacted Water

by

Andrew Blake Holmes

A thesis
presented to the University of Waterloo
in fulfillment of the thesis
requirement for the degree of
Doctor of Philosophy
in
Chemical Engineering (Water)

Waterloo, Ontario, Canada, 2019

Examination committee membership

External examiner	Dr. Susan Baldwin Professor, Department of Chemical and Biological Engineering, University of British Columbia.
Supervisor	Dr. Frank Gu Professor, Department of Chemical Engineering and Applied Chemistry, University of Toronto (Adjunct, University of Waterloo).
Committee member	Dr. Mark Pritzker Professor, Department of Chemical Engineering, University of Waterloo.
Committee member	Dr. William Anderson Professor, Department of Chemical Engineering, University of Waterloo.
Internal-external member	Dr. Wayne Parker Professor, Department of Civil and Environmental Engineering, University of Waterloo.

Author's declaration

This thesis consists of material all of which I authored or co-authored: see Statement of Contributions included in the thesis. This is a true copy of the thesis, including any required final revisions, as accepted by my examiners.

I understand that my thesis may be made electronically available to the public.

Statement of contributions

The research chapters of this thesis are a compilation of a series of co-authored papers. I am the first-author on all 6 original chapters resulting from written papers, and was primarily responsible for experimental planning, experimental study, generation of figures, data analysis and discussion writing. The contributions of co-authors for each chapter are outlined below.

Chapter 1

Andrew Holmes (AH) wrote this review of Se removal techniques in full with input from Frank Gu (FG).

Chapter 2

AH was responsible for all experiment design and Se analytical protocol development. Diogo de Oliveira Livera (DdOL) ran the radical study experiments. Daid A. Khan (DK), Shannon M. McBride (SM) and AH ran the photocatalytic experiments. AH designed the Se analytical protocol for all analytic work done herein. AH performed the data analysis and prepared all figures. AH wrote the paper. FG supervised the project, contributed reagents, materials, analysis tools, and critically reviewed the paper.

Chapter 3

AH was responsible for all experiment design and Se analytical protocol development. Kayleanna Giesinger (KG) assisted with experimental work throughout the project, providing suggestions for modifying and optimizing experiments. AH performed the data analysis, prepared all figures and wrote the manuscript. FG supervised the project, contributed reagents, materials, analysis tools, and critically reviewed the paper.

Chapter 4

AH was responsible for all experiment design. Jane Ye (JY) assisted with experimental work throughout the project, providing suggestions for modifying and optimizing experiments. AH performed the data analysis, prepared all figures and wrote the manuscript. FG supervised the project, contributed reagents, materials, analysis tools, and critically reviewed the paper.

Chapter 5

AH was responsible for all experiment design. KG assisted with experimental work throughout the project, providing suggestions for modifying and optimizing experiments. AH performed the data analysis, prepared all figures and wrote the manuscript. FG supervised the project, contributed reagents, materials, analysis tools, and critically reviewed the paper.

Chapter 6

AH was responsible for all experiment design. DdOL ran the radical study experiments. DK assisted in lab work involving the synthesis of the noble metal deposited photocatalysts and ran some of the photocatalytic experiments. AH designed the Se analytical protocol for all analytic work done herein. AH performed the data analysis and prepared all figures. AH wrote the paper. FG supervised the project, contributed reagents, materials, analysis tools, and critically reviewed the paper.

Abstract

Selenium (Se) contaminated water derived from global industrial activities such as power generation, oil extraction and refining, coal and mineral mining, metal smelting, and agricultural irrigation can bioaccumulate in aquatic organisms and presents is toxic to many organisms, including humans. Se represents an extremely difficult contaminant to remove from wastewater due to its solubility, toxicity and state of matter over different oxidation states. At low concentrations, Se is an essential trace dietary element and consumed in foods and supplements. However, at higher concentrations Se becomes toxic, leading to selenosis in animals. Since the therapeutic window for Se is narrow, a slight increase in concentration can lead to toxic effects. Se exists naturally in inorganic forms, with selenite (SeO_3^{2-}) and selenate (SeO_4^{2-}) being the predominant species of interest due to their toxicity and solubility.

The objective of this thesis research focuses on (1) evaluating photocatalytic treatment of Se-rich industrial wastewaters and (2) the development of catalyst materials to improve photocatalytic activity, selectivity and recoverability. The industrial wastewaters considered in this research are flue gas desulphurization wastewater (FGDW), mine-impacted water (MIW) and synthetic mine-impacted brine (SMIB). Photocatalysis reduction on TiO_2 was found to effectively and selectively remove selenate in the presence of many dissolved species commonly found in industrial wastewater, providing a powerful alternative to conventional Se removal techniques. Catalyst materials were synthesized to improve both their activity and selectivity towards Se reduction products.

This work demonstrates, for the first time, that photocatalysis using TiO_2 can be effective at removing Se from raw flue gas desulphurization wastewater (FGDW), which is produced during the operation of coal-fired power plants. Selenate was reduced to less than 1 μg/L as Se in FGDW with concentrations of many competing co-existing ions exceeding 2,500x that of selenate. This work also uncovered the mechanisms of electron transfer through kinetic modelling, which have substantial impact on the understanding of photocatalytic reduction in a complex Se-TiO_2 photocatalytic system. The simultaneous generation of solid elemental selenium (Se^0) and hydrogen selenide (H_2Se) through two consecutive first-order reductions is reported under a direct Z-scheme photocatalyst arrangement between photodeposited Se and TiO_2.

In addition, the photocatalytic reduction on TiO_2 was evaluated for selenate removal from mine-impacted water (MIW) and was shown to remove Se to less than 1 μg/L. In this study, we uncover a unique advantage of photocatalytic reduction of selenate in MIW, largely the ability to selectively reduce selenate from more than 500 μg/L to less than 1 μg/L. The significant Se decrease was observed in the presence of the more thermodynamically favourable electron acceptor, nitrate and at high concentrations of sulfate. Selective photocatalysis is highly desired in complex water sources that contain a variety of dissolved species in addition to the target species for efficient use of the UV energy supplied. The electron transfer mechanism proposed involves electrons from the TiO_2 conduction band being responsible for the reduction of selenate to Se^0

while both carbon dioxide radicals ($CO_2^{\bullet -}$) and Se conduction band electrons are considered responsible for the further reduction of Se^0 to H_2Se.

The production of brine from MIW enables a reduction in water volume of 6-8 times, while increasing the concentration of target species in the water, such as selenate. As a result, the photocatalytic reduction of selenate in synthetic mine-impacted brine (SMIB) was also thoroughly investigated. Considering the two possibilities for Se reduction products ($Se^0_{(s)}$ vs. $H_2Se_{(g)}$), the ability to control the generation of a particular product was explored during the photocatalytic reduction of selenate over TiO_2 in SMIB. Photocatalytic reduction can effectively remove Se from an initial Se concentration of > 3,300 μg/L in SMIB to < 2 μg/L Se. An increase in solution temperature led to a marked increase in selenate removal kinetics and an increase in selectivity towards $H_2Se_{(g)}$, while increasing the concentration of formic acid led to an increase in selenate removal kinetics and an increase in the selectivity towards $Se^0_{(s)}$. A bivariate response surface analysis was used to present the selectivity of Se reduction product as high as 99% gaseous H_2Se or > 85% solid Se^0, under varying reaction conditions. Finally, a two-pronged electron transfer model is proposed to explain the selectivity towards $Se^0_{(s)}$ vs. $H_2Se_{(g)}$ under varying conditions: (i) $Se^0_{(s)}$ is produced by direct reduction of selenate by TiO_2 conduction band electrons and (ii) H_2Se gas is produced by electrons transferred into Se^0, followed by a reduction of Se^0 to H_2Se or through a direct reduction by $CO_2^{\bullet -}$.

Finally, this approach provides flexibility towards the final state of Se after treatment, which allows for two different possible options of Se capture and recovery; direct solid Se capture from the catalyst and scrubbing processes to recover gaseous H_2Se. A materials engineering approach was then implemented to achieve enhanced tunability towards desired Se reduction products. Heterogenous nanoscale photocatalysts were synthesized by depositing noble metal nanoparticles (Au, Ag, Pt and Pd) onto TiO_2, which demonstrated work-function dependent bimodal selectivity of final products during the photocatalytic reduction of selenate to Se^0 or H_2Se. The Se-noble metal-TiO_2 (Se-NM-TiO_2) photocatalytic system is structured in a direct Z-scheme arrangement, when Au, Ag or Pt are used, allowing for high selectivity towards H_2Se. In contrast, Pd acted as an electron sink which decreased the reducibility of the photogenerated electrons, ultimately causing a higher selectivity towards Se^0. Au-TiO_2 offers the largest H_2Se selectivity of all catalysts tested, while Pd-TiO_2 (highest work function) offers the highest selectivity to solid Se^0 generation. This study elucidates electron transport mechanisms and Fermi level equilibration via quantized double-layer charging effects of the Se-NM-TiO_2 system.

Overall, this thesis advances the understanding of photocatalytic reduction of selenate in FGD, MIW and SMIB. It expands the knowledge of Se speciation during and after photocatalytic treatment and elucidates electron transfer mechanisms responsible for the two-stage reduction of selenate in impacted water. Photocatalytic treatment of Se in these complex waters provides a selective, chemical-reductant-free catalytic reduction process capable of removing Se to < 1 μg/L. This thesis advances the understanding of photocatalytic advanced reduction processes, primarily towards the reduction of selenate and expands our current understanding of the complex Se-TiO_2 heterogeneous semiconducting photocatalyst system. Finally, the ability to selectively reduce selenate in complex industrial waters allows for the development of new wastewater treatment system configurations to effectively treat complex water streams.

Acknowledgements

Firstly, I am grateful to my supervising professor, Dr. Frank Gu, for giving me the chance to work in an innovative and exciting research team, and for many opportunities throughout my graduate school experience. Your guidance was critical to my development and allowed me to tackle a large variety of research programs. This encouragement to diversify allowed me to learn and develop in ways that have shaped how I approach undefined problems. I also wish to thank my thesis committee members, Professor Mark Pritzker, Professor William Anderson, Professor Wayne Parker, for their constructive comments, guidance, and encouragement of my research. I am also very grateful to my external examiner, Professor Sue Baldwin, for participating in my thesis defence, and providing constructive comments towards my thesis.

To Alberto Gonzalez, Doug McKay and Farid Vaezi, my external advisors, thank you for your guidance and support, critical feedback and contributions to making this technology evaluation more robust, while working with actual mine impacted water in the quest to find a novel solution to address a very complex, multidimensional problem. Your input helped sculpt and direct the research towards developing a relevant integrated treatment approach with a promising future.

To Janet Goodfellow and Len deVlaming, thank you for your initial insight and guidance on the topic of Se removal from industrial wastewater, and for your support and contributions.

To Kevin McVey, Kammy Sra, Gabriel Sabadell and Neil Thomson, my external advisors for the SIP sensing of nanoparticles section of my thesis, thank you for your critical contributions and guidance throughout technology development. To Adrian Mellage, thank you for your contributions towards our successful application of SIP to detect nanoparticles in the subsurface.

I want to thank my predecessor graduate students, Tim Leshuk and Stuart Linley, from which I learned the bulk of my knowledge in environmental nanoscience from. I thank you for leading the way in environmental studies within the Frank Gu Lab and for taking the time to teach me along the way. I want to thank my graduate student colleagues and friends I met or collaborated with throughout my studies: Diogo de Oliveira Livera, Zac Young, Stuart Linley, Tim Leshuk, Michelle Si, Harish Krishnakumar, David Wulff, Paul Chen, Sandy Liu, Mohit Verma, Noor Bahsoun, Mostafa Saquib, Aaminah Ahmad, Sukrit Rajpal, Lori Pollit, Jeff Watchorn, Mahtab Roshandel, Jacob Rogowski, Sarah LeBlanc, Erin Bedford, Jiang Xu, Adrian Mellage and Wanis Nafo, for your friendship and support throughout, as well as for your help and encouragement. I am fortunate to have shared this experience with you all. I would like to thank my co-op students Daid Khan, Shannon McBride, Aleksei Angell, Kayleanna Giesinger, Megan Thomson, Nick Rasmussen, Jane Ye, Kathryn Toffolo and KaHo Wong for your tremendous experimental help during your time working on the Se water treatment team. The opportunity to supervise you all was an invaluable experience and I thank you for your dedication and engagement.

Finally, I am grateful for the financial support provided to me throughout my Ph.D. candidacy: Natural Sciences and Engineering Research Council of Canada (NSERC) Alexander Graham Bell Scholarship - Canadian Graduate Doctoral Scholarship, Ontario Graduate Scholarship, the Waterloo Institute for Nanotechnology (WIN) Nanofellowship, the University of Waterloo (UW) President's Graduate Scholarship, and the UW Graduate Research Studentship.

I would like to dedicate this thesis to my parents, who have always loved, supported and encouraged me throughout my graduate pursuits.

Table of Contents

List of Figures

List of Tables

1 Introduction

This chapter is modified from:

Holmes, A.B. and Gu, F.X., 2016. Emerging nanomaterials for the application of selenium removal for wastewater treatment. *Environment Science: Nano* 3(5), 982–996.

1.1 Selenium as an environmental concern

The bioaccumulation of selenium (Se) resulting from global industrial activities (i.e. coal and mineral mining, metal smelting, oil extraction and refining, and agricultural irrigation) in aquatic organisms is of great concern due to its toxicity. Se is an extremely difficult contaminant to remove from wastewater due to its solubility, toxicity, and state of matter over different oxidation states. Recently, the application of nanomaterials to remove Se from wastewater has received increasing interest from the power generation and industrial mining sectors. Several classes of nanomaterials such as nanoscale adsorbents, catalysts and reactants, have shown great potential to remove Se in a wide range of oxidation states. This review article provides a summary of current selenium removal technologies, highlights the gaps in these technologies and focuses on emerging nanomaterials capable of removing selenium oxyanions from wastewater to ultra-low μg/L limits. Recent literature has focused on the modification of different nanomaterials in order to achieve high surface adsorbing activity, high reactivity, selectivity and sustainability in efforts to remove selenium oxyanions. The majority of promising nanotechnologies for selenium removal are undergoing intense research and development in efforts to advance the technology to wastewater treatment markets. These nanomaterials have the ability to remove selenium contaminants to previously unachievable ultra-low levels, while implementing reliable and sustainable treatment techniques.

1.2 Background

Selenium (Se), a recalcitrant environmental contaminant, has received global awareness and concern. Se is a naturally occurring non-metal in the Earth's crust. In addition to natural causes, industrial activities such as coal and mineral mining, metal smelting, oil extraction and refining, and agricultural irrigation can cause concentrated releases of this otherwise trace element (Burau, 1985; Conde and Sanz Alaejos, 1997).

The World Health Organization (WHO) currently holds a provisional guideline value of 40 μgL^{-1} (ppb) as the maximum concentration limit (MCL) in drinking water (World Health Organization, 2011). The United States Environmental Protection Agency (U.S. EPA) published a MCL of 50 μgL^{-1} (ppb) as the national primary drinking water regulations and 5 μgL^{-1} (ppb) as the aquatic life chronic limit (U.S. EPA, 2014). Recently, stricter guidelines have been proposed by the EPA water quality criteria for the protection of aquatic life: 1.2 μgL^{-1} (ppb) in lentic ecosystems (still freshwater) and 3.1 μgL^{-1} (ppb) in lotic ecosystems (flowing freshwater) (U.S. EPA and Office of Water, 2015). These new stringent guidelines have had ramifications on global industrial activities, requiring more robust and reliable selenium treatment technologies.

Se exhibits four oxidation states (-II, 0, IV, VI) and varying its chemical form can drastically change the biological response (Christensen et al., 1989; Gissel-Nielsen et al., 1984). At low concentrations, Se is an essential trace dietary element in foods and supplements and exists in a variety of organic and inorganic forms. Organic forms include selenomethionine (animal and plant sources), selenocysteine (animal sources), while inorganic forms include selenate and selenite (mainly supplement sources) (Rayman, 2000). However, at high concentrations, Se becomes toxic, leading to selenosis in animals (Yang et al., 1983). Since the therapeutic window for Se is narrow, a slight increase in concentration can lead to toxic effects (Conde and Sanz Alaejos, 1997; Papp et al., 2007; Rayman, 2000).

In the environment, Se naturally exists in inorganic forms: selenide (Se^{2-}), elemental selenium (Se^0), selenite SeO_3^{2-} (Se^{4+}) and selenate SeO_4^{2-} (Se^{6+}) (Parida et al., 1997). Figure 1-1 illustrates the various stable forms of inorganic selenium as a function of pH and redox potential conditions and compares it to the more familiar sulfur. Both SeO_4^{2-} and SeO_3^{2-} are the predominant soluble inorganic species in contaminated surface waters (Sharmasarkar and Vance, 2002). Generally, SeO_4^{2-} and SeO_3^{2-} oxyanions are more toxic and more bioavailable than organic selenium species with selenite being the more toxic of the two (Pérez-Corona et al., 1997).

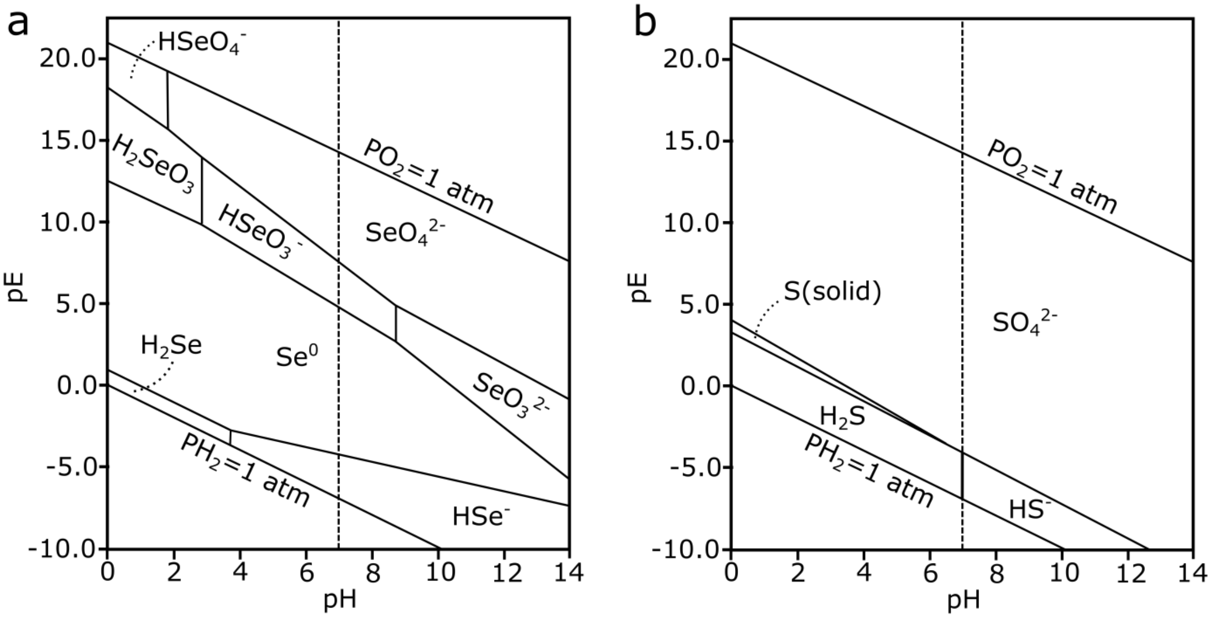

Figure 1-1**.** pE-pH diagram for Se-O-H system at 298 K (a) and S-O-H system at 298 K (b) for comparison. Figure adapted from Santos et al. (2015).

Se removal from industrial wastewaters can be difficult and costly due to the combination of high volume (1000s of L/s) and dilute (ppm or ppb) contaminated streams. Various treatment methods can be applied for selenium removal, including but not limited to: chemical precipitation, adsorption, ion exchange, membrane filtration, chemical reduction and biological removal. Many of these technologies have been developed for full scale treatment of Se contamination (Frankenberger Jr. et al., 2004; Higgins et al., 2009; Mavrov et al., 2006; Nishimura et al., 2007; Twidwell et al., 1999). Each technology has its drawbacks and most conventional Se removal processes are incapable of producing treated streams with less than 5 μgL^{-1} (Santos et al., 2015).

Recent advances in nanotechnology offer great potential for pollution prevention, treatment and remediation (Wei et al., 2011). Nanotechnology applied to Se promises selective removal from complex wastewater, reusable green adsorbents, increased active sites for selenium adsorption and reduction, increased catalytic activity and many more advantages.

Here, this review aims to provide an overview of recent advances in nanotechnologies for selenium removal from industrial wastewater. Current selenium treatment technologies are discussed, followed by a summary of the gaps inherent in these technologies. The major nanomaterials applied for selenium removal are critically reviewed based on their performance, sustainability and limitations. The obstacles constraining full scale implementation and the research challenges are also discussed.

1.3 A summary of current technologies for selenium removal

A variety of selenium removal technologies have been developed for use with industrial wastewater. Due to the various treatment applications it is challenging to identify the most effective treatment option for a particular case. Selenium removal can be achieved by physical, adsorptive, oxidative/reductive and biological techniques. Conventional wastewater treatments , such as lime neutralization, are ineffective since no insoluble hydroxides are formed (Lottermoser, 2007). A comparison and summary of the current technologies for selenium removal can be found in Table 1-1.

Table 1-1. Comparison of current selenium removal techniques

Current Selenium Removal Technology	Key Features	Advantages	Limitations	Reference
Physical Removal Techniques				
Membrane (RO or NF)	Pump Se contaminated water through membranes impermeable to Se oxyanions	- Capable of removing Se to <5 µg/L	- High cost - Energy Intensive - Reject stream concentrated in Se	(Richards et al., 2011)
Evaporation Ponds	Evaporate water leaving Se impurities in solid phase	- Lower cost if using solar energy	- Climate dependant - Large footprint	(Manning and Burau, 1995)
Adsorption Removal Techniques				
Ion Exchange	Wastewater flows through granular chemicals (ion exchange resins) packed in a column	- Renewable (>90%) exchange resins - Concentrates Se wastewater volume	- Competing ions limit effectiveness - Further treatment required	(Nishimura et al., 2007)
Ferrihydrite adsorption	Addition of ferric salts alongside NaOH forms ferrihydrite; adsorbs selenite and co-precipitates out of solution	- US EPA best demonstrated available technology (BDAT) - Simple	- Not proven Se <5 µg/L - Ineffective on Selenate	(Balistrieri and Chao, 1990; Higgins et al., 2009)
Activated Alumina	$Al(OH)_3$ is used as an adsorbent for selenium	- Simple	- Ineffective on Selenate	(Ippolito et al., 2009)
Oxidation/Reduction Removal Techniques				
ZVI	ZVI acts as an electron donor to drive the reduction of selenium oxyanions	- Simultaneous reduction of selenate and adsorption of selenite	- Spent ZVI disposal - Competing oxyanions can reduce effectiveness	(Yoon et al., 2015; Huang et al., 2013; Frankenberger Jr. et al., 2004)
Galvanic Cementation	Various metals are used to catalyze the ZVI reduction	- Increased reduction of selenate	- Higher cost when compared to ZVI	(Y. Zhang et al., 2005)
Ferrous Hydroxide	Iron(II) acts as an electron donor to drive the reduction of selenium oxyanions	- US EPA best demonstrated available technology (BDAT) - Widely implemented	- Not proven Se <5 µg/L - Large quantity of chemical waste	(Twidwell et al., 1999)
Electrocoagulation	A direct electrical current applied to an electrochemical cell produces iron(II)	- Simultaneous heavy metals removal	- Not proven Se <5 µg/L - Complex pre-treatment	(Mavrov et al., 2006)
Biological Removal Techniques				
Microbial Reduction	Se-reducing bacteria use selenate and selenite as terminal electron acceptors during cellular respiration	- Capable of removing Se to <5 µg/L	- Presence of nitrates increase carbon dosage (eg. methanol) - Intensive pre-treatment required	(Staicu et al., 2015b; Stolz and Oremland, 1999)
Microbial/Algal Volatilization	Bacteria/algae convert aqueous Se to volatile Se compounds in gaseous phase	- Low costs - Can be applied in-situ	- Seasonal - Subsequent treatment required - Not proven Se <5 µg/L	(Sors et al., 2005; Souza et al., 1999)
Phytoremediation	Plant uptake and volatilization of Se through cellular pathways	- Minimal operator supervision - Able to treat large volumes	- Not proven Se <5 µg/L - Long residence time, large footprint	(Gao et al., 2000; Lin and Terry, 2003)

1.3.1 Physical & mechanism removal techniques

Membrane separation techniques can be employed to remove selenate and selenite from aqueous solution. Both selenium species have an approximate size of 3-4 angstrom (0.3-0.4 nm) and thus require very small pore size nanofiltration (NF) or reverse osmosis (RO) for successful removal. RO has shown superior performance and has been pilot- and field-tested to reduce Se levels below 5 μg/L with a 94% retention (Richards et al., 2011). The main limitation of membrane separation techniques is the high cost due to the required high operating pressures.

Several evaporation techniques are available, including evaporation ponds, enhanced evaporation systems and evaporation/crystallization technologies. These evaporation systems require a large area, have comparably large residence times and risk contamination of groundwater and surrounding ecosystems (Manning and Burau, 1995).

1.3.2 Adsorption removal techniques

Ferrihydrite (iron (III) oxyhydroxide) adsorption of selenium has been identified as the Best Demonstrated Available Technology (BDAT) for selenium removal from industrial wastewater by the U.S. EPA (Rosengrant, 1990). Selenite is adsorbed more effectively than selenate, which is more strongly affected by the presence of sulfate, bicarbonate and other anionic species. The addition of ferric chloride with sodium hydroxide forms ferrihydrite and subsequently adsorbs selenite and co-precipitates from solution. This process can generate large volumes of sludge to be dewatered with the use of centrifuges, belt presses, or plate and frame presses (Higgins et al., 2009). The main disadvantages of this removal technique are the large quantities of chemical sludge generated that requires disposal, the large cost of ferric chloride and caustic or lime necessary to cause the co-precipitation, the inability to remove selenate and the inability to remove selenium to low μg/L (<5 μg/L) (Balistrieri and Chao, 1990). Iron oxides such as magnetite, hematite and goethite are examples of natural formed mineral media that adsorb selenite via an inner-sphere bidentate surface complex (two covalent bonds) and selenate via an outer-sphere hydrated complex (electrostatic interaction) (Rovira et al., 2008).

Ion exchange is a versatile physicochemical method for wastewater treatment. During treatment, SeO_4^{2-} and SeO_3^{2-} in the aqueous phase are exchanged for desired ions (i.e. Cl^-, SO_4^{2-}, PO_4^{3-}, etc.) as the wastewater flows through a bed of ion exchange resins packed in a column.

Conventional adsorbents used for selenium removal fall under one of the following categories: organic resins, minerals, oxides, and carbon-based bio-adsorbents (Santos et al., 2015).

Selenate successfully removed by polyamine-type weakly basic ion exchange resins over a wide pH range of 3 to 12, while selenite is optimally treated at pH 10 (Nishimura et al., 2007). An important factor when considering IX methods is the effect of competing ions in solution to the adsorptive capacity of selenium. Polyamine-type weakly basic ion exchange resins are strongly affected by the presence of sulfate, to the extent of reducing the selenate removal by 50% (Nishimura et al., 2007).

Activated alumina (AA) or aluminum hydroxide is used as an adsorbent for selenium. AA is a porous aluminum oxide which has a high adsorptive capacity due to its surface area. Unlike activated carbon, which does not adsorb selenium very well, activated alumina has been used for selenium removal. The application of aluminum salts in a selenium removal system operates very similar to that of a ferrihydrite co-precipitation system (Ippolito et al., 2009).

1.3.3 Oxidation/reduction removal techniques

Se can be successfully removed from aqueous solution through chemical reduction to elemental Se^0 and solid metal selenides. Chemical reduction of selenate and selenite has been achieved through the use of zero valent iron, more commonly known as elemental iron.

Zero valent iron (ZVI) can be used as a reductant for selenate and selenite. The iron acts as both a catalyst and an electron donor for the reduction reaction (Frankenberger Jr. et al., 2004). The ZVI surface is oxidized and provides both ferrous and ferric iron adsorption sites for the selenium oxyanions. This iron surface complex is known as green rust, which is the form of ZVI required to chemically reduce both selenate and selenite to elemental selenium (Myneni et al., 1997). Selenate, the more recalcitrant of the two species, is reduced to selenite by green rust which in turn is either reduced further to elemental selenium or adsorbed to the ferrihydrite amorphous solids formed through the redox reaction with ZVI. Elemental iron can be deployed in an active or passive treatment and has been implemented in passive reactive barriers (PRBs) for selenate removal (Morrison et al., 2002). Recent advancements in active treatment have found many ways to enhance reactivity. Liang et al. investigated the significant enhancement of selenite removal in the presence of a weak magnetic field allowing for comparable removal at neutral conditions

(Liang et al., 2014). Elemental iron is also able to directly remove selenocyanate ($SeCN^-$), an ambidentate ligand that can coordinate to Fe^0 directly. Previously, this was a two-step process involving chemical oxidation of $SeCN^-$ to Se(IV) followed by the co-precipitation with a ferric coagulant (Meng et al., 2002). Some disadvantages of the used ZVI, include significant production of waste from spent ZVI and non-specific interaction with competing oxyanions that can oxidize ZVI (Huang et al., 2013; Yoon et al., 2015). The addition of certain metal catalysts and nanoscale ZVI can improve reactivity and reduce the overall waste generation. Nanoscale ZVI treatment will be discussed in detail in a later section.

Catalyzed reduction (galvanic cementation) utilizes copper or nickel to improve ZVI reactivity. The copper and nickel act as catalysts, that generate a greater electrochemical potential between the elemental iron and selenium oxyanions (Y. Zhang et al., 2005). The addition of copper to ZVI has shown to double the reduction rate of selenate at a neutral pH, compared to non-catalyzed ZVI treatment. Similarly, coupling ZVI with nickel increased the selenate reduction rate by a factor of nearly 25 (in the presence of 2 mg/L selenium at neutral pH) (Huang et al., 2013; NSMP Working Group, 2007).

Ferrous hydroxide is capable of reducing selenate to selenite, followed by subsequent ferrihydrite adsorption, at pH 8-9 (Twidwell et al., 1999). Unfortunately, ferrous hydroxide is also capable of reducing selenium species to toxic hydrogen selenide gas. Similar disadvantages as ferrihydrite adsorption are encountered with this technique, as previously discussed.

Electrocoagulation (EC) is another technique used to remove selenium from wastewater. A direct electrical current applied to an electrochemical cell produces ferrous iron from oxidation of the iron anode. The ferrous has excellent adsorption and co-precipitation properties for selenium oxyanions and can remove up to 98.7% (Mavrov et al., 2006). The application of EC for separation of colloidal biogenic selenium has shown up to 93% removal (Staicu et al., 2015b). However, EC has not shown promise at reducing selenium concentrations to the recent strict guidelines of 1-5 µg/L.

1.3.4 Biological removal techniques

Selenium can be removed from industrial wastewaters by biological methods. Microbial reduction, microbial and fungal volatilization and phytoremediation are the major biological approaches to remove selenium from industrial wastewater.

Microbial reduction is the leading method for biologically removing selenium from an aqueous medium. Selenium-reducing bacteria use selenate and selenite as terminal electron acceptors during cellular respiration and are able to operate under many different environments: methanogenic, sulfate-reducing, denitrifying and hydrogenotrophic conditions (Yarlagadda V. Nancharaiah and Lens, 2015). The soluble and toxic selenate and selenite are reduced to insoluble elemental selenium through biomineralization mechanisms. Biogenic selenium, now insoluble, must then be removed from aqueous medium. Due to its surface charge and nanometer size, colloidal properties of biogenic selenium, make its removal from liquid phase difficult (Staicu et al., 2015b). Recently, many have studied the nature of biogenic selenium synthesized by complex microbial populations (Husen and Siddiqi, 2014; Jain et al., 2015; Oremland et al., 2004; Staicu et al., 2015b). Extracellular polymeric substances (EPS) on the surface of biogenic selenium are the main detriment of its colloidal properties and the cause of the difficulties in solid/liquid separation. Colloidal stability caused by the EPS adds to the challenge of attaining ultra-low selenium guidelines.

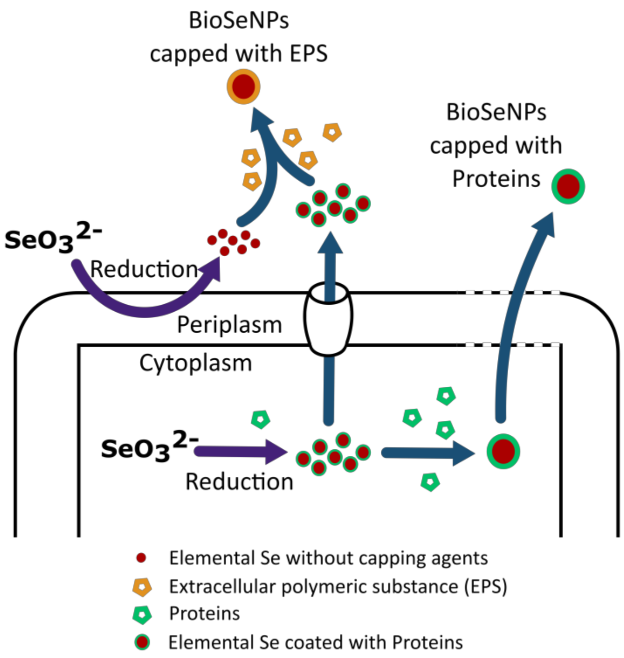

Figure 1-2. Schematic representation of the removal of selenite and growth of elemental selenium to form BioSeNPs. Figure adapted from Jain et al. (2015).

Another challenge faced by selenate-respiring bacteria is due to the fundamental thermodynamics of reduction potential. Based on comparison of calculated free energies, assuming H_2 is the electron donor, the reduction of SeO_4^{2-} to SeO_3^{2-} will occur only after the reductions of O_2 to H_2O and NO_3^- to N_2 (denitrification) since they have a higher reduction potential and therefore are more thermodynamically favored (Stolz and Oremland, 1999). As a result, an anaerobic and nitrate free environment is optimal for successful selenium removal. This may require a pre-treatment step or concurrent treatment for nitrate removal by the biological population.

Microbial fuel cells (MFCs) have been used to remove selenite from wastewater, simultaneously generating electricity and removing selenium in a single-chamber MFC. MFCs can use microbes to oxidize organic substrates, reduce selenite to elemental selenium and generate electricity. A removal level of 99% of Se was achieved from feed streams containing 50 and 200 mg L^{-1} Se demonstrate the potential of using MFC technology for Se removal from wastewater (Catal et al., 2009). This technology is in early stages of development and much work must be done to realize this potential.

Microbial selenium volatilization is another method of selenium removal from wastewaters. Many strains of bacteria (i.e. pseudomonas stutzeri NT-I (Kagami et al., 2013; Kuroda et al., 2011)) are able to aerobically convert SeO_4^{2-}, SeO_3^{2-} and Se^0 into $(CH_3)_2Se_2$ and $(CH_3)_2Se$ which are gaseous Se compounds (Sors et al., 2005). An advantage to volatilizing selenium is the potential to recapture the selenium for sustainable utilization. However, this method has its disadvantages as well: sensitivities to incoming environmental conditions (pH, temperature, inhibitor species, etc.), excess nutrition demands of biological population, longer start-up and down-times. (Souza et al., 1999).

Phytoremediation for selenium removal is another remediation technique. Constructed wetlands that make use of phytoremediation of selenium are a common passive method of removal. Phytoremediation of selenium involves plant uptake and volatilization through cellular pathways similar to microbial volatilization (Lin and Terry, 2003). Although significant removal of selenium (both selenate and selenite) has been shown, establishment of a wetland can take up to two years for complete remediation availability (Gao et al., 2000). Phytoremediation requires a significant investment in long-term passive treatment and is not a viable option for most industrial wastewater applications. Fungal systems have shown similar effectiveness for selenium removal in low pH wastewaters (Espinosa-Ortiz et al., 2015).

At first glance, biological remediation techniques appear to be most promising due to comparably low capital and operating costs, low chemical usage and ability to reduce selenium concentration to below 5 ppb. However, biological treatment requires pH and temperature adjustments in order to operate optimally, post-treatment to remove biological oxygen demand (BOD), a carbon and nutrient source, an extended start-up, trouble shoot time and long periods of time for start-up to acclimate the seed biological population and can be very site sensitive (Yarlagadda V. Nancharaiah and Lens, 2015; Santos et al., 2015).

1.4 Gaps in current Se removal technology

Although reliable, physical-mechanical removal techniques such as membrane nanofiltration and reverse osmosis are energy- and cost-intensive. The best demonstrated available technology (BDAT) advised by the US EPA is ferrous hydroxide reduction of selenate to selenite followed by co-precipitation with ferrihydrite although comes at a high cost of chemical use and chemical sludge disposal. These reliable yet expensive techniques are no longer sustainable for removal of selenium below 5 ppb. Thus, it is important to develop a selective, robust and reliable technique to remove selenium to <1-3 ppb from large volumes of wastewater containing relatively low concentrations (1-15 ppm) of selenium.

A number of technologies (i.e. biological reduction, ferrous hydroxide reduction, iron co-precipitation, ZVI reduction, etc.) have been applied on a full scale for selenium removal from industrial wastewater. Although biological removal technologies have their advantages, substantial obstacles remain when trying to meet the recent stringent guidelines imposed by the U.S. EPA. Competition with co-contaminants (i.e. NO_3^-, O_2, metals and other competing electron acceptors), addition of a carbon source and nutrients, need for pH and temperature adjustment that consumes chemicals and energy, and the colloidal nature of the biomineralized selenium nanoparticles requiring advanced post-treatment separation. Thus, a need exists for research into the assessment of recovered selenium from wastewater for reuse in other industrial applications.

Reduction removal techniques including catalyzed ZVI and reduction/adsorption removal techniques using metal oxides have shown promise in removing selenium from wastewater and are being developed. Both adsorption and redox techniques are highly dependent on the surface properties and surface area which provide the solid/liquid interface for chemical interaction. Two main limiting factors in the removal of selenium are: selectivity of selenium oxyanions relative to competing anions and the quantity of active sites for either adsorption or reduction. In order to increase selenium removal efficiency, both the selectivity and the quantity of active sites must be increased.

1.5 Developing and prospective applications of nanotechnology for Se removal

Nanomaterials have advantageous properties including high surface area and activity as well as increased selectivity to selenium oxyanions, resulting in increased selenium removal from wastewater. Nanomaterials are defined as materials smaller than 100 nm in at least one dimension. At the nanoscale, materials possess unique size-dependent properties, many of which can be applied to selenium removal from wastewater. These novel attributes make nanomaterials excellent adsorbents, catalysts and reductants. The most significant properties of these particles are small size, large surface area, high reactivity, great catalytic potential and large number of active sites (Ali, 2012) for removal of selenium oxyanions.

Several emerging nanotechnologies applied to selenium removal from industrial wastewater are discussed in this section. The two main techniques for removal reported herein are either adsorption (non-destructive) or reduction (destructive). A summary and comparison of the nano-adsorbents can be found in Table 1-2.

Table 1-2. Comparison of adsorption capacities (Q_m) reported in literature for Se(IV) & Se(VI) using nanomaterials

Nano Adsorbent Material	Se species	Initial Se Conc. (mg/L)	Adsorbent Conc. (g/L)	pH	T (K)	Ads. Capacity[§] Q_m (mg/g)	Reference
Ligand Immobilized Nanocomposites (LINs)							
DSDH immobilized on mesoporous silica	Se(IV)	1-80	0.5	2.5	-	111.12	(Awual et al., 2015b)
MBHB immobilized on mesoporous silica	Se(IV)	1-80	0.5	2.5	-	93.56	(Awual et al., 2015a)
HMBA immobilized on mesoporous silica	Se(IV)	1-80	0.5	2.5	-	103.73	(Awual et al., 2014)
Nanomaterial Metal Oxides							
Nanocrystalline Al oxide impregnated chitosan	Se(IV) & Se(VI)	1	1.75	6.8	298	4.0, 4.0	(Yamani et al., 2014)
Nano- $MnFe_2O_4$	Se(IV) & Se(VI)	0.25-10	2.5	2-6	RT	6.6, 0.8	(Gonzalez et al., 2010)
Nano- $CuFe_2O_4$	Se(IV) & Se(VI)	1-25	0.4	7.4	298 ± 1	14.1, 5.97	(Sun et al., 2015)
Nano-magnetite	Se(IV)	0.1-1	0.1	6	298	6.0	(Wei et al., 2011)
Mn_3O_4 Nanomaterial	Se(IV) & Se(VI)	0.25-10	2.5	2-6	RT	1.0, 0.9	(Gonzalez et al., 2011)
Fe-Mn Binary Oxide	Se(IV) & Se(VI)	5-500	2	4	295 ± 1	41.02, 19.84	(Szlachta and Chubar, 2013)
Nano-Anatase (n-TiO2)	Se(IV)	30	5	5	293	7.0	(Zhang et al., 2009)
Nano-Anatase Colloid (n-TiO2)	Se(IV)	0.1-1.5	2	6-7	RT	25	(Fu et al., 2012)
n-TiO2 impregnated MWCNTs	Se(IV)	1	-	1-4	RT	55.56	(Bakather and Atieh, 2015)
Nanomaterial Graphene Oxides							
Magnetic Nanoparticle-Graphene Oxide (MGO)	Se(IV) & Se(VI)	5	1	7	RT	4.99, 2.97	(Fu et al., 2014)
Layered Double Hydroxides (LDHs)							
Mg-Al-CO_3 LDH (alkoxide-free synthesis)	Se(IV) & Se(VI)	250	2	7	295 ± 2	120, 45	(Chubar, 2014)
Calcined Mg/Fe HTlc	Se(IV)	50	1	6	303	33	(Das et al., 2007)
Mg/Fe HTlc	Se(IV)	50	1	6	303	25	(Das et al., 2002)
Mg-Al-CO_3 LDH (Low Se Conc.)	Se(IV) & Se(VI)	0.02-0.05	-	7	298	0.045, 0.045	(Yang et al., 2005)
Mg-Al-Cl LDH (High Se Conc.)	Se(IV)	500-1,000[†]	-	9	298	178	(You et al., 2001)
Chitosan-montmorillonite	Se(VI)	22	0.5	7	-	8.0	(Bleiman and Mishael, 2010)

[§] Adsorptive capacities are highly dependent on starting conditions (pH, initial concentration, etc.). It is important to consider this when comparing two adsorption technologies. [†] Equilibrium concentration during adsorption

1.5.1 Distinct advantages of nanomaterials for Se removal

The use of nanomaterials has significant advantages for the field of wastewater treatment, in particular selenium removal from industrial wastewater. Several different nanophenomena enable nanoscale adsorbents, catalysts and reductants to outperform their micro and macro scale counterparts. These nanomaterials have the ability to remove selenium contaminants to previously unachievable ultra-low levels, all the while implementing sustainable methods. The high surface adsorption activity, reactivity, selectivity and sustainable treatment capability are the four major factors underlying selenium removal from wastewater.

High surface adsorption activity - High surface area is a major factor for multi-phase interface reactions, such as a liquid/solid adsorption processes. All the nanotechnologies described herein have larger adsorption capacities due to the increased surface area provided by nanoscale structures. Nanocrystalline metal oxides such as iron oxide, titanium dioxide and manganese oxide have been shown to outperform their macro-scale counterparts in terms of the adsorption capacities for selenium oxyanions (Jordan et al., 2013; Sun et al., 2015; Wei et al., 2011; Zhang et al., 2009).

High catalytic and redox reactivity - The ability to functionalize nano-surfaces is one reason for their high reactive rates. Functionalization of metal oxide nano-surfaces is common to increase reactivity of nanoparticles (Wu et al., 2008). Synthesized iron oxide nanoparticles are able to increase selenium sorption efficiently due to the increased surface area and functionalized surfaces (Gui et al., 2015). Both nZVI and $nTiO_2$ have the ability to reduce and adsorb selenium oxyanions. nZVI has been shown to reduce selenite about three times faster than micro-scale ZVI (Ling et al., 2015). This nano-reductant is widely recognized as a superior particle for many environmental remediation applications due to its reactivity, mobility and paramagnetic properties.

Selectivity - The ability to selectively remove selenate and selenite from industrial wastewater in the presence of a variety of co-contaminants is a desirable and essential treatment feature. Commonly, selenium-contaminated wastewaters also contain nitrates, phosphates, sulphates, salts, heavy metals and many other anionic species which compete for the active adsorption or reduction sites of the selenium removal treatment system. The main advantage of nanotechnology over conventional selenium removal techniques involves the superior selectivity of nanomaterials to form complexes with selenium oxyanions in wastewater.

Several researchers have developed nanomaterials capable of selectively removing selenite and selenate in the presence of many co-contaminants. The ability to selectively adsorb SeO_3^{2-} is a result of inner sphere complexation (covalent bond formation) with the nano-adsorbent material (Chubar, 2014). Ligand immobilized nanocomposites, such as Mg-Fe-CO_3 layered double hydroxide (LDH)-coated cellulose fibers and commercially available ion exchange resin impregnated with ferric oxide nanoparticles exhibited selectivity towards selenite in the presence of the commonly encountered anionic species (Awual et al., 2015b; Chen and An, 2012; Pan et al., 2010). 3-(2-aminoethylamino) propyltrimethoxysilane (AAPTS) immobilized onto multi-wall carbon nanotubes demonstrated selectivity towards selenate (along with As(V) and Cr(VI)) in the presence of other anionic species (Peng et al., 2015).

Sustainable treatment capability – Sustainable treatments use little energy and consume a small amount of reagents in the interest of designing an environmentally and economically sustainable treatment process. Sustainable treatment systems can be implemented utilizing nanomaterials such as $nTiO_2$ to remove selenium oxyanions with minimal wastewater processing equipment. Nanocrystalline TiO_2 photocatalytically reduces of selenium oxyanions to elemental selenium (Nu Hoai Nguyen et al., 2005). The use of a nano-catalyst allows for recycling of the nanomaterial as it is not consumed in the redox reaction itself. The recycling of nanomaterials is an important step in designing a full-scale wastewater treatment system. Nanomaterials require lower contact time (1-15 min) (Ali, 2012), lower dose (in μgL^{-1}) and are more effective at removing selenium oxyanions to microgram level limits (total Se <5 μgL^{-1}) than conventional adsorbents and catalysts.

1.5.2 Ligand immobilized nanocomposites (LINs)

Ligand immobilized nanocomposites (LINs) are developed by immobilizing ligands such as Schiff base ligands on a nanostructure to support the capture of selenium oxyanions. Schiff base ligands are selective complexing agents towards heavy transition metal ions and group 16 oxyanions, in particular selenite. They have the general structure R2C=NR' (R'≠H). The imine nitrogen in the ligand is basic and demonstrates pi-acceptor and sigma-donor properties. This enables the ligand to form complexes with Se(IV) and with transition metals (Awual et al., 2014).

Awual et al. have combined ligands with varying adsorption capacities into one adsorbent. All of these ligands have a common property: ability to selectively remove selenite from wastewater in the presence of competing ions(Awual et al., 2015b, 2015a, 2014). The ligands are listed as follows:

a) (3-(3-(methoxycarbonyl)benzylidene)hydrazinyl) benzoic acid (MBHB) ligand,

b) 6-((2-(2-hydroxy-1naphthoyl)hydrazono)methyl) benzoic acid (HMBA) ligand,

c) N,N-di(3-carboxysalicylidene)-3,4-diamino-5-hydroxypyrazole (DSDH) ligand.

The ligands are immobilized onto a mesoporous silica substrate, similar to the fabrication of self-assembled monolayers on mesoporous supports (SAMMS). The presence of competing anions and cations did not hinder selenite adsorption since competing ions exhibited almost zero sorption capacity on the nanocomposite, suggesting high selectivity for selenium(IV) ions (Awual et al., 2015a). This is a very attractive property because most adsorption techniques are carried out in the presence of competing ions in real wastewater. Another main advantage of this adsorbent is its reusability. In order to counteract their high cost recyclability is crucial for feasible implementation. A simple wash with a high pH solution desorbs the selenium compounds from the adsorbent.

One disadvantage of LINs is the requirement of a very low pH (optimal performance at pH 2.5) which makes this process hard to implement on a large scale. Below the isoelectric point, the adsorbent surface is positively charged which enhances electrostatic interaction with selenate (Awual et al., 2015b). Costs will also go up substantially due to the need to neutralize the wastewater.

A similar LIN was prepared by immobilizing 3-(2-aminoethylamino)-propyltrimethoxysilane (AAPTS) onto multi-wall carbon nanotubes (MWCNTs). This adsorbent selectively extracts As(V), Cr(VI) and Se(VI) at low pH values (Peng et al., 2015). Very few selective adsorbents target selenate, which makes this nano-adsorbent attractive. MWCNTs are currently used for detection, sensing and speciation of selenium in wastewater at a relatively small laboratory scale.

Further research is required in order to test the responsiveness of LINs at higher flow rates, carry out economic feasibility studies for scale-up and conduct environmental tests to determine behaviour at neutral pH, differing salinity, differing temperature, etc. Nevertheless, the ability to selectively adsorb selenium (VI) and (IV) is a large step towards a more realistic and cost-effective adsorbent.

1.5.3 Nanocrystalline metal oxides

The development of nanocrystalline metal oxides (NMOs) over the past few years with higher adsorption capacity, have enhanced the capability of adsorption technologies for selenium removal from wastewater. NMOs have a higher surface area and an increased number of active adsorption sites. Several NMOs have been thoroughly characterized as highly ordered chemical structures. NMO forms of aluminum, titanium, manganese and iron oxides have all been used as effective adsorbents for selenite and selenate.

While the increased adsorption efficiencies of NMOs are attractive, the problem of expensive separation after use exists. Due to high energy filtration or centrifugation required for separation of the NMOs, regeneration costs can escalate quickly. As a result, many researchers have been looking into immobilization techniques to achieve the NMO's increased adsorption capacity without the increased costs of separation for regeneration and reuse.

1.5.3.1 Iron oxide

Possibly the most common NMO used for selenium removal by adsorption is iron oxide and iron oxide modified materials. Synthesized nanostructured iron oxide particles are able to increase this sorption efficiently due to increased surface area and functionalized surfaces. Naturally occurring iron oxide minerals have a great effectiveness as adsorbents for selenium species. The sorption of both selenite and selenate by different iron oxide nanoparticles (goethite, ferrihydrite, magnetite) has been shown to be effective. Selenate adsorbs onto the surface of maghemite via bidentate outer-sphere complex was shown in Figure 3 (Jordan et al., 2013). Selenite adsorbs onto the surface of iron oxides via much stronger inner-sphere complexes and as a result adsorbs to a much higher extent (Fu et al., 2014). The design of adsorbents with high removal capacity for both selenate and selenite is technically challenging due to these two separate adsorption mechanisms.

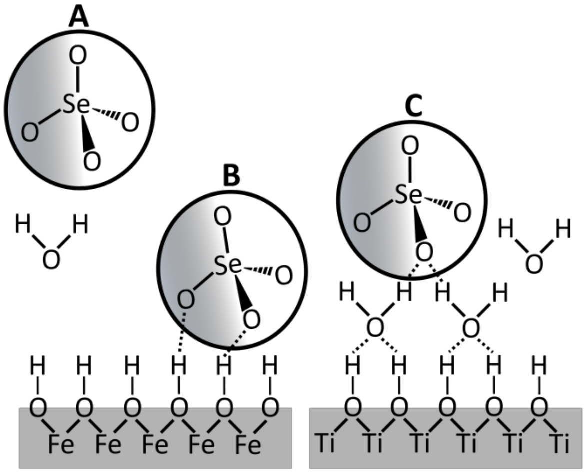

Figure 1-3. Schematic of SeO_4^{2-} surface species. Aqueous species (A), outer-sphere complex as derived for maghemite surfaces (B) and extended outer-sphere complex as derived for anatase surfaces (C). Figure adapted from Jordan et al. (2013).

Nano-magnetite has been widely used in the removal of various contaminants and is a low-cost nano-adsorbent alternative. Nano-magnetite was found to be a better adsorbent for selenite compared to nZVI, which is a better adsorbent for selenate (Wei et al., 2011). Gonzalez et al. investigated producing iron(III) oxide nanoparticles by microwave-assisted synthetic techniques and found the technique produced a superior adsorbent nanoparticle for both selenate and selenite (Gonzalez et al., 2012).

A hybrid adsorbent produced by impregnating hydrated ferric oxide nanoparticles with a commercially available anion-exchange resin (D-201) improved sorption selectivity towards selenite. The study proved to remove selenite from 2 mg/L to less than 0.01 mg/L even in the presence of the commonly encountered anions (Pan et al., 2010).

Research developments focused on the design of a recoverable adsorbent are very important when considering the fate of nano-adsorbents for selenium removal. Zelmanov and Semiat designed ferric oxide/hydroxide nanoparticles to adsorb selenium, achieving residual selenium concentrations less than 10 ppb while maintaining at least 95%-98% regeneration efficiency of the selenium with the nano adsorbent (Zelmanov and Semiat, 2013). They developed a process to recover the adsorbent material for reuse via membrane filtration and produce a highly concentrated selenium solution. Selenium recovery from wastewater is desirable to offset treatment costs and enable the reuse of a valuable rare element. Potential industries interested in the reuse of selenium range from dietary supplements and fertilizers to electronics, photovoltaics and imaging (Yarlagadda V. Nancharaiah and Lens, 2015).

1.5.3.2 Titanium dioxide

A remarkable amount of research effort has been dedicated to the study of nanocrystalline titanium dioxide (n-TiO_2) in past years. The application of n-TiO_2 for both selenite and selenate adsorption is one of the fields advanced by this large research initiative. Zhang et al. have shown that n-TiO_2 removes selenite and selenate, but is far less effective at removing selenate via adsorption (Zhang et al., 2009). Photocatalytic activity is an added benefit of n-TiO_2 which is able to reduce selenate to selenite in order to effectively remove both soluble contaminants. Some treatment options utilize n-TiO_2 for its reduction capabilities under the exposure to UV light and an electron hole scavenger as a result.

Sorption of selenite onto n-TiO_2 from aqueous solution is comparatively fast and effective, reaching equilibrium within 5.0 minutes (Zhang et al., 2009). This quick equilibrium is crucial to a successful treatment alternative for full scale applications. TiO_2 in the anatase form was found to be more effective than rutile for adsorbing selenite. The weak sorption behavior of selenate onto anatase is due to low affinity of selenate toward the mineral surface (Jordan et al., 2011).

Colloids of n-TiO_2 show increased adsorption capacity although the problem to retain and recycle the n-TiO_2 exists and is a major logistical issue. Many attempts have been made to immobilize n-TiO_2 in a way which does not reduce the selenite adsorption capacity. One researcher claims to have increased the adsorption capacity of nano-anatase while immobilizing it onto a nano-structure. Titanium-impregnated multi-walled carbon nanotubes (MWCNTs) can remove selenite from wastewater streams at higher capacities than nano-anatase (Bakather and Atieh, 2015).

As discussed, selenate foes not readily adsorb onto n-TiO_2 due to its low affinity to mineral surfaces. The reduction of selenate to selenite can be achieved by photoreduction on the surface of nano-anatase in the presence of an electron hole scavenger, such as formic acid. Figure 1-4 illustrates the photocatalytic mechanism for selenate reduction. Yang et al. have shown that selenate can be effectively removed this way (W. Yang et al., 2013).

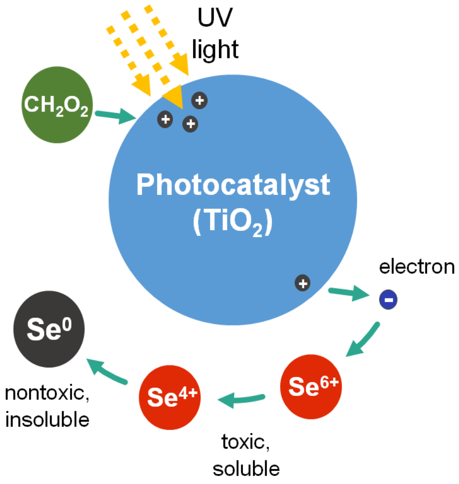

Figure 1-4. Schematic of Se^{6+} and Se^{4+} photoreduction by TiO_2 mechanism using formic acid as an electron hole scavenger.

The effect of different organic electron hole scavengers on the photocatalytic reduction of selenite and selenate was studied by Tan et al. The research team found that photoreduction of selenium anions occurred only in the presence of formic acid, methanol and ethanol (T.T.Y. Tan et al., 2003a). Photocatalytic reactions are initiated by photogenerated holes (h^+) and electrons (e^-) when the TiO_2 photocatalyst is illuminated by UV light. Previously, the team had investigated the effect of Ag-loaded TiO_2 on the photocatalytic reduction of selenate. When unmodified TiO_2 photocatalyst was used, the elemental selenium formed from the reduction of selenate was further reduced to selenide in the form of H_2Se upon the exhaustion of selenate in solution. The modified Ag-TiO_2 photocatalyst produced H_2Se simultaneously with the reduction of selenate (T.T.Y. Tan et al., 2003c). The simultaneous reduction of selenate to hydrogen selenide gas can be attributed to the electron transfer across the p-n junctions formed by the p-type Se and n-type TiO_2 semiconductors (Tan et al., 2002). Tan et al. demonstrated that unmodified TiO_2 does not generate hydrogen selenide gas directly but only upon the exhaustion of selenate in solution. This information can be used to understand and control the production of toxic hydrogen selenide gas during the reduction and removal of selenate in wastewater. Selenium oxyanion reduction has been used in parallel with adsorption mechanisms of selenite to remove selenium contaminants and has been used to photoreduce both selenate and selenite to elemental selenium (Nu Hoai Nguyen et al., 2005). In this research, Nu Hoai Nguyen et al. found that Millennium PC500 outperformed both Degussa P25 and Millenium PC25 & PC50 (all commercially available nanocrystalline TiO_2). The degree of reduction can be difficult to control, so that a portion of the selenium can be reduced below elemental selenium to form selenide or hydrogen selenide gas (H_2Se), which are extremely toxic species.

Other photocatalysts, such as zirconia mixed titania (TiZr), showed higher photocatalytic activity than standard n-TiO_2 during the reduction of selenite to elemental selenium (Aman et al., 2011). Many known modifications to titanium photocatalysts can be made to further improve selenium oxyanion reduction.

1.5.3.3 Aluminum oxide

Nanocrystalline aluminum (III) oxide or alumina has the ability to adsorb selenium oxyanions. Yamani et al. successfully developed nanocrystalline aluminum oxide-impregnated chitosan beads (AICB) as an adsorbent for both selenite and selenate. The chitosan beads provide a hydrogel matrix for the aluminum oxide to interact with water without dissolving. In addition, chitosan exhibits weak selenium adsorption to complement the aluminum oxide adsorption sites (Yamani et al., 2014). Yamani et al. also showed that nanocrystalline titanium dioxide-impregnated chitosan beads adsorb selenium in the same manner, although to a lesser extent. As with many other adsorption techniques, the presence of competing ions (such as sulphate and phosphate) hinders the adsorption capacity of the AICB due to the non-selective adsorption of anions by aluminum oxide.

Aluminum can modify the surface of SiO_2 in a binary oxide system ($Al(III)/SiO_2$) enhancing the oxyanion adsorption capacity and making the overall surface charge more positive. This unique feature can be successfully applied to selenium oxyanion removal. Selenite forms bidentate inner-sphere complexes (two covalent bonds) with $Al(III)/SiO_2$ achieving adsorption capacities for selenite and selenate of 32.7 and 11.3 mg/g, respectively (Chan et al., 2009).

1.5.3.4 Manganese iron oxide

Manganese iron oxide ($MnFe_2O_4$ – a.k.a. jacobsite) nanoparticles prepared through hydrothermal methods show excellent adsorption capacity towards selenium oxyanions. Nano-$MnFe_2O_4$ has been shown to have a higher adsorption capacity for selenium oxyanions than naturally occurring magnetite (Gonzalez et al., 2010). The removal of selenate or selenite is pH independent between pH 2 to 6 and occurs within five minutes of contact time. The presence of competitive ions Cl^- and NO_3^- had no significant effect, whereas, SO_4^{2-} and PO_4^{3-} competed with the selenium ions. The same research team later looked into the adsorption of selenium oxyanions on engineered manganese oxide (Mn_3O_4) nanomaterials which was found to have similar adsorption capacities toward selenate, but a reduced adsorption capacities towards selenite by a factor of six (Gonzalez et al., 2011).

Recently, another research team followed up on this research by measuring the effect of cobalt and copper in the place of manganese in the nanoparticles. Sun et al. found that the adsorption capacity of selenite and selenate followed the trend $CuFe_2O_4 > CoFe_2O_4 >> MnFe_2O_4$, which is consistent with the order of hydroxyl group content and surface charge on the bimetal oxide (Sun et al., 2015). The research team found the replacement of copper for manganese increased the Langmuir maximum adsorption capacity from 6.6 mg/g and 0.8 mg/g to 14.1 mg/g and 5.97 mg/g for selenite and selenate, respectively (Sun et al., 2015). Similar adsorption mechanisms were observed with selenite and selenate forming inner- and outer- sphere complexes, respectively. In the same way, Szlachta, et al. showed that Fe-Mn hydrous oxides have a high selenite adsorptive capacity with a maximum of 41.02 mg/g at pH 4 (Szlachta and Chubar, 2013).

1.5.4 Nanoscale zero valent iron (nZVI)

Research in the uses of nanoscale zero-valent iron (nZVI) for environmental remediation techniques has proven to be a popular topic for metal and organic removal from groundwater. nZVI is an efficient method for selenite and selenate removal from wastewater. Selenium oxyanions are reduced by nZVI through the same mechanisms described previously for micro-ZVI, but with a threefold increase in removal rate due to the higher surface area and more active sites (Ling et al., 2015). See Figure 1-5 for a conceptual model on the reduction of selenite on nZVI. nZVI also exhibits higher removal rates than nanoscale iron oxides ($Fe(OH)_3$), nanoscale TiO_2, and activated alumina.

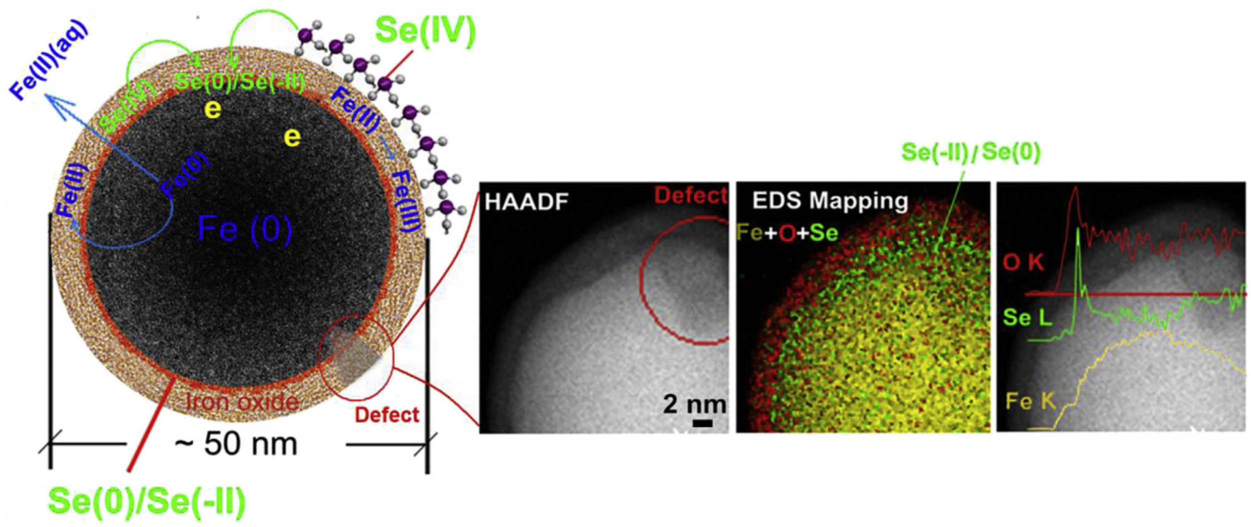

Figure 1-5. A conceptual model of the reactions of Se(IV) in core-shell structured nanoscale zero-valent iron. Figure reprinted with permission from Ling et al. (2015).

The ability of nZVI to both reduce and adsorb selenium occurs because of the oxidation of the elemental iron on the outer surface forming “green rust”. The redox reaction oxidizes Fe^{0} to Fe(II) and Fe(III) and reduces Se (VI) and Se(IV) to Se^{0} and Se (-II). Se(IV) adsorbs on the iron oxide outer surface of the particle and is then reduced to Se(-II) and Se^{0}, forming a layer of Se^{0} at the iron oxide-Fe(0) interface of the ZVI nanoparticle to a depth of as much as 6 nm on the surface (Ling et al., 2015). This treatment was shown to be capable of removing 1.3 mM selenite from water within three minutes of nZVI dosing. A similar redox process involving nZVI removes Se(VI) from wastewater and reduces it to Se(-II). Researchers were able to reduce 96% of the initial selenate from 4 ppm initial concentration, which represents a slightly lower removal rate when compared to Se(IV) (Olegario et al., 2009).

Investigation of selenate reduction in a hybrid ZVI/Fe_3O_4/Fe^{2+} (hZVI) system showed that it was able to improve the removal efficiency compared to unmodified ZVI. hZVI achieved the most effective selenate removal compared to any of the other non-hybrid (ZVI, Fe^{2+} and Fe_3O_4 alone) or partial-hybrid systems (ZVI/Fe^{2+}, Fe_3O_4/Fe^{2+} and ZVI/Fe_3O_4) (Tang et al., 2016). ZVI was the primary electron donor for selenate reduction, Fe_3O_4 served as a primary reduction site for selenate and Fe^{2+} participates in selenate reduction together with ZVI. Furthermore, Fe^{2+} was retained on the passivated surface of ZVI and Fe_3O_4, to sustain the reactivity of hZVI for rapid removal of selenate.

Immobilization techniques for treatment with nZVI have been studied in order to reduce recoverability costs. Quamme et al. entrapped nZVI in calcium alginate beads for remediation of selenium species in aqueous medium. Although bare nZVI demonstrated quicker and more efficient remediation (>97% removal in 3 h), the impregnated alginate beads were easily separated from the wastewater for disposal (<85% removal in 12 h) (Quamme et al., 2012). Iron/iron oxide functionalized membranes were developed for selenium reduction and adsorption from coal-fired power plant scrubber water at an industrial scale. Aggregation of impregnated iron oxide nanoparticles was avoided to maintain their surface area via immobilization within a polyacrylic acid (PAA)-coated polyvinylidene fluoride (PVDF) membrane (Gui et al., 2015).

1.5.5 Graphene oxide

Graphene oxide has also gained much attention recently as one of a number of emerging materials with attractive nanoscale properties. Hydrophobic graphene oxide monolayers have demonstrated promising performance in removal of heavy metals and selenium oxyanions, due to its high surface area and ample surface hydroxyl and carboxyl functional groups. Free-standing graphene oxide foam (GOF) is an excellent adsorbent for a wide range of heavy metal ions such as Cd^{2+}, Pb^{2+}, Zn^{2+}, and Fe^{3+} (Lei et al., 2014). The superior adsorption properties originate from the large surface area provided by the three-dimensional interconnected porous nanostructure of the GOF comprised of many graphene oxide sheets.

Researchers have applied the superior adsorption ability of graphene oxide to selenium removal from aqueous solutions. Fu et al. combined magnetic nanoparticles with graphene oxide to more easily separate and regenerate the absorbent for full-scale selenium removal from wastewater. The magnetic nanoparticle-graphene oxide (MGO) composite adsorbent shows a high binding capacity for both selenite and selenate. The MGO contains at least two types of hydroxyl binding sites for Se(IV) and Se(VI) located on the iron oxide nanoparticles and on the graphene oxide sheets, leading to higher adsorption capacities than pure Fe_3O_4 nanoparticles or pure graphene oxide. The MGO composites removed > 99.9% selenite and 80% selenate at a MGO dosage of 1 g L^{-1} (Fu et al., 2014).

1.5.6 Layered double hydroxide (LDH) nanocomposites

Layered double hydroxide (LDH) nanocomposites are capable of anion exchange and are promising nanomaterials for selenium oxyanion removal. LDHs are considered anionic clays; a common mineral of this family is hydrotalicite (Mg-Al-CO_3)(Kwon et al., 1988). LDH nanocomposites can incorporate anions between the hydroxide layers and act as transport vehicles leading to applications in catalysis, medical science and separation technologies (Figure 1-6).

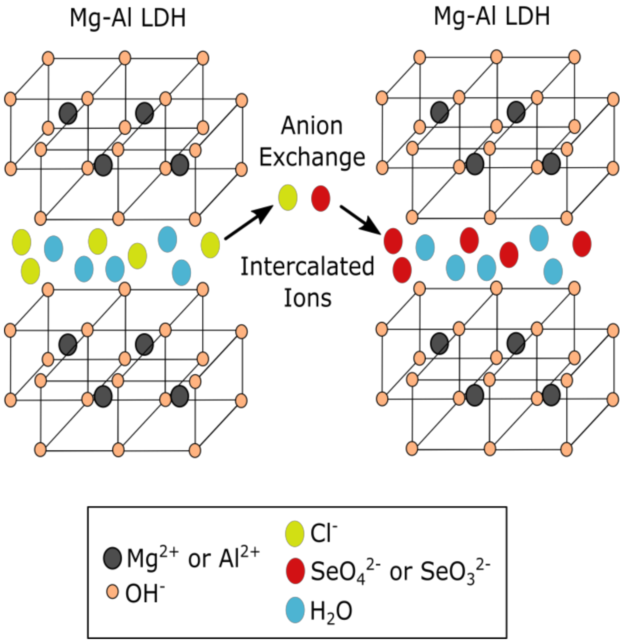

Figure 1-6. Schematic representation of LDH structure for selenium oxyanion removal. Figure adapted from Kameda et al. (2014).

Recent advances in the production process for LDHs have increased their adsorptive capacity and made promising strides towards technical feasibility for ion exchange in wastewater applications. A novel Mg-Al LDH synthesis involving an alkoxide-free sol-gel process produced a marked increase in adsorptive capacity towards selenite and selenate (Chubar et al., 2013). The alkoxide-free process increases the surface area and functional groups as well as the number of interlayer species.

The adsorption of selenite by Mg-Al-CO_3 LDHs has been shown to be much greater than that of selenate in most cases. According to the underlying mechanism proposed by Chubar the inner-sphere complexation (covalent bond formation) is the leading mechanism along with ion exchange via surface OH^- and interlayer CO_3^{2-} species for selenite. In contrast, the sorption of selenate is driven only by ion exchange (Chubar, 2014).

Mg-Al LDHs can be doped with different metals to increase the adsorption and removal of their target anion species (Kameda et al., 2014). Kameda et al. found that Mg-Al-Cl LDH doped with Fe^{2+} was able to remove Cr(VI) through anion exchange of $Cr_2O_7^{2-}$ with the intercalated Cl^-. The same group also found that the same nanomaterial was superior to its non-Fe^{2+} doped counterpart for As(V) removal (Kameda et al., 2015). The excellent performance of this LDH for Cr(VI) and As(V) removal is due to both the anion exchange properties of Mg-Al LDH and reducing activity of the Fe^{2+}-doped Mg-Al LDH. Other modifications have been made to LDH nanomaterials to enhance their adsorptive capacity. Mg-Fe-CO_3 LDHs coated on cellulose fibers were used to selectively adsorb and identify different species of selenium in river and lake water at extremely low concentrations (≤ 0.2 ppb) (Chen and An, 2012). The adsorption of selenite from dilute synthetic aqueous solutions (20 ppb), meant to mimic power-plant effluents, onto LDHs occurs to a lesser extent, as expected (Yang et al., 2005).

The flexibility of the LDH platform is another advantage for the removal of inorganic oxyanions (e.g. arsenite, chromate, selenite, selenate, etc.). With the recent advances in LDH synthesis along with different doping techniques the future for selenium oxyanion removal via LDH adsorption is very promising. The main advantage of LDHs over conventional anionic exchange is their much higher anion exchange capacity for targeted oxyanions. Also, the rate at which LDH adsorption removes harmful selenium oxyanions far surpasses that of current biological treatment (Goh et al., 2008). Currently, the main limitations for the use of LDHs include leaching of precursor metals from LDH into the wastewater at low pH, costly regeneration and raising of pH of wastewater in the presence of calcined LDHs (Goh et al., 2008).

1.5.7 Polymer-clay nanocomposites

Over the past years, polymer-clay nanocomposites have been studied for environmental applications such as sorbents for anionic pollutants. Chitosan-montmorillonite nanocomposites have been well studied for the adsorption of a vast array of anionic pollutants and are able to selectively adsorb selenate from contaminated waters (Celis et al., 2012).

Polymer polycations such as PDADMAC, chitosan and PVP-co-S have been tested. Chitosan had the highest affinity towards adsorption of selenate (>99% removal) (Bleiman and Mishael, 2010). The removal of selenium by the chitosan-montmorillonite nanocomposite was influenced by the polymer loading of the composite. The nanocomposites where two polymer layers were intercalated within the clay were more effective at selenate removal. In the presence of excess sulfate (competing anion) selenium removal was favoured for selective removal over a wide range of polymer loadings in the nanocomposite. Selectivity increased with the extent of polymer loading.

The regeneration of the chitosan-montmorillonite was accomplished with a wash of dilute sodium hydroxide in order to raise the pH to desorb the selenate from the surface of the nanocomposite. Desorption of selenium was achieved with 44% efficiency. Although this is a relatively low desorption efficiency, the performance of the nanocomposite adsorbent increased by 50% after the first wash (Bleiman and Mishael, 2010). This is an indication that optimization opportunities exist, which warrants further research for this adsorption technology.

1.6 Recyclability and reusability of nanomaterials

Several factors including size, charge and colloidal stability make nanoparticles very difficult to separate post-treatment. Due to cost and public health concerns, it is important to retain and recycle the nanomaterials for subsequent treatment cycles. Several methods have been used for separating nanoparticles from aqueous solution - mainly magnetism, cross-flow filtration and centrifugation (Ali, 2012). Due to the high flow rates generally encountered in selenium removal, the latter two options are not as economically attractive.

Post-separation of magnetic particles is made possible by applying a magnetic field to the treated wastewater. The most common magnetically separated nanoparticles are iron oxide and functionalized iron oxide particles for selectively removing selenium from aqueous solution. Iron oxide nanoparticles exhibit superparamagnetic properties resulting in a strong magnetic moment when placed in an external magnetic field. Fu et al. synthesized functionalized water-dispersible magnetic nanoparticle-graphene oxide (MGO) composites in order to remove selenium oxyanions from wastewater (Fu et al., 2014). This MGO composite underwent 10 cycles of sorption-elution with approximately only 1% reduction in selenium removal over the entire 10 cycles.

Recently, a large research effort has focused on designing immobilized nanoparticle treatment systems to avoid post treatment separation all together. Immobilization techniques vary depending on the nanomaterial used for selenium removal. Self-assembled monolayer ligands immobilized on mesoporous silica were cycled through a sorption-elution-reuse cycle eight times only losing approximately 1% efficiency per cycle (Awual et al., 2015b). Many immobilization techniques hinder the treatment efficiency of the nanoparticles. Considerable research has been done to develop simple immobilization techniques which maintain, or in some cases, improve removal efficiency. Researchers claim to have increased the adsorption capacity of nano-anatase after immobilizing it onto multi-walled carbon nanotubes (Bakather and Atieh, 2015). Nanocrystalline aluminum oxide was impregnated in chitosan beads and nZVI was entrapped in calcium alginate beads for use in ion-exchange water treatment systems for selenium removal (Quamme et al., 2012; Yamani et al., 2014). Similarly, Mg-Fe-CO_3 LDHs were coated on cellulose fibers in order to retain the valuable nanomaterial for subsequent treatment cycles (Chen and An, 2012). Immobilization allows selenium removal technologies to exhibit desired properties of nanomaterials all while maintaining a recyclable platform for regeneration and reuse.

Regeneration of the selenium removing nano-adsorbent particles is highly pH dependent. Adsorption of selenium oxyanions is optimal at lower pH, while desorption is optimal at high pH. Nano-adsorbents are commonly washed with a low-strength sodium hydroxide elution solution in between cycles in order to desorb the selenium contaminants (Awual et al., 2014; Fu et al., 2014; Kameda et al., 2014; Quamme et al., 2012). The regeneration of the nano-reducing particles is less common since the reducing agents are generally oxidized into metal oxides, which can still act as an adsorbent for selenium oxyanions. Mainly, the immobilization of nano-reducing agents allows for simple capture and replacement within the treatment system.

1.7 Research challenges

Nanotechnology applied to selenium removal from wastewater has a promising future; however, several obstacles exist to full-scale treatment systems of real wastewater. Some nanotechnologies are close to full scale implementation; while others require significant research before consideration for industrial applications. Given the many advantages of nanomaterials, further research into advanced nanotechnologies for wastewater treatment is warranted.

The major research challenges for full-scale industrial wastewater treatment include: operating pH, unknown adverse health impacts, cost-effectiveness and ability to scale up.

The first main research challenge is that nano-adsorbents are most effective in low pH ranges. Se-containing wastewaters such as FGD and acid mine drainage wastewaters have low pHs. Typically solid precipitation and pre-treatment of highly contaminated wastewater involves the addition of lime ($Ca(OH)_2$) which raises the pH of the wastewater. A nanotechnology would ideally be used as a polishing step intended to remove total selenium to a concentration of <5 ppb. Much research is needed to expand the pH operating range of nano-adsorbents and integrating the nanotechnologies within existing wastewater treatment systems.

Secondly, more research is required to study the safety profiles of the nanomaterials. Some of them are non-biodegradable and can enter into the human body through different pathways (Pisanic II et al., 2007). The study of the behaviour of nanoparticles in the environment, as well as their ecotoxicology has been a primary concern for scientists and environmental regulators. Compared to conventional or other emerging contaminants, nanoparticles pose some new challenges for scientists. Many engineered nanoparticles are functionalized and this significantly affects their behaviour. Changes in functionalization by environmental factors can lead to changes in reactivity and behaviour in the environment (Mueller and Nowack, 2008; Nowack and Bucheli, 2007). These changes make it very hard to establish accurate toxicity tests on nanoparticles when they are subject to change depending on differing environmental factors. The mobility and release of nanoparticles as well as their health effects still require more research before full scale implementation.

Thirdly, the cost-effectiveness of nanomaterials can be improved by improving the regeneration and reuse of the materials. The cost of nanomaterials is relatively high, with the exception of $nTiO_2$ and iron oxide nanoparticles (Qu et al., 2013).

Finally, the ability to scale up to full scale wastewater treatment plants is crucial for further development of nanomaterials for selenium removal from wastewater. Further research into immobilization and recycling techniques of nanomaterials is vital in order to utilize nanomaterials in large scale reactors.

1.8 Conclusions

Nanotechnology offers highly promising and effective solutions to treating selenium contaminated wastewaters. Global interest on selenium removal technologies has increased due to the recent findings on the effects of chronic exposure of aquatic life to Se (U.S. EPA and Office of Water, 2015). The new limits have already placed pressure on coal mining, coal fired power plants, agricultural and mining practices to upgrade their wastewater treatment systems in order to diminish their effluent selenium levels.

Nanotechnology is a favorable option to reduce selenium concentrations to meet the microgram level permissible limits. These nanomaterials exhibit high surface adsorbing activity, high reactivity, selectivity and sustainable treatment capability to remove soluble selenium oxyanions from wastewater. Recycling of nanomaterials provides a cost-effective strategy to enable these specialized nanomaterials to be used on an industrial scale. Many of these technologies show great promise in the laboratory and require further research and development to become commercially available but are ideal candidates for fast and inexpensive technologies. We can better facilitate the transfer of these nanomaterials from the laboratory to the wastewater treatment market by cooperation through academia, industry and government partnerships.

1.9 Thesis structure

1.9.1 Aims

Given the challenges facing Se removal from industrially impacted water, the objective of my research is to develop a treatment methodology which can overcome the many limitations and challenges of conventional Se removal techniques. The focus is on the photocatalytic reduction of Se oxyanions in industrially impacted waters and demonstration of the many advantages in the use of nanomaterial photocatalysts for the removal of Se to below 2 $\mu g\ L^{-1}$. Photocatalysis with TiO_2 is an exceptionally powerful advanced reduction process (ARP) that has been proven to eliminate a variety of toxic inorganic materials, including Se. Given that TiO_2 is an abundant, chemically stable, low-cost and recyclable photocatalytic material, it represents a suitable starting material to prove the viability of Se photocatalytic reduction processes for industrial water sources. Therefore, the primary goal of this thesis is to evaluate the potential of heterogeneous photocatalysis to treat Se oxyanion compounds in flue gas desulphurization wastewater (FGDW), mine-impacted water (MIW) and brines generated from both FGDW and MIW, as well as applying nanotechnology engineering principles to develop novel materials and catalyst recycling systems to facilitate and support deployment of these methods at industrial scales. The specific aims of this thesis are as follows:

(1) Assess the effectiveness of photocatalytic reduction for the removal of selenate using TiO_2 in high concentration sulfate-containing wastewaters such as FGDW, and evaluate the optimum operating conditions for Se removal;
(2) Assess the effectiveness of photocatalytic reduction for the removal of selenate over TiO_2 in the presence of more thermodynamically favorable electron acceptors such as nitrate in MIW and determine the ideal operating conditions for Se removal;
(3) Probe and understand the mechanisms for selective reduction of selenate on TiO_2 in the presence of more thermodynamically favorable electron acceptors, such as nitrate, in MIW and elucidate the mechanism responsible for the selective two-stage Se reduction;
(4) Expand upon mine-impacted water treatment knowledge to better understand the treatment of high-concentration Se brines and tune the treatment conditions for controllable Se product generation to engineer for Se recovery;

(5) Design nanomaterial photocatalysts which can help tune the final Se product selectivity toward either solid elemental Se or gaseous hydrogen selenide gas by engineering the catalyst's photogenerated electron affinity;

1.9.2 Research chapters

The research portion of this thesis is organized into five chapters (Chapters 2-6). I begin by assessing the viability of photocatalytic reduction of selenate (SeO_4^{2-}) over TiO_2 as a treatment method for selenium (Se) removal from flue gas desulphurization wastewater (FGDW). In Chapter 2, entitled *Photocatalytic reduction of selenate in flue gas desulphurization wastewater: Study of kinetic factors to elucidate a direct Z-scheme reaction mechanism*, I elucidate the mechanisms of electron transfer involved in the simultaneous generation of elemental selenium (Se^0) and hydrogen selenide (H_2Se) through two consecutive first-order reductions under a direct Z-scheme photocatalyst arrangement between photo-deposited Se and TiO_2. The effects of many operating parameters (pH, temperature, wastewater matric composition, electron donor type and concentration, selenate concentration, catalyst concentration, dissolved oxygen concentration) on reaction kinetics are investigated.

In Chapter 3, entitled *Factors affecting kinetics of the photocatalytic reduction of selenate over TiO_2 in mine impacted water*, the focus is on the treatment of selenate containing mine-impacted water (MIW) through photocatalytic reduction on TiO_2. MIW and FGDW have similar water composition profiles with the exception of nitrate contained in MIW. Similar reactor parameters and conditions are investigated as in Chapter 2, in order to understand the impact of the presence of nitrate. The existence of a selective reduction pathway of selenate in a complex wastewater is reported, allowing for effective selenate reduction in the presence of high concentrations of sulfate and nitrate. The integration of a photocatalytic selenate reduction with subsequent biological nitrate reduction is considered. Investigation into the effects of various electron hole scavengers (EHS) (i.e. acetic acid, ethanol, methanol, glycerol and formic acid) on photocatalytic reaction kinetics is completed to assess EHS compatibility with downstream biological reduction processes and the use of unreacted EHS as an electron donor for biological nitrate reduction.

In Chapter 4, entitled *Selective removal of Se through selenate specific photocatalytic reduction over TiO_2 in the presence of nitrate and sulphate in mine impacted water*, I investigate the primary mechanistic drivers for selective reduction of selenate in the presence of sulfate, nitrate, carbonate and other dissolved species in complex industrial wastewaters. The competitive adsorption between sulfate (~2,000x molar concentration of selenate) and the competition for electrons with nitrate (~250x molar concentration of selenate) affect the reduction of selenate through unique mechanisms, although selective reduction is still achieved. We proposed an electron transfer mechanism in which TiO_2 conduction band electrons are responsible for the reduction of selenate to elemental Se (Se^0) and both carbon dioxide radicals ($CO_2^{\bullet -}$) and Se conduction band electrons are responsible for the further reduction of Se^0 to hydrogen selenide (H_2Se).

In Chapter 5, entitled *Tunable production of elemental Se vs H_2Se through photocatalytic reduction of selenate in synthetic mine impacted brine: Engineering a recoverable Se product*, I investigate the tunability of Se reduction products ($Se^0_{(s)}$ vs. $H_2Se_{(g)}$) during the photocatalytic reduction of selenate over TiO_2, using formic acid as an electron hole scavenger, in synthetic mine-impacted brines (SMIB). By using temperature and electron donor (i.e. formic acid) concentration as the variables, the selectivity towards generating either Se reduction product can be controlled, while effectively removing Se from SMIB to $< 2\ \mu g\ L^{-1}$ from an initial Se concentration of $> 3,300\ \mu g\ L^{-1}$. It is shown that an increase in solution temperature leads to a marked increase in selenate removal kinetics and an increase in selectivity towards $H_2Se_{(g)}$, while increasing the concentration of formic acid leads to an increase in selenate removal kinetics and a decrease in the selectivity towards $H_2Se_{(g)}$. Thus, photocatalysis presents a unique approach for the generation of gaseous H_2Se or solid Se^0, both of which have a high potential for recovery and reuse from mine-impacted water and brine. With proper design and safety considerations, the advantages of recovering Se from waste streams provides an economical solution to a global environmental challenge.

In Chapter 6, entitled *Enhanced photocatalytic selectivity of noble metallized TiO_2 (Ag-, Au-, Pt- and Pd-TiO_2) nanoparticles in the reduction of selenate in water: Tunable Se reduction product $H_2Se_{(g)}$ vs. $Se_{(s)}$*, I deposit noble metals (Au, Ag, Pt and Pd) onto TiO_2 to produce heterogeneous nanoscale photocatalysts. These catalysts exhibit work-function dependent bimodal selectivity of final products during the photocatalytic reduction of selenate to elemental Se (Se^0) or hydrogen selenide gas (H_2Se). A catalyst design approach for product selectivity is presented, as compared to the reactor parameter control approach presented in Chapter 5 and allows for control of the Se reduction product selectivity which is highly desired depending on the water treatment and Se recovery goals. The Se-noble metal-TiO_2 (Se-NM-TiO_2) photocatalytic system is structured in a direct Z-scheme arrangement, when Au, Ag or Pt are used, allowing for high selectivity towards gaseous H_2Se. In contrast, Pd acts as an electron sink which decreased the reducibility of the photogenerated electrons and shifted the selectivity towards solid Se^0. Tunability of the Se reduction product is key in designing a sustainable treatment approach with a potential for Se capture and reuse.

In the final concluding chapter (Chapter 7), I combine the major research findings, highlight major breakthroughs outlined in this thesis and provide a way forward for the transition from photocatalytic reduction of selenate at a laboratory scale into industrially relevant operating systems. A number of recommendations are made that suggest ways to improve catalyst efficiency, better understand the final fate of Se and develop a feasible technology for practical development.

2 Photocatalytic reduction of selenate in flue gas desulphurization wastewater: Study of kinetic factors to elucidate a direct Z-scheme reaction mechanism

This chapter is modified from:

Holmes, A.B., Livera, D., Khan, D., McBride, S., and Gu, F. (in preparation). Photocatalytic reduction of selenate in flue gas desulphurization wastewater: Study of kinetic factors to elucidate a direct Z-scheme reaction mechanism.

2.1 Summary

In this paper, we uncover mechanisms of electron transfer through kinetic modelling which have a substantial impact on the understanding and viability of photocatalytic reduction of selenate (SeO_4^{2-}) on TiO_2 as a treatment method for selenium (Se) removal from flue gas desulphurization wastewater (FGDW). Herein, the simultaneous generation of elemental selenium (Se^0) and hydrogen selenide (H_2Se) through two consecutive first-order reductions is reported under a direct Z-scheme photocatalyst arrangement between photodeposited Se and TiO_2. In this work, we demonstrate the ability to reduce selenate in FGDW containing co-existing ions with concentrations more than 2,500 times that of selenate. High concentrations of Ca^{2+} and SO_4^{2-} contribute to a high apparent activation energy (90.09 kJ mol^{-1}) leading to the production of mainly H_2Se gas as a reaction product. The reaction occurs through a Langmuir-Hinshelwood (LH) mechanism under an adsorption-limited regime, while dissolved oxygen (DO) is inhibitory to the reduction through the formation of hydroperoxyl radicals ($^{\bullet}O_2H$) responsible for the re-oxidation of Se^0 back to SeO_4^{2-}. Based on this understanding of the reaction mechanisms, the complete removal (< 1 μg L^{-1}) of selenate through photocatalytic reduction on TiO_2 in FGDW is shown for the first time.

2.2 Introduction

Selenium (Se) and its compounds are seen around the world as environmental contaminants resulting from industrial activities such as coal and mineral mining, metal smelting, oil extraction/refining, agricultural irrigation and coal-fired power plants (Santos et al., 2015). At low levels, Se is an essential micronutrient to animals with a very narrow therapeutic window and a tendency to bioaccumulate (Hamilton, 2004). At higher concentrations, Se is toxic and the effects depend on various factors, including its oxidation state. To limit the health impact of Se, governments and environmental regulators such as the World Health Organization (WHO) currently hold a provisional guideline value of 40 μg L^{-1} as the maximum concentration limit (MCL) in drinking water. Recently, stricter guidelines of 1.5 μg L^{-1} and 3.1 μg L^{-1} in lentic and lotic ecosystems respectively, have been proposed by the United States Environmental Protection Agency (U.S. EPA) for the protection of aquatic life.

Primarily, Se species in wastewater exist in the inorganic forms of selenate (SeO_4^{2-}), selenite (SeO_3^{2-}) and their protonated anions $HSeO_4^-$ and $HSeO_3^-$. Se can also exist in a variety of other compounds; however, selenate is the dominant species of concern due to its high mobility, toxicity and low affinity to soil interfaces (Zawislanski et al., 2003). Hence, selenate is the dominant Se species in industrially produced wastewaters such as wet flue gas desulphurization wastewater (FGDW) from coal-fired electric generating power plants (Lenz and Lens, 2009). Several available selenate removal technologies utilize physical, chemical or biological treatment techniques. Physical removal techniques such as reverse osmosis and evaporation/crystallization technologies are high cost and energy intensive (Richards et al., 2011). Adsorptive removal techniques such as ion exchange, ferrihydrite adsorption and activated alumina have demonstrated little success at reaching below 10 $\mu g\ L^{-1}$ Se due to the low affinity of selenate to mineral surfaces resulting from weak outer-sphere complex surface interactions (Ippolito et al., 2009; Rovira et al., 2008). In addition, physical removal techniques merely concentrate selenate and other ions into a brine stream, rendering the subsequent treatment of brine a major problem. Chemical removal techniques require long retention times and high operating and chemical costs to achieve sufficient removal of selenate (Mavrov et al., 2006). Biological reduction techniques are the most widely implemented method to convert selenate to elemental selenium although they are highly sensitive to fluctuating FGDW composition, operating parameters and biomass health, and so are difficult to control (Jain et al., 2015; Staicu et al., 2015b). Therefore, a need exists for the development of a robust and effective selenate removal technology.

Heterogenous photocatalytic reduction of selenate on semiconductor materials, such as titanium dioxide (TiO_2), has shown great potential for selenate removal (Holmes and Gu, 2016; Leshuk et al., 2018; Nguyen et al., 2005b). Photocatalysis exploits the unique electronic band structure of semiconductors to catalyze redox reactions. Upon irradiation with high-energy light, electrons are excited into the conduction band (e_{cb}^-) and electron holes form in the valence band (h_{vb}^+). This e_{cb}^--h_{vb}^+ pair can recombine within a few nanoseconds (Schneider et al., 2014), or it can be captured by species interacting with the semiconductors surface. An acceptor capturing the e_{cb}^- is reduced while a donor reacting with the h_{vb}^+ is oxidized, while the semiconductor catalyst remains unchanged. Utilization of an electron hole scavenger, such as methanol, ethanol (T.T.Y. Tan et al., 2003a), formic acid (FA) (Kikuchi and Sakamoto, 2000; Sanuki et al., 1999; T.T.Y. Tan et al., 2003b), sodium formate (Nguyen et al., 2005b), or ethylenediaminetetraacetic acid (EDTA) (Labaran and Vohra, 2014), can limit the recombination of the e_{cb}^--h_{vb}^+ pairs and markedly increase the efficacy of selenate reduction. Among these hole scavengers, FA demonstrates the highest electron hole scavenging potential leading to the highest selenate reduction rates (T.T.Y. Tan et al., 2003a).

Previous studies which investigated the photocatalytic reduction of Se oxyanions were primarily conducted in a solution prepared with DI and a Se oxyanion salt (Kikuchi and Sakamoto, 2000; Labaran and Vohra, 2014; Nguyen et al., 2005b; T.T.Y. Tan et al., 2003b, 2003a). However, FGDW is comprised of high concentrations of other anions and cations, such as Cl^-, CO_3^-, SO_4^- and Ca^{2+}, which can influence the overall reduction markedly (Al-Abed et al., 2008). Nakajima et al. investigated the photocatalytic reduction of selenate in simulated FGDW and observed that the reduction rate is inhibited in the presence of sulfate (Nakajima et al., 2013, 2011). The studies suggested that selenate in simulated FGDW could not be removed by photocatalytic reduction due to the excess amount of co-existing SO_4^{2-}.

Herein, the authors provide insight into the selenate reduction mechanism and provide further understanding to overcome kinetic limitations even in the presence of SO_4^{2-} and other co-existing ions in FGDW. The specific objectives of this study are to (1) investigate the ability of TiO_2 to remove selenate from FGDW, and (2) examine the various factors influencing the reaction to better understand the mechanism and optimize FGDW treatment.

2.3 Materials and methods

2.3.1 Materials

Flue gas desulphurization wastewater (FGDW) was provided by a coal-fired power plant in the southeastern United States from two separate sampling locations in their wastewater treatment process and stored at 4 °C in the dark. The first sampling location of the FGDW was the effluent of the hydrocyclones, primarily used for coarse calcium sulphate solid removal. The second sampling location followed coagulation-flocculation (CF) pretreatment of the effluent from the hydrocyclones. Briefly, the CF pretreatment included lime addition, settling, pH adjustment, organo-sulfide addition, ferric chloride addition, polymer addition, settling and sand filtration. FGDW was then subsampled in aliquots and passed through a 1.5 μm glass microfiber filter. A full chemical analysis of the industrial FGDW (after CF pretreatment) can be found in Table A-1. The effect of CF pretreatment on the photocatalytic removal of Se is shown in Figure A-1 and discussed in Appendix A. In some studies, simulated FGDW was generated by dissolving reagent grade salts in DI water at similar concentrations to industrial FGDW to run controlled experiments.

Titanium dioxide nanoparticles (Aeroxide P25, ~10-50 nm particle diameter, 55 m^2 g^{-1} surface area, Acros) were used as received. P25 TiO_2 nanoparticles have been extensively studied and characterized in the literature and is often used as a benchmark photocatalyst. Formic acid (ACS reagent, 97%, Alfa Aesar) was used as an electron hole scavenger. Sodium selenate (<0.1% impurities, BioXtra, Sigma-Aldrich), calcium chloride (anhydrous, ACS reagent >96%, Sigma-Aldrich), magnesium chloride (anhydrous >98%, Sigma-Aldrich), sodium chloride (reagent grade, Sigma-Aldrich), sodium sulphate (anhydrous reagent grade >99%, Sigma-Aldrich), hydrochloric acid (37%), sodium hydroxide (ACS grade, Sigma-Aldrich) were used to synthesize simulated FGDW.

2.3.2 Photocatalytic experiments

The photocatalytic reactor apparatus consists of an air tight stainless-steel reactor vessel of 1.0 L capacity with a quartz-window through which UV is irradiated. The experimental apparatus is illustrated in Figure A-2. FGDW was added to an internal PTFE liner followed by formic acid and TiO_2. The suspension was stirred for 1 hour under nitrogen to allow dark adsorption before UV irradiation. Samples of FGDW were taken throughout the treatment to determine both total and dissolved Se, through unfiltered and filtered samples, respectively. The apparatus was exposed to varying UV wavelengths and intensities while the solution temperature, pH, h_{vb}^{+} scavenger concentration, TiO_2 concentration and Se concentration were also varied. Three UV lamps were used to vary photon irradiance (E_p). The irradiance absorbable by TiO_2 (230-388 nm) varies with the lamp used: (1) UVA fluorescent bulbs (Philips F20T12/BL, λ_{Peak} = 365 nm, $E_p = 1.069 \times 10^{15}$ photons cm^{-2} s^{-1}), (2) UVC fluorescent bulbs (Atlantic Ultraviolet 15225-L70, λ_{Peak} = 254 nm, $E_p = 3.776 \times 10^{15}$ photons cm^{-2} s^{-1}), and (3) UVA fluorescent bulb (Blak Ray B-100A 95-0044-22, λ_{Peak} = 365 nm, $E_p = 9.891 \times 10^{15}$ photons cm^{-2} s^{-1}). Photon irradiance was determined through potassium ferrioxalate actinometry (Bowman and Demas, 1976; Hatchard and Parker, 1956) in each lamp-reactor pair to enable evaluation of experimental apparatus variation. Variation in fluence was used instead of operating time to make our results comparable with other studies. Unless otherwise noted, the photocatalytic experiments were completed using a Blak Ray lamp under the following conditions: 300 K, pH 3, 300 mg L^{-1} formic acid, 0.2 g L^{-1} P25 TiO_2, λ_{Peak} = 365 nm, and $E_p = 9.891 \times 10^{15}$ photons cm^{-2} s^{-1}.

2.3.3 $O_2^{\bullet-}$ / $^{\bullet}O_2H$ radical experiments

Dihydroethidium (DHE, BioReagent > 95%, Sigma-Aldrich) was used to quantitatively detect superoxide radical ($O_2^{\bullet-}$) generated by TiO_2 photoreduction in the presence of O_2. The fluorescence of the product formed from the reaction of DHE and oxidative molecules was measured by a fluorimeter and converted into a molar generation rate using a calibration curve for 2-hydroxyethidium obtained by reacting known amounts of DHE with potassium nitrosodisulfonate (Fremy's Salt, Sigma-Aldrich), which has been demonstrated to yield the same superoxide-specific oxidation product (Laurindo et al., 2008). To investigate the role of H_2O_2 in the system, a spectrophotometric method was employed based on the reduction of Cu(II) by H_2O_2 in the presence of excess 2,9-dimethyl-1,10-phenanthroline (DMP, >95%, Sigma-Aldrich). Further details on the radical experiments are provided in Appendix A.

2.3.4 Analytical methods

Se concentration was determined in accordance with the U.S. EPA suggested Se determination technique (APHA 2009, Method 3114B/C) using hydride generation inductively coupled plasma optical emission spectroscopy (HG-ICP-OES, Teledyne Prodigy ICP and Cetac HGX-200 advanced membrane hydride generation system, LOD = 1 µg L^{-1}). Both dissolved and total Se were determined by HG-ICP-OES following acid digestion protocol U.S. EPA Method 3050B (U.S. EPA, 1996). The insoluble Se fraction (considered to be elemental Se) present in the water was calculated by the difference of total and dissolved Se concentrations. Gaseous H_2Se was calculated from the difference between the initial total Se in the water and total Se in the TiO_2 suspension after UV exposure. Based on several past studies on photocatalytic reduction of selenate on TiO_2 (Nguyen et al., 2005b; Sanuki et al., 1999; T.T.Y. Tan et al., 2003a), the gaseous Se species is assumed to be H_2Se although direct identification of the gaseous Se species is a challenging task (Kot and Namiesńik, 2000; Uden, 2002). Speciation of selenate and selenite was done with and without an acid pre-reduction prior to HG-ICP-OES, respectively. Pre-reduction involving acid digestion of the sample ensures all remaining Se(VI) in solution is converted to Se(IV), which can then be completely reduced to Se(-II) by sodium borohydride, within the hydride generation system.

Nitrate concentration was determined using ion chromatography (IC, Dionex LC10-2 equipped with a low-capacity Dionex IonPac AS17-C IC column, LOD = 0.033 mg L^{-1}). Total organic carbon (TOC, APHA 5310B, combustion temperature 800 °C), chemical oxygen demand

(COD, APHA 5220D), biochemical oxygen demand (BOD, APHA 5210B), anion concentration by ion chromatography (bromide, chloride, fluoride, nitrate, nitrite and sulfate, EPA 300.0), speciated alkalinity (as $CaCO_3$, EPA 310.2), and total and dissolved metals by inductively coupled plasma mass spectrometry (ICPMS, EPA 200.2/6020A and APHA 3030B/6020A) were measured according to standard methods by ALS Environmental (Waterloo, ON, Canada), a laboratory accredited by the Canadian Association for Laboratory Accreditation (CALA) according to international standards (ISO 17025).

2.3.5 Experimental methodology

Various experiments are conducted to understand the nature of the photocatalytic reduction mechanism of selenate in FGDW. First, the speciation of Se throughout the reaction is investigated to better understand the two reduction reactions occurring concurrently. Then, both the effect of temperature and salt concentration experiments are completely, to highlight their impact on the apparent activation energy of the reaction. These experiments are followed by investigations into the effect of electron hole scavenger concentration, selenate concentration, catalyst concentration, pH and dissolved oxygen concentration on the selenate photocatalytic reduction reaction. Finally, from the results of these experiments and the thorough investigation of the photocatalytic reduction in FGDW, the reaction mechanism is proposed and discussed in detail.

2.4 Results and Discussion

2.4.1 Se speciation during selenate photocatalytic reduction

Experiments were conducted to understand the speciation of Se during the photocatalytic reduction of selenate in FGDW to better understand the removal mechanism. Figure 2-1 shows the removal of selenate (SeO_4^{2-}) and the generation of both solid elemental Se (Se^0) and hydrogen selenide gas (H_2Se) during the photocatalytic reduction of selenate over TiO_2, using formic acid as an electron hole scavenger in FGDW. The reaction vessel was purged with nitrogen to remove produced hydrogen selenide gas during the reaction. SeO_4^{2-} is reduced directly to Se^0, bypassing the intermediate SeO_3^{2-}, in a six-electron reduction of SeO_4^{2-}, see Figure A-3 in Appendix A. The photocatalytic reduction of SeO_4^{2-} follows a two-step reaction outlined in eq. 2.1 & 2.2, with the reduction of SeO_4^{2-} to Se^0 followed by the further reduction to H_2Se. Pseudo first-order kinetic models developed for the simultaneous reductions of SeO_4^{2-} and Se^0 (eq. 2.3 through 2.5) fit well with experimental data (Figure 2-1). It should be noted that the heterogenous nature of the photocatalytic system is discussed in more detail using Langmuir-Hinshelwood models in a later section. Derivation of this model can be found in Appendix A.

$$SeO_4{}^{2-}{}_{(aq)} + 8H^+ + 6e_{cb}^- \overset{k_1}{\rightarrow} Se^0{}_{(s)} + 4H_2O \quad (E^0 = 0.5\text{ V } vs.\text{ SHE}) \tag{2.1}$$

$$Se^0{}_{(s)} + 2H^+ + 2e_{cb}^- \overset{k_2}{\rightarrow} H_2Se_{(g)} \quad (E^0 = -0.6\text{ V } vs.\text{ SHE}) \tag{2.2}$$

$$\left[SeO_4{}^{2-}{}_{(aq)}\right] = \left[SeO_4{}^{2-}{}_{(aq)}\right]_0 e^{-k_1 t} \tag{2.3}$$

$$\left[Se^0{}_{(s)}\right] = \frac{k_1\left[SeO_4{}^{2-}{}_{(aq)}\right]_0}{k_2 - k_1}\left(e^{-k_1 t} - e^{-k_2 t}\right) \tag{2.4}$$

$$\left[H_2Se_{(g)}\right] = \left[SeO_4{}^{2-}{}_{(aq)}\right]_0 \left[1 + \frac{1}{k_1 - k_2}\left(k_2 e^{-k_1 t} - k_1 e^{-k_2 t}\right)\right] \tag{2.5}$$

where k_1 and k_2 are $0.657\ cm^2/10^{20}\ photons$ and $1.397\ cm^2/10^{20}\ photons$ respectively.

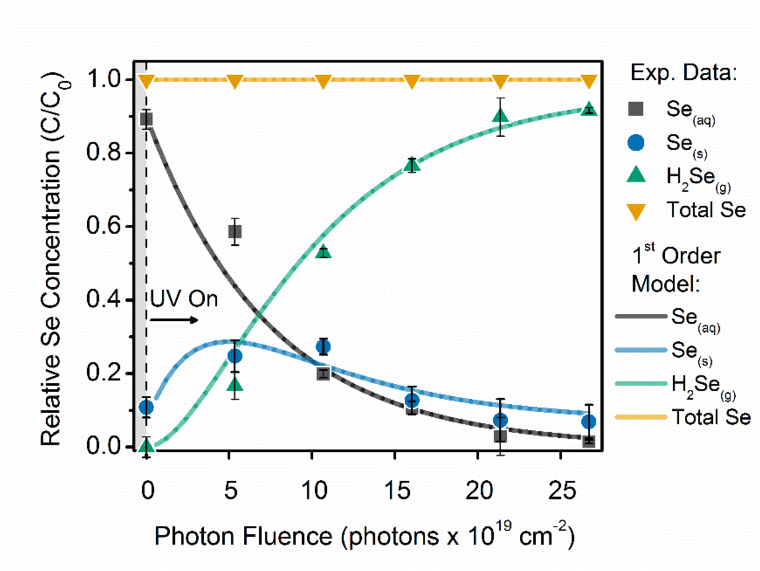

Figure 2-1. Variation of relative Se concentrations with fluence during the photocatalytic reduction of selenate in FGDW. Model estimates are obtained by fitting a first-order consecutive reduction of selenate to elemental selenium and hydrogen selenide to experimental data.

The standard potential for the reduction outlined in eq. 2.2 (-0.6 V *vs.* SHE) is more negative than the conduction band (CB) of TiO_2 (-0.1 V *vs.* SHE); thus, it is thermodynamically unfavourable for electrons in the TiO_2 CB to reduce Se^0. Since the reaction proceeds with simultaneous production of H_2Se and Se^0, experimentally this suggests a more complex mechanism for the reductions than that given by eq. 2.1 and 2.2. Previous researchers who focused on the photoreduction of selenate in DI water claimed that the two-step reduction of selenate, in eq. 2.1 & 2.2, are completely independent consecutive reactions where eq. 2.2 only occurred after eq. 2.1 was near completion and selenate was near exhaustion (T.T.Y. Tan et al., 2003b, 2003a). The generation of H_2Se did not occur during the selenate reduction but was only observed when the selenate ions were nearly exhausted from the solution (Tan et al., 2002). Tan et al attributed this characteristic two-step reaction to the difference in reduction potentials of the Se^0/Se^{2-} and Se^{6+}/Se^0 couples. See Figure 2-2a for the electronic band structure of the Se-TiO_2 system. Since the Se^0/Se^{2-} couple lies above the TiO_2 conduction band, the reduction of Se^0 to H_2Se is thermodynamically unfavourable (Tan et al., 2002). However, from our experimental findings H_2Se generation is observed from the beginning of the reaction and hence warrants further investigation.

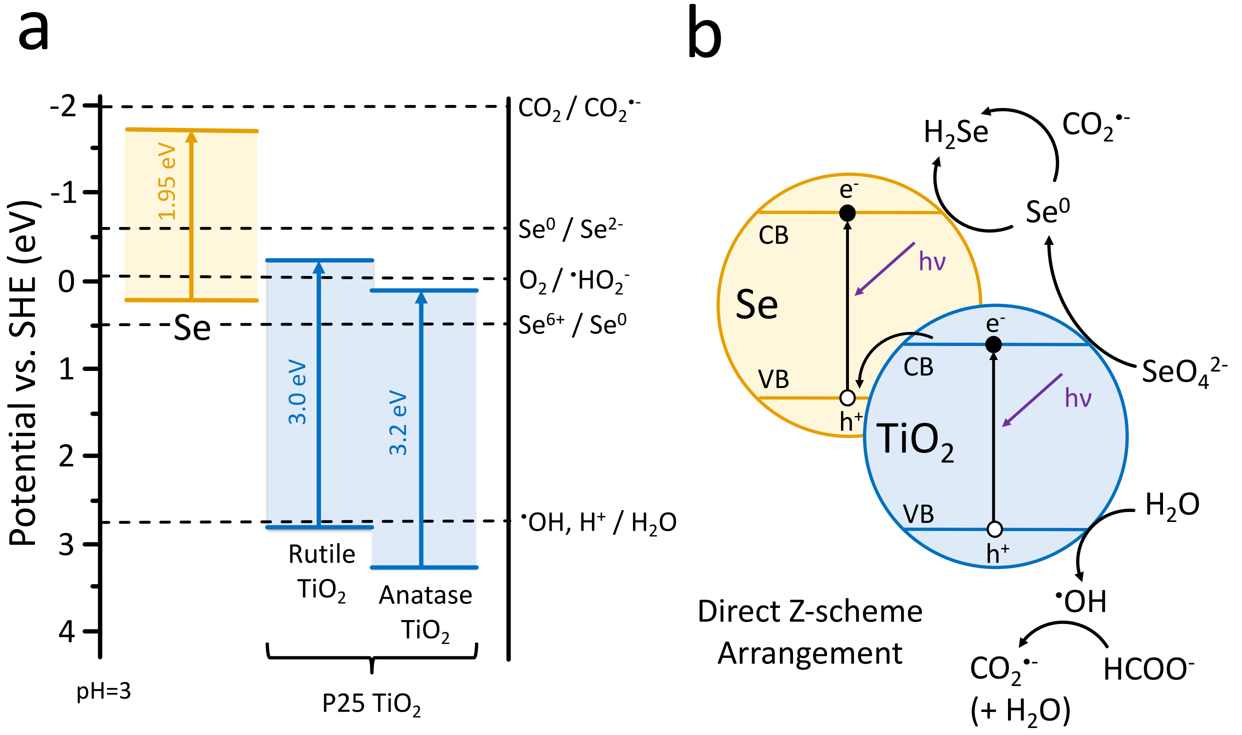

Figure 2-2. (a) Schematic comparison of band edge positions of Se and TiO_2 together with the standard potentials of the relevant redox couples and (b) Schematic illustration of the mechanism for charge carrier separation in Se-TiO_2 direct Z-scheme photocatalyst arrangement.

Others have proposed different mechanisms for H_2Se gas generation in the unique Se-TiO_2 photocatalytic system to try to explain the further reduction of Se^0 to H_2Se. Kikuchi and Sagamoto proposed the Se^0 to H_2Se reduction occurs due to the accumulation of electrons in the bulk of TiO_2 causing an increase in the TiO_2 conduction band potential (Kikuchi and Sakamoto, 2000). Tan et al. proposed Se-photogenerated electrons are responsible for Se reduction to H_2Se, which is highly favourable from a thermodynamic standpoint (Tan et al., 2002). The authors claim that an accumulation of electrons in the interior of TiO_2 (n-type semiconductor) and the accumulation of holes in Se (p-type semiconductor) could set up an electric field directed from the bulk of Se towards the bulk of TiO_2. This electric field acts as a forward bias to the p-n junction interface between Se and TiO_2, reducing the width of the space charge layer and decreasing the energy barrier for electron transfer from TiO_2 and Se (Dalven, 1990). However, this proposed mode of electron transfer does not fully explain why Se-photogenerated electrons do not reduce Se to H_2Se while selenate exists in solution.

A new model must be proposed to explain the continuous generation of H_2Se gas throughout the entire photocatalytic reaction. We postulate that two separate pathways occur for the reduction of $Se_{(s)}$ to $H_2Se_{(g)}$: (1) reduction by photogenerated electrons in Se and (2) by carbon dioxide radicals ($CO_2^{\bullet-}$) generated through the oxidation of formic acid, as shown in Figure 2-2b. During photocatalytic reduction of FGDW, the latter reaction pathway may be more pronounced in the presence of a variety of other dissolved species in the wastewater. Various reaction conditions are probed throughout this work to elucidate the possibility of both reduction mechanisms.

2.4.2 Apparent activation energy for selenate reduction

Temperature controlled experiments were completed to investigate the effects of temperature on the reaction kinetics for the reduction of selenate in FGDW. An Arrhenius plot of the apparent first-order rate constants was used to calculate an apparent activation energy (E_{aa}) of 90.09 ± 6.09 kJ mol^{-1} for the reduction of selenate in the presence of formic acid in FGDW (Figure 2-3a).

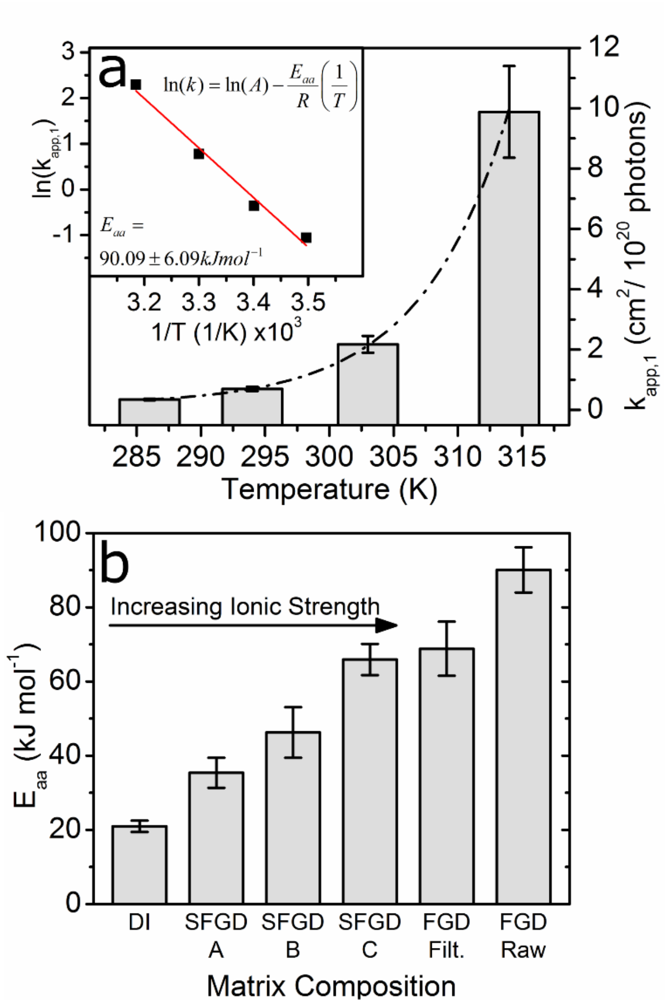

Figure 2-3. (a) Apparent first-order rate constant as a function of reaction temperature for the photocatalytic reduction of selenate in FGDW (inset shows Arrhenius plot) and (b) apparent activation energy for the reduction of selenate in varying matrix compositions of deionized water (DI), simulated flue gas desulphurization wastewater (SFGD), filtered (Filt.) and unfiltered (Raw) industrial flue gas desulphurization wastewater (FGD). The matrix compositions for each of the SFGD and FGD are given in Table 2-1 for comparison.

Treatment of the temperature dependent data according to the Eyring equation can yield the enthalpy and entropy of activation:

$$ln\left(\frac{k}{T}\right) = -\frac{\Delta H^{\dagger}}{RT} + ln\left(\frac{k_B}{h}\right) + \frac{\Delta S^{\dagger}}{R} \tag{2.6}$$

where $\Delta H^{\dagger}$ and $\Delta S^{\dagger}$ are the apparent enthalpy and entropy of activation, and R, k_B and h are the gas, Boltzmann and Planck constants, respectively, thus yielding $\Delta H^{\dagger}$ = 87.6 kJ mol^{-1} and $\Delta S^{\dagger}$ =

-33.4 J K^{-1} mol^{-1} shown in Figure A-4. The small negative value of $\Delta S^{\dagger}$ indicates a weakly associative mechanism in the transition state, which could correspond to surface reactions of adsorbed selenate consistent with the Langmuir-Hinshelwood (L-H) model.

This large temperature dependence of the kinetics is another phenomenon that the previous models posed by Tan et al. and Kikuchi and Sakamoto fail to address. In photocatalytic systems, three main factors affect the temperature dependence: (1) intrinsic semiconductor properties, (2) rate of decomposition of radical intermediates and (3) solution film mass transport associated with adsorption of reactants and desorption of products (Ye et al., 2016). Firstly, intrinsic semiconductor properties such as the bandgap, charge carrier density, mobility and separation efficiency are dependent on temperature, and typically are negatively correlated with reaction rate. However, within the studied temperature range of 285-315 K, these are likely to change only slightly for TiO_2 and the true activation energy (E_a) of the photocatalytic reaction should be near zero (Nurlaela et al., 2016). Secondly, the primary source of radical formation during the reduction of SeO_4^{2-} is the reaction of hydroxyl radicals with formate, which has a very low activation energy of 9 ± 5 kJ mol^{-1} and is therefore unlikely to cause the large E_{aa} (Ervens et al., 2003). In addition, E_{aa} was determined for reactions with either formic acid or methanol as electron hole scavengers (Figure A-5) confirming that the temperature sensitivity was not specific to a particular radical intermediate. Lastly, we postulate that the mass transport associated with adsorption of reactants to active sites and the desorption of products from active sites on the catalyst is likely another cause of the large E_{aa}. To clarify, the rate of adsorption to active sites differs from bulk adsorption from the aqueous phase to the solid-liquid interface which typically slows down with increasing temperature (Kersten and Vlasova, 2013). Less than a quarter of the sites on the surface of TiO_2 are photocatalytically active and are largely inhibited by diffusion within the shear surface to allow reactants to migrate to the active sites (Muggli and Backes, 2002). E_{aa} is an indication of the enthalpy associated with adsorption of reactants or desorption of products from the active sites of the photocatalyst.

In addition, a larger E_{aa} is common for gas generating photocatalytic reactions due to the increased rate of desorption of gases at higher temperatures (Hu et al., 2010). The desorption of produced gases has a profound effect on the catalytic activity, especially since H_2Se is known to poison catalytic surfaces, similar to H_2S (Argyle and Bartholomew, 2015). For example, the simultaneous photocatalytic removal of nitrate and oxalic acid on Au-TiO_2 results in apparent activation energies of 34 and 42 kJ mol^{-1}, respectively due to the generation and desorption of the CO_2 gaseous product (Anderson, 2012, 2011). The E_{aa} for the reduction of selenate, nitrate and O_2 in DI over TiO_2 are found to be 20.96 ± 1.52 kJ mol^{-1}, 29.34 ± 4.15 kJ mol^{-1} and 29.36 ± 3.71 kJ mol^{-1} respectively (Figure A-6). Due to the similarities in E_{aa} of these three reduction reactions, we suggest that the most likely contribution comes from reactant adsorption and CO_2 desorption, resulting from the oxidation of formic acid, on the TiO_2 surface. Finally, the increased temperatures lead to decreased solubility of both H_2Se and CO_2 gases, which can ultimately lead to push the reaction forward at higher temperature, resulting in higher activation energy.

2.4.3 Effect of FGDW matrix composition on activation energy

Experiments were completed to test the effects of competing ions in FGDW on the E_{aa} of the reduction of selenate. The apparent activation energies for the reduction of selenate on TiO_2 in several synthetic flue gas desulphurization wastewaters (SFGD) are shown in Table 2-1 and Figure 2-3b. As mentioned previously, the photoreduction of selenate in DI has a relatively low E_{aa} of 20.96 ± 1.52 kJ mol^{-1}. The presence of ions in the wastewater has a large impact on both the apparent activation energy and the reaction rate constant. Table A-1 presents the full characterization of the FGDW where it can be seen that SO_4^{2-}, HCO_3^-, Cl^-, Mg^{2+}, Ca^{2+} and Na^+ are all significant ions in the FGDW with a total dissolved solids (TDS) concentration of 4.62 g L^{-1}. A series of experiments were completed to understand the full effect of the co-existing ions on the photoreduction of selenate over TiO_2.

Table 2-1. Apparent activation energy for the reduction of selenate and major ionic components in varying matrix compositions of deionized water (DI), simulated flue gas desulphurization wastewater (SFGD), filtered (Filt.) and unfiltered (Raw) industrial flue gas desulphurization wastewater (FGD).

Matrix	Major Component Concentration (mg L^{-1})							Apparent Activation Energy (kJ mol^{-1})
	Ca^{2+}	Mg^{2+}	Na^{+}	Cl^{-}	SO_4^{2-}	SeO_4^{2-}, as Se	$Se^0_{(s)}$, as Se	
DI	0	0	0	0	0	0.250	0	20.96 ± 1.52
SFGD A	0	500	700	1,767	1,045	0.250	0	35.39 ± 4.02
SFGD B	0	500	969	1,767	1,670	0.250	0	46.24 ± 6.83
SFGD C	831	500	969	3,237	1,670	0.250	0	65.93 ± 4.22
FGD Filt.	831	190	158	1,070	1,670	0.249	0	68.82 ± 7.30
FGD Raw	831[a]	190[a]	158[a]	1,070[a]	1,670[a]	0.249 [a]	0.007	90.09 ± 6.09

[a]Values represent components in the dissolved phase, filtering required for analysis

Figure 2-3b demonstrates that E_{aa} increases with rising ionic strength of the SFGD. It should be noted that the E_{aa} for SFGD C and 0.2 μm filtered FGD, which have identical calcium and sulfate concentrations, were 65.93 ± 4.22 and 68.82 ± 7.30 kJ/mol, respectively. Filtering the FGD resulted in a decrease in E_{aa} likely due to the removal of fine particulate matter, such as $CaSO_4$ and solid Se^0, contributing to an inhibition of mass transfer. Both the presence of SO_4^{2-} and Ca^{2+} contributed to increases in activation energy of selenate reduction.

Anions, such as SO_4^{2-}, PO_4^{3-} and HCO_3^- have been known to specifically adsorb onto the surface of TiO_2 (Sheng et al., 2013), competing for active sites required for selenate and formate for the photoreduction of Se. In addition, SO_4^{2-} has been reported to contribute to photo-induced aggregation of TiO_2 nanoparticles (Shih et al., 2012), further reducing their effective surface area and, consequently, photocatalytic performance. Cations, such as Mg^{2+}, Ca^{2+} and Na^+ can contribute towards aggregation of the TiO_2 nanoparticles by inducing electric double layer charge screening, following DLVO theory, reducing the surface area of interaction and hence the reaction rate (Hotze et al., 2010). Similarly, Yang et al. found that the photoreduction of nitrate using TiO_2 for the regeneration of ion exchange brine was greatly inhibited by the presence of SO_4^{2-} (T. Yang et al., 2013).

Similarly, an increase in salt concentration can lead to a decrease in solubility of H_2Se and CO_2 gases, through a process known as salting out (Spycher and Pruess, 2005). This decreased solubility allows for faster product removal at higher temperatures, through the bubbling out of solution which ultimately drives the reaction forward.

2.4.4 Effect of temperature and formic acid concentration on the reduction rate

The combined effects of both temperature and formic acid concentration on the photocatalytic reduction rate of selenate were also examined. Higher concentrations of formic acid should ultimately lead to increased e_{cb}^{-}-h_{vb}^{+} separation and higher concentrations of available $CO_2^{\bullet -}$radicals, increasing both reduction pathways for $Se_{(s)}$ to H_2Se proposed in Figure 2-2. Response surface methodology was used to develop an empirical model for the combined effects of temperature and formic acid concentration on the apparent first-order rate constant of selenate reduction in FGDW, following a central composite design described in Table 2-2 to yield the results summarized in Table A-2.

Table 2-2. Corresponding variable levels and coded variables of the experimental variables in the response surface study.

Designation	Factor	Range and level				
		$-\sqrt{2}$	-1	0	1	$\sqrt{2}$
x_1	Temperature (K)	279	285	300	315	321
x_2	Formic Acid Concentration (mg L^{-1})	17	100	300	500	583

The least squares regression fit of the response surface is presented in Figure 2-4, described by the relationship,

$$\hat{y} = 1.9161 + 1.7093x_1 + 0.8246x_2 + 0.0283{x_1}^2 - 0.2029{x_2}^2 + 0.8855x_1x_2 \quad (2.7)$$

or described in natural variables as,

$$k_{app,1} = 8.303 - (7.885 \times 10^{-2})T - (8.136 \times 10^{-2})C_{HCO_2H} + (1.730 \times 10^{-4})T^2 - (5.121 \times 10^{-6})C_{HCO_2H}^2 + (2.952 \times 10^{-4})TC_{HCO_2H} \quad (2.8)$$

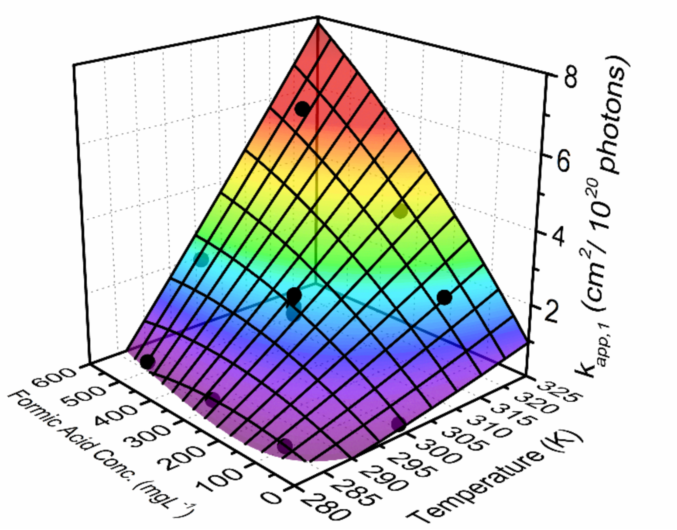

Figure 2-4. Response surface fit of the apparent first-order rate constant of photocatalytic reduction of selenate in FGDW as a function of temperature and formic acid concentration.

Canonical analysis can be done to determine maxima and minima of the surface located outside the experimental domain, although in the case of photocatalytic water treatment, temperatures outside the experimental domain do not have any important physical significance due to the freezing and boiling points of water. ANOVA and regression diagnostics for the response surface are presented in Table A-3 and Figure A-7 respectively. Notably, ANOVA indicated the presence of a major interdependence between temperature and formic acid concentration with a significant x_1x_2 term, whereas the individual quadratic terms, $x_1{}^2$ and $x_2{}^2$, are considered insignificant in the model.

The results of this study confirm the interdependence of temperature and formic acid concentration on the apparent first-order reaction rate constant. The increase in formic acid concentration increases the e_{cb}^{-}-h_{vb}^{+} separation, concentration of $CO_2{}^{\bullet -}$radicals and reaction rate constant as a result. However, temperatures above 12 °C must be reached to achieve any observable reduction of selenate. Temperatures of FGDW leaving the flue gas scrubbers can be as high as 60 °C due to contact with flue gas exiting the coal burner (Higgins et al., 2009). Temperature-enhanced treatment is a major advantage of photocatalytic reduction of selenate for the treatment of FGDW when compared to other treatment techniques as a result.

2.4.5 Selenate adsorption is a limiting factor

Heterogeneous photocatalytic kinetics are often described by the Langmuir-Hinshelwood (L-H) model:

$$r = -\frac{dC}{dt} = k_r\theta = \frac{k_r KC}{1+KC} \tag{2.9}$$

where r is the reaction rate, C is the concentration of selenate, k_r is the reaction rate constant, θ is the fraction of occupied catalyst surface sites defined by the Langmuir adsorption isotherm and K is the Langmuir adsorption constant. At low selenate concentrations, integration of eq. 2.9 yields the typical pseudo-first order equation:

$$ln\left(\frac{C_0}{C}\right) = k_r Kt = k_{app,1}t \tag{2.10}$$

where $k_{app,1}$ is the apparent first-order rate constant and t is the reaction time. Linearizing eq. 2.9 allows for determination of k_r and K.

$$\frac{1}{r_0} = \frac{1}{k_r KC_0} + \frac{1}{k_r} \tag{2.11}$$

where r_0 is the initial rate of reaction.

Regression of $1/r_0$ against $1/C_0$ yielded k_r = 6.557 x 10^{-4} mg L^{-1} s^{-1} and K = 0.523 L mg^{-1}, shown in Figure 2-5a. For the typical concentrations found in FGDW, these values represent an adsorption-limited regime (*i.e.*, KC << 1). The measured value of K is comparable to values previously reported for adsorption of selenate on TiO_2 (Zhang et al., 2009). The adsorption-limited regime could be coupled with internal diffusion through the shear surface as discussed previously as the adsorption experiments generally do not account for the direct adsorption to an active site, but simply bulk adsorption to the liquid-solid interface (Muggli and Backes, 2002; Nowotny et al., 2006).

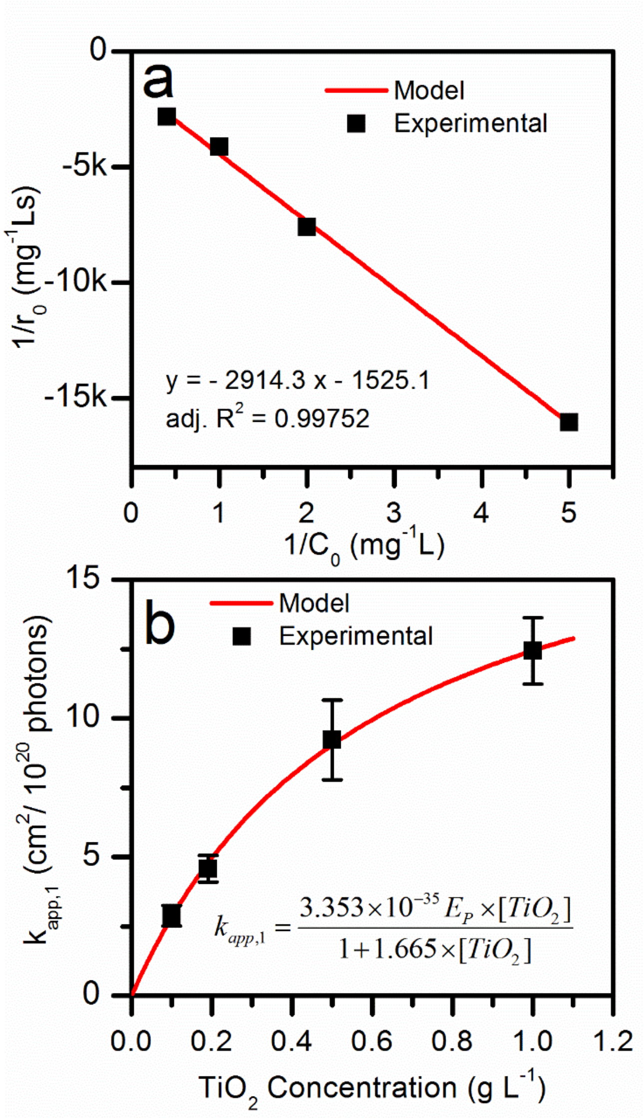

Figure 2-5. (a) Langmuir-Hinshelwood plot showing the dependence of the initial photocatalytic degradation rate, r_0, on the initial concentration of selenate, C_0, and (b) Effect of TiO_2 concentration on the apparent first-order rate constant for the photocatalytic reduction of selenate in simulated FGDW.

Experiments in which the concentration of TiO_2 for the reduction of selenate in FGDW waas varied also revealed a relationship between the reaction rate and amount of TiO_2 in suspension, shown in Figure 2-5b. The asymptotical behaviour is attributed to the decrease of UV transmittance caused by the increase in solid photocatalyst particles in suspension. This phenomenon has been observed in many studies where heterogeneous photocatalysis is used to reduce contaminants by UV/TiO_2 systems (Schneider et al., 2014). The relationship between TiO_2 concentration and apparent first-order reaction rate constant for the PC reduction of SeO_4^{2-} in FGDW can be adequately described by the following relation:

$$k_{app,1} = \frac{3.353\times10^{-35} E_P \times [TiO_2]}{1+1.665[TiO_2]} \tag{2.12}$$

where $k_{app,1}$ is the first order apparent rate constant in cm^2 $photons^{-1}$, E_P is the photon irradiance in photons cm^{-2} s^{-1} and $[TiO_2]$ is the TiO_2 concentration in g L^{-1}.

Under an adsorption-limited regime with low concentrations of SeO_4^{2-}, the internal diffusion through the shear surface around TiO_2 of both aqueous SeO_4^{2-} and formate can be the rate determining step and highly dependent on temperature.

The adsorption of selenate onto TiO_2 and the photoreduction rate is highly dependent on pH (Figure 2-6). pH plays an important role in the photocatalytic reduction of selenate by impacting the adsorption of selenate and formate onto the surface of the photocatalyst prior to reduction. The adsorption of selenate onto TiO_2 occurs initially through an outer-sphere complex and is driven by electrostatic interaction between selenate and the positively charged surface of TiO_2 (Jordan et al., 2011). TiO_2 has an isoelectric point of 5.6, thus at pH below 5.6 the surface becomes positively charged (McNamee et al., 2005). The lower the pH, the more positively charged the surface becomes, leading to higher adsorption capacity and higher photocatalytic reduction rate shown in Figure 2-6. At pH 6, the reduction of selenate in FGDW does not occur because the adsorption of selenate and formate is greatly hindered above the isoelectric point of TiO_2. As long as the surface charge of the photocatalyst is below the isoelectric point the reduction can proceed with increasing rate as the surface charge increases.

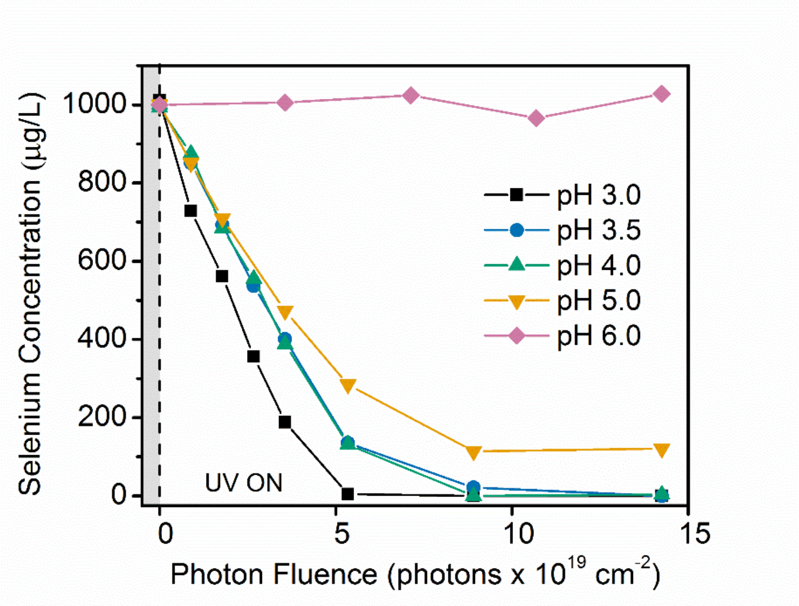

Figure 2-6**.** Photocatalytic removal of selenium from simulated FGDW under varying pH.

2.4.6 Effect of dissolved oxygen on selenate reduction

The presence of dissolved oxygen (DO) is known to hinder the efficacy of photocatalytic reduction processes because it competes with the catalyst for photogenerated electrons (Peiró et al., 2006). Its detrimental effect was confirmed by experiments shown in Figure 2-7a. When N_2 sparging was switched to ambient air, the concentration of dissolved Se gradually increased and at times approached the initial concentration, suggesting the re-oxidation of elemental selenium by reactive oxygen species. Consequently, it was of interest to investigate the generation rates of superoxide and hydrogen peroxide. Hydroxyl radicals ($^{\bullet}$OH) were not probed, since they were assumed to be effectively scavenged by the formate ions present in solution.

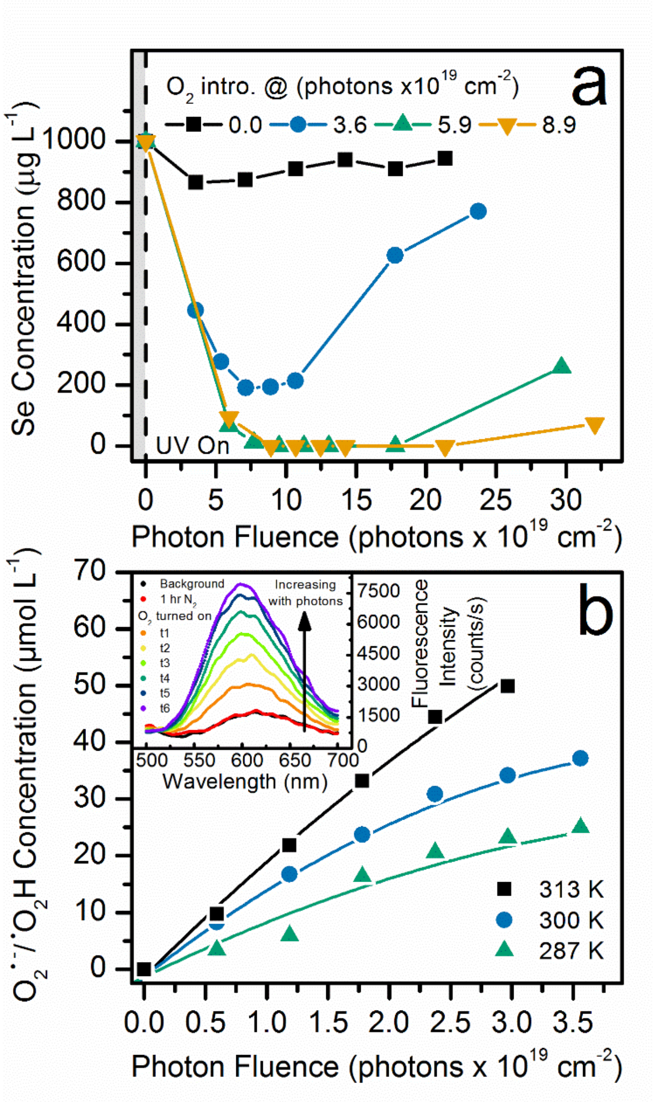

Figure 2-7. (a) Effect of oxygen by varying O_2 exposure times via ambient air purge on the photocatalytic reduction of selenate in simulated FGDW and (b) Generation curve of $O_2^{\bullet-}$ / $^{\bullet}O_2H$ during O_2 exposure at varying temperatures with inset of fluorescent spectra of DHE probe molecule product after reaction with $O_2^{\bullet-}$ / $^{\bullet}O_2H$.

A hydrogen peroxide assay was carried out as described in Appendix A, but the generation of H_2O_2 was not observed to any appreciable extent and its role in the oxidation of Se^0 back to SeO_4^{2-} at the experimental conditions was discounted. The presence of formate did not interfere with the Cu/DMP method, as confirmed by separate control experiments involving spiking H_2O_2 into the solution at varied concentrations.

Since the experimental pH values are well below the pKa of $O_2^{\bullet-}$ of roughly 4.8 (Abreu and Cabelli, 2010; Sheng et al., 2014) at which Se reduction was conducted, it was expected that superoxide would be mostly present in the form of the protonated hydroperoxyl radical ($^{\bullet}O_2H$). Unlike $O_2^{\bullet-}$, which has reducing properties, $^{\bullet}O_2H$ can act as a powerful oxidant in many reactions. A growing fluorescence signal was observed during air sparging when excited at 480 nm, which was not observed during nitrogen sparging, as depicted in the inset of Figure 2-7b. The use of superoxide dismutase (SOD) at a loading of 600 U mL^{-1} diminishes the fluorescence signal by 40%, which can be explained by most of the superoxide being protonated.

Finally, the effect of temperature on the production of hydroperoxyl radical was used to probe the activation energy of the electron transfer from TiO_2 to O_2, similar to the electron transfer to selenate. Figure 2-7b illustrates the increase in production rate of hydroperoxyl radicals with the increase in temperature. The apparent activation energy (E_{aa}) was calculated to be 23.21 ± 1.93 kJ/mol. Which is comparable to the E_{aa} experimentally determined for the photocatalytic reduction of selenate and nitrate in DI to be, 23.24 ± 3.64 kJ/mol and 27.67 ± 4.08 kJ/mol respectively.

2.4.7 Proposed reduction mechanism

As shown in Figure 2-2a, from the energy potentials of conduction bands (CB) of Se (-1.71 V *vs.* SHE), rutile TiO_2 (-0.28 V *vs.* SHE) and anatase TiO_2 (0.12 V *vs.* SHE), only Se is more negative than the standard potential of the Se^0/Se^{2-} redox couple (-0.6 V *vs.* SHE) from the energy potentials of the valence bands (VB) of Se (0.24 V *vs.* SHE), rutile TiO_2 (2.72 V *vs.* SHE) and anatase TiO_2 (3.32 V *vs.* SHE), only anatase and rutile TiO_2 are more positive than the standard potential of the $OH^{\bullet}/H_2O$ redox couple (2.7 V *vs.* SHE). In this regard, the reduction of Se^0 to H_2Se is likely occurring at the CB of Se or by the produced carboxyl radicals while the oxidation of the electron hole scavenger formic acid would occur at the VB of TiO_2. In a direct Z-scheme photocatalytic system, shown in Figure 2-2b, upon simultaneous light excitation, both Se and TiO_2 phases can generate excited e^--h^+ pairs. The excited electrons from the CB of rutile TiO_2 can transfer to combine with the photogenerated holes of Se and preserve the electrons with stronger reducibility in the CB of Se and holes with stronger oxidizability in the VB of TiO_2 (Nosaka and Nosaka, 2016b; Xu et al., 2018). The TiO_2 (P25, Aeroxide) used in this study is known to be a mixed-phase crystalline combination of rutile and anatase, with >80% anatase and the remainder rutile and amorphous. It is postulated that the accumulation of electrons in the interior of TiO_2, a n-type semiconductor, and the accumulation of holes in Se, a p-type semiconductor, could set up an electric field directed from the bulk of Se towards the bulk of TiO_2.

The following sequence of elementary reactions is the proposed mechanism of photoreduction of SeO_4^{2-}:

$$TiO_2 + hv \rightarrow {h_{vb,TiO2}}^{+} + {e_{cb,TiO2}}^{-} \tag{2.13}$$

$$Se^0 + hv \rightarrow {h_{vb,Se}}^{+} + {e_{cb,Se}}^{-} \tag{2.14}$$

$$HCOOH + 2{h_{vb,TiO2}}^{+} \rightarrow CO_2 + 2H^+ + 2e^- \tag{2.15}$$

$$H_2O + {h_{vb,TiO2}}^{+} \rightarrow HO^{\bullet} + H^+ \tag{2.16}$$

$$HCOOH \leftrightarrow HCOO^- + H^+ \tag{2.17}$$

$$HCOO^-{}_{ads} + {h_{vb,TiO2}}^{+} \rightarrow {CO_2}^{\bullet -} + H^+ \tag{2.18}$$

$$HCOO^- + HO^{\bullet} \rightarrow {CO_2}^{\bullet -} + H_2O \tag{2.19}$$

$${CO_2}^{\bullet -} + {e_{cb,TiO2}}^{-} \rightarrow CO_2 + 2{e_{cb,TiO2}}^{-} \text{ (Current-doubling effect)} \tag{2.20}$$

$${SeO_4}^{2-} + 8H^+ + 6{e_{cb,TiO2}}^{-} \leftrightarrow Se^0 + 4H_2O \tag{2.21}$$

$$Se^0 + 2H^+ + 2{e_{cb,Se}}^{-} \leftrightarrow H_2Se \tag{2.22}$$

$$Se^0 + 2H^+ + 2{CO_2}^{\bullet -} \leftrightarrow H_2Se + 2CO_2 \tag{2.23}$$

During the oxidation of formic acid, either directly through an electron-hole on the TiO_2 surface (eq. 2.18) or through reaction with a hydroxyl radical (eq. 2.19), a carboxyl radical (${CO_2}^{\bullet -}$) is produced. The produced carboxyl radical can decay in different ways: injection of its free electron into the CB of TiO_2 (eq. 2.20, known as the current doubling effect (Yang et al., 2015)), transfer of an electron to reduce Se^0 to H_2Se (eq. 2.23) or transfer of an electron to one of the many other electron acceptors present in FGDW. As mentioned previously, the reduction of Se^0 to H_2Se (-0.6 V *vs.* SHE) is thermodynamically possible through direct transfer of e_{CB,Se^-} (-1.71 V *vs.* SHE) or by the carboxyl radical (-2.0 V *vs.* SHE). The carboxyl radical pathway can be affected greatly by the presence of species competing for adsorption sites on the TiO_2 surface. In the presence of sulfate, the surface anionization can lead to weakening of the interaction between ${CO_2}^{\bullet -}$ and TiO_2, inhibiting the current doubling effect, but increasing the amount of ${CO_2}^{\bullet -}$ available to react with Se^0 (Sheng et al., 2013). This is a possible explanation for the constant H_2Se generation observed in Figure 2-1, a marked deviation from selenate reduction in DI water treatment experiments. In the case of DI water selenate reduction, the presence of a two-stage reduction may be due to the fact that ${CO_2}^{\bullet -}$ is reacting with the CB of TiO_2 towards the current-doubling effect and unavailable for reduction of Se^0 until selenate is completely removed (Tan et al., 2002). Tan et al. have shown that formic acid is the most effective organic electron hole scavenger, which may be due to the current-doubling effect observed with only formic acid (T.T.Y. Tan et al., 2003a).

2.5 Conclusions

This study investigated the feasibility of photocatalytic reduction using TiO_2 to remove selenate from FGDW and analyzed the complex kinetic factors influencing the rate of reaction. Photocatalytic reduction using TiO_2 can effectively remove selenate from both simulated and industrial FGDW. A direct Z-scheme photocatalyst arrangement between photodeposited Se and TiO_2 allows for the preservation of electrons with stronger reducibility in the CB of Se and holes with stronger oxidizability in the VB of TiO_2. High levels of Ca^{2+} and SO_4^{2-} contribute to a high apparent activation energy. Due to the high temperatures of effluent FGDW this is advantageous, resulting in a more efficient treatment as compared to conventional Se removal techniques which require heat removal prior to Se removal via biological reduction. In the presence of dissolved oxygen, the reduction of selenate is reversed through the re-oxidation of elemental Se by photogenerated hydroperoxyl radicals. Minimal selenite was generated as an intermediate as selenate was reduced directly to elemental Se and H_2Se gas. The major reduction product is H_2Se gas as the reduction of selenate proceeds to completion. With safety considerations, the proper handling of H_2Se gas products is a critical step in the process engineering design of a fully integrated treatment system. Furthermore, given that photocatalytic reduction of selenate presents a robust and effective Se removal technique capable of removing Se to below 1 ug/L, further investigation into other industrial sectors producing Se impacted water such as mining, agriculture and photovoltaics is of great interest.

3 Factors affecting kinetics of photocatalytic reduction of selenate over TiO_2 in mine impacted water

This chapter is modified from:

Holmes, A.B., Giesinger, K., and Gu, F. (in preparation). Factors affecting kinetics of the photocatalytic reduction of selenate over TiO_2 in mine impacted water.

3.1 Summary

Photocatalytic reduction on TiO_2 is a promising non-biological technique for selenate removal from mine-impacted water (MIW) to remove Se from > 500 to < 1 μg L^{-1}. Selenate reduction is most effective at low pH (< PZC_{TiO2} = 5.6-6.2), higher temperatures (between 20-60°C) and in a low dissolved oxygen (DO) environment (< 3.5 mg/L DO). A TiO_2 catalyst dose of 0.5 g/L was found optimal for selenate reduction. The effect of various electron hole scavengers was studied to determine the optimal type and concentration range leading to fast selenate reduction. Total Se photoreduction was achieved with all tested electron hole scavengers and found to increase in rate in the following order: acetic acid < ethanol < methanol < glycerol < formic acid. Marginal differences in the selectivity of Se^0 or H_2Se formation were observed with glycerol and formic acid as both favour the generation of H_2Se under the conditions studied. During the selective photocatalytic reduction of selenate in MIW, the organic hole scavenger is added in excess (300-600 mg/L) to allow for faster kinetics. Most of the organic hole scavenger remains in solution after the Se is largely removed and may subsequently be utilized for downstream denitrification as an electron donor.

3.2 Introduction

The introduction of selenium (Se) into aquatic ecosystems through anthropogenic activity is a rising global concern (Tan et al., 2016). Industrial activity such as the mining and smelting of metal ores, mining and combustion of coal, oil extraction and refining, and agricultural activities on seleniferous soils, disturb subsurface Se-rich deposits and introduce Se into surface aquatic environments (Hopkins et al., 2013; Schiavon and Pilon-Smits, 2017). Se is an essential nutrient for animals and humans, although it has a very narrow therapeutic window between deficiency and toxicity (El-Ramady et al., 2015). The most common soluble forms of Se found in the surface environment are the toxic Se oxyanions selenate (SeO_4^{2-}) and selenite (SeO_3^{2-}), which require reduction to the less soluble, biologically inert, elemental Se (Se^0) and selenides (M_nSe, H_2Se, etc.) for the removal from water.

Mine-impacted water (MIW) rich in Se is produced when natural sources of water drainage, such as rain and snowmelt, infiltrate into waste rock piles and tailings on an operating or abandoned mine. The composition of this water depends heavily on the geology of the underlying deposit and the overlying strata. MIW can contain varying concentrations of dissolved constituents from the underlying strata, such as sulfate, carbonate, nitrate, selenate and many dissolved metals (Nordstrom et al., 2015). Mine drainage can be acidic to alkaline, whereas areas high in carbonate content have near-neutral mine drainage (NMD) because H^+ ions produced from pyrite oxidation are neutralized by excessive carbonates naturally occurring in the overburden or added to the valley fill (Giam et al., 2018). Under these near-neutral conditions, dissolved Se is commonly found in its fully oxidized selenate form, a highly bioavailable and mobile compound in the environment (Fan et al., 2015).

Several conventional reduction processes can mitigate Se contamination of MIW including direct chemical amendment (Santos et al., 2015), reverse osmosis (Richards et al., 2011), adsorption (Rovira et al., 2008) and biological treatment options such as constructed wetlands (Martin et al., 2018) and bioreactors (Y. V. Nancharaiah and Lens, 2015). Bioreactors have been successfully implemented as a method for Se removal from MIW on a pilot-and full-scale (Lenz et al., 2008; Luek et al., 2014). However, challenges remain for the disposal and stability of Se contaminated bioreactor sludge (Mal et al., 2017, 2016), microbial community start-up time and toxicity of effluents due to the possible production of organo-selenium compounds such as selenomethionine (LeBlanc and Wallschläger, 2016).

Photocatalytic reduction on semiconductor materials, mainly titanium dioxide (TiO_2), has shown great potential for removal of several contaminants of interest such as nitrate (Marks et al., 2016; Shaban et al., 2016; Sun et al., 2016), nitrite (Luiz et al., 2012), chromate (Choi et al., 2017), bromate (Xiao et al., 2017), perchlorate (Jia et al., 2016) selenite (Nguyen et al., 2005b) and selenate (T.T.Y. Tan et al., 2003a; Leshuk et al., 2018; Holmes and Gu, 2016). Upon irradiation of a photocatalyst with high-energy light, electrons are excited into the conduction band (e_{cb}^-) and electron holes form in the valence band (h_{vb}^+). An electron acceptor capturing the e_{cb}^- is reduced while an electron donor reacting with the h_{vb}^+ is oxidized, whereas the semiconductor catalyst remains unchanged. In the case of Se removal, the photogenerated e_{cb}^- can reduce SeO_4^{2-} to Se^0 or H_2Se under the right conditions. Utilization of an electron hole scavenger, an easily oxidizable organic material, such as methanol, ethanol, or formic acid, can limit the recombination of the e_{cb}^--h_{vb}^+ pairs, thus markedly increasing the efficacy of reduction, through mediating the transfer of electrons to selenate to reduce the oxidation state of Se.

Recently, many studies have attempted to use photocatalytic methods to treat complex wastewaters such as MIW, while investigating the impacts of dissolved species such as sulfate, carbonate, nitrate, heavy metals and many others (Rioja et al., 2016; Choi et al., 2014; T. Yang et al., 2013). These studies investigated how the mechanisms of reactant adsorption and product desorption from the photocatalyst can be affected by a complex water matrix and highlight the challenges faced when photocatalysis is to be implemented in real complex water applications. Many previous studies investigating the photocatalytic reduction of selenate and selenite were primarily conducted in DI solutions prepared with Se oxyanion salts (Kikuchi and Sakamoto, 2000; Labaran and Vohra, 2014; Nguyen et al., 2005b; T.T.Y. Tan et al., 2003b, 2003a). Nakajima et al. investigated the photocatalytic reduction of selenate in simulated flue gas desulphurization wastewater (FGDW), a complex wastewater with many anions and cations, and observed a considerable inhibition of the reduction rate in the presence of sulfate (Nakajima et al., 2013, 2011). The studies suggested that selenate in simulated FGDW could not be removed by photocatalytic reduction due to the excess concentration of SO_4^{2-} which competes for adsorption sites on TiO_2 with selenate. Our recent study (Chapter 2), on the photocatalytic reduction of selenate in real FGDW revealed that the mechanism of adsorption and photocatalytic reduction of selenate changes considerably, although we were able to remove selenate to less than 1 μg/L in the complex wastewater matrix. Thermally activated simultaneous generation of elemental selenium (Se^0) and hydrogen selenide (H_2Se) through consecutive first-order reductions was proposed under a direct Z-scheme photocatalyst arrangement between photo-deposited Se and TiO_2.

Herein, the authors investigate the photocatalytic reduction of selenate over TiO_2 in mine-impacted water (MIW); focusing on various factors that impact the kinetics of reduction including: pH, temperature, dissolved oxygen, concentration of catalyst, electron hole scavenger type and concentration and MIW pre-treatments. The primary goal of this work is to understand the conditions which optimize the removal of selenate in MIW. Given that treatment of MIW is unique depending on the water source, parameters for Se treatment were independently investigated to understand the kinetic effects of varying parameters and envision a photocatalytic Se removal process within an overall water treatment system.

3.3 Materials and Methods

3.3.1 Materials

Mine-impacted water (MIW) was received from an operating mine in North America and stored at 4 °C in the dark. Titanium dioxide nanoparticles (Aeroxide P25, ~10-50 nm particle diameter, 55 m^2 g^{-1} surface area, Acros) were used as received. P25 TiO_2 nanoparticles have been extensively studied and characterized in the literature and are often used as a benchmark photocatalyst. Formic acid (ACS reagent, 97%, Alfa Aesar) was used as an electron hole scavenger. Sodium selenate (<0.1% impurities, BioXtra, Sigma-Aldrich), calcium sulphate (anhydrous, ACS reagent >96%, Sigma-Aldrich), sodium chloride (reagent grade, Sigma-Aldrich), sodium nitrate (>99%, ReagentPlus, Sigma-Aldrich), hydrochloric acid (37%), and sodium hydroxide (ACS grade, Sigma-Aldrich) were used to simulate MIW for more controlled experiments.

3.3.2 Photocatalytic reduction of selenate experiments

The photocatalytic reactor apparatus consists of an air tight stainless-steel reactor vessel of 1.0 L capacity with a quartz window through which UV was irradiated onto the mixing TiO_2 suspension. TiO_2 nanoparticles (0.2 g/L) were stirred into 400 mL of MIW in a polytetrafluoroethylene (PTFE) beaker (76 mm diameter) along with an electron hole scavenger for the reduction reaction. The air-tight stainless-steel vessel with a quartz window was purged by bubbling N_2 gas throughout the reaction to remove any H_2Se gas generated and flowing through two subsequent liquid scrubbers of $CuSO_4$ and NaOH, respectively (Sanuki et al., 1999; T.T.Y. Tan et al., 2003b). The TiO_2-MIW suspension was stirred in the dark under a N_2 gas purge for 1 h to attain adsorption-desorption equilibrium of the inorganics with the TiO_2 surface as well as to remove dissolved oxygen, and then placed in the photoreactor and exposed to UV light while stirring. Filtered and unfiltered 5 mL aliquots were sampled periodically to measure the dissolved and total Se concentrations, respectively. The reactor vessel was exposed to UV light using a UVA fluorescent bulb that was filtered to only supply UVA (λ = 365 nm) light (Blak Ray B-100A 95-0044-22). The UV intensity (I_{UV}) at the height of the solution-air interface within the vessel was 11.03 mW/cm^2 (measured with a UVA/B light meter, Sper Scientific, NIST certified calibration). The energy dosage was varied instead of operating time to make our results comparable with other photocatalytic studies. The energy reported on the x-axis, in units of kWh/m^3, is the received energy by the suspension, not the electrical energy required by the UV lamp. Due to low conversion efficiencies of medium pressure UV lamps the required energy will be more depending on the conversion efficiency of the UV lamp being utilized in the reactor set-up.

3.3.3 Analysis

Se concentration was determined in accordance with the U.S. EPA suggested Se determination technique (APHA 2009, Method 3114B/C) using Hydride Generation Inductively Coupled Plasma Optical Emission Spectroscopy (HG-ICP-OES, Teledyne Prodigy ICP and Cetac HGX-200 advanced membrane hydride generation system, LOD = 1 $\mu g\ L^{-1}$). Both dissolved and total Se were determined by HG-ICP-OES following acid digestion protocol U.S. EPA Method 3050B (U.S. EPA, 1996). The insoluble Se fraction (considered to be elemental Se) present in the water was calculated by the difference of total and dissolved Se concentrations. Gaseous H_2Se was calculated from the difference between the initial total Se in the water and total Se in the TiO_2 suspension after UV exposure. Based on several past studies on photocatalytic reduction of selenate on TiO_2 (Nguyen et al., 2005b; Sanuki et al., 1999; T.T.Y. Tan et al., 2003a), the gaseous Se species is assumed to be H_2Se, although the direct identification of gaseous Se species is a challenging task (Kot and Namieśnik, 2000; Uden, 2002). Analytical chemistry of Se is currently a developing field with researchers looking into new and improved approaches to measure gaseous and solid Se species concentrations (Santos et al., 2015).

Dissolved oxygen content was determined through the use of a lab-bench probe (Thermo Scientific Orion Star A213 benchtop meter). Total organic carbon (TOC, APHA 5310B, combustion temperature 800 °C), chemical oxygen demand (COD, APHA 5220D), biochemical oxygen demand (BOD, APHA 5210B), anion concentration by ion chromatography (bromide, chloride, fluoride, nitrate, nitrite and sulfate, EPA 300.1), total ammonia (Watson et al., 2005), speciated alkalinity (as $CaCO_3$, EPA 310.2), and total and dissolved metals by inductively coupled plasma mass spectrometry (ICPMS, EPA 200.2/6020A and APHA 3030B/6020A) were measured according to standard methods by ALS Environmental (Calgary, AB, Canada), a laboratory certified by the Canadian Association for Laboratory Accreditation (CALA) according to international standards (ISO 17025). Total and dissolved Se concentrations measured at the University of Waterloo were confirmed by ALS Environmental on a number of analytical checks.

3.4 Results and Discussion

3.4.1 Reduction of selenate to solid Se^0 and gaseous H_2Se in MIW

Photocatalytic experiments were conducted to investigate the speciation of Se during the Se removal in MIW to better understand the mechanism of Se removal. Figure 3-1 presents the effect of incident UVA energy on SeO_4^{2-}, Se^0 and H_2Se concentrations resulting from photoreduction of selenate in MIW over TiO_2. The photocatalytic reduction of SeO_4^{2-} undergoes a two-step reaction outlined in eq. 3.1 & 3.2, with the reduction of SeO_4^{2-} to Se^0 followed by further reduction to H_2Se.

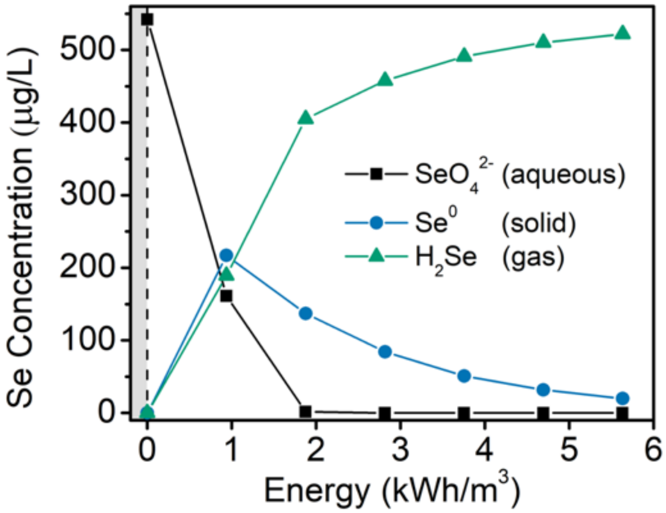

Figure 3-1. Effect of incident UVA energy on the photocatalytic reduction of selenate in mine impacted water over TiO_2 using formic acid as an electron hole scavenger. (Reaction conditions: 300 mg L^{-1} formic acid, 0.2 g/L TiO_2, 37 °C, pH 4.5)

$$SeO_4{}^{2-}{}_{(aq)} + 8H^+ + 6e^-_{cb} \xrightarrow{k_1} Se^0{}_{(s)} + 4H_2O \quad (E^0 = 0.5 \text{ V } \textit{vs.} \text{ SHE}) \qquad (3.1)$$

$$Se^0{}_{(s)} + 4H^+ + 2e^-_{cb} \xrightarrow{k_2} H_2Se_{(g)} \quad (E^0 = -0.6 \text{ V } \textit{vs.} \text{ SHE}) \qquad (3.2)$$

Both products of selenate reduction, H_2Se and Se^0, are removed from the MIW solution through the gas phase with N_2 purging and from the solid phase by filtering the catalyst from the suspension, respectively. The photocatalytic reduction of Se in MIW was able to lower concentration to less than 2 µg L^{-1} Se in the treated effluent after 2.0 kWh/m^3 of incident energy. At lower energies, nearly equal amounts of H_2Se and Se^0 are produced. Once the selenate is largely removed from solution, the solid Se^0 starts to convert to gaseous H_2Se and is then removed from the system. The colour of the catalyst that is filtered out of solution changes from its native white (colour of TiO_2) to red-pink (colour of solid elemental Se) during the first stage of reduction between 0 and 2.0 kWh/m^3, and then slowly changes back to white at higher energies. Thus, during the first stage of reduction selenate is being reduced to elemental Se (eq. 3.1), which is being deposited onto the surface of TiO_2. After near exhaustion of selenate from solution, at around 2.0 kWh/m^3, the elemental Se on the surface of TiO_2 is further reduced to H_2Se gas and removed from solution (eq. 3.2).

A follow-up experiment was conducted to determine the stability of the intermediate solid Se^0 half-way through the complete removal of selenate from MIW (Figure 3-2). The MIW and TiO_2 suspension was exposed to UV for 1 hour (1.13 kWh/m^3), followed by a 5-hour period of dark mixing, while the total Se and dissolved Se were measured every hour. Figure 3-2 shows the selenate concentration reduces from 542 μg/L to around 200 μg/L during the initial 1 hr of UV exposure and holds at approximately 200 μg/L for the remainder of the dark mixing period. The amount of solid Se^0 produced during the 1 hour of UV exposure holds steady over the next 2.5 hours of dark mixing and begins to slowly decrease from 2.5 to 5 hours of dark mixing, accounting for a 30% reduction of solid Se^0. It is postulated that during this time the solid Se^0 is reduced to $H_2Se_{(g)}$ through thermal excitation of the valence band electrons in the Se^0 due to thermally accessible defects (Kasap et al., 2015).

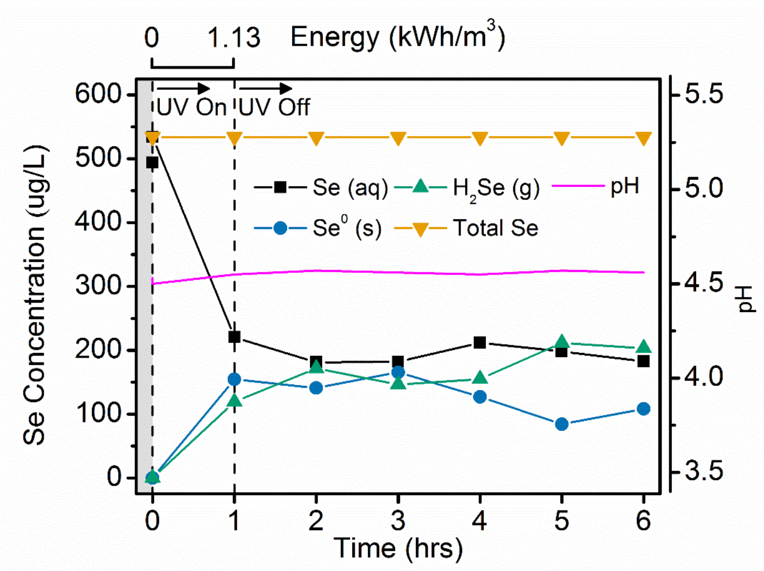

Figure 3-2. Partial photocatalytic reduction of selenate in MIW, with 1 hour of UV exposure, followed by 5 hours of dark mixing to determine the stability of selenate and solid Se^0 (Reaction conditions: 300 mg/L glycerol, 0.2 g/L TiO_2, pH 4.5, 37C).

3.4.2 Effect of solution chemistry on selenate removal by TiO_2

3.4.2.1 Effect of pH

The acidity or basicity of mine-impacted water drainage depends heavily on the geology of the underlying deposit and the overlying strata (U.S. EPA, 2011). Mine drainage is neutral to alkaline in some areas in North America because H^+ ions produced from pyrite oxidation are neutralized by carbonates naturally occurring in the overburden or added to the valley fill (Giam et al., 2018; Petty et al., 2010). As a result of the high carbonate concentrations, the incoming pH of mine-impacted water tends to be neutral to alkaline, which influences the photocatalytic reduction process significantly.

pH is known to highly influence the photoreduction process of selenate due to the outer-sphere complexes formed between TiO_2 and the selenate anion (Jordan et al., 2011). Given the point-of-zero charge (PZC) of TiO_2 (PZC = 5.6-6.2 (Jiang et al., 2008; Suttiponparnit et al., 2010)), the zeta potential is positive at pHs under ~6. Under these acidic conditions, anionic selenate is electrostatically attracted to the positively charge TiO_2 surface. This attraction contributes to a stronger outer-sphere adsorption of selenate, which is a key first step in the photocatalytic reduction process. Thus, we studied the effect of pH on the photocatalytic reduction of selenate in MIW. Experiments were conducted under controlled pH conditions, using the same concentration of electron hole scavenger for each trial, followed by pH adjustment with either NaOH or HCl to maintain the desired pH throughout the entire experiment. Figure 3-3 presents the experimental results of this study, showing that the extent of selenate reduction decreases with increasing pH (pH range 3.5-6.6). When the pH of the solution is raised above the PZC of TiO_2, the reaction markedly slows, resulting from the inhibition of electrostatic-mediated outer-sphere adsorption of selenate onto TiO_2.

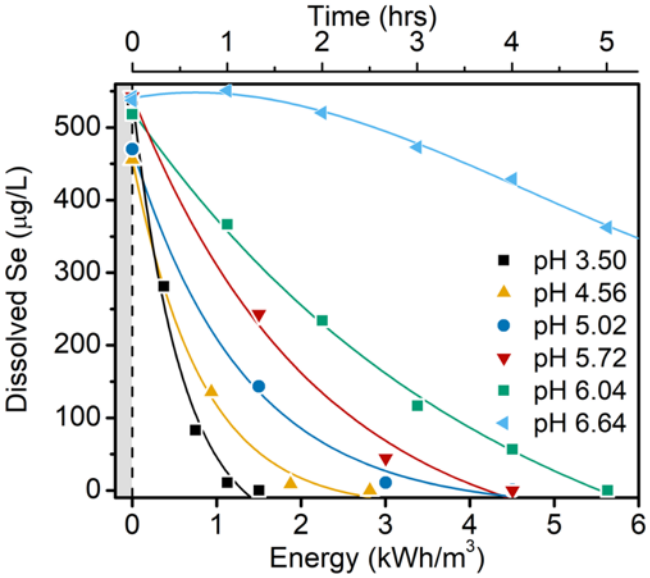

Figure 3-3. Selenate removal from mine impacted water using formic acid as an electron donor under varying pH. (Reaction conditions: 300 mg L^{-1} formic acid, 0.2 g/L TiO_2, 37 °C)

Experiments without pH control were also conducted at different initial pH of the solution. Under these conditions, the reduction of selenate was completely inhibited above an initial pH of 5.0, likely due to the pH rise during the photoreduction (Figure B-1). At a pH_0 of 5.0, photoreduction begins in a similar manner to that presented in Figure 3-3; however after 1 kWh/m^3 of UV exposure the reaction suddenly stops and no more Se is removed from solution. At a pH_0 of 5.5, photoreduction fails to remove any Se from the MIW. These experiments suggest that the pH of the solution increases during either dark adsorption or UV exposure. Control experiments were conducted to determine the nature of pH variation throughout the reduction of selenate. When the electron donor formic acid is added at concentrations of 300 and 100 mg/L, initial pH of the MIW drops from ~8.5 to 4.5 and 5.5, respectively. An additional amount of HCl was then added to the solution of 100 mg/L formic acid to bring the pH_0 to 4.5 and maintain similar initial reaction kinetics. The photocatalytic reduction of selenate proceeded similarly to when pH was controlled, although the pH increased substantially more in the case of 100 mg/L formic acid (Figure B-2). The pH increase is likely due to the abstraction of H^+ ions from solution for the production of reduction products such as H_2Se. The oxidation of formic acid to CO_2 is minimal throughout the reaction (< 3%), as indicated by TOC concentration measurements before and after the reaction and thus not likely a major cause of increasing pH.

3.4.2.2 Effect of temperature

Experiments were completed to investigate the effects of temperature on the reaction kinetics for the reduction of selenate in MIW. The Arrhenius plot of the apparent first-order rate constants (inset of Figure 3-4) was used to calculate an apparent activation energy (E_{aa}) of 31.83 ± 7.07 kJ mol^{-1} for the reduction of selenate in MIW, using formic acid as an electron donor. The respective Se removal curves at each temperature are given in Figure B-3. The existence of a high apparent activation energy was documented in Chapter 2, although the activation energy of MIW is smaller than the 90.09 kJ mol^{-1} found for the treatment of FGD wastewater. This is likely due to the fact that the TDS of this MIW is much lower at 2.25 g/L compared to the 4.62 g/L in FGD. The conclusion from our previous work is that the high TDS or ionic strength of the wastewater (primarily from Ca^{2+} and SO_4^{2-}) leads to a higher apparent activation energy of the photocatalytic reaction. Thermally accessible defects in photo-deposited $Se_{(s)}$ cause greater electron excitation at higher temperatures, while high levels of Ca^{2+} and SO_4^{2-} contribute to a high E_{aa} caused by bend bending at the electrolyte-catalyst interface.

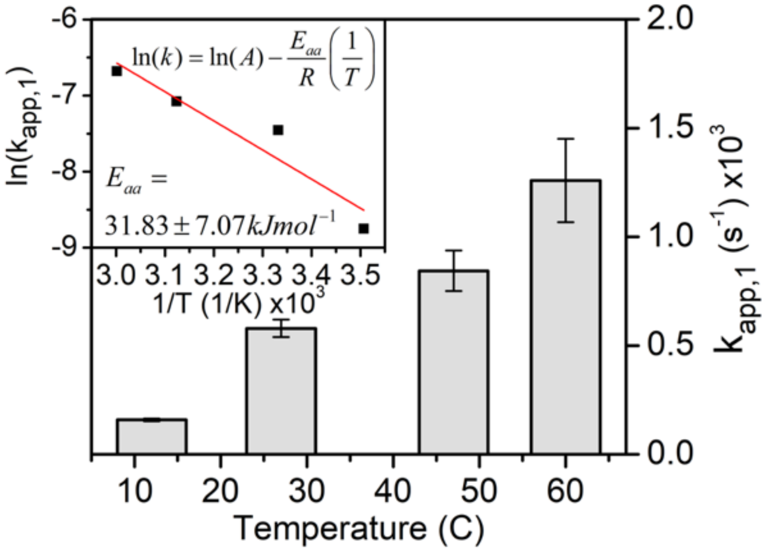

Figure 3-4. Apparent first-order rate constant as a function of reaction temperature for the photocatalytic reduction of selenate in MIW with inset Arrhenius plot. (Reaction conditions: 300 mg L^{-1} formic acid, 0.2 g/L TiO_2, pH 4.5).

Total mass balances were completed during experiments in order to investigate the role temperature plays on the generations of, $Se_{(s)}$ and $H_2Se_{(g)}$. Figure B-4 contains Se mass balances throughout the photoreduction of selenate from MIW at four temperature (12 °C, 27 °C, 37 °C and 47 °C). Selectivity of solid Se product is calculated by:

$$S\left(Se^0_{(s)}\right)_t = \frac{\left[Se^0_{(s)}\right]_t}{\left[SeO_4^{-2}\right]_0 - \left[SeO_4^{-2}\right]_t} \tag{3.3}$$

The only possible reduction products are $Se_{(s)}$ and $H_2Se_{(g)}$, thus the selectivity of $H_2Se_{(g)}$ is simply calculated as $1 - S\left(Se^0_{(s)}\right)_t$. Table 3-1 highlights the maximum percent of $Se_{(s)}$ generation (calculated by $[Se_{(s)}]_t$ / $[Se_{Total}]_0$) during the run and the initial selectivity of solid Se. At lower temperatures, the selectivity of the solid Se product is much higher and more $Se_{(s)}$ is generated during the reaction. $Se_{(s)}$ is an intermediate product, which is further reduced to $H_2Se_{(g)}$, hence at lower temperatures this second reaction (Outlined in Eq. 3.1) is inhibited. The kinetics of the overall reaction is slower as well (Figure B-4), at lower temperatures leading to increased reaction times needed to achieve to same Se removal.

Table 3-1. Maximum $Se_{(s)}$ generation and initial selectivity of $Se_{(s)}$ with varying temperatures.

Temperature (°C)	Maximum $Se_{(s)}$ Generation	Average $\mathbf{S}\left(\mathbf{Se}^{0}_{(s)}\right)_{t}$
12	56.3 %	78.9 %
27	38.8 %	45.2 %
37	40.0 %	53.4 %
47	32.6 %	44.5 %

Within Se-TiO_2 photocatalytic systems, the large temperature dependence arises for two main reasons: intrinsic semiconductor properties and solution film mass transport associated with adsorption of reactants and desorption of products. To explain the former, the photodeposited Se^0 contains thermally accessible defects which reduce the bandgap of Se, allowing for greater electron excitation at higher temperatures (Kasap et al., 2015). The simultaneous inhibition of the overall reduction reaction and the increase in selectivity to $Se_{(s)}$ suggests that the reduction of $Se_{(s)}$ to $H_2Se_{(g)}$ is a bottleneck at lower temperatures. This result reinforces the theory of thermally accessible defects within amorphous Se which allow the second reaction and therefore the entire selenate reduction to proceed at a faster rate at higher temperatures. A threshold temperature appears to occur between 12°C and 27°C, above which an increase in temperature has much less of an effect on the reaction rate.

3.4.2.3 Effect of dissolved oxygen (DO)

Selenate removal from MIW via photocatalytic reduction on TiO_2 was compared for five different durations of nitrogen (N_2) purge of 0, 5, 10, 20 and 60 minutes, which resulted in initial dissolved oxygen (DO) concentrations of 6.3, 5.0, 3.8, 3.3 and 2.7 mg/L, respectively. As shown in Figure 3-5, selenate removal by photocatalytic reduction required 3.3 mg/L DO or lower to achieve effective Se removal. O_2 is known to react with photogenerated electrons in the conduction band of TiO_2, forming superoxide radicals ($O_2^{\bullet -}$), and at low pH the protonated hydroperoxyl radical ($^{\bullet}O_2H$), a very powerful oxidant (Turolla et al., 2015). The $^{\bullet}O_2H$ radical can oxidize elemental $Se_{(s)}$ back to selenate, greatly inhibiting the reaction. Throughout the photocatalytic reaction DO is decreasing, indicating the conversion of molecular oxygen into redox byproducts, see Figure B-5. During the 5 and 10 min N_2 purge experiments the DO concentrations initially exceeds the required 3.3 mg/L. However, as the UV exposure progresses, the DO in both experiments drops down to 2.6 and 2.5 mg/L, respectively. Although the DO dipped below the threshold concentration to initiate the selenate reduction reaction, the reaction still did not proceed. It is postulated that the produced $^{\bullet}O_2H$ generated under the initial UV exposure, is responsible for an oxidizing environment which inhibits selenate reduction regardless of final DO concentration.

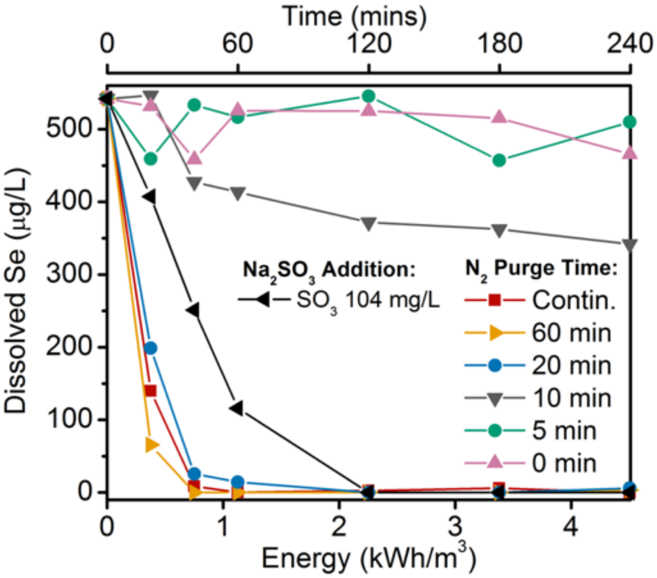

Figure 3-5. Selenate removal from mine impacted water using formic acid as an electron donor with varying N2 purge times which result in varying concentrations of dissolved oxygen or the addition of the oxygen scavenger, Na_2SO_3. (Reaction conditions: 300 mg L^{-1} formic acid, 0.5 g/L TiO_2, 37 °C, pH 4.5)

N_2 purging is an effective method of DO removal in a laboratory environment but is not practical for many large industrial applications. Industrial scale DO removal techniques include membrane contactors, cold water vacuum deaeration, hot water stripping deaeration and the use of oxygen scavengers (Pabby et al., 2008). The most commonly used oxygen scavenger for low pressure systems is sodium sulfite (Na_2SO_3) which reacts with low concentrations of oxygen to form sodium sulfate (Na_2SO_4). An experiment was conducted to demonstrate selenate reduction in MIW utilizing Na_2SO_3. A dose of 104 mg/L Na_2SO_3 was added to achieve an initial DO level of 2.2 mg/L, sufficiently below the concentration threshold of 3.3 mg/L determined previously through the N_2 purge experiments. The reduction of selenate in this trial was slower than that during the 20 and 60 min N_2 purge times, even though the initial DO concentrations were much lower. This is likely a result of the interaction between TiO_2 and sodium sulfite and sulfate prior to UV exposure. Both sulfite and sulfate are known to adsorb effectively to TiO_2 surfaces and compete for adsorption sites with selenate (Sheng et al., 2013; T. Yang et al., 2013).

3.4.2.4 Effect of concentration of catalyst

The removal of selenate under varying concentrations of TiO_2 was investigated within a working range of 0 - 1.0 g/L TiO_2 in suspension. As observed in Figure 3-6, selenate removal increases with increasing TiO_2 concentration, but the rate increase flattens out at higher TiO_2 concentrations, to yield a maximum reduction rate constant of 5.13×10^{-3} s^{-1}. The asymptotical behaviour is attributed to an increase in scattering phenomena caused by the increase in solid photocatalyst particles in suspension. This phenomenon has been observed in many studies where heterogeneous photocatalysis is applied to reduce contaminants by UV/TiO_2 systems (Fotiou et al., 2015; Valari et al., 2015). The relationship between TiO_2 concentration and apparent first-order reaction rate constant for the photocatalytic reduction of SeO_4^{2-} in MIW can be adequately described by the following relation:

$$k_{app,1} = \frac{2.023\times10^{-3} I_{UV}\times[TiO_2]}{1+4.352[TiO_2]} \tag{3.4}$$

where $k_{app,1}$ is the first order apparent rate constant in s^{-1}, I_{UV} is the intensity of UV light in mW cm^{-2} (for our experiment I_{UV} = 11.03 mW cm^{-2}) and $[TiO_2]$ is the TiO_2 concentration in g L^{-1}.

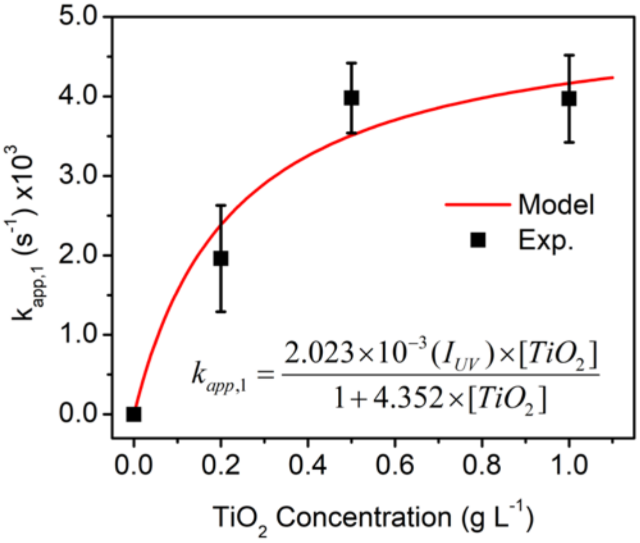

Figure 3-6. Apparent first-order reaction rate constants for the reduction of selenate in mine impacted water as a function of TiO_2 concentration. (Reaction conditions: 300 mg L^{-1} formic acid, 37 °C, pH 4.5)

3.4.2.5 Effect of electron hole scavenger

The effects of various organic electron hole scavengers (methanol, ethanol, acetic acid, glycerol and formic acid) were investigated to determine the optimal photocatalytic reduction rates of selenate in MIW. As shown in Figure 3-7, the use of 300 mg L^{-1} formic acid achieves the fastest Se removal rate. Se photoreduction was achieved with all tested electron hole scavengers with increasing Se removal rates in accordance to the following order: acetic acid < ethanol < methanol < glycerol < formic acid. All experiments were initially completed at a nominal concentration of 300 mg L^{-1}, however in the instance of acetic acid, ethanol and methanol the photoreductions were quite slow and their concentrations were increased to 800 mg L^{-1} to better characterize the reduction kinetics.

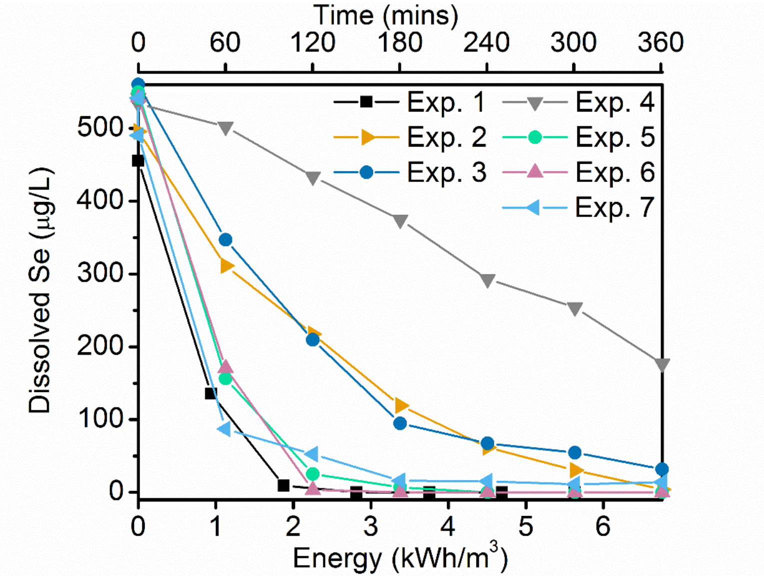

Figure 3-7. Selenate reduction in mine impacted water while using various electron hole scavenger types and concentrations. (1) 300 mg L^{-1} formic acid, (2) 800 mg L^{-1} methanol, (3) 800 mg L^{-1} ethanol, (4) 800 mg L^{-1} acetic acid, (5) 300 mg L^{-1} acetic acid and 100 mg L^{-1} formic acid, (6) 100 mg L^{-1} formic acid, and (7) 800 mg L^{-1} glycerol. (Reaction conditions: 0.2 g/L TiO_2, 37 °C, pH 4.5)

Previous studies investigating the effect of organic hole scavengers on the photocatalytic reduction of selenium oxyanions, found a similar trend for the order of increasing Se removal rates with electron hole scavengers of ethanol < methanol < formic acid (T.T.Y. Tan et al., 2003a). Reasons for formic acid being the most efficient hole scavenger are its ability to compete with the selenate ion, and most likely sulfate ions, for the TiO_2 surface sites, its rapid mineralization and ability to form reducing radicals, such as $CO_2^{\bullet -}$. Tan et al. reported no Se photoreduction with the use of acetic acid, whereas our study showed acetic acid capable of reducing some selenate (Exp. 4 in Figure 3-7). The experiments were done under very similar operating conditions, with the exception of a higher concentration of Se in the water being treated (20 ppm Se(VI)) in the work done by Tan et al. It is likely that under excess concentration of selenate, acetic acid is incapable of competing for adsorption sites on the surface of TiO_2 and thus rendered ineffective at scavenging electron holes.

Photocatalytic reduction can selectively remove Se from MIW containing many other competing ions in the complex real water source (as shown in Figure 3-8c & f). As a result, it may be advantageous to couple photocatalytic Se removal with biologic nitrate reduction to meet the effluent limit guidelines for both Se and nitrate. This offers many advantages over conventional biological reduction of both selenate and nitrate, namely no formation of organic selenium species, such as selenomethionine and other discrete organic Se species with a potentially increased bioavailability (LeBlanc and Wallschläger, 2016). During selective Se removal in the presence of nitrate, most of the organic hole scavenger remains in solution after Se is largely removed (as shown in Figure 3-8c & f). Therefore, the residual organic scavenger can subsequently be utilized in downstream denitrification. The denitrification process would convert the electron donor to CO_2 in the final biological step so no residual organics species would have to be removed further downstream.

The removal of Se prior to biological nitrate removal has numerous advantages: (1) no Se contamination of the bioreactor sludge; (2) biological process can be designed for denitrification only; (3) generation of a recoverable, concentrated Se-containing residual; and (4) compatible electron donors can be used for both photocatalytic and biological processes.

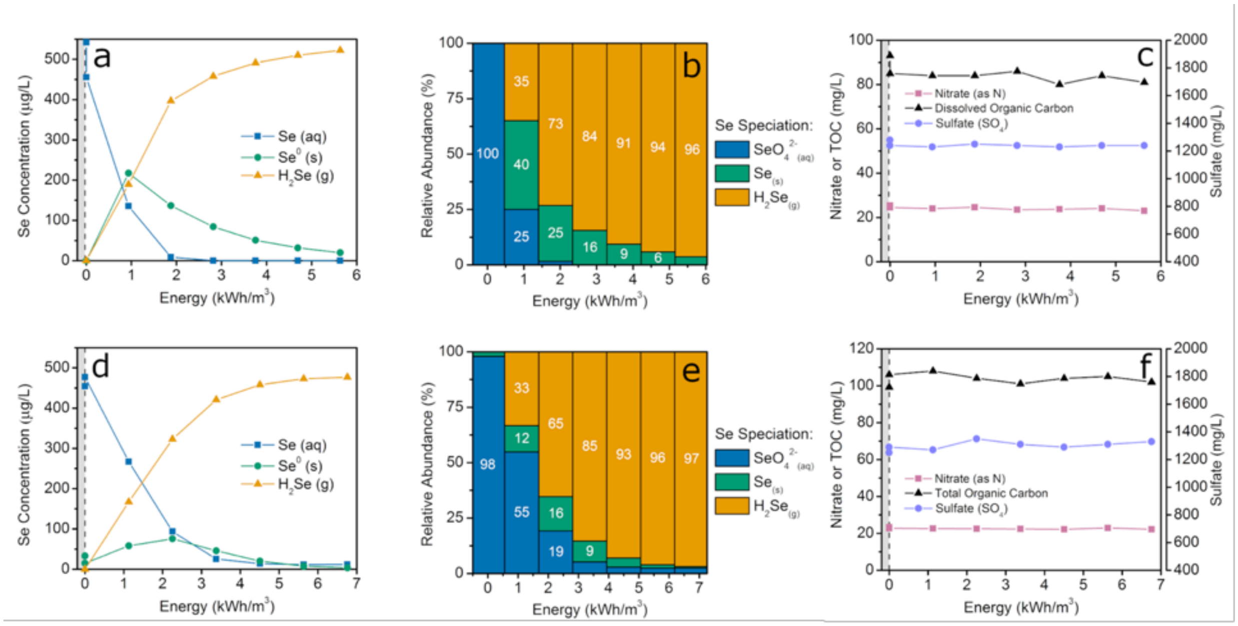

Figure 3-8. Selenate reduction in MIW using 300 mg L^{-1} formic acid (a-c) and glycerol (d-f) as electron hole scavenger. (a/d) Se mass balance, (b/e) Se percentage speciation, and (c/f) Concentrations of nitrate, sulfate and organic carbon during selenate photocatalytic reduction. (Reaction conditions: 0.2 g/L TiO_2, 37 °C, pH 4.5)

The primary electron donors used for biological denitrification are acetic acid, glycerol, methanol and ethanol (Bill et al., 2009; Strong et al., 2011). Formic acid has been used as an electron donor in the denitrification process as well, although bioreactor acclimation is required in order to ensure the microbes can effectively utilize formic acid as a carbon source (Li et al., 2015; Nishimura et al., 1980; R. H. Gerber, 1986). A closer look at the comparison of the use of formic acid and glycerol as electron hole scavengers for Se removal is presented in Figure B-6, showing that with a concentration of 300 mg L^{-1} glycerol nearly matches the Se removal rates using formic acid, whereas formic acid greatly outperforms glycerol at only 100 mg L^{-1}. Figure 3-8 compares the reduction of selenate and production of Se^0 and H_2Se in MIW when using 300 mg L^{-1} of either formic acid or glycerol. Both glycerol and formic acid provide selective Se removal in the presence of nitrate and sulfate in MIW, leaving the nitrate and sulfate in solution. Inspection of Figure 3-8b & e shows the removal of aqueous selenate is faster with formic acid, due to a larger proportion of solid Se^0 generation. The actual amount of H_2Se generation for both trials is very similar, with the total amount of Se remaining in solution ($SeO_4^{2-}{}_{(aq)}$ + $Se^0{}_{(s)}$) nearly equal for both formic acid and glycerol. It is postulated that formic acid generates more Se solid due to the fact that it adsorbs more favorably to the surface of TiO_2 through electrostatic forces, whereas glycerol adsorbs weakly through van der Waals forces and hydrogen bonding.

Aside, from a higher selenate reduction rate constant, the addition of formic acid also leads to a lower pH. The titration curve for formic acid is presented in Figure B-7 and compared to that for HCl in MIW. As discussed previously, lower pH leads to faster selenate photocatalytic reduction. The addition of HCl for pH reduction can be done followed by an addition of NaOH to raise the pH after treatment. However, this method adds to the already elevated total dissolved solids (TDS) in the treated water and is unfavorable. The presence of formic acid reduces pH, but is a dissolved species that will be removed in the subsequent biological reduction of nitrate. Thus, formic acid is considered a suitable electron donor for this photocatalytic process.

To ensure that the use of electron hole scavengers is scalable to a larger industrial process, industrial grade sources of both glycerol and formic acid were acquired and tested. An economical source of glycerol from Environmental Operating Solutions, Inc. called MicroC4200, which contains 72 wt% glycerol was tested. Comparison of industrial glycerol from MicroC4200 to lab grade glycerol is shown in Figure B-8. The lab grade glycerol shows faster selenate photocatalytic reduction kinetics, likely due to the presence of close to 5 wt% NaCl in MicroC4200, which could inhibit the adsorption of selenate onto TiO_2 through charge screening of the electrostatic adsorption. The increase of ionic strength in solution can also lead to increased aggregation of TiO_2 reducing catalytic surface area, following DLVO theory (Hotze et al., 2010). A source of industrial grade formic acid was acquired and compared to the results with lab grade formic acid (Figure B-9). The industrial grade formic acid and lab grade formic acid exhibit similar selenate removal kinetics as well as the selectivity between solid Se^0 and gaseous H_2Se production.

3.4.2.6 Effect of MIW pretreatment

Three separate precipitation pretreatments of mine-impacted water through the addition of $Ca(OH)_2$, Na_2CO_3 and $Ba(OH)_2$, were investigated to determine the effects of removing CO_3^{2-}, Ca^{2+} and SO_4^{2-}, respectively. Lime softening ($Ca(OH)_2$ addition) was done at pH 9.5, $CaCO_3$ precipitation (Na_2CO_3 addition) at pH 11, $BaSO_4$ precipitation ($Ba(OH)_2$ addition) at pH 9.5. All solution were returned to pH 7 using HCl before storage in the refridgerator.

Figure 3-9 presents the effect of the three precipitation pretreatments on the subsequent reduction of selenate in order to compare the effect of the removal of CO_3^{2-}, Ca^{2+} and SO_4^{2-}. The removal of CO_3^{2-} appears to have very little effect on the photocatalytic reduction of selenate in mine-impacted water. Previous researchers have demonstrated that HCO_3^- or CO_3^{2-} can act as an electron hole scavenger, consuming $OH^\bullet$ radicals in solution and electron holes (h^+) on the surface of TiO_2 (Arakawa and Sayama, 2000; Ni et al., 2007), leading to slightly faster kinetics in the presence of CO_3^{2-}, in this case in raw MIW. During the removal of Ca^{2+} via $CaCO_3$ precipitation, 13% of the aqueous selenate was removed. This removal was likely due to selenate adsorption on precipitated $CaCO_3$. However, the kinetics of photocatalytic degradation remained similar to that observed with the raw MIW, with a marginally faster initial selenate reduction rate.

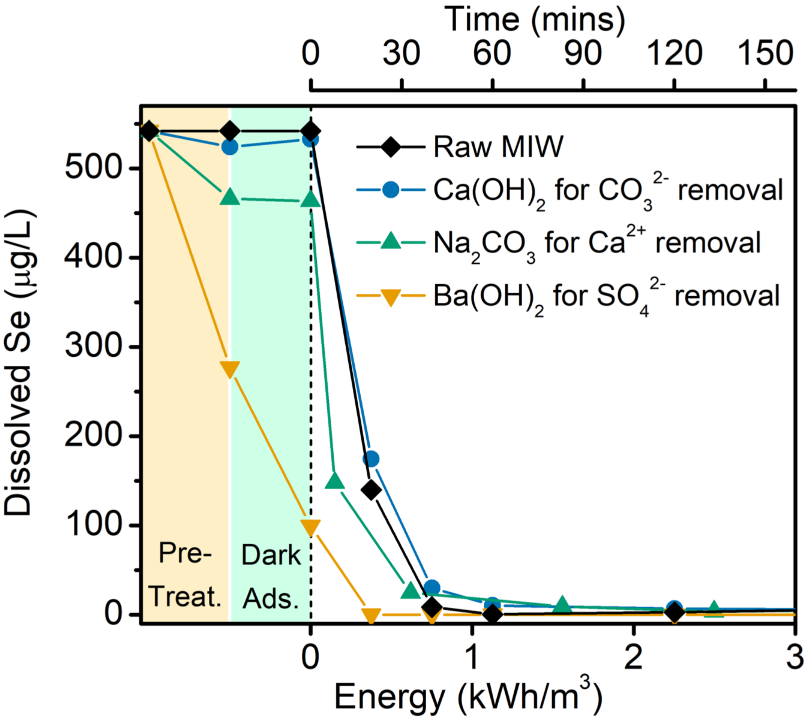

Figure 3-9. Comparison of varying pretreatments prior to the photocatalytic reduction of selenate over TiO_2 in mine-impacted water. (Reaction conditions: 0.2 g/L TiO_2, 37 °C, pH 4.5, 300 mg/L glycerol)

During the removal of SO_4^{2-}, via $BaSO_4$ precipitation, 49% of the aqueous selenate was removed. It is hypothesized that Se removal during $BaSO_4$ precipitation is attributed to selenate adsorption onto $BaSO_4$ precipitates rather than $BaSeO_4$ precipitation, due to the relatively high solubility of $BaSeO_4$. Removal of SO_4^{2-} allowed for selenate to adsorb to the TiO_2 during the dark adsorption, accounting for an additional 33% selenate removal, which did not occur in the other trials. With only 18% of the initial selenate remaining in solution at the start of the photocatalytic reduction, the reduction is fully completed over the first sampling interval. The presence of SO_4^{2-}

is known to obstruct the adsorption of selenate on the surface of TiO_2, limiting the selenate coverage of reaction sites (Nakajima et al., 2013, 2011; T. Yang et al., 2013).

3.5 Conclusions

The photocatalytic reduction on TiO_2 is a promising non-biological technique for selenate removal from MIW in order to remove Se below 1 μg L^{-1}. Selenate is reduced to solid elemental Se (Se^0) and gaseous hydrogen selenide (H_2Se) in a 6 electron and 2 electron heterogeneous photocatalytic reaction, respectively. The product selectivity towards solid Se^0 versus gaseous H_2Se is influenced by many factors, including temperature and electron hole scavenger. Regardless of the high sulfate, nitrate, and carbonate concentrations and the presence of various trace metals contained in MIW the photocatalytic reaction was able to reduce selenate under different reaction conditions from >500 μg L^{-1} Se to < 1 μg L^{-1}.

Below the point of zero charge of TiO_2 (PZC_{TiO2}= 5.6-6.2), faster kinetics are achieved at lower pHs due to the positive zeta potential of the catalyst surface and increased electrostatic attraction and outer-sphere adsorption of selenate. The highest pH able to achieve significant Se removal was pH 6.04 while the best kinetics were observed at pH 3.50. Temperature plays a major role in the reduction of selenate, which has an activation energy of 31.83 kJ mol^{-1}. Higher temperatures lead to higher selectivity toward H_2Se as well as faster selenate removal kinetics. The reaction is inhibited in the presence of dissolved oxygen (DO). The removal of DO prior to selenate removal was successfully achieved through N_2 purging to strip O_2 and the use of an oxygen scavenger, Na_2SO_3, which is a more scalable and practical DO removal alternative. Experiments were conducted to determine the effect of TiO_2 concentration of the reaction kinetics. A range of 0-1.0 g/L TiO_2 was studied with the optimal TiO_2 dosage concentration of 0.5 g/L.

The impact of various electron hole scavengers on the kinetics of selenate photocatalytic reduction was investigated. Se photoreduction was achieved with all tested electron hole scavengers with Se removal rates increasing in the following order: acetic acid < ethanol < methanol < glycerol < formic acid. Marginal differences to the selectivity of Se^0 vs. H_2Se were observed between glycerol and formic acid, which are both selective towards H_2Se generation under the conditions studied. The photocatalytic removal of selenate appears to be selective, leaving nitrate and sulfate essentially unreduced, a phenomenon which is thoroughly discussed in the next chapter. As a result, it may be advantageous to couple photocatalytic Se removal with biologic nitrate reduction, in order to meet the effluent limit guidelines for both Se and nitrate. During the selective Se removal in the presence of nitrate, the majority of the organic hole scavenger remains in solution after the Se is fully removed and can then be utilized for the downstream denitrification as an electron donor and converted to CO_2 which can be removed from the effluent.

4 Selective removal of Se through selenate specific photocatalytic reduction over TiO_2 in the presence of nitrate and sulfate in mine impacted water

This chapter is modified from:

Holmes, A.B., Giesinger, K., Ye, J., and Gu, F. (in preparation). Selective removal of Se through selenate specific photocatalytic reduction over TiO_2 in the presence of nitrate and sulfate in mine impacted water.

4.1 Summary

Selective photocatalysis is desired for complex water sources that contain a variety of dissolved species in addition to the species targeted for removal. Mine-impacted water (MIW) can contain varying concentrations of dissolved species such as sulfate, carbonate, nitrate, selenate, organic matter and metals. The removal of selenate from MIW is desired, given its potential toxicity in aquatic ecosystems. In this study, we present results of bench-scale testing of photocatalytic reduction (PR) of selenate in MIW, mainly the ability of PR to selectively reduce selenate from >500 μg L^{-1} to < 2 μg L^{-1}. The significant Se decrease was observed in the presence of the more energetically favourable electron acceptor nitrate and high concentrations of sulfate. The competitive adsorption and reduction of selenate on TiO_2 in the presence of sulfate, chloride, carbonate and nitrate was investigated using formic acid as an electron hole scavenger. According to our proposed electron transfer mechanism, TiO_2 conduction band electrons are responsible for the reduction of selenate to elemental Se (Se^0) while both carbon dioxide radicals ($CO_2^{\bullet\,-}$) and Se conduction band electrons are responsible for the further reduction of Se^0 to hydrogen selenide (H_2Se).

4.2 Introduction

Photocatalysis in water has been conventionally considered to be a non-selective process. Research in selective photocatalysis is a rapidly developing field (Kou et al., 2017). In recent years, many researchers have been focusing on various strategies to improve the selectivity of photocatalysis and increase its industrial feasibility. Reactive radical-mediated photocatalytic oxidation and reduction can behave non-selectively through the production of reactive radicals such as hydroxyl radicals ($OH^{\bullet}$) and carbon dioxide radicals ($CO_2^{\bullet\,-}$), respectively, which are ubiquitous in their reactivity towards species in a complex wastewater (Asghar et al., 2015). Many attempts have been made to modify photocatalysts to allow for selective removal of target species in complex wastewaters. The strategies for enhancing selective photocatalysis can be divided into two categories: modification of photocatalyst properties or change of external operating conditions (Kou et al., 2017). Some examples of selective photocatalysis include selective reduction of Cr(VI) through size exclusion over a ZnO@ZIF-8 core-shell heterostructure (Wang et al., 2016), selective organic oxidation on TiO_2 through controlled mass transport (Ghosh-Mukerji et al., 2003), selective removal of methyl violet over methyl orange using TiO_2 microspheres with exposed

{001} facets (Xiang et al., 2011), and selectively reducing nitrate to N_2 on TiO_2 by managing the hole scavenger conditions (Doudrick et al., 2013).

Selective photocatalysis is desired since water sources usually contain a variety of dissolved species in addition to the target species. Mine-impacted water (MIW) can contain varying concentrations of many compounds such as sulfate, carbonate, nitrate, selenate, organic matter and dissolved metals (Nordstrom et al., 2015). The removal of selenate from MIW is desired due to its toxicity in aquatic ecosystems at low μg/L concentrations (L. C. Tan et al., 2018). The photocatalytic reduction of selenate on TiO_2 in water proceeds through the two following reduction reactions:

$$SeO_4{}^{2-}{}_{(aq)} + 8H^+ + 6e^-_{cb} \rightarrow Se^0{}_{(s)} + 4H_2O \tag{4.1}$$

$$Se^0{}_{(s)} + 2H^+ + 2e^-_{cb} \rightarrow H_2Se_{(g)} \tag{4.2}$$

The initial reduction of selenate into immobilized elemental Se ($Se^0{}_{(s)}$) removes it from the dissolved Se species in the water. Elemental Se can be further reduced to hydrogen selenide ($H_2Se_{(g)}$). Photocatalytic reduction of selenate has the unique advantage of recovery as either elemental Se in the solid phase or H_2Se through gas scrubbing techniques (Nguyen et al., 2005b). Se has numerous uses in the photovoltaics, glass and steel manufacturing and electronics industries (Holmes and Gu, 2016; Yarlagadda V. Nancharaiah and Lens, 2015).

Conventionally, bioreactors have been implemented as a method for Se removal from MIW on a pilot-scale (Lenz et al., 2008; Luek et al., 2014). Challenges remain with disposal and stability of Se-contaminated bioreactor sludge (Mal et al., 2017, 2016), microbial community start-up time and the elevated toxicity of effluents as a result of the production of organo-selenium compounds such as selenomethionine (LeBlanc and Wallschläger, 2016). In addition, the microbial communities responsible for metabolization of selenium oxyanions can only do so in the absence of electron acceptors with a higher reduction potential. Both O_2 and NO_3^- are more energetically favourable electron acceptors than Se oxyanions and thus, NO_3^- reduction can occur prior to selenate reduction in anaerobic bioreactors ($E'_{0,\,O_2/H_2O}$= +0.81 V > $E'_{0,\ NO_3{}^-/N_2}$= +0.75 V > $E'_{0,\ SeO_4{}^{2-}/SeO_3{}^{2-}}$= +0.48 V > $E'_{0,\ SeO_3{}^{2-}/Se^0}$= +0.21 V > $E'_{0,\ SO_4{}^{2-}/SO_3{}^{2-}}$= -0.516 V (Y. V. Nancharaiah and Lens, 2015)). For MIW treatment, the development of a process capable of removing selenate prior to biological denitrification process is desired due to the numerous advantages achieved by removing Se from the biological process.

In this study, we present experimental results on the photocatalytic reduction of selenate tests using MIW. The results demonstrate that Se can be selectively removed from >500 µg L^{-1} to < 2 µg L^{-1} in the presence of a more energetically favourable nitrate electron acceptor (~ 250x molar concentration of selenate) and high concentrations of sulfate (~ 2,000x molar concentration of selenate). The competitive adsorption and reduction of selenate on TiO_2 in the presence of sulfate, chloride, carbonate and nitrate was thoroughly investigated using formic acid as an electron hole scavenger. The primary goal of this work is to explain the phenomena of selective reduction of selenate and to propose primary reaction pathways to better understand the complex photocatalytic reduction of selenate to elemental Se and further to H_2Se.

4.3 Materials and methods

4.3.1 Materials

Mine impacted water (MIW) was received from an operating mine in North America and stored at 4 °C in the dark. Synthetic mine impacted water (SMIW) was produced by dissolving reagent grade salts in DI water to mimic the concentrations in MIW. Titanium dioxide nanoparticles (Aeroxide P25, ~10-50 nm particle diameter, 55 m^2 g^{-1} surface area, Acros) were used as received. P25 TiO_2 nanoparticles have been extensively studied and characterized in the literature and are often used as a benchmark photocatalyst. Formic acid (ACS reagent, 97%, Alfa Aesar) was used as an electron hole scavenger. Sodium selenate (<0.1% impurities, BioXtra, Sigma-Aldrich), sodium sulphate (anhydrous, ACS reagent >96%, Sigma-Aldrich), sodium chloride (reagent grade, Sigma-Aldrich), sodium carbonate (reagent grade, Sigma-Aldrich), sodium nitrate (>99%, ReagentPlus, Sigma-Aldrich), hydrochloric acid (37%), and sodium hydroxide (ACS grade, Sigma-Aldrich) were used as received.

4.3.2 Removal of selenate through photocatalytic reduction

The photocatalytic reactor apparatus consists of an air tight stainless-steel reactor vessel of 1.0 L capacity with a quartz-window through which UV was irradiated. Impacted water was added to an internal PTFE liner followed by formic acid and TiO_2. The air tight stainless-steel vessel with a quartz window was purged by bubbling N_2 gas throughout the reaction to remove any H_2Se gas generated and flowing it through two subsequent liquid scrubbers of $CuSO_4$ and NaOH, respectively (Sanuki et al., 1999; T.T.Y. Tan et al., 2003b). The mixture was stirred in the dark for 1 h to attain adsorption-desorption equilibrium with the TiO_2 surface as well as to remove any dissolved oxygen, and then placed in the photoreactor and exposed to UV light while being stirred. Samples were collected throughout the treatment to determine both the total and dissolved Se by analyzing unfiltered and filtered samples, respectively. The reactor vessel was exposed to UV light using a UVA fluorescent bulb with a wavelength filter which only supplied UVA (λ = 365 nm) light (Blak Ray B-100A 95-0044-22). The UV intensity was measured to be $I_{UV} = 11.03\, mW/cm^2$ with a UV-A light meter (Sper Scientific, NIST certified calibration) at the surface of the water within the reaction chamber through the quartz window. We varied the energy dosage instead of operating time to make our results comparable with other studies.

4.3.3 Analysis

Se concentration was determined in accordance with the U.S. EPA suggested determination technique (APHA 2009, Method 3114B/C) using hydride generation inductively coupled plasma optical emission spectroscopy (HG-ICP-OES, Teledyne Prodigy ICP and Cetac HGX-200 advanced membrane hydride generation system, LOD = 1 μg L^{-1}). Both dissolved and total Se were determined by HG-ICP-OES following acid digestion protocol U.S. EPA Method 3050B (U.S. EPA, 1996). The insoluble Se fraction (considered to be elemental Se) present in the water was calculated by the difference of total and dissolved Se concentrations. Gaseous H_2Se was calculated from the difference between the initial total Se in the water and total Se in the TiO_2 suspension after UV exposure. Based on several past studies on photocatalytic reduction of selenate on TiO_2 (Nguyen et al., 2005b; Sanuki et al., 1999; T.T.Y. Tan et al., 2003a), the gaseous Se species is assumed to be H_2Se, although the direct identification of gaseous species is a challenging task (Kot and Namieśńik, 2000; Uden, 2002). Se analytics is currently a major developing field of study, with researchers looking into new and improved approaches to gaseous and solid Se speciation analytical techniques (Santos et al., 2015).

Total organic carbon (TOC, APHA 5310B, combustion temperature 800 °C), chemical oxygen demand (COD, APHA 5220D), biochemical oxygen demand (BOD, APHA 5210B), anion concentration by ion chromatography (bromide, chloride, fluoride, nitrate, nitrite and sulfate, EPA 300.1), total ammonia (Watson et al., 2005), speciated alkalinity (as $CaCO_3$, EPA 310.2), and total and dissolved metals by inductively coupled plasma mass spectrometry (ICPMS, EPA 200.2/6020A and APHA 3030B/6020A) were measured according to standard methods by ALS Environmental (Calgary, AB, Canada), a laboratory accredited by the Canadian Association for Laboratory Accreditation (CALA) according to international standards (ISO 17025). Total and dissolved Se concentrations determined at the University of Waterloo were confirmed by ALS Environmental on a number of analytical checks.

4.4 Results and Discussion

4.4.1 Selective reduction of selenate by TiO_2 in MIW

During the photocatalytic reduction of selenate in MIW, other co-existing anions (i.e. nitrate, sulfate, carbonate and chloride) can interact with the treatment process. However, throughout the photocatalytic treatment, it is found that these anions remain relatively stable in solution, and are not preferentially reduced over Se (Figure 4-1). Molar ratios for $NO_3^- : SeO_4^{2-} = 250$ and $SO_4^{2-} : SeO_4^{2-} = 1{,}940$ demonstrating that selenate is present at very low level compared to nitrate and sulfate. Oxyanions have been shown to compete with the adsorption sites on TiO_2 during photocatalytic reactions with complex wastewaters (Marks et al., 2016; T. Yang et al., 2013). However, during the photoreduction experiment, dissolved selenium (initially present as selenate) is reduced by 99.6% during the experiment, while sulfate was not reduced and 6.1% nitrate is removed throughout the UV exposure. Of the nitrate that is removed, 57% is reduced to ammonia (0.8 mg/L as N) and the remainder is reduced to a volatile species, assumed to be N_2O or N_2 gas. Thus, sulfate and nitrate largely remained in solution throughout the UV exposure in the presence of TiO_2, while dissolved Se was reduced through the photocatalytic reduction. This result suggests the existence of a selective photocatalytic reaction mechanism for selenate on TiO_2, which is present at 100-2,000x lower molar concentrations. The elucidation of such a mechanism is the primary focus of the experiments and discussion herein.

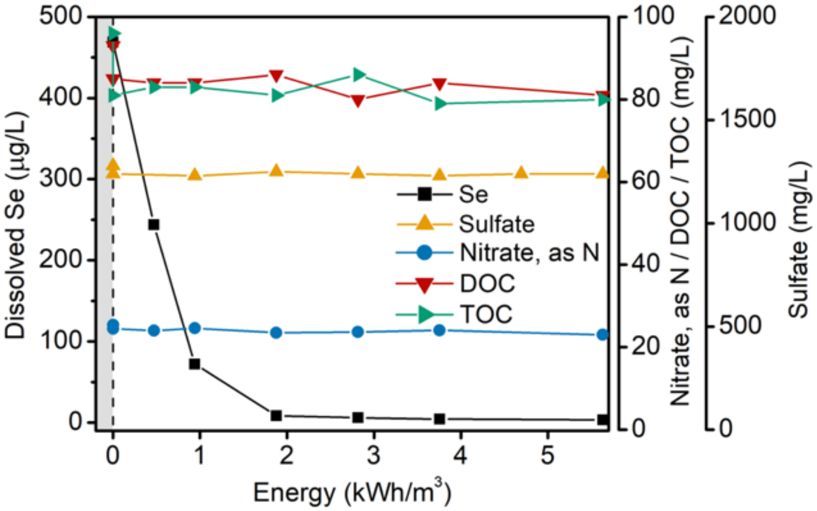

Figure 4-1. Selenate removal from mine-impacted water using formic acid as an electron donor while sulfate and nitrate remain in solution, highlighting the selective reduction of selenate in a complex real water system. (Reaction conditions: 300 mg L^{-1} formic acid, 0.2 g/L TiO_2, 37 °C, pH 4.5)

Figure 4-2 presents the electronic band energy levels of TiO_2 and Se and compares the reduction potentials of various reactions of interest. The reduction potential of nitrate ($E'_{0,\ NO_3^-/N_2}$= +0.75 V) is well below the conduction band of TiO_2 and thus is expected to proceed under favourable photocatalytic conditions. However, as shown in Figure 4-1, when compared to selenate reduction nitrate is minimally removed. Many researchers investigating the photocatalytic reduction of nitrate on TiO_2 have reported that due to the low interaction of nitrate with the surface of TiO_2, nitrate is reduced in solution mainly by the radical intermediate $CO_2^{\bullet -}$ upon the oxidation of the electron hole scavenger (Doudrick et al., 2013; Sowmya and Meenakshi, 2015; F. Zhang et al., 2005). The reduction potential of sulfate ($E'_{0,\ SO_4^{2-}/SO_3^{2-}}$= -0.516 V) is above the conduction band of TiO_2 and thus may not readily proceed on TiO_2. However, the reduction of Se^0 to H_2Se is also above the conduction band of TiO_2 and is able to proceed under these conditions, which does not explain the inert behaviour of sulfate entirely. To date, no reports of the photocatalytic reduction of sulfate on TiO_2 have appeared, suggesting that the electron transfer mechanism resulting in selenate and nitrate reduction does not occur for sulfate.

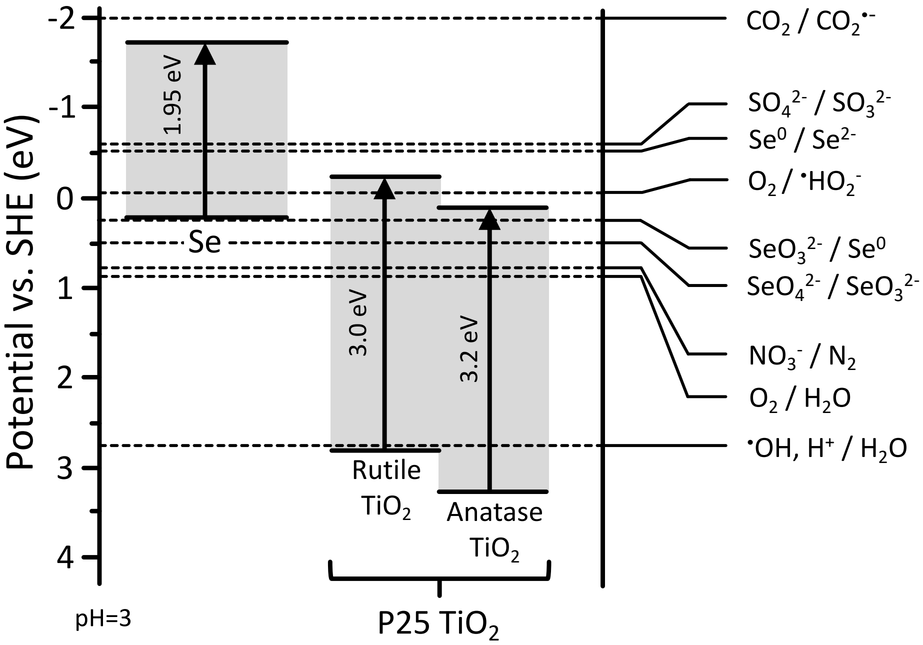

Figure 4-2. Schematic comparison of band edge positions of Se and TiO_2 together with the standard potentials of relevant redox couples.

4.4.2 Effect of co-existing anions

Several photocatalytic experiments were conducted to determine the effect of the competing anions in MIW on the reduction of selenate to Se^0 and H_2Se (Eq. 4.1 & 4.2). A list of experiments on the effect of various co-existing anions used to test the changes in the reduction of selenate on TiO_2 is given in Table 4-1. A concentration of 6.3×10^{-2} mM Se (approximately 10x the concentration of Se in MIW) as selenate was used in the mono-, dual-, triple- and quad-anion experiments to ensure the initial adsorption of selenate onto TiO_2 is less than 20% of the initial selenate concentration. This was done to minimize the kinetic effects on the subsequent photoreduction while still getting comparable results to learn about the competing anions in MIW from a ground-up approach. Anywhere from 30-50% Se of the selenate from an initial 6.6×10^{-3} mM, the actual Se concentration in the MIW, is adsorbed onto TiO_2 in DI and skews the comparison of the Se reduction data.

Table 4-1. Summary of competing anion experiments for the photocatalytic reduction of selenate.

Experiment number		SeO_4^{2-} conc. (mM)	Cl^- conc. (mM)	NO_3^- conc. (mM)	SO_4^{2-} conc. (mM)	CO_3^- conc. (mM)
Mono-anion competing effect	1	6.3×10^{-2}	-	-	-	-
	2	6.3×10^{-2}	1.0	-	-	-
	3	6.3×10^{-2}	10.0	-	-	-
	4	6.3×10^{-2}	-	1.0	-	-
	5	6.3×10^{-2}	-	10.0	-	-
	6	6.3×10^{-2}	-	-	1.0	-
	7	6.3×10^{-2}	-	-	10.0	-
	8	6.3×10^{-2}	-	-	-	1.0
	9	6.3×10^{-2}	-	-	-	10.0
Dual-anion	10	6.3×10^{-2}	-	1.0	1.0	-
	11	6.3×10^{-2}	-	1.0	-	1.0
	12	6.3×10^{-2}	-	-	1.0	1.0
Triple-anion	13	6.3×10^{-2}	1.0	1.0	1.0	-
	14	6.3×10^{-2}	1.0	1.0	-	1.0
	15	6.3×10^{-2}	1.0	-	1.0	1.0
Quad-anion	16	6.3×10^{-2}	1.0	1.0	1.0	1.0
SMIW	17	6.6×10^{-3}	0.1	1.8	13.0	3.2
MIW	18	6.6×10^{-3}	0.1	1.8	13.0	3.2

As shown in Figure 4-3, we can see that Cl^- has a minimal effect on either the reduction of selenate to solid Se^0 (based on the disappearance of dissolved Se in Figure 4-3a) or the reduction of solid Se^0 to gaseous H_2Se (based on the disappearance of solid Se in Figure 4-3b). Full mass balance tracking of each Se species throughout the mono-anion competition experiments are given in Figure 4-4. At 10 mM Cl^- the reduction of selenate to Se^0 is delayed slightly (Figure 4-3a), which can also be seen in the slightly smaller solid Se peak in Figure 4-3b. This is likely due the contribution of chloride to charge screening which induces aggregation of TiO_2 nanoparticles, decreasing the surface area on which selenate can adsorb and react (Hotze et al., 2010).

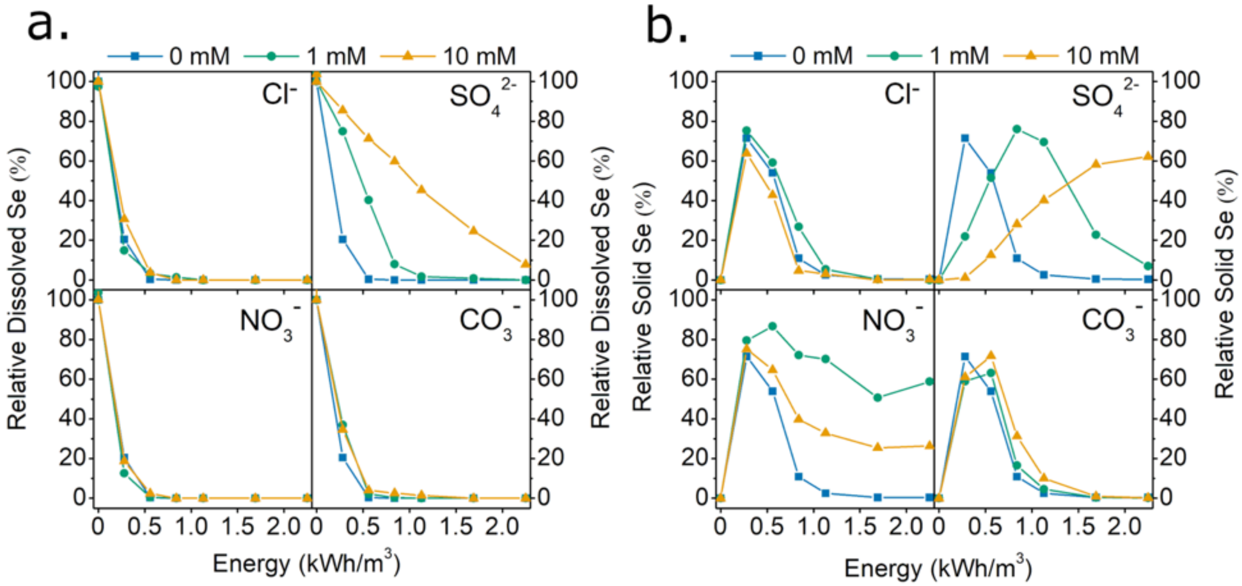

Figure 4-3. Effect of co-existing anions on the photocatalytic reduction of selenate in water: mono-anion competition. (a) dissolved Se and (b) solid Se during UV exposure.

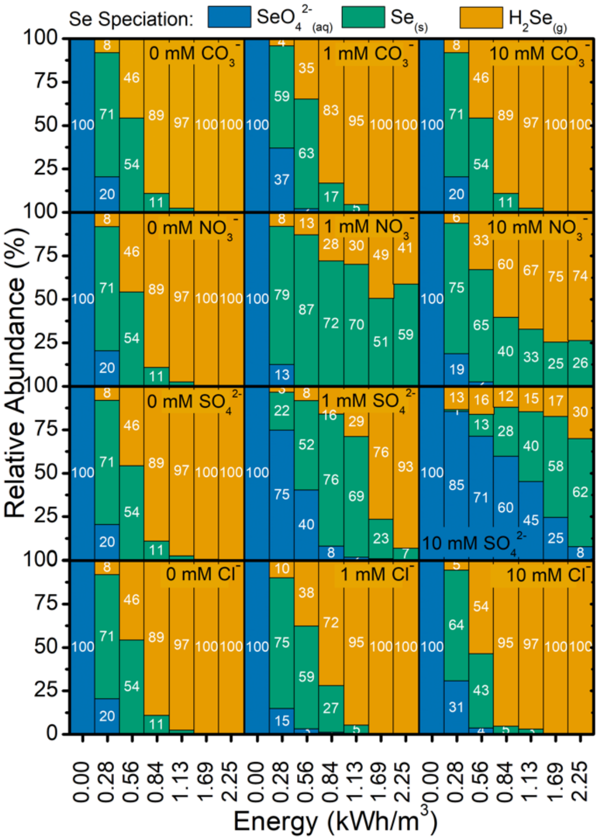

Figure 4-4. Se speciation during the photocatalytic reduction of selenate in water with co-existing mono-anions.

CO_3^- (or more properly dissolved CO_2 at the experimental pH) also had a minimal effect on the reaction with no effect on the reduction of selenate to Se^0 (Figure 4-3a), but possibly a small lag in the second reduction of Se^0 to H_2Se based on the small shift in the peak of maximum solid Se^0 by 0.3 kWh/m^3 (Figure 4-3b) . CO_3^- has been seen to act as an electron hole scavenger in some photocatalytic systems on TiO_2 (Ni et al., 2007), which could lead to an increased production of photoactive electrons in the conduction band of TiO_2. However, due to the high pKa of carbonate, it exists nearly entirely as H_2CO_3 at pH 3 in these experiments, which is known to dissociate into H_2O and CO_2. Thus, CO_3^- may not affect the reduction of selenate by TiO_2 due to its possible removal from solution in a gaseous form.

SO_4^{2-} has a major impact on the reduction of selenate to solid Se^0 as evident in the large inhibition of dissolved Se removal in Figure 4-3a. This is believed to be due to the competitive adsorption of sulfate over selenate on TiO_2 which has been reported in many studies showing inhibition of photocatalytic reactions in the presence of sulfate (Nakajima et al., 2013, 2011; T. Yang et al., 2013). The solid Se generation curves are attenuated along the x-axis, consistent with the inhibition of the reduction of selenate to solid Se^0. However, the impact of sulfate on the further reduction of Se^0 to H_2Se is less apparent. A close inspection of the solid Se^0 curves in Figure 4-3b shows a slight decrease in the peak solid Se^0 amount when a concentration of 10 mM sulfate is present. Although the peak is not fully shown in the data recorded, it is not likely to reach the ~75% Se^0 found for the DI baseline, but closer to 60%. This indicates that sulfate may also promote Se^0 reduction to H_2Se at higher concentrations.

NO_3^- has negligible impact on the reduction on selenate to solid Se^0 (Figure 4-3a), although interestingly it has a profound impact on the reduction of Se^0 to H_2Se (Figure 4-3b). Nitrate appears to inhibit the reduction of Se^0 to H_2Se greatly, as reflected by flattening of the peak of Se^0 as it becomes resistant to the photocatalytic reduction under UV exposure. 1 mM NO_3^- causes the greatest inhibition of Se^0 reduction, whereas the inhibition decreases and more H_2Se is generated at a higher concentration of 10 mM NO_3^-. These results indicate that nitrate is affecting the electron transfer responsible for reduction of Se^0 to H_2Se, although the effect of the ratio of nitrate to selenate, formate, or TiO_2 on electron transfer inhibition is not yet fully understood.

Next, we investigated the effect of combining the four anions in dual-anion and triple-anion competition experiments to probe the confounding effects of multiple anions on the reduction of selenate on TiO_2. The results of these experiments are presented in Figure 4-5. Each dual-anion competition experiment was conducted using 1 mM concentration of the competing anions.

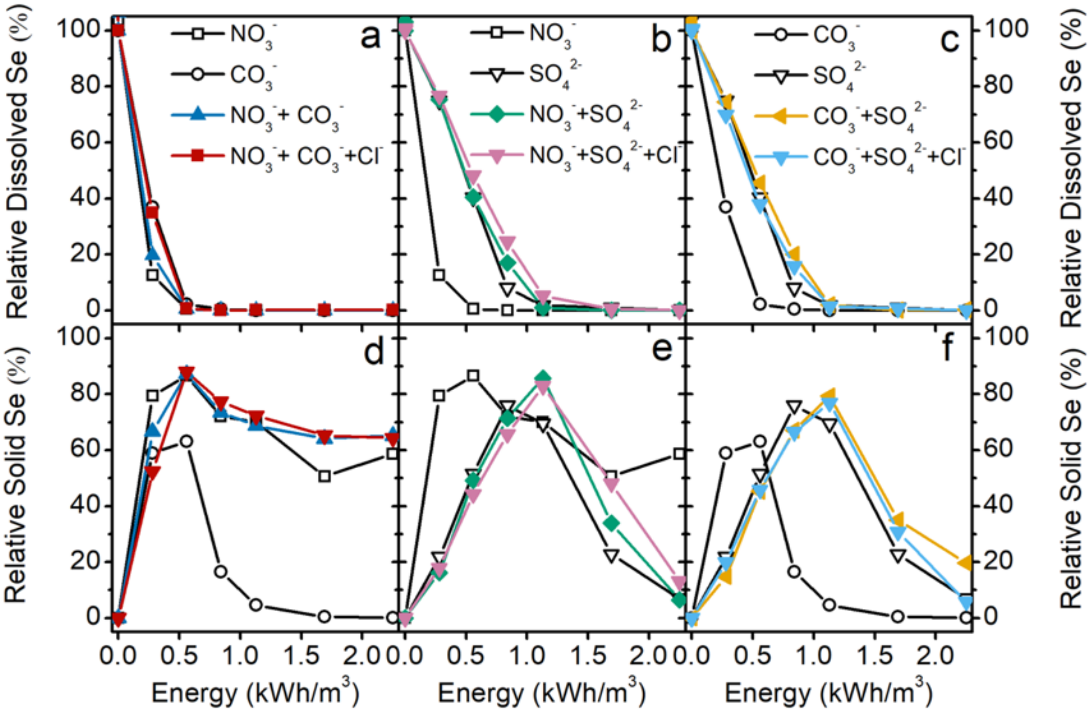

Figure 4-5. Effect of co-existing anions on the photocatalytic reduction of selenate in water: Dual- and Triple-anion competition. (a-c) dissolved Se and (d-f) immobilized solid Se during UV exposure of varying dual- and triple- anion competing for catalyst reactive sites.

Upon addition of NO_3^- and CO_3^-, the reduction of selenate to Se^0 remains unchanged (Figure 4-5a), similar to that observed in the mono-anion NO_3^- and CO_3^- experiments. While the reduction of Se^0 to H_2Se is inhibited in a similar manner as in the mono-nitrate competition experiment (Figure 4-5d). Upon the addition of SO_4^{2-} and CO_3^-, the reduction of selenate to Se^0 follows a similar inhibition as the mono-sulfate experiment (Figure 4-5c). While the reduction of Se^0 to H_2Se follows the mono-sulfate experiment, with a small lag in the second reduction of Se^0 reflected by a shifted peak of Se^0 by 0.3 kWh/m^3 (Figure 4-5f), similar to the mono-carbonate experiment. Again, these results are to be expected due to the minimal impact of carbonate and its likely removal from the water in the form of CO_2.

Upon addition of NO_3^- and SO_4^{2-}, the reduction of selenate to Se^0 follows a similar inhibition as the mono-sulfate experiment (Figure 4-5b). Thus, the presence of nitrate still appears not to impact the electron transfer mechanism driving the reduction of selenate. Interestingly, the reduction of Se^0 to H_2Se follows the mono-sulfate experiment, even in the presence of nitrate, which was previously shown to inhibit Se^0 reduction (Figure 4-5e). We postulate that the inhibition mechanism is lost when sulfate is present due to the displacement of nitrate from the surface of TiO_2 through competitive adsorption mechanisms. The impact of nitrate is not completely lost, as reflected by the relative Se^0 peak matching that of the mono-nitrate experiment, demonstrating a small inhibition of Se^0 reduction in this dual-anion experiment.

The addition of 1 mM Cl^- onto each of these three dual-anion experiments was completed to investigate the added impact of Cl^-. These experiments show that the presence of Cl^- has little effect on the reduction of selenate or Se^0. These results verify the limiting impacts Cl^- have on the photocatalytic system (Figure 4-5).

Figure 4-6 shows the effects of the four anions (CO_3^-, Cl^-, NO_3^- and SO_4^{2-}) altogether at 1 mM concentration in synthetic mine-impacted water (SMIW) and MIW on the photocatalytic reduction of selenate. The four-anion competition at 1mM experiment was done twice: once at a Se concentration of 0.063 mM similar to that used in the single and dual anion competition experiments and at a Se concentration of 0.0066 mM similar to the MIW and SMIW Se concentration. The concentrations in SMIW were set to match those of the four studied anions as well as selenate. The reduction of selenate to Se^0 in SMIW and MIW is very similar, with the exception of the first time point of UV exposure where the dissolved Se concentration in SMIW is slightly higher than expected. This could be due to analytical or experimental error because the dissolved Se curve match up very well through the rest of the UV exposure.

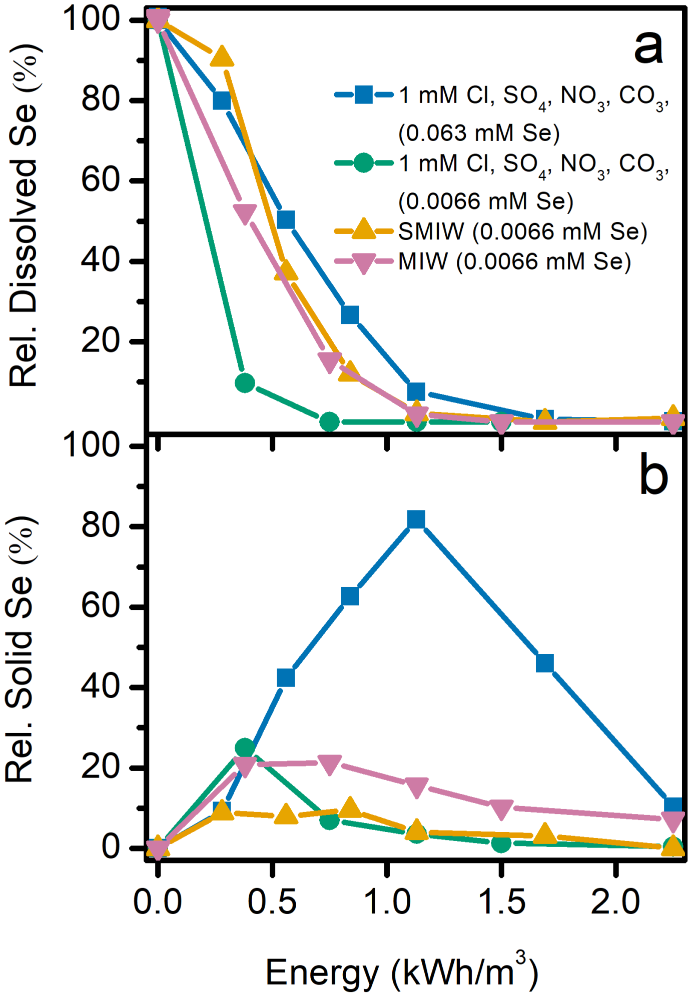

Figure 4-6. Quad-anion competition experiment (sulfate, nitrate, chloride and carbonate at 1 mM concentration), synthetic mining-impacted water (SMIW) and mine-impacted water (MIW) compared for the photocatalytic reduction of selenate with the relative dissolved Se (a) and the relative solid Se (b).

The amount of Se^0 generated during the quad-anion experiment at a Se concentration of 0.063mM is similar to that which was observed during the NO_3^- and SO_4^{2-} dual-anion experiment, with a maximum relative solid Se^0 of 80%. The peak Se^0 value generated in MIW and SMIW are much lower, at only 20% and 10% respectively. The peaks are also shifted significantly to earlier in the reaction, thus suggesting that the Se^0 to H_2Se reduction in both SMIW and MIW is much faster. A likely explanation for this is the change in the initial selenate concentrations. The initial selenate concentration in the quad-anion experiment was 6.3×10^{-2} mM to be comparable to the mono-, dual- and triple-anion experiment performed previously, whereas the initial concentration of selenate used in the SMIW and MIW experiments was 6.6×10^{-3} mM. A follow-up experiment was completed to confirm that the concentration of selenate, or the ratio of selenate to TiO_2 was in fact the main reason for a change in overall maximum $Se_{(s)}$ peak height. In the presence of 1 mM nitrate, sulfate, carbonate and chloride experiment and only 6.6×10^{-3} mM selenate, the peak $Se_{(s)}$ is 25%, similar to that observed for the MIW and SMIW experiments. The ratio of selenate to sulfate, nitrate and formate likely plays a major role in both the reduction of selenate to Se^0 and Se^0 to H_2Se. The flattening on the $Se_{(s)}$ peak can be seen in SMIW and MIW likely due to the interaction of a varying sulfate-to-nitrate ratio.

MIW contains naturally occurring trace levels of more than 20 identified metals, all of which can interact with the complex photocatalytic reduction mechanism and the photogenerated radical species. The exceptional agreement between the selenate and Se^0 reduction in SMIW and MIW shows that the interaction between selenate, nitrate, sulfate, formate and TiO_2 is strong enough to accurately predict the outcome of the treatment of MIW using TiO_2 and formic acid.

4.4.3 Mechanism of selenate removal by TiO_2

The mechanism of electron transfer that drives the reduction of selenate to Se^0 and further reduction of Se^0 to H_2Se will now be discussed, based on experimental evidence found herein. The photocatalytic mechanism for SeO_4^{2-} transformation is very complicated, consisting of consecutive and parallel reduction steps, and involving many radical intermediates and products. We will propose a rather simplified mechanism, given by the equations provided in Table 4-2, but recognize that many other parallel reactions occur in a complex water source.

Table 4-2. Comparison of standard reduction potentials and thermodynamic data provided for the primary reactions and the driving reactive species.

Reaction	Thermodynamic data (vs. SHE)	Refs.	Eq. #
Reactive Species			
$TiO_2 + hv \rightarrow e^-_{CB,TiO2} + h^+_{VB,TiO2}$	Utilizing λ=220-388nm $E_{CB,TiO_2} = 0.3V$ $E_{VB,TiO_2} = 3.5V$	(Nosaka and Nosaka, 2016b)	(4.3)
$HCOOH \leftrightarrow HCOO^- + H^+$	$pK_a = 3.75$	(Barcarella et al., 1955)	(4.4)
$H_2O + h^+_{VB,TiO2} \rightarrow HO^\bullet + H^+$	$E^0(HO^\bullet/H_2O) = 2.27V$	(Nosaka and Nosaka, 2016a)	(4.5)
$HCOO^- + h^+_{VB,TiO2}(HO^\bullet) \rightarrow H^+ + CO_2^{\bullet-}(+OH^-)$	$E^0(CO_2/CO_2^{\bullet-}) = -2.0V$	(Perissinotti et al., 2001)	(4.6)
$Se^0 + hv \rightarrow e^-_{CB,Se} + h^+_{VB,Se}$	$E_{CB,Se} = -1.8V$ $E_{VB,Se} = 0.2V$	(Benkhedir et al., 2004)	(4.7)
Se Reactions			
$SeO_4^{2-} + 8H^+ + 6e^-_{CB,TiO2} \rightarrow Se^0 + 4H_2O$	$E^0(SeO_4^{2-}/Se^0) = 0.5V$ $E_{CB,TiO_2} = 0.3V$	(Sanuki et al., 1999)	(4.8)
$Se^0 + 2H^+ + 2e^-_{CB,Se}(2CO_2^{\bullet-}) \rightarrow H_2Se(+2CO_2)$	$E^0(Se^0/H_2Se) = -0.6V$ $E^0(CO_2/CO_2^{\bullet-}) = -1.8V$ $E_{CB,Se} = -1.7V$	(Benkhedir et al., 2004; Perissinotti et al., 2001)	(4.9)
N Reactions			
$NO_3^- + e^-_{CB,TiO2}(CO_2^{\bullet-}) \rightarrow NO_3^{2-}(+CO_2)$[a]	$E^0(NO_3^-/NO_3^{\bullet 2-}) = -1.1V$ $E^0(CO_2/CO_2^{\bullet-}) = -1.8V$	(Doudrick et al., 2013; F. Zhang et al., 2005)	(4.10)
$NO_3^- + 10H^+ + 8e^-_{CB,TiO2}(8CO_2^{\bullet-}) \rightarrow NH_4^+ + 3H_2O(+8CO_2)$ $2NO_3^- + 12H^+ + 10e^-_{CB,TiO2}(10CO_2^{\bullet-}) \rightarrow N_2 + 6H_2O(+10CO_2)$ $2NO_3^- + 2H^+ + 2e^-_{CB,TiO2}(2CO_2^{\bullet-}) \rightarrow NO_2^- + H_2O(+2CO_2)$ $2NO_2^- + 8H^+ + 6e^-_{CB,TiO2}(6CO_2^{\bullet-}) \rightarrow N_2 + 4H_2O(+6CO_2)$	$E^0(NO_3^-/NH_4^+) = 0.88V$ $E^0(NO_3^-/N_2) = 1.25V$ $E^0(NO_3^-/NO_2^-) = 0.84V$ $E^0(NO_2^-/N_2) = 1.45V$ $E^0(CO_2/CO_2^{\bullet-}) = -1.8V$	(Hérissan et al., 2017; Doudrick et al., 2013; F. Zhang et al., 2005)	(4.11) (4.12) (4.13) (4.14)

[a] The initial single electron reduction of nitrate is the most negative reduction potential to overcome.

4.4.3.1 Role of competitive sulfate adsorption on TiO_2

As shown in Figure 4-3a, SO_4^{2-} was the only competing species to affect the reduction of selenate to Se^0 (Eq. 4.8). We propose that this is due to the competitive and specific adsorption of sulfate to the surface of TiO_2. Adsorption experiments were conducted to confirm this theory, see Figure 4-7. These experiments confirm that SO_4^{2-} is the only species to greatly affect the initial adsorption of selenate onto TiO_2 surfaces. The four experiments containing SO_4^{2-} at varying concentration (1mM, 10mM, SMIW and MIW) all show a marked decrease in the adsorption of selenate. On the other hand, NO_3^- and CO_3^- do not affect the adsorption of selenate to any appreciable extent at both 1 and 10 mM. Cl^- appears to slightly decrease adsorption at a 10 mM concentration possibly due to its effect in promoting aggregation of TiO_2 through charge screening effects, thus decreasing surface area for adsorption (Hotze et al., 2010).

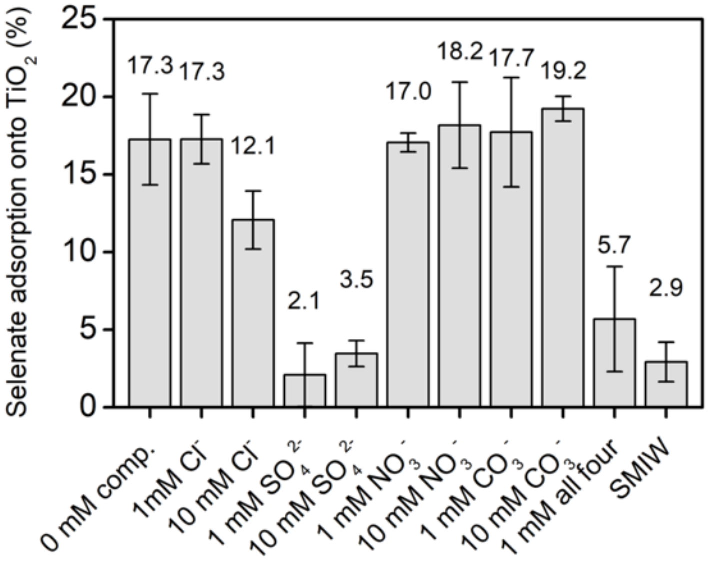

Figure 4-7. Adsorption of selenate onto TiO_2 under varying concentrations of competing anions species. All adsorption tests, with the exception of SMIW, were completed with and initial selenate concentration of 6.3 x 10^{-2} mM (as Se), under pH 3, [TiO_2] = 0.2 g/L conditions. SMIW adsorption test was under identical conditions but with 6.6 x 10^{-3} mM (as Se) selenate.

This experiment confirms that selenate reduction is greatly affected when it is displaced from the surface of TiO_2, suggesting that the driving reduction mechanism is a surface related phenomenon. The photogenerated electrons in the conduction band of TiO_2 have sufficient reduction potential (E^0 = 0.3V vs SHE) to reduce the SeO_4^{2-}/Se^0 redox pair (E^0 = 0.5V vs SHE) and are likely the main reactive species to drive the reduction of selenate to Se^0. Now direct electron transfer may be challenging since adsorption of selenate on TiO_2 is reported to involve an outer-sphere complex (Jordan et al., 2011; Zhang et al., 2009). However, a very small fraction of selenate molecules may selectively adsorb onto TiO_2 surfaces at low pH (Horányi, 2003). Although direct outer-sphere electron transfer has been well documented (Ramaswamy and Mukerjee, 2011), the likelihood of electron transfer interference by other species in the complex matrix is strong. If selenate adsorbs exclusively through outer-sphere complexes, an intermediate electron shuttling molecule may be required to bring the photoactive electrons to the hydrated selenate molecule.

4.4.3.2 Role of nitrate interaction interference with electron transfer

As shown in Figure 4-3b, NO_3^- can play a significant role in the inhibition of the reduction of Se^0 to H_2Se. NO_3^- photocatalytic reduction on TiO_2 with formic acid has been studied extensively and the reduction is believed to proceed through reaction with $CO_2^{\bullet -}$ radicals following a series of complex reactions summarized in Eq. 4.10-4.14. It has been shown that direct e_{CB}^- reduction of NO_3^- is not possible in the absence of formic acid due to the very negative redox potential of the $NO_3^-/NO_3^{\bullet 2-}$ (E^0= -1.1V vs SHE) (Hérissan et al., 2017). However, NO_3^- reduction is possible in the presence of formic acid as the carboxyl radical ($CO_2^{\bullet -}$), a very strong reducing species (E^0= -2.0V vs SHE), is generated (Eq. 4.6 (Hérissan et al., 2017; Perissinotti et al., 2001)). As $CO_2^{\bullet -}$ is responsible for the reduction of nitrate, the presence of nitrate would scavenge these $CO_2^{\bullet -}$ radicals from solution. Thus, it is postulated that the inhibition of reduction of Se^0 to H_2Se is due to the scavenging of $CO_2^{\bullet -}$ radicals in solution that would normally reduce Se^0 to H_2Se.

In order to assess this proposed mechanism for the further reduction of Se^0 to H_2Se, a series of experiments was conducted to determine the effect of competing anions on the first order reaction rate constants for both the photocatalytic removal of selenate and nitrate (Table 4-3). During the photocatalytic reduction of only nitrate or selenate on TiO_2 with 0.0065 M formic acid, the 1st order reaction rate constants are 1.18×10^{-5} s^{-1} and 2.60×10^{-3} s^{-1}, respectively. Selenate reduction rate is two-orders of magnitude faster than that of nitrate, although the relative concentrations reflect a similar two-orders of magnitude difference. When both nitrate and selenate are present, the rate constants remain relatively unchanged (the slight increase may be attributed to experimental and analytical error), showing little impact of each anion on the reduction of selenate to Se^0, which was also shown earlier in Figure 4-3a. Upon addition of Cl^-, a similar marginal impact is found for both 1st order reaction rate constants. Upon the addition of SO_4^{2-}, the 1st order reaction rate constants for selenate and nitrate reduction decrease by factors of 8 and 90, respectively.

Table 4-3. Effect of competing anions on the first-order reaction rate constant for the photo-reduction of selenate and nitrate in synthetic mine-impacted water.

	SeO_4^{2-} conc. (mM)	NO_3^- conc. (mM)	Cl^- conc. (mM)	SO_4^{2-} conc. (mM)	$k_{1,\ Se}$ (s^{-1})	$k_{1,\ Nitrate}$ (s^{-1})
Exp. 1	-	3.4	-	-	-	1.18×10^{-5}
Exp. 2	1.3×10^{-2}	-	-	-	2.60×10^{-3}	-
Exp. 3	1.3×10^{-2}	3.4	-	-	3.35×10^{-3}	1.76×10^{-5}
Exp. 4	1.3×10^{-2}	3.4	49.9	-	2.78×10^{-3}	1.60×10^{-5}
Exp. 5	1.3×10^{-2}	3.4	49.9	17.9	0.37×10^{-3}	0.02×10^{-5}

The decease of the 1st order rate constant for the reduction of selenate to Se^0 upon the addition of SO_4^{2-} is due to the competitive adsorption onto TiO_2 surface. The 8-fold reduction in rate can be attributed to this phenomenon. Thus, the further 90-fold decrease in the rate of reduction of nitrate must be due to more than just the competitive adsorption of SO_4^{2-} onto the surface of TiO_2. It is postulated that due to the low affinity of nitrate for TiO_2 surfaces (lower than selenate, sulfate and formate) the presence of sulfate may reduce the adsorption of nitrate far more than it does reduce the adsorption of selenate.

4.4.3.3 Proposed reaction mechanism

It is known that H_2O and formic acid adsorb molecularly and dissociatively (through the formate anion) on the surface Ti atoms in aqueous solution, respectively (Gong et al., 2006; Vittadini et al., 2000). During adsorption, H_2O and formic acid act as Lewis bases, while the Ti atoms act as Lewis acids, accepting electrons during the adsorption process. Because the Lewis basicity of the dissociative formic acid is much higher than molecular H_2O, the adsorption of formic acid is much stronger than H_2O. Lewis base strength correlates well with other measures of basicity such as pKa. Using this approach, the stronger the Lewis base, the higher affinity it has for Ti atoms on the surface of TiO_2. The order of increasing pKa is as follows: Cl^- (-5.6 (Robinson, 1936)) < NO_3^- (-1.38 (Dean, 1985)) < H_2O (0.0) < SeO_4^{2-} (1.8 (Séby et al., 2001)) < SO_4^{2-} (1.99 (Marshall and Jones, 1966)) < $HCOO^-$ (3.75 (Barcarella et al., 1955)).

In the presence of much weaker Lewis bases such as Cl^- and NO_3^- the adsorption of selenate and formate remains unchanged, explaining why increasing their concentration has no effect on the reduction of selenate to Se^0. This idea is also able to explain why sulfate was the only competitive anion tested that significantly decreased the adsorption of selenate onto TiO_2. Sulfate is the only anion with a stronger Lewis basicity than selenate, and thus propensity for Ti surface sites (or oxygen vacancies) on the TiO_2 surface. Although CO_3^- has a much higher pKa, it exists nearly entirely as H_2CO_3 at the pH 3, which is known to dissociate into H_2O and CO_2 and be removed from solution as gas. This suggests why CO_3^- concentration did not affect the adsorption of selenate or formate onto TiO_2.

On the other hand, in the presence of sulfate, which can adsorb selectively to the active catalytic sites on the surface of TiO_2 (Horányi, 2003; Sheng et al., 2013), selenate and nitrate adsorption is greatly reduced. When sulfate is added in similar concentrations found in MIW, the photocatalytic reduction 1st order reaction rate constant of selenate was decreased by 8x, whereas nitrate was impacted far greater, exhibiting a decrease by 90x (Table 4-3). Nitrate and selenate do not directly compete for adsorption sites, as seen by the minimal effect nitrate concentration had on the initial reduction of selenate to Se^0 (Figure 4-3a) and the unaffected selenate adsorption to TiO_2 (Figure 4-6). However, the presence of nitrate clearly has an impact on the further reduction of Se^0 to H_2Se (Figure 4-3b). Thus, the driving reactive species that reduces selenate to Se^0 is likely independent of that which reduces nitrate (likely $e^-_{CB,TiO2}$) and the reactive species responsible for reducing nitrate ($CO_2^{\bullet-}$) may also be partly responsible for further reducing Se^0.

During the experiment when only nitrate and selenate were subjected to photocatalytic reduction on TiO_2 with formic acid, the presence of nitrate inhibited the reduction of Se^0 to H_2Se (Figure 4-3b). One explanation for this result is that available $CO_2^{\bullet-}$ radicals normally responsible for the reduction of Se^0 to H_2Se are scavenged by NO_3^-. It is possible that the photogenerated electrons in the Se conduction band ($e^-_{CB,Se}$) are being scavenged by NO_3^- as well, although direct electron transfer has been shown to not occur (Hérissan et al., 2017). It is possible that the reduction of Se^0 to H_2Se involves both $CO_2^{\bullet-}$ and $e^-_{CB,Se}$, and the slow reduction of Se^0 that occurs in the presence of NO_3^- could be a result of Se^0 reduction by $e^-_{CB,Se}$ (Figure 4-3a). Tan et al. claimed that the photocatalytic reduction of Se^0 to H_2Se (E^0= -0.6V vs SHE) is entirely driven by $e^-_{CB,Se}$ (E^0= -1.8V vs SHE), but also mentioned that reduction by $CO_2^{\bullet-}$ is possible but not investigated in their work (T.T.Y. Tan et al., 2003c). Given the results of our competing anion studies and what is known about nitrate photocatalytic reduction pathways, the reduction of Se^0 to H_2Se appears to proceed according to both $CO_2^{\bullet-}$ and $e^-_{CB,Se}$.

During the experiment when nitrate, sulfate and selenate were subjected to similar photocatalytic reduction conditions, Se^0 reduction to H_2Se proceeded similarly to that when only selenate and sulfate are present, as if nitrate is not present. This suggests that sulfate is able to displace nitrate from the double layer of the TiO_2 surface, making it harder for the nitrate molecules to scavenge the $CO_2^{\bullet-}$ radicals. This explanation is reinforced by the fact that nitrate reduction significantly decreases in the presence of sulfate.

A proposed mechanism of electron transfer for the reduction of selenate to Se^0 and Se^0 to H_2Se is presented in Figure 4-8. Following this discussion, a selenate removal mechanism can be described as follows: (1) selenate is directly reduced to Se^0 through the photogenerated electrons in the TiO_2 conduction band and (2) Se^0 is further reduced to H_2Se through a combination of photogenerated electrons in the Se conduction band and $CO_2^{\bullet-}$ radicals.

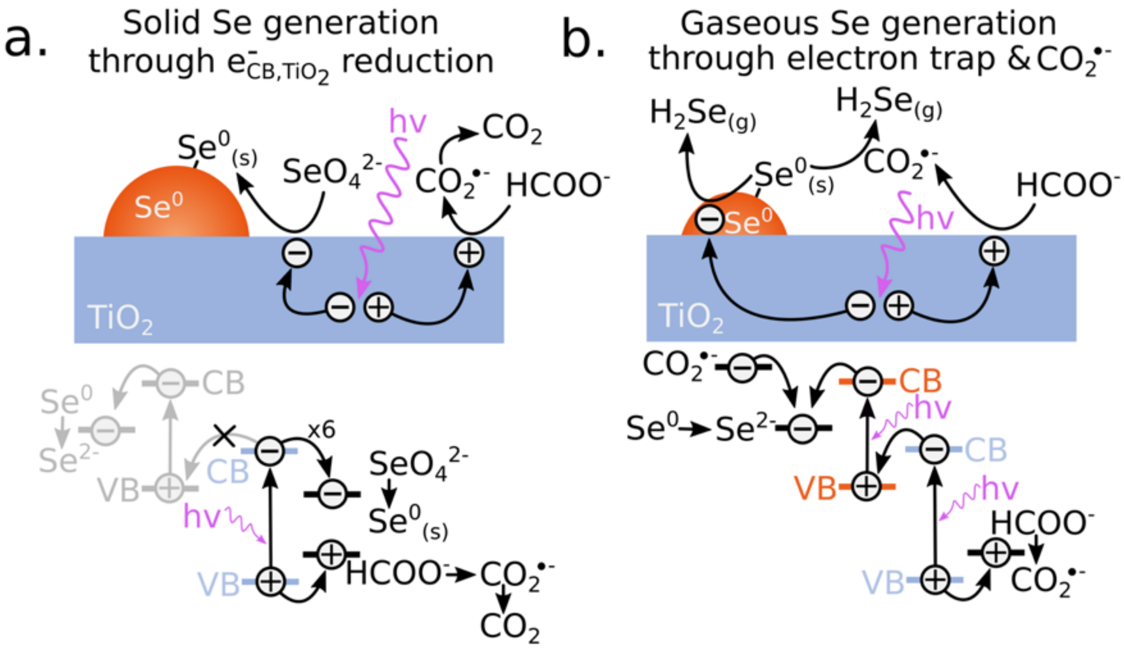

Figure 4-8. Schematic representation of the mechanisms (top) and the electronic transitions (bottom) proposed to explain the reduction of selenate and solid Se^0 in the photocatalytic reduction on TiO_2. (a) selenate reduction to solid Se^0 through conduction band electrons in TiO_2 and (b) reduction of Se^0 to H_2Se gas through either $CO_2^{\bullet-}$ reduction or an electron trap in Se^0 which is responsible for self-reduction from Se^0 to H_2Se gas.

4.5 Conclusions

The results presented herein are fundamental to progressing photocatalytic selenium reduction techniques for mine-impacted water and similar complex industrially-impacted water sources. The interaction between the photocatalyst with non-target constituents in the water is integral to the success of a photocatalytic system, especially for Se removal. The use of TiO_2 with an electron hole scavenger leads to selective removal of selenate in the presence of nitrate, sulfate, other competing anions and trace metals in the impacted water. According to the electron transfer mechanism proposed herein, $e^-_{CB,TiO2}$ is responsible for the first reduction of selenate to Se^0 and both $CO_2^{\bullet -}$ and $e^-_{CB,Se}$ are responsible for further reduction of Se^0 to H_2Se. Photocatalytic reduction on TiO_2 still has some limitations such as the affinity for SO_4^{2-} which leads to a slower selenate reduction rate. The relative proportions of nitrate, sulfate, selenate and formate present appear to play a large role in the final fate of Se and need to be investigated further to be able to accurately predict and tune a treatment towards a particular Se reduction product. The variable concentrations characteristic of seasonal mine-impacted water flow poses a challenge to predictability of Se photocatalytic treatment. However, this work sheds light on the mechanisms of electron transfer and highlights the main drivers of this reduction reaction (mainly sulfate and nitrate). Such information can be used to develop predictive quantitative models and design specialized catalysts to achieve favorable Se reduction products under variable conditions.

5 Tunable production of elemental Se vs H_2Se through photocatalytic reduction of selenate in synthetic mine impacted brine: Engineering a recoverable Se product

This chapter is modified from:

Holmes, A.B., Giesinger, K., and Gu, F. (in preparation). Tunable production of elemental Se vs H_2Se through photocatalytic reduction of selenate in synthetic mine impacted brine: Engineering a recoverable Se product.

5.1 Summary

In this paper, we investigate the tunability of Se reduction products ($Se^0_{(s)}$ vs. $H_2Se_{(g)}$) during the photocatalytic reduction of selenate on TiO_2, using formic acid as an electron hole scavenger, in synthetic mine-impacted brines (SMIB). Photocatalytic reduction can effectively remove Se from SMIB to < 2 μg/L from an initial Se concentration of > 3,300 μg/L in under 10×10^{19} photons cm^{-2}. An increase in solution temperature leads to a marked increase in selenate removal kinetics and an increase in selectivity towards $H_2Se_{(g)}$, while increasing the concentration of formic acid leads to an increase in selenate removal kinetics and a decrease in the selectivity towards $H_2Se_{(g)}$. A bivariate response surface analysis was used to elucidate the mechanism behind the production of >99% gaseous H_2Se or >85% solid Se^0, under varying reaction conditions. Finally, a two-pronged electron transfer model is proposed to explain the selectivity towards $Se^0_{(s)}$ vs. $H_2Se_{(g)}$ under varying conditions: (i) $Se^0_{(s)}$ is produced through direct reduction of selenate by TiO_2 conduction band electrons and (ii) H_2Se gas is produced through electrons transferred into Se^0 followed by a reduction of Se^0 to H_2Se or through direct reduction by $CO_2^{\bullet -}$.

5.2 Introduction

Mine-impacted water (MIW) rich in selenium (Se) is generated when natural sources of water drainage such as snowmelt and rainfall infiltrate into waste rock piles and tailings on an operating or abandoned mine and dissolve various inorganic species depending on the geology of the underlying deposit or the overlying strata. MIW can contain varying concentrations of dissolved constituents such as sulfate, carbonate, nitrate, selenate and many dissolved metals (Nordstrom et al., 2015). The removal of selenate from MIW has become of prime interest due to possible aquatic toxicity concerns. Elevated Se levels in aquatic ecosystems pose a great threat to aquatic life and thus affects organisms on higher trophic levels, such as humans, due to Se bioaccumulation (Hamilton, 2004).

Known Se removal techniques include chemical precipitation, biological removal, adsorption, ion exchange and membrane filtration (Holmes and Gu, 2016). Many of these technologies have been developed for pilot or full-scale treatment of Se contamination. However, these technologies face challenges to meet the new water quality criteria proposed by the United States Environmental Protection Agency (U.S. EPA) with an aquatic toxicity limit of 1.5 μg/L in lentic ecosystems (U.S. EPA Office of Water, 2016) due to the large volumetric flowrates common with MIW (Santos et al., 2015). Biological removal and chemical precipitation remove selenate through reduction to insoluble Se. However, each of these techniques have their own drawbacks including sensitivity to fluctuating MIW composition, operating parameters and biomass health, rendering such processes difficult to operate (Jain et al., 2015; Staicu et al., 2015b). Ion exchange and membrane filtration systems physically remove selenate by concentrating it into a reject stream, known as a brine. These technologies can generate highly concentrated brines, 4-8 times that of the original TDS, thus generating a brine stream with increased concentration of all dissolved components, including selenate. The advantages to Se removal from mine-impacted brine (MIB) include lower volume of treatment, higher Se concentration increasing kinetics of treatment and easier Se recovery from the impacted stream.

Recovery of Se from impacted water is of great interest and a primary focus of research from several researchers focusing on biological reduction of Se (Cordoba and Staicu, 2018; Hageman et al., 2017; Staicu et al., 2015a; Zhang et al., 2018). However, the separation of solid Se^0 from biological matter remains a challenging task. When Se^0 is produced intracellularly, lysis of the bacterial cell and recovery from biomass must occur to harvest Se^0. When produced extracellularly, Se^0 has to be separated from bacteria through size exclusion techniques integrated with complex filtering mechanisms (Zhang et al., 2018). Photocatalysis presents a unique opportunity to generate H_2Se gas or Se^0 solid from selenium-containing industrially-impacted water.

Previous studies investigating photocatalytic reduction of selenate on TiO_2 were primarily focused on a simple solution of sodium selenate in DI (Kikuchi and Sakamoto, 2000; Labaran and Vohra, 2014; Nguyen et al., 2005b; T.T.Y. Tan et al., 2003b, 2003a). These investigations reported that selenate reduction to Se^0 preceded the reduction of Se^0 to H_2Se, with H_2Se generation expected after SeO_4^{2-} is removed from solution. However, MIB also contains high concentrations of other anions and cations, such as Cl^-, NO_3^-, CO_3^-, SO_4^- and Ca^{2+}, which can influence photoreduction of selenate (Al-Abed et al., 2008). Nakajima et al. investigated the photocatalytic reduction of selenate in simulated flue gas desulphurization wastewater, and observed a significant inhibition in the reduction rate in presence of sulfate (Nakajima et al., 2013, 2011). This inhibition is attributed to the competition from sulfate for adsorption sites on TiO_2. This multi-site competition of anions in real complex wastewaters for adsorption on TiO_2, particularly in brines, provides alternate pathways for electrons during the reduction of selenate.

Herein, we present a method of generating either H_2Se gas or solid Se^0, through the photocatalytic reduction of selenate in synthetic mine-impacted brine. Both alternatives allow for unique opportunities of Se recovery. This study focuses on optimizing reactor conditions towards increasing the photocatalytic reduction kinetics and understanding the photogenerated electron transfer mechanisms responsible for generating either $H_2Se_{(g)}$ or $Se_{(s)}$ during the reduction of selenate. A bivariate response surface analysis uncovers the reaction conditions required for production of >99% gaseous H_2Se and >85% solid Se^0. We propose a two-pronged electron transfer model to explain the selectivity towards solid Se^0 or gaseous H_2Se under varying conditions: (i) solid Se^0 is produced through reduction of selenate by TiO_2 conduction band electrons and (ii) H_2Se gas is produced either through electrons transferred into Se^0 followed by a reduction of Se^0 to H_2Se or through a direct reduction by $CO_2^{\bullet -}$.

5.3 Materials and Methods

5.3.1 Materials

MIW was received from an operating mine in North America and stored at 4 °C in the dark. Synthetic mine impacted brine (SMIB) was produced by dissolving reagent grade salts in MIW to raise concentrations to industrial MIW brine levels to run controlled experiments. Titanium dioxide nanoparticles (Aeroxide P25, ~10-50 nm particle diameter, 55 $m^2\ g^{-1}$ surface area, Acros) were used as received. P25 TiO_2 nanoparticles have been extensively studied and characterized in the literature and are often used as a benchmark photocatalyst. Formic acid (ACS reagent, 97%, Alfa Aesar) was used as an electron hole scavenger. Sodium selenate (<0.1% impurities, BioXtra, Sigma-Aldrich), calcium sulphate (anhydrous, ACS reagent >96%, Sigma-Aldrich), sodium chloride (reagent grade, Sigma-Aldrich), sodium nitrate (>99%, ReagentPlus, Sigma-Aldrich), hydrochloric acid (37%), calcium hydroxide (ACS grade, Sigma-Aldrich), barium hydroxide (ACS grade, Sigma-Aldrich), and sodium hydroxide (ACS grade, Sigma-Aldrich) were used to synthesize SMIB.

5.3.2 Preparation of SMIB

SMIB was produced to mimic brine produced through membrane processes such as reverse osmosis (RO), or ion exchange processes. The brine was made from mine-impacted water by adding in appropriate amounts of $NaNO_3$, Na_2SO_4, NaCl and $CaSO_4$ to raise the concentrations of the primary anions and cations to match a realistic produced brine complex matrix. SMIB A was prepared by the addition of the salts listed above. Next, SMIB A underwent a $Ca(OH)_2$ addition step at pH 11 to remove carbonates, the main buffering component in the brine, through the precipitation of $CaCO_3$. This precipitation was completed by slow mixing (100-150 rpm) for 2 hours followed by filtering through a 0.2 μm polyethersulfone (PES) membrane. This precipitation step was implemented in order to mimic a high-density sludge (HDS) system which is used in mine-impacted water treatment to remove dissolved metals membrane generated brine. The carbonate in SMIB adds substantial pH buffer capacity, making it difficult to adjust the pH for photocatalytic tests. The $Ca(OH)_2$ addition reduced the alkalinity (as $CaCO_3$) from 200 mg/L to 34 mg/L. This carbonate-reduced brine is referred to as SMIB B. Next, $Ba(OH)_2$ was added to SMIB B to partially remove sulfate as $BaSO_4$. This precipitation was completed under slow mixing (100-150 rpm) for 2 h to allow for precipitation of salts followed by filtering through a 0.2 μm polyethersulfone (PES) membrane. This precipitation step was implemented primarily to understand the effect of sulfates on the photocatalytic reduction of selenate in SMIB. The $BaSO_4$ salt precipitation reduced the sulfate concentration from 1,700 mg/L to 690 mg/L. This sulfate-reduced brine is referred to as SMIB C. The full matrix composition of each SMIB can be found in Table C-1.

5.3.3 Removal of selenate through photocatalytic reduction

The photocatalytic reactor apparatus consists of an air tight stainless-steel reactor vessel of 1.0 L capacity with a quartz-window through which UV was irradiated. SMIB was added to an internal PTFE liner followed by formic acid and TiO_2. The air tight stainless-steel vessel with a quartz window was purged with bubbling N_2 gas throughout the reaction to remove any H_2Se gas which was then passed through two subsequent liquid scrubbers of $CuSO_4$ and NaOH, respectively (Sanuki et al., 1999; T.T.Y. Tan et al., 2003b). The mixture was stirred in the dark for 1 h to attain adsorption-desorption equilibrium of inorganics with the TiO_2 surface as well as to remove any dissolved oxygen and then placed in the photoreactor and exposed to UV light while being stirred. Samples of SMIB were taken throughout the treatment to determine both total and dissolved Se, through unfiltered and filtered samples, respectively. The reactor vessel was exposed to UV light using a UVA fluorescent bulb that had a wavelength filter which only supplied UVA ($\lambda = 365$ nm) light (Blak Ray B-100A 95-0044-22). The photon irradiance E_p was determined to be 9.891×10^{15} photons cm^{-2} s^{-1}. Photon irradiance was determined through potassium ferrioxalate actinometry (Bowman and Demas, 1976; Hatchard and Parker, 1956). Control of fluence was used instead of operating time to make our results comparable with other studies.

5.3.4 Analysis

Se concentration was determined in accordance with the U.S. EPA suggested Se determination technique (APHA 2009, Method 3114B/C) using hydride generation inductively coupled plasma optical emission spectroscopy (HG-ICP-OES, Teledyne Prodigy ICP and Cetac HGX-200 advanced membrane hydride generation system, LOD = 1 µg L^{-1}). Both dissolved and total Se were determined by HG-ICP-OES following acid digestion using the protocol U.S. EPA Method 3050B (U.S. EPA, 1996). The insoluble Se fraction (considered to be elemental Se) present in the water was calculated from the difference of total and dissolved Se concentrations. Gaseous H_2Se was calculated from the difference between the initial total Se in the water and total Se in the TiO_2 suspension after UV exposure. Based on several past studies on photocatalytic reduction of selenate on TiO_2 (Nguyen et al., 2005b; Sanuki et al., 1999; T.T.Y. Tan et al., 2003a), the gaseous Se species is assumed to be H_2Se, although the direct identification of gaseous Se species is a challenging task (Kot and Namiesńik, 2000; Uden, 2002). Se analytics is currently a major developing field of study, with researchers looking into new and improved approaches for gaseous and solid Se speciation analytical techniques (Santos et al., 2015).

Total organic carbon (TOC, APHA 5310B, combustion temperature 800 °C), chemical oxygen demand (COD, APHA 5220D), biochemical oxygen demand (BOD, APHA 5210B), anion concentration by ion chromatography (bromide, chloride, fluoride, nitrate, nitrite and sulfate, EPA 300.1), total ammonia (Watson et al., 2005), speciated alkalinity (as $CaCO_3$, EPA 310.2), and total and dissolved metals by inductively coupled plasma mass spectrometry (ICPMS, EPA 200.2/6020A and APHA 3030B/6020A) were measured according to standard methods by ALS Environmental (Calgary, AB, Canada), a laboratory accredited by the Canadian Association for Laboratory Accreditation (CALA) according to international standards (ISO 17025). Total and dissolved Se concentration done at the University of Waterloo were confirmed by ALS Environmental on a number of analytical checks.

5.4 Results and Discussion

5.4.1 Photocatalytic reduction of selenate in synthetic mine impacted brine

Figure 5-1 shows the Se removal in SMIB A, B and C via photocatalytic reduction of selenate over TiO_2. In order to compare the SMIBs, the pH was maintained at pH 4.5 throughout the entire reaction with NaOH and HCl, temperature was maintained at 37°C, TiO_2 was added in 0.2 g/L concentration and formic acid was added at 300 mg/L. The apparent first-order reaction rate constant for the reduction of selenate in SMIB A and B are very similar: 1.30 ± 0.04 and 1.21 ± 0.05 cm^2 / 10^{20} photons, respectively. The presence of carbonates does not seem to affect the photocatalytic reduction of selenate. Although it is worth noting that the 300 mg/L formic acid addition in SMIB A causes a reduction of pH from 8.16 to 3.74 and in SMIB B causes a reduction of pH 7.81 to 3.18. The lower pH is reached due to the reduced buffering capacity of the brine. In this experiment, the pH is controlled and maintained at pH 4.5 to highlight the presence of carbonate and sulfate as the sole factors affecting the photocatalytic reduction of selenate, although pH effects are discussed later on. In addition, the addition of $Ba(OH)_2$ enables some selenate removal through adsorption onto the barium sulfate precipitate, which was responsible for 19% removal of Se prior to the photocatalytic reduction of selenate. The apparent first-order reaction rate constant for the reduction of selenate in SMIB C is also higher (2.14 ± 0.07 cm^2 / 10^{20} photons) than that in SMIB A and B. The presence of sulfate is known to hinder the adsorption of selenate on the surface of TiO_2 by limiting its coverage of reaction sites (T. Yang et al., 2013).

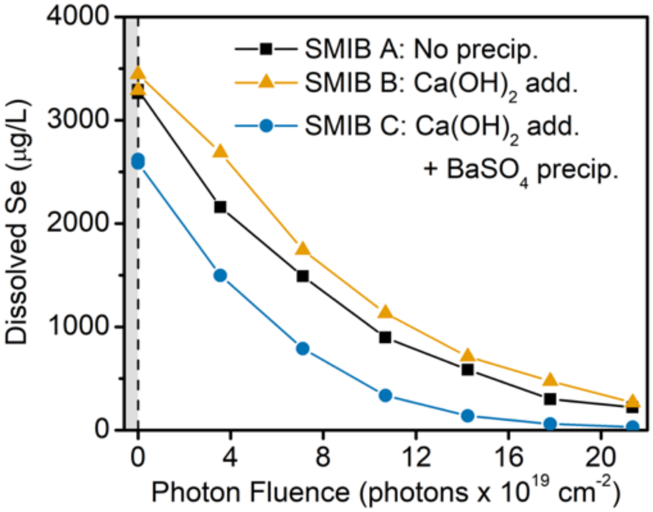

Figure 5-1. Effect of brine pretreatment/ preparation on photocatalytic reduction of selenate in synthetic mine impacted brine (SMIB). Reaction conditions: 0.2 g L^{-1} TiO_2, pH 4.5, 300 mg L^{-1} formic acid and 37°C.

The removal of selenate through photocatalytic reduction can follow either the reduction of SeO_4^{2-} to Se^0 or further reduction of Se^0 to H_2Se. These reductions are presented in equations 5.1 and 5.2. Selectivity ($S(x)_t$) of the specific Se reduction product, either $Se^0_{(s)}$ or $H_2Se_{(g)}$, can be calculated using equations 5.3 and 5.4, respectively.

$$SeO_4{}^{2-}{}_{(aq)} + 8H^+ + 6e^-_{cb} \overset{k_1}{\rightarrow} Se^0{}_{(s)} + 4H_2O \tag{5.1}$$

$$Se^0{}_{(s)} + 2H^+ + 2e^-_{cb} \overset{k_2}{\rightarrow} H_2Se_{(g)} \tag{5.2}$$

$$S\left(Se^0_{(s)}\right)_t = \frac{\left[Se^0_{(s)}\right]_t}{\left[SeO_4^{-2}\right]_0 - \left[SeO_4^{-2}\right]_t} \tag{5.3}$$

$$S\left(H_2Se_{(g)}\right)_t = \frac{\left[H_2Se_{(g)}\right]_t}{\left[SeO_4^{-2}\right]_0 - \left[SeO_4^{-2}\right]_t} \tag{5.4}$$

The relative Se speciation during photocatalytic reduction of selenate in SMIB A, B and C are presented in Figure C-1, Figure C-2 and Figure C-3, respectively. The selectivity of $Se^0_{(s)}$ generation in the photocatalytic reduction of selenate in SMIB A is the highest among the three brine formulations, with an average $S\left(Se^0_{(s)}\right)_t$ of 0.468. During the reduction of selenate in SMIB B and C the $S\left(Se^0_{(s)}\right)_t$ is 0.311 and 0.328, respectively. Given these results, it is postulated that sulfate does not have much of an effect on the selectivity of $Se^0_{(s)}$ vs $H_2Se_{(g)}$ during the photoreduction, since SMIB B and C have very different sulfate concentrations yet yield the same ratio of Se reduction products. We then hypothesize that carbonate plays more of a major role in the selectivity towards $Se^0_{(s)}$. Previous researchers have demonstrated that HCO_3^- or CO_3^{2-} act as electron hole scavengers, consuming $OH^\bullet$ radicals in solution and h^+ on the surface of TiO_2 (Arakawa and Sayama, 2000; Ni et al., 2007). This could explain why the reaction rate for the reduction of selenate in SMIB A is slightly faster than in SMIB B, which had carbonate removed.

SMIB B best represents the brine produced in a membrane or ion exchange process followed by an HDS processing step, common in the treatment of mine-impacted water. As a result, SMIB B is the primary focus of this paper and hereafter is just referred to as SMIB. The photocatalytic reduction of selenate in SMIB on TiO_2 appears to primarily remove selenate in the presence of many other oxyanions and cations. The SMIB contains nitrate, sulfate and carbonate, all of which compete for the adsorption and reduction sites on TiO_2. The concentrations of sulfate and nitrate over the span of the UV exposure and Se removal are shown in Figure C-6 to remain nearly fully intact throughout the experiment. Since nitrate and sulfate removal are <3% and <1%, respectively, when 99% Se has been removed the reduction process appears to be preferential for selenate.

5.4.2 *Increasing kinetics of Se reduction in SMIB by increasing temperature*

Figure 5-2a-c show the effect of temperature on the photocatalytic reduction of selenate in SMIB. The removal of selenate is faster at higher temperature. The apparent first-order reaction constants for the reduction at 12°C, 47°C, and 62°C are 0.96 ± 0.08 $cm^2/10^{20}$ photons, 4.83 ± 0.46 $cm^2/10^{20}$ photons and 8.16 ± 0.41 $cm^2/10^{20}$ photons, respectively. Calculation of the activation energy of selenate removal from an Arrhenius plot (Figure C-5.) yields $E_{aa} = 34.29$ kJ mol^{-1}.

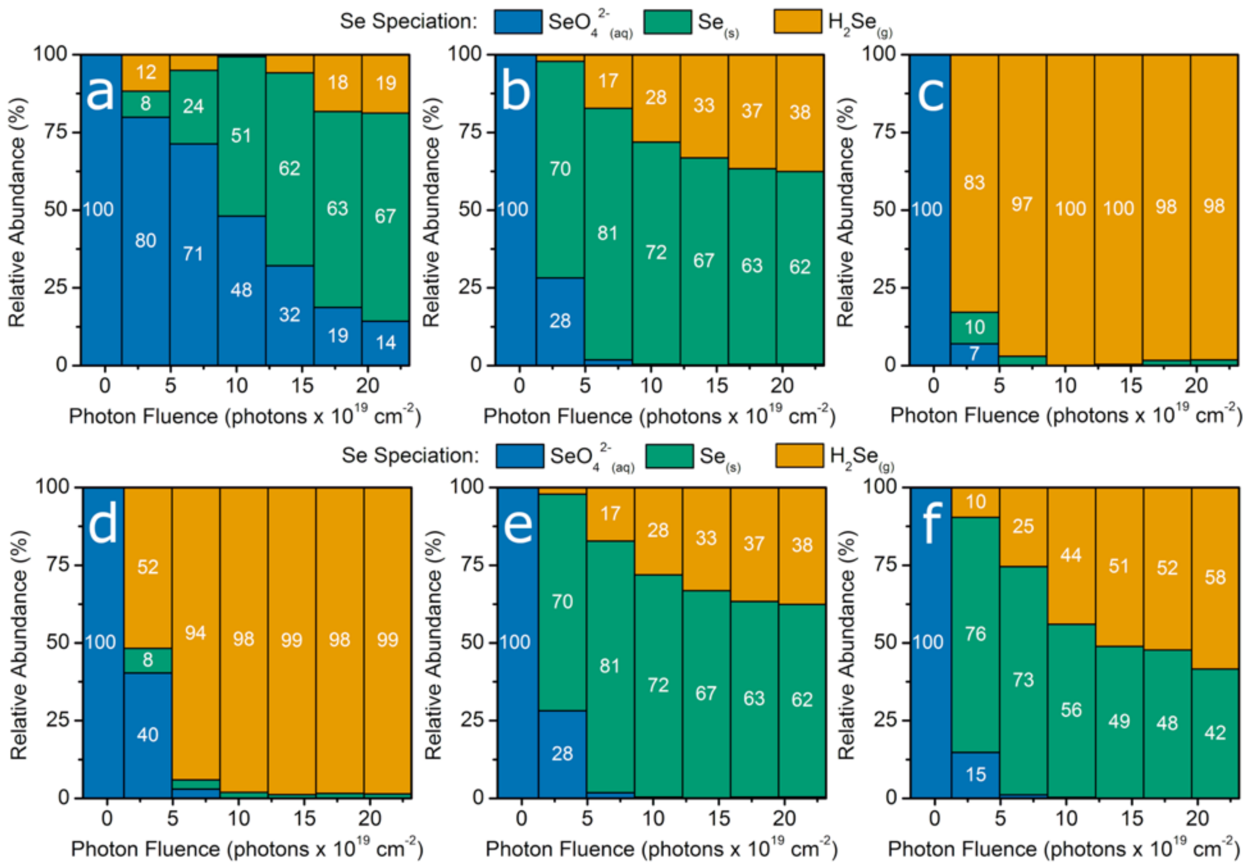

Figure 5-2. Relative Se speciation during photocatalytic reduction of selenate under varying temperature and formic acid concentration conditions (a) 12°C, (b) 47°C, (c) 62°C, (d) 300 mg/L formic acid, (e) 600 mg/L formic acid, and (f) 1,200 mg/L formic acid. Reaction conditions 47°C, 600 mg/L formic acid, 0.5 g/L TiO_2, pH 3 unless otherwise noted.

The temperature dependence of photocatalytic reduction of nitrate has been reported previously (Anderson, 2012, 2011). Anderson reported that the activation energies for the simultaneous photocatalytic removal of nitrate and oxalic acid over Au-TiO_2 are 34 and 42 kJ/mol, respectively, due to the generation and desorption of the CO_2 gaseous product. These activation energies are in line with the findings of this study. Higher E_{aa}'s are commonly observed for gas generating photocatalytic reactions due to the increased desorption of gases at higher temperatures (Hu et al., 2010). The desorption of produced gases has a major effect on photocatalytic activity, especially when the generated H_2Se is known to poison catalytic surfaces, similar to H_2S (Argyle and Bartholomew, 2015).

We postulate that mass transport associated with adsorption of reactants to active sites and the desorption of products from active sites on the catalyst is likely to cause larger E_{aa}. The active sites on TiO_2 tend to bend defects in the crystal lattice and areas where two different crystalline phases (rutile and anatase) are in contact. Adsorption involves less than a quarter of the active sites on the surface of TiO_2 and thus diffusion to and from these active sites is critical for high photocatalytic activity (Muggli and Backes, 2002). Thus, E_{aa} is an indication of the enthalpies associated with adsorption of reactants or desorption of products from the active sites of the photocatalyst.

Upon inspection of % Se speciation in Figure 5-2a-c, it is obvious that not only is the selenate removal rate increasing with increasing temperature, but the relative selectivity to H_2Se gas increases with increasing temperature as well. An overall discussion of the mechanism for this electron transfer process is discussed in a later section in this chapter.

5.4.3 *Effect of formic acid concentration of the selectivity of Se product*

Formic acid plays two critical roles during the reduction of selenate in SMIB. Primarily, it functions as an electron hole scavenger, allowing for greater separation of the photogenerated electron and electron hole pairs, thus extending the reducibility of the TiO_2 e^-_{CB}. Secondly, formic acid adjusts the pH, from approximately 8 to between 3-5. Low pH favors faster kinetics in the photoreduction of selenate on TiO_2 (Tan et al., 2002). Previous studies compared various small organic molecules for their function as an electron hole scavenger in the photocatalytic reduction of selenate over TiO_2 and the use of formic acid attained the highest reduction rates of Se (T.T.Y. Tan et al., 2003a).

Figure 5-2d-f shows the effect of formic acid concentration on the photocatalytic reduction of selenate in SMIB. The removal of selenate is slightly faster at higher concentration of formic acid. The apparent first-order reaction constants for the reduction at 300, 600, and 1,200 mg/L formic acid are 4.67 ± 0.63 $cm^2/10^{20}$ photons, 4.83 ± 0.46 $cm^2/10^{20}$ photons and 6.22 ± 0.59 $cm^2/10^{20}$ photons, respectively. However, a decrease in formic acid concentration greatly increases the selectivity to $H_2Se_{(g)}$, causing the ratio of $H_2Se : Se^0$ to rise. This is an indication that the reduction reaction of Se^0 to H_2Se is inhibited at higher formic acid concentrations.

5.4.4 *Effect of increasing TiO_2 concentration on the selectivity of Se product*

The effect of TiO_2 concentration is evident by comparing Figure 5-2c to Figure 5-3 where 0.5 g/L and 1.0 g/L TiO_2 were used, respectively. Under similar reaction conditions (62°C, 600 mg/L formic acid, pH 3) a drastic change results by introducing twice the TiO_2 into the reactor. The moves the reaction from generating primarily $H_2Se_{(g)}$ (>98% H_2Se) to generating primarily $Se^0_{(s)}$ (>85% Se^0) as a result of doubling the TiO_2 concentration. This result is surprising because increasing the TiO_2 concentration while holding the formic acid concentration constant essentially reduces the relative available formic acid per unit area of the TiO_2 catalyst. In the previous discussion, we saw that a decrease in formic acid concentration leads to an increase in the production of H_2Se rather than a decrease. One possible explanation could be that concentrations the nanoparticles aggregate extensively at higher TiO_2, reducing the overall surface area available for reduction and entrapping solid Se^0 in the interior of TiO_2 aggregates (Degabriel et al., 2018). Additionally, an increase in TiO_2 decreases the photon penetration into the solution and could affect the availability of photogenerated electrons in areas behind the UV absorption region (Schneider et al., 2014).

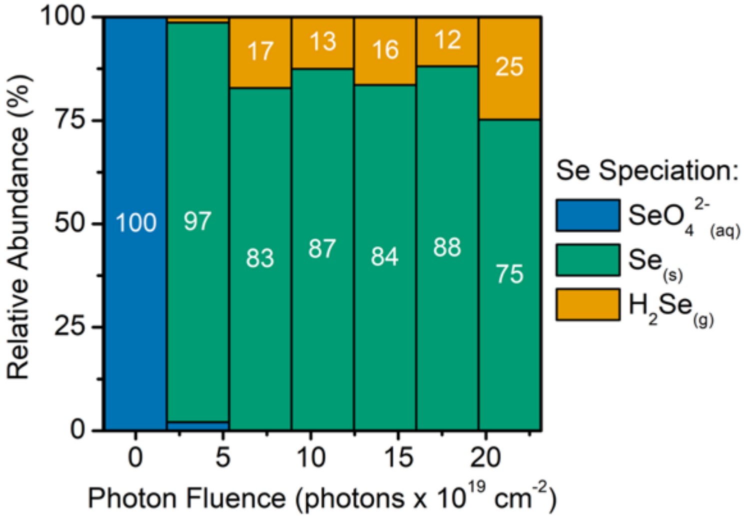

Figure 5-3. Relative Se speciation during photocatalytic reduction of selenate under 62°C, 600 mg/L formic acid, 1.0 g/L TiO_2, pH 3 reaction conditions.

5.4.5 *Combined effect of temperature and formic acid concentration on reduction*

In response to understanding the complex interaction between temperature and formic acid concentration and their impact on both the apparent first-order reaction rate constant and the selectivity of the Se reduction product, further investigation was desired. Response surface methodology was used to develop an empirical model for the combined effects of temperature and formic acid concentration on the apparent first-order rate constant of selenate reduction in SMIB, following a central composite design described in Table 5-1. The results of this analysis are summarized in Table C-2. This response surface analysis allows us to investigate the effect of the bivariate compounding factors of temperature and formic acid concentration on the photocatalytic reduction of selenate in SMIB.

Table 5-1. Range, levels and coding of the experimental variables in the response surface study for the apparent first-order reaction rate constant.

Designation	Factor	Range and level				
		$-\sqrt{2}$	-1	0	1	$\sqrt{2}$
x_1	Temperature (°C)	12	19	37	55	62
x_2	Formic acid concentration (mg L^{-1})	25	193	600	1007	1175

The least squares regression fit of the response surface is presented in Figure 5-4 and described by the relationship

$$\hat{y} = 4.6407 + 2.3589x_1 + 0.6077x_2 - 0.0773{x_1}^2 - 1.1607{x_2}^2 + 0.3104x_1x_2 \tag{5.5}$$

or described in natural variables as,

$$k_{app,1} = -2.807 + (1.113 \times 10^{-1})T + (8.264 \times 10^{-3})C_{CH_2O_2} - (7.917 \times 10^{-5})T^2 - (6.949 \times 10^{-6})C_{CH_2O_2}^2 + (4.236 \times 10^{-5})TC_{CH_2O_2} \tag{5.6}$$

where T is in °C and $C_{CH_2O_2}$ is in mg L^{-1}.

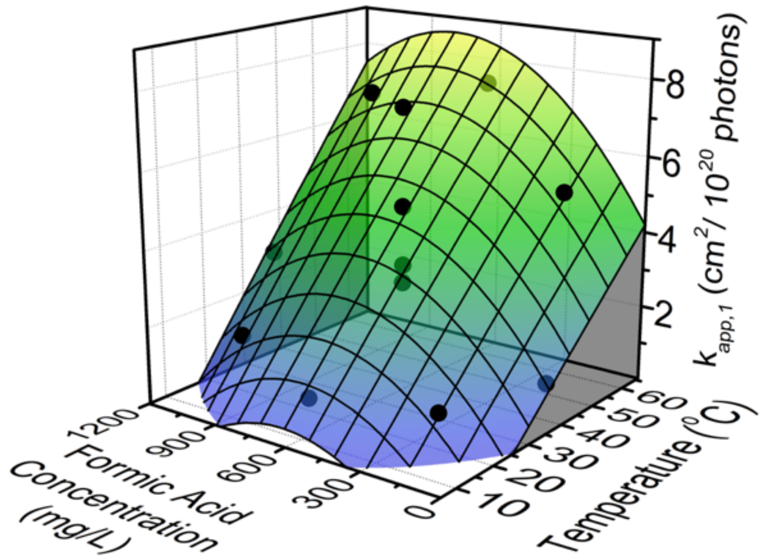

Figure 5-4. Response surface fit of the apparent first-order reaction rate constant for the photocatalytic reduction of selenate in SMIB as a function of temperature and formic acid concentration. Reaction conditions: pH 3 and 0.5 g L^{-1} TiO_2.

Regression diagnostics and analysis of variance (ANOVA) for the response surface are presented in Figure C-7 and Table C-3, respectively. Notably, ANOVA indicates that the overall regression of the response surface is statistically significant (p value 0.0362). However, the only statistically significant individual term is temperature when determining the apparent first-order rate constant (p value of 0.0028), whereas all other terms ($C_{CH_2O_2}$ and all second order terms) are not statistically significant (p value > 0.05). In other words, the primary variable of influence on the reaction rate for the reduction of selenate is the temperature of reaction. The concentration of formic acid plays a smaller role in determining the reaction rate, likely because all experiments were conducted with formic acid present in excess. The lowest concentration of formic acid used 25 mg/L, corresponds to a 13:1 formic acid : selenate ratio, and the theoretical molar ratio of formic acid to Se is 8:1 to supply 8 electrons for the reduction of selenate to hydrogen selenide gas. A slight reduction in the reaction rate at higher concentrations of formic acid occurs, presumably due to competition for adsorption/reduction sites on TiO_2, thus inhibiting the reduction of selenate.

Response surface methodology is also used to develop an empirical model for the combined effects of temperature and formic acid concentration on the selectivity of selenate reduction product, either to solid elemental Se or to gaseous hydrogen selenide gas, following the same central composite design described in Table 5-1. The results are summarized in Table C-4.

The least squares regression fit of the response surface is presented in Figure 5-5, and described by the relationship

$$\hat{y} = 0.5736 - 0.2389x_1 + 0.1831x_2 - 0.0667{x_1}^2 + 0.1428{x_2}^2 + 0.1774x_1x_2 \tag{5.7}$$

or described in natural variables as,

$$S\left(Se^0_{(s)}\right) = 1.356 - (1.232 \times 10^{-2})T - (1.480 \times 10^{-3})C_{CH_2O_2} - (2.090 \times 10^{-4})T^2 + (8.612 \times 10^{-7})C^2_{CH_2O_2} + (2.422 \times 10^{-5})TC_{CH_2O_2} \tag{5.8}$$

$$S\left(H_2Se_{(g)}\right) = 1 - S\left(Se^0_{(s)}\right) \tag{5.9}$$

where T is in °C and $C_{CH_2O_2}$ is in mg L^{-1}.

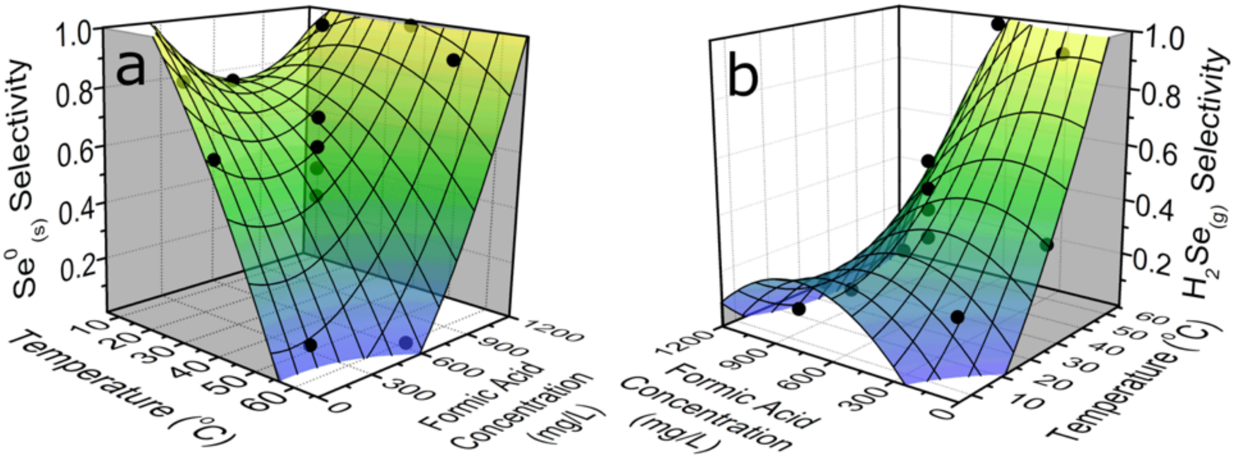

Figure 5-5. Response surfaces of selectivity of Se product generation (a) $Se^0_{(s)}$ selectivity and (b) $H_2Se_{(g)}$ selectivity during the photocatalytic reduction of selenate in synthetic mine impacted brine.

Regression diagnostics and analysis of variance (ANOVA) for the response surface are presented in Figure C-8 and Table C-5, respectively. Since the selectivity of $H_2Se_{(g)}$ is simply 1-S($Se^0_{(s)}$), the ANOVA was only conducted on the response surface for the selectivity towards $Se^0_{(s)}$. Notably, ANOVA indicated that every term in the quadratic model is statistically significant when determining the selectivity to solid elemental Se (p value < 0.05). In comparison to the response model for the reaction rate constant, $k_{app,1}$, the quadratic terms as well as the bivariate interaction term play a major role in the selectivity of Se product. In other words, the concentration of formic acid has a much greater impact on determining the final Se product generated from the photocatalytic reduction of selenate in SMIB than it does on determining the reaction rate. It is postulated that the surface interaction with adsorbed selenate and formate on TiO_2 is a major factor.

An increase in temperature decreases the adsorption onto TiO_2 due to the outer-sphere complexes between both selenate and formate with the TiO_2 surface (Savory and McQuillan, 2013; Zhang et al., 2009; Gong et al., 2006). At higher temperature, formate adsorbs less strongly to TiO_2 surfaces due primarily to outer-sphere complexes formed between formate and TiO_2 (101) at pH 3 (Savory and McQuillan, 2013) so that selenate is less able to adsorb. Under conditions of excess formic acid concentrations, the increased adsorption of formate at lower temperatures does not make a difference because the surface is already fully saturated (Figure 5-5a). Under conditions of high formic acid concentration, formate greatly outnumbers the molecules of selenate (700x molar concentration of selenate) for adsorption sites on TiO_2.

Formic acid adsorption occurs most readily at lower temperatures and higher formic acid concentration and the selectivity to $Se^0_{(s)}$ is highest under these conditions (>95%, see Figure 5-5a). Under the conditions of low formic acid concentration and high temperatures, less formic acid adsorbs and the selectivity to $Se^0_{(s)}$ is the lowest (<10%, see Figure 5-5a). The proposed mechanism behind the relationship between formate adsorption and Se product selectivity is discussed in the following section.

5.4.6 Mechanism of photocatalytic selenate reduction

The photocatalytic reduction of selenate can follow one of two pathways: reduction of aqueous SeO_4^{2-} to Se^0 and the further reduction of Se^0 to H_2Se. The two reduction reactions occur at different reduction potentials (SeO_4^{2-} / Se^0, $E^0 = 0.5$ V *vs.* SHE and Se^0 / H_2Se, $E^0 = -0.6$ V), with the further reduction of Se^0 to H_2Se above the reduction potential of the TiO_2 conduction band ($E_{CB,anatase}$= -0.1V, $E_{CB,rutile}$= 0.3V (Nosaka and Nosaka, 2016b)). Due to thermodynamic constraints, the TiO_2 conduction band electrons do not have enough reduction potential to reduce Se^0 to H_2Se. Thus, the electrons must be excited through another pathway, such as Se-photogeneration to drive the reduction to H_2Se. It is also of interest to determine which semiconducting material, TiO_2 or Se, is responsible for supplying photogenerated electrons for the reduction of selenate to Se^0. The redox potential of selenate to Se^0 ($E^0 = 0.5$ V *vs.* SHE) is not within the bandgap of Se ($E_{CB,Se} = -1.7$ V, $E_{VB,Se} = 0.2$ V *vs.* SHE (Benkhedir et al., 2004)) and hence the selenate reduction by Se photogenerated electrons is not thermodynamically viable.

Temperature affects both the reduction of selenate to Se^0 and Se^0 to H_2Se. Higher temperature leads to faster reduction rates for both reactions (Figure 5-2a-c). The increase in reaction rate for the reduction of selenate is likely due to mass transfer limitations. At higher temperatures more unoccupied active sites on TiO_2 are available for selenate because both sulfate and formate, primarily adsorbed through outer sphere complexes (Savory and McQuillan, 2013), will desorb at a faster rate. Selenate is known to adsorb through outer-sphere complexes as well. However, due to the relative concentration of selenate compared to sulfate and formate, the net availability of active sites on the TiO_2 surface will increase, speeding up the reduction of selenate. It is postulated that the increase in reaction rate for the reduction of Se^0 to H_2Se is due to thermally accessible defects in Se^0 which reduce the bandgap of Se, allowing for greater electron excitation at higher temperatures (Kasap et al., 2015). Thus, it is proposed that access to defects within the Se bandgap allow for faster production of H_2Se gas.

Experimental data and thermodynamic considerations strongly suggest that the further reduction of Se^0 to H_2Se (E^0 = -0.6 V *vs.* SHE) is the result of either Se conduction band electrons ($E_{CB,Se}$ = -1.7 V *vs.* SHE) or reduction by the very strongly reducing species carbon dioxide radical ($CO_2^{\bullet -}$) (E^0= -2.0V vs SHE) (Hérissan et al., 2017; Perissinotti et al., 2001). When formic acid is present, the produced $CO_2^{\bullet -}$ has several different pathways of decay: it can inject electrons into the TiO_2 conduction band (a phenomenon known as current-doubling effect (Yang et al., 2015)), transfer an electron to Se^0 to run the reduction to H_2Se, dimerize to form oxalate (Curtin et al., 2004; Kai et al., 2018), or transfer an electron to one of the various electron acceptors present in the complex SMIB solution. A major factor influencing the favoured pathway of decay is the concentration of formic acid. As discussed previously, Figure 5-5a shows that under conditions of low formate adsorption the primary Se reduction product is H_2Se and under high formate adsorption the primary Se reduction product is Se^0.

Both selenate and Se^0 reduction reactions involving Se have two opposing responses to formic acid concentration. Firstly, high formate concentration leads to higher e^-/h^+ separation and high $CO_2^{\bullet -}$ generation through h^+ scavenging, contributing to an increase in selenate and Se^0 reduction, respectively (Perissinotti et al., 2001; T.T.Y. Tan et al., 2003a). However, high formate concentration also limits selenate adsorption through competitive adsorption for active sites on the TiO_2 surface (T.T.Y. Tan et al., 2003b). At excess concentrations of formic acid, $CO_2^{\bullet -}$ may dimerize to form oxalate before it can reduce Se^0 to H_2Se (Curtin et al., 2004; Kai et al., 2018). The chelation between oxalate and Se has been reported (Khan and Berk, 2015). It is postulated that oxalate may lead to a protective inner-sphere shell around photodeposited Se^0, preventing further reduction of Se^0 with non-dimerized $CO_2^{\bullet-}$ molecules in solution. Thus, even though an increase in formic acid concentration may increase the selenate reduction rate, it can actually lead to an inhibition of the Se^0 reduction when formic acid concentration exceeds 1,000 mg/L, as seen in Figure 5-5a.

5.5 Conclusions

This study investigated the viability of photocatalytic reduction using TiO_2 to remove selenate from synthetic mine-impacted brines (SMIB) and focused on the tunable nature of the production of solid Se^0 vs H_2Se gas through varying photoreactor parameters of temperature and formic acid concentration. Photocatalytic reduction on TiO_2 can effectively remove Se from SMIB to < 2 μg/L from an initial Se concentration 3,300 μg/L at under 10×10^{19} photons cm^{-2}. The reduction of SO_4^{2-} concentration from 1,700 to 723 mg/L leads to an increase of the apparent first-order reaction rate constant by 77%, indicating that SO_4^{2-} is a primary competitor for adsorption sites with SeO_4^{2-} on TiO_2. On the other hand, the presence of HCO_3^- leads to a higher selectivity for solid Se^0.

An increase in solution temperature leads to a marked increase in SeO_4^{2-} removal kinetics and an increase in selectivity towards gaseous H_2Se, while increasing the concentration of formic acid in the SMIB slightly increases SeO_4^{2-} removal kinetics and decreases the selectivity towards gaseous H_2Se. Increasing the concentration of TiO_2 from 0.5 g/L to 1.0 g/L causes a drastic change in selectivity towards solid Se^0 from <1% to >85%, respectively. A bivariate response surface analysis was used to elucidate the mechanism behind the production of >99% gaseous H_2Se or >85% solid Se^0. A two-pronged electron transfer model was proposed to explain the selectivity towards solid Se^0 vs gaseous H_2Se under varying conditions: (i) solid Se^0 is produced through direct reduction of selenate by TiO_2 conduction band electrons and (ii) H_2Se gas is produced either through electrons transferred into Se^0 followed by a reduction of Se^0 to H_2Se or through a direct reduction by $CO_2^{\bullet-}$.

Photocatalysis presents a unique approach for the generation of gaseous H_2Se or solid Se^0, both of which have a high potential for Se recovery from mine-impacted water and brine. Although handling H_2Se does pose a safety concern due to its toxicity, the proposed process provides an alternative solution to address a global environmental challenge with proper design and safety considerations.

6 Enhanced photocatalytic selectivity of noble metallized TiO_2 (Ag-, Au-, Pt- and Pd-TiO_2) nanoparticles in the reduction of selenate in water: Tunable Se reduction product $H_2Se_{(g)}$ vs. $Se_{(s)}$

This chapter is modified from:

Holmes, A.B., Daid, K., Livera, D., and Gu, F. (in preparation). Enhanced photocatalytic selectivity of noble metallized TiO_2 (Ag-, Au-, Pt- and Pd-TiO_2) nanoparticles in the reduction of selenate in water: Tunable Se reduction product $H_2Se_{(g)}$ vs. $Se_{(s)}$.

6.1 Summary

Selenium (Se) contamination as a result of anthropogenic activity (i.e. mining, power generation and oil and gas refining) is becoming a global concern due to its associated aquatic toxicity concerns. Herein, heterogenous nanoscale photocatalysts were synthesized by depositing noble metal nanoparticles (Au, Ag, Pt and Pd) onto TiO_2, which demonstrated work-function dependent bimodal selectivity of final products during the photocatalytic reduction of selenate to elemental Se (Se^0) or hydrogen selenide gas (H_2Se). The Se-noble metal-TiO_2 (Se-NM-TiO_2) photocatalytic system is structured in a direct Z-scheme arrangement, when Au, Ag or Pt are used, allowing for high selectivity towards H_2Se. In contrast, Pd acted as an electron sink which decreased the reducibility of the photogenerated electrons, ultimately causing a higher selectivity towards Se^0. Au-TiO_2 offers the largest H_2Se selectivity of all catalysts tested, while Pd-TiO_2 (highest work function) offers the highest selectivity to solid Se^0 generation. This study elucidates electron transport mechanisms and Fermi level equilibration via quantized double-layer charging effects of the Se-NM-TiO_2 system and sheds light on advanced reduction processes using nanoscale heterogeneous catalysts. Finally, the proposed approach provides flexibility toward the final state of Se after treatment, by allowing for two different possible options of Se capture and recovery: direct solid Se capture from the catalyst and scrubbing to recover gaseous H_2Se. The tunability of the Se reduction product is key in designing a sustainable treatment approach with a potential for Se capture and reuse.

6.2 Introduction

Selenium (Se) is a naturally occurring metalloid element, which is essential for all living organisms including humans in trace amounts. Of all the essential elements, Se has one of the narrowest therapeutic windows between dietary deficiency (< 40 μg/day) and toxicity (> 400 μg/day) (Fordyce, 2013), which makes it important to carefully control human and aquatic exposure to Se. Se can enter surface waterways through a variety of sources, including agricultural runoff, mining, industrial production, coal-powered thermal electric generation and other anthropogenic activities (Holmes and Gu, 2016; Santos et al., 2015). The World Health Organization (WHO) and the U.S. Environmental Protection Agency (U.S. EPA) recognize the dangers of Se and have mandated maximum acceptable levels for Se in water of 10 μg/L and 1.5 μg/L, respectively (World Health Organization, 2011; U.S. EPA Office of Water, 2016). Se exists in many organic and inorganic forms, but the high solubility and bioavailability of inorganic species such as selenite (SeO_3^{2-}) and selenate (SeO_4^{2-}) makes these oxoanions the primary focus for removal from water.

Se removal using bioreactors (Lai et al., 2014; Mal et al., 2017) and wetland remediation (Mooney and Murray-Gulde, 2008) have been studied, but the advanced operating complexity, high start-up costs and large footprint requirement have limited the practical application of these techniques. Alternatively, Se adsorptive techniques which rely on the affinity of SeO_3^{2-} and SeO_4^{2-} to the surface of designed adsorbents such as ferrihydrite (iron (III) oxyhydroxide), hematite, goethite, activated alumina or various ion exchange resins have been explored (Ippolito et al., 2009; Rovira et al., 2008). However, the weak bond between SeO_4^{2-} and mineral surfaces through an outer-sphere adsorption complex makes adsorptive techniques much less effective (Jordan et al., 2013). Photocatalytic techniques have been shown to remove both SeO_3^{2-} and SeO_4^{2-} with great efficiency (Nakajima et al., 2013; Nguyen et al., 2005b; T.T.Y. Tan et al., 2003a).

Photocatalytic reactions driven by semiconductors such as TiO_2 are initiated by UV light absorption. Upon UV irradiation, electrons (e^-) are excited into the conduction band (CB) and positive charge carriers known as electron holes (h^+) form in the valence band (VB). Both charge carriers migrate to the TiO_2 surface, driving the reduction and oxidation reactions. However, large quantum inefficiencies in TiO_2 photocatalysis resulting from e^--h^+ recombination present important challenges to the overall efficiency of the redox reactions. One method of decreasing photogenerated charge carrier recombination is the use of an electron hole scavenger such as formic acid that readily reacts with the photogenerated holes in the VB and preserves the electrons in the CB of TiO_2 (T.T.Y. Tan et al., 2003a, 2003b). However, this method has its limitations and can only extend the lifetime of photogenerated charge carriers by a restricted amount and yields a maximum band shift of only -0.53 eV (Di Valentin and Fittipaldi, 2013). As a result, many researchers have focused their efforts towards synthesis strategies that improve TiO_2 photocatalytic activity such as deposition of other materials, dye sensitization, doping and metallization. TiO_2 metallization involves depositing noble metals such as Ag, Au, Pt and Pd onto the TiO_2 surface and have been widely used in environmental photocatalysis (Y. Chen et al., 2017; Choi et al., 2017; Kumar and Rao, 2017; Liu et al., 2017; Tan et al., 2015; Vaiano et al., 2016; Wu et al., 2015). In this case, it is proposed that the metal/TiO_2 heterojunction influences the charge carrier transfer process on the TiO_2 particles (Giannakas et al., 2017; T. H. Tan et al., 2018). The difference between the work function of the metal islands and the Fermi level of TiO_2 results in the formation of a Schottky barrier between these two materials. Upon UV irradiation, CB electrons flow from the TiO_2 particles to the metal and increase the charge carrier separation. Semiconductor-metal composites have been suggested for a wide variety of environmental applications (Hernández-Ramírez et al., 2017; Lou et al., 2017; Paul et al., 2017; Zhu et al., 2017), including Ag-TiO_2 for the reduction and removal of selenate from water (T.T.Y. Tan et al., 2003c).

The introduction of elemental Se, a second photosensitive semiconducting material upon the photoreduction of selenate adds another complexity into the charge transfer model of this process (Tan et al., 2002; T.T.Y. Tan et al., 2003b; T. T. Y. Tan et al., 2003). This heterogeneous photocatalytic system has been shown to further enhance the transfer and separation of photogenerated charge carriers (Rockafellow et al., 2010; Zheng et al., 2017). Photodeposited elemental Se has complementary band positions to TiO_2, promoting the activity of photocatalytic reactions through the further spatial separations of excited electrons and holes within the interfacial area. The arrangement of two such semiconductors can form one of two possible arrangements: heterojunction-type or direct Z-scheme (Low et al., 2017). This arrangement influences the charge carrier transfer mode between the two semiconducting materials. In heterojunction-type photocatalytic systems, the photogenerated electrons transfer between conduction bands directly, while the photogenerated holes move between adjacent valence bands. Although this arrangement does encourage greater spatial isolation and decreased undesirable recombination, it also reduces the redox ability of photogenerated electrons and holes (Low et al., 2017). In a direct Z-scheme, the photogenerated electrons in the CB of TiO_2 migrate through a conductive interface to combine with the photogenerated holes in the VB of Se. This maintains the strong reducibility of the electrons in the CB of Se and the strong oxidizability of the holes in the VB of TiO_2.

Herein, we probe the complex Se-TiO_2 photoreduction system with metallized TiO_2 heterogeneous photocatalysts (Ag-, Au-, Pt- and Pd-TiO_2) with different metal work functions to understand the electron transfer phenomena during the photocatalytic reduction of selenate in water in the presence of an electron hole scavenger, formic acid. Additionally, the selectivity of the reduction of SeO_4^{2-} to solid elemental Se (Se^0) and the further reduction of Se^0 to hydrogen selenide gas (H_2Se) is investigated over the various noble metal deposited photocatalysts.

6.3 Materials and Methods

6.3.1 Materials

All chemicals used were analytical reagent grade. Titanium dioxide nanoparticles (Aeroxide P25, ~10-50 nm particle diameter, 55 m^2 g^{-1} surface area, Acros) were used as received. P25 TiO_2 nanoparticles have been extensively studied and characterized in the past and are often used as a benchmark photocatalyst. All reagent solutions were prepared with deionized water (Milli-Q). Formic acid (ACS reagent, 97%, Alfa Aesar) was used as an electron hole scavenger. Sodium selenate (Sigma-Aldrich, BioXtra, <0.1% impurities), urea (Sigma-Aldrich, 8M in high purity water), $HAuCl_4$ (Sigma-Aldrich, 99.999%), $AgNO_3$ (Sigma-Aldrich, ≥99%), $H_2PtCl_6 \cdot 6H_2O$ (Sigma-Aldrich, ACS reagent, ≥37.50% Pt basis), $PdCl_2$ (Sigma-Aldrich, ≥99%), NaOH (Sigma-Aldrich, ACS reagent), NaCl (EMD, ACS reagent), Dihydroethidium (DHE, Sigma-Aldrich, BioReagent > 95%), potassium nitrosodisulfonate (Fremy's Salt, Sigma-Aldrich) were used as received.

6.3.2 Nanoparticle Synthesis and Characterization

Au-TiO_2 synthesis. Nanometer-sized Au particles were deposited on the surface of TiO_2 by the deposition-precipitation method 1 g of TiO_2 was added to 100 mL of an aqueous solution of $HAuCl_4$ (5.9×10^{-4} mol L^{-1}) and urea (0.42 mol L^{-1}) (Zanella et al., 2002). The initial pH was 2.4. The suspension thermostated at 90 °C was then vigorously stirred for 5 h before being centrifuged, washed, dried and calcined at 300 °C for 3 hours. These particles were prepared with a loading of 1 wt.% Au on TiO_2 (Au-TiO_2).

Ag-TiO_2 synthesis. Nanometer-sized Ag particles were deposited on the surface of TiO_2 by a photodeposition technique (Chan and Barteau, 2005, p. 2). 1 g of TiO_2 was added to 200 mL of an aqueous solution of $AgNO_3$ (4.6×10^{-4} mol L^{-1}) and formic acid (1.3×10^{-2} mol L^{-1}). The suspension was exposed to UVA (λ=365nm) irradiation for 2 hours (11.0 mW/cm^2 supplied from Blak Ray B-100A) to ensure complete reaction and then centrifuged, washed and calcined at 300 °C for 3 hours. These particles were prepared with a loading of 1 wt.% Ag on TiO_2 (Ag-TiO_2).

Pt-TiO_2 synthesis. Nanometer-sized Pt particles were deposited on the surface of TiO_2 by a photodeposition technique (Vaiano et al., 2016, p. 2). 1 g of TiO_2 was added to 200 mL of an aqueous solution of H_2PtCl_6 (2.6×10^{-4} mol L^{-1}) and formic acid (1.3×10^{-2} mol L^{-1}). Under an inert atmosphere (N_2), the suspension was exposed to UVA (λ=365nm) irradiation for 4 hours (11.0 mW/cm^2 supplied from Blak Ray B-100A) to ensure complete reaction and then centrifuged, washed and calcined at 300 °C for 3 hours. These particles were prepared with a loading of 1 wt.% Pt on TiO_2 (Pt-TiO_2).

Pd-TiO_2 synthesis. Nanometer-sized Pd particles were deposited on the surface of TiO_2 by a photodeposition method (Papp et al., 1993). 1 g of TiO_2 was added to 200 mL of an aqueous solution of $PdCl_2$ (4.7×10^{-4} mol L^{-1}), of NaCl (2.6×10^{-3} mol L^{-1}) and formic acid (1.3×10^{-2} mol L^{-1}). Under an inert atmosphere (N_2), the suspension was pH adjusted with 1M NaOH to pH 11, then exposed to UVA (λ=365nm) irradiation for 6 hours (11.0 mW/cm^2 supplied from Blak Ray B-100A) to ensure complete reaction and then centrifuged, washed and calcined at 300 °C for 3 hours. These particles were prepared with a loading of 1 wt.% Pd on TiO_2 (Pd-TiO_2).

Particle size and deposit structure was analyzed by TEM (Philips CM-10, 60 keV) for each TiO_2, Ag-TiO_2, Au-TiO_2, Pt-TiO_2, and Pd-TiO_2. The hydrodynamic diameter of the particles in water was measured by DLS (Brookhaven 90Plus Particle Size Analyzer, lognormal volume-weighted median diameter). The surface area of the particles (pre-dried at 200 °C in N_2) was calculated from the Brunauer–Emmett–Teller (BET) equation using data from N_2 adsorption isotherms obtained at 77 K (Micrometrics Gemini VII 2390 Surface Area Analyser). High resolution transmission electron microscopy (HR-TEM, FEI Titan 80-300 LB) and Electron energy loss spectroscopy (EELS, Gatan K2 Direct Detection Camera) were used to examine the Se deposits on TiO_2.

6.3.3 Batch photocatalytic reduction experiments

The photocatalytic reactor apparatus consists of an air tight stainless-steel reactor vessel of 1.0 L capacity with a quartz-window through which UV was irradiated. The experimental apparatus is illustrated in Figure D-1. Sodium selenate solution (0.06 mM as Se) was added to an internal PTFE liner followed by formic acid (6.5 mM) and catalyst, either TiO_2 or x-TiO_2 (x = Ag, Au, Pt, Pd) (0.2 g/L), followed by probe sonication of the suspension to disperse the catalyst. The reactions were controlled at 300 K and pH 3 (Using 1M HCl and NaOH to pH adjust). The suspension was stirred for 1 hour under nitrogen to allow dark adsorption before UV irradiation. Samples of the suspension were collected throughout the treatment to determine both total and dissolved Se through unfiltered and filtered samples respectively. The apparatus was exposed to UV supplied by UVA fluorescent bulbs (Philips F20T12/BL, λ_{Peak} = 365 nm, photon irradiance, $E_p = 1.069 \times 10^{15}$ photons cm^{-2} s^{-1}). Photon irradiance was determined using potassium ferrioxalate actinometry for each lamp-reactor pair to enable comparison of the data with experimental apparatus variation (Bowman and Demas, 1976; Hatchard and Parker, 1956). Variation in fluence was used instead of operating time to make our results comparable with other studies.

6.3.4 $O_2^{\bullet -}$ / $^{\bullet}O_2H$ radical experiments

Dihydroethidium (DHE) was added to quantitatively detect superoxide radical ($O_2^{\bullet -}$) generated by the TiO_2 photocatalytic reduction system in the presence of O_2 supplied by ambient air. The fluorescence of the product formed from the reaction of DHE and oxidative molecules, 2-hydoxyethidium, was measured by a fluorimeter and converted into a molar generation rate using a calibration curve for 2-hydroxyethidium generated by reacting known amounts of DHE with potassium nitrosodisulfonate (Fremy's Salt), which has been demonstrated to yield the same superoxide-specific oxidation product (Laurindo et al., 2008).

6.3.5 Analytical methods

Se concentration was determined in accordance with the U.S. EPA suggested Se determination technique (APHA 2009, Method 3114B/C) using hydride generation inductively coupled plasma optical emission spectroscopy (HG-ICP-OES, Teledyne Prodigy ICP and Cetac HGX-200 advanced membrane hydride generation system, LOD = 1 $\mu g\ L^{-1}$). Both dissolved and total Se were determined by HG-ICP-OES following the acid digestion protocol U.S. EPA Method 3050B. Solid elemental Se was determined by the difference of total and dissolved Se concentrations. Gaseous H_2Se was calculated from the difference between the initial total Se in the water and total Se in the TiO_2 suspension after UV exposure.

6.4 Results and Discussion

6.4.1 Characterization of the Ag-, Au-, Pt- and Pd-TiO_2

The Ag, Au, Pt and Pd deposited on TiO_2 formed metal islands on the surface of TiO_2 ranging from 2-6 nm in diameter on the TiO_2. TEM images for each catalyst are presented in Figure 6-1 and the average size of each noble metal deposit is presented in Table 6-1. Both the BET surface area and the hydrodynamic diameter of each particle, presented in Table 6-1, remain unchanged after noble metal deposition, confirming that the synthesis procedures did not alter reactive surface area or cause mass aggregation of the TiO_2.

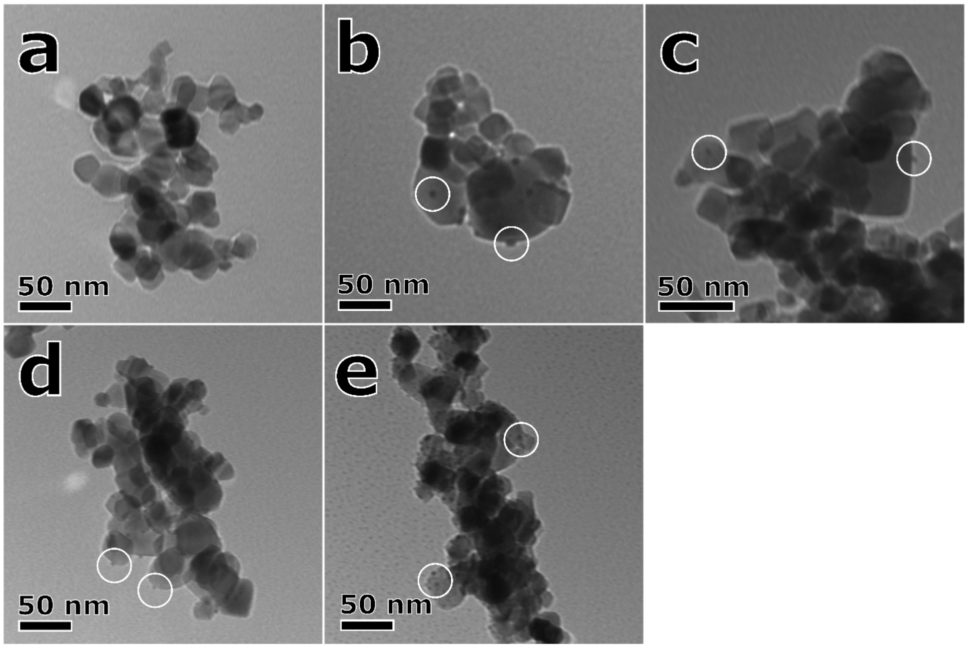

Figure 6-1. TEM micrographs of (a) TiO_2 nanoparticles deposited with (b) Au, (c) Pt, (d) Pd, and (e) Ag. Noble metal deposits are circled in white in the respective images.

Table 6-1. Brunauer–Emmett–Teller (BET) surface area, dynamic light scattering (DLS) hydrodynamic diameter analysis of noble metal deposited on TiO_2, and diameter of noble metal deposits.

	TiO_2	Au-TiO_2	Ag-TiO_2	Pt-TiO_2	Pd-TiO_2
BET Surface Area (m^2 g^{-1})	56.02	52.31	54.65	55.62	56.26
Hydrodynamic diameter (nm)	112.7	113.5	118.8	106.8	108.3
Noble metal deposit diameter (nm)	--	6.0 ± 1.5	2.9 ± 0.3	3.5 ± 0.8	2.5 ± 0.3

The Ag-, Au-, Pt- and Pd-deposited TiO_2 were white, purple, grey and brown in colour respectively. An image of the four synthesized catalysts beside the unmodified TiO_2 is provided in Appendix D for comparison (Figure D-2). Of note, the Ag-TiO_2 was reddish-brown prior to the calcination step and the colour change is a strong indication of oxidation of surface Ag to predominantly ionic Ag species (AgO and Ag_2O) through calcination in ambient air. Identification of AgO or Ag_2O through surface characterization by XPS is challenging when the average size of the silver nanoparticles (2.9 ± 0.3 nm) is smaller than the inelastic mean free path for Ag of 5.7 nm at 1486 eV (Tanuma et al., 2011). However, Ag-TiO_2 is known to undergo surface oxidation due to its low stability in air (Mogal et al., 2014). Control experiments were conducted to compare the Ag-TiO_2 before and after calcination in attempt to understand the effect of surface oxidation of Ag. Figure D-3b shows the photocatalytic reduction of selenate with Ag-TiO_2 pre- and post-calcination, showing minimal changes to the kinetics of selenate degradation and that the calcined sample performed marginally faster. This oxide coating on Ag may have complex interactions with the surface interactions with ions in the water, transfer of electrons through the catalyst surface and the tunneling of electrons to Se during the reduction process. The effect of the weight percent (wt%) of Ag deposited on TiO_2 on selenate reduction was investigated as well. Figure D-3a shows the photocatalytic reduction of 5 mg/L (as Se) selenate by 1.0, 0.5 and 0.1 wt% Ag deposited on TiO_2. The Ag loading on the photocatalyst does not appear to have a strong effect on the reduction kinetics of selenate.

The four noble metals Ag, Au, Pt and Pd were selected based on their varying work functions of 4.26 eV (Dweydari and Mee, 1975), 5.1 eV (Eastman, 1970), 5.2 eV (Yu and Spicer, 1968) and 5.5 eV (Yu and Spicer, 1968), respectively *vs.* vacuum (or -0.18 eV, 0.66 eV, 0.76 eV and 1.06 eV respectively *vs.* SHE). Figure 6-2 illustrates a schematic comparison of band edge positions of Se, TiO_2 and these four noble metals (Ag, Au, Pt and Pd) together with the standard potentials of relevant redox couples for the reduction reactions of selenate. The reduction of selenate follows two key reduction reactions presented in equation 6.1 and 6.2.

$$SeO_4{}^{2-}{}_{(aq)} + 8H^+ + 6e^-_{cb} \rightarrow Se^0{}_{(s)} + 4H_2O \quad (E^0 = 0.5\text{ V } vs.\text{ SHE}) \tag{6.1}$$

$$Se^0{}_{(s)} + 2H^+ + 2e^-_{cb} \rightarrow H_2Se_{(g)} \quad (E^0 = -0.6\text{ V } vs.\text{ SHE}) \tag{6.2}$$

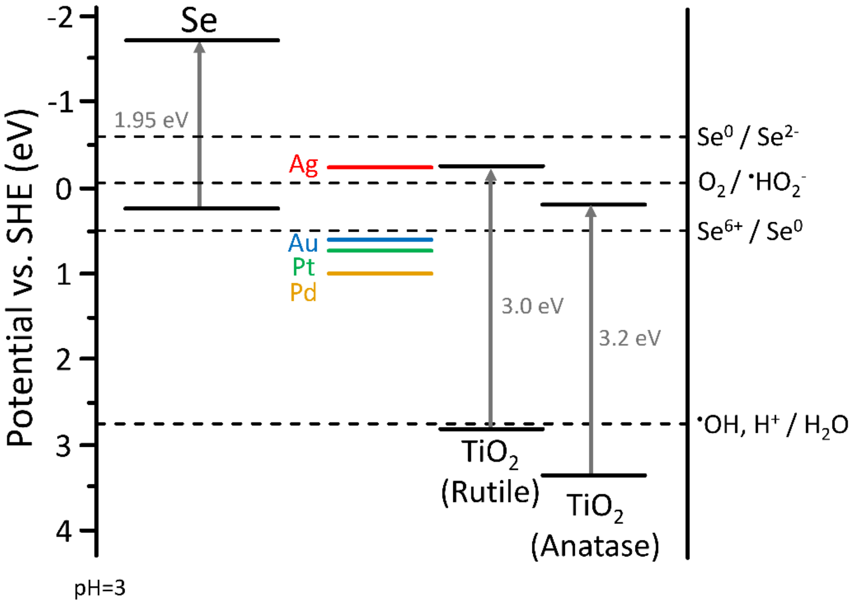

Figure 6-2. Schematic comparison of band edge positions of Se, TiO_2 and relevant noble metals work functions (Ag, Au, Pt and Pd) together with the standard potentials of relevant redox couples

The photocatalytic reduction of selenate is unique in that an intermediate product of the total 8 e^- reduction, solid elemental Se ($Se^0_{(s)}$), is a photosensitive semiconducting material itself. As $Se^0_{(s)}$ is produced, it is photodeposited onto a mixed-phase crystalline combination of rutile and anatase TiO_2, similar to the photodeposition of the noble metals onto TiO_2 and alters the reduction potential of the heterogeneous catalyst structure. The TiO_2 (P25, Aeroxide) used in this study is known to be a mixed-phase crystalline combination of rutile and anatase, with >80% anatase and the remainder rutile and amorphous. The further reduction of $Se^0_{(s)}$ to $H_2Se_{(g)}$ has an energy potential more negative (-0.6 V *vs.* SHE) than the conduction band (CB) of rutile TiO_2 (-0.28 V *vs.* SHE) and anatase TiO_2 (0.12 V *vs.* SHE). Thus, the further reduction must occur at the CB of solid Se itself (-1.71 V *vs.* SHE), in a reduction reaction. While comparing the energy potentials of valence bands (VB) of Se (0.24 V *vs.* SHE), rutile TiO_2 (2.72 V *vs.* SHE) and anatase TiO_2 (3.32 V *vs.* SHE), only anatase and rutile TiO_2 are more positive than the standard potential of the $OH^\bullet/H_2O$ redox couple (2.7 V *vs.* SHE).

6.4.2 Selenate reduction on unmodified TiO_2

Experiments were conducted to investigate the photocatalytic reduction of selenate on unmodified TiO_2, for comparison to the noble metal deposited TiO_2 catalysts. During the photoreduction of selenate on TiO_2, Se goes through a clear two-stage reduction as outlined in equations 6.1 and 6.2. Figure 6-3a presents dissolved Se concentration as a function of photon fluence remaining in a solution initially containing 5 mg/L (as Se) selenate solution with formic acid as an electron hole scavenger. The initial drop of ~ 800 µg/L before UV exposure is attributed to adsorption of selenate to the TiO_2 surface. The initial reduction of selenate in the first stage between 0 and 1.0×10^{19} photons/cm^2 follows zero order kinetics with the zeroth order rate ($k_{Se,0} = 6.210 \frac{mol \cdot cm^2}{L \cdot 10^{24}\, photons}$). After 1.0×10^{19} photons/cm^2 of UV exposure, the kinetics of Se removal drastically slows, signaling the beginning of the second stage of reduction. The colour of the catalyst, shown schematically in Figure 6-3a, changes from its native white (colour of unmodified TiO_2) to red-orange (colour of solid elemental Se) during the first stage of reduction, after which the colour changes back to white. Thus, during the first stage of reduction selenate is being reduced to elemental Se onto the surface of TiO_2. After near exhaustion of selenate from solution, at around 1.0×10^{19} photons/cm^2 and an aqueous Se concentration of 100 µg/L, the elemental Se on the surface of TiO_2 is further reduced to H_2Se gas (equation 6.2). Figure 6-3b-e present the transmission electron microscope (TEM) micrograph of TiO_2 after 1.0 photons $\times 10^{19}$ cm^{-2} of UV exposure and elemental analysis done by electron energy loss spectroscopy (EELS) images. These images clearly indicate an even distribution of Se on the surface of the unmodified TiO_2 catalyst. The thickness of elemental Se deposited onto the surface of TiO_2 is likely less than 1 nm, based on the electron energy loss spectroscopy line scans and HR-TEM images of the Se deposited TiO_2 (Figure D-4).

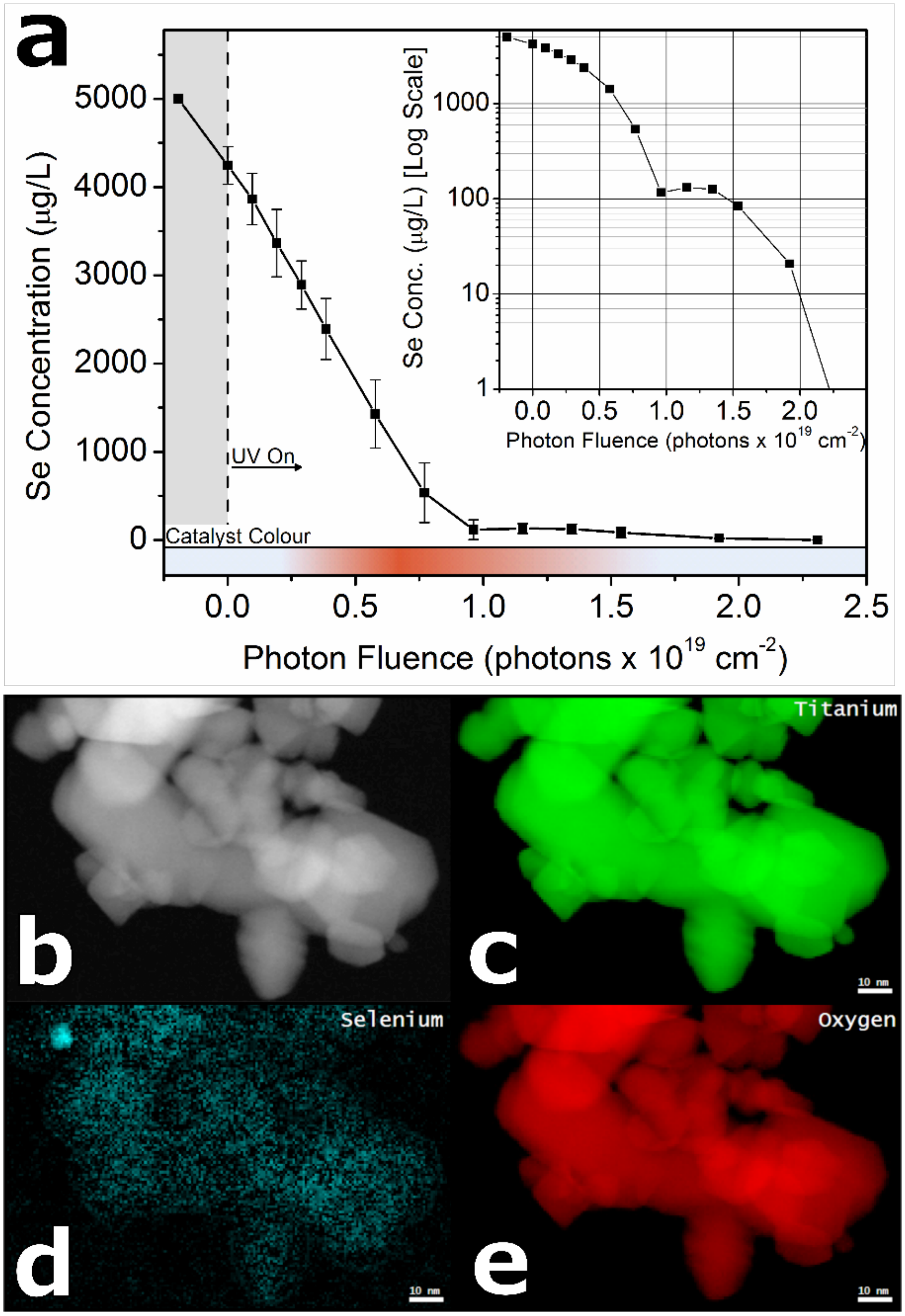

Figure 6-3. (a) Selenate photocatalytic reduction by unmodified TiO_2 nanoparticles. Inset graph is identical data plotted on a log scale to highlight the two-step reduction reaction. (b) Transmission electron microscope (TEM) micrograph of TiO_2 after 1.0 photons × 10^{19} cm^{-2} of UV exposure and elemental analysis done by electron energy loss spectroscopy (EELS) images of (c) titanium, (d) selenium, and (e) oxygen.

A follow-up experiment was completed to determine the rate of both solid elemental Se and H_2Se gas generation throughout the photocatalytic reduction process. This Se mass balance experiment, presented in Figure 6-4, shows the proportion of aqueous selenate, solid elemental Se and gaseous hydrogen selenide gas over the span of 2.5×10^{19} photons/cm^2 exposure of UV. As expected, the proportion of solid elemental Se was confirmed to increase until ~ 1.0×10^{19} photons/cm^2, when the concentration of selenate in the solution reached below 100 µg/L, after which it decreased back to zero over the remainder of the reaction. Interestingly, the generation of H_2Se gas product begins after initial UV exposure and increases much more rapidly after the inflection point in the reduction reaction between the first and second stage at ~ 1.0×10^{19} photons/cm^2. The experiment suggests that both reduction of selenate and elemental Se occur simultaneously, but that photogenerated electrons reduce primarily selenate during the first half of the reaction and elemental Se during the second half of the reaction.

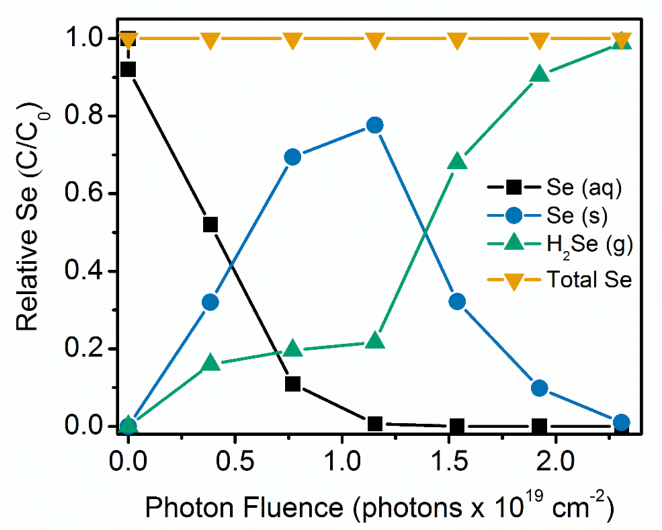

Figure 6-4. Se speciation during photocatalytic reduction with unmodified $nTiO_2$, tracking Se species $SeO_4^{-2}{}_{(aq)}$, elemental $Se_{(s)}$, and $H_2Se_{(g)}$.

The reduction of selenate on unmodified TiO_2 generates marginal amounts of H_2Se during the initial stages of UV exposure (0.0-1.3×10^{19} photons cm^{-2}), then much larger amounts after the disappearance of selenate from solution (1.3-2.6×10^{19} photons cm^{-2}). The proposed explanation for this is an energy barrier, known as a p-n junction barrier with a reverse bias, as a result of a p-type and n-type semiconductor material in contact with different work functions. A reverse bias occurs when the n-type semiconductor is connected to a positive terminal or a redox reaction pulling electrons away from the junction (Bard et al., 2002). One such flux of electrons away from the p-n junction occurs during the reduction of selenate to Se^0, which utilizes photogenerated electrons from TiO_2. During the first stage of UV exposure, this energy barrier prevents e^- transferring from the TiO_2 conduction band into Se^0, so that e^- follow a path of less resistance to reduce selenate to Se^0. When selenate is depleted from the system, and electrons continue to accumulate in the conduction band of TiO_2, causing an increase in the driving force of electrons through the p-n junction. Once the electric field increases beyond some critical value, the p-n depletion zone breaks down and electrons begin to flow through non-destructively and reversibly (Bard et al., 2002) and a marked increase of H_2Se generation is observed. Kikuchi and Sakamoto initially proposed a similar electron accumulation model after measuring an increase of potential of the suspension toward the end of selenate reduction (Kikuchi and Sakamoto, 2000).

6.4.3 Selenate reduction on Au-, Ag-, Pt- and Pd- TiO_2

Similar mass balance experiments were conducted using the noble metal-deposited TiO_2 catalysts to understand how the various noble metals and their work functions, affect the final fate of photogenerated electrons driven to reduce selenate or elemental Se. 5 mg/L (as Se) selenate solutions were reduced by the noble-metal deposited TiO_2 catalysts in the presence of 300 mg/L formic acid. The $Se_{(aq)}$, $H_2Se_{(g)}$ and $Se_{(s)}$ profiles are presented in Figure 6-5a, b and c, respectively, for TiO_2, Ag-, Au-, Pt- and Pd-TiO_2 photocatalytic trials.

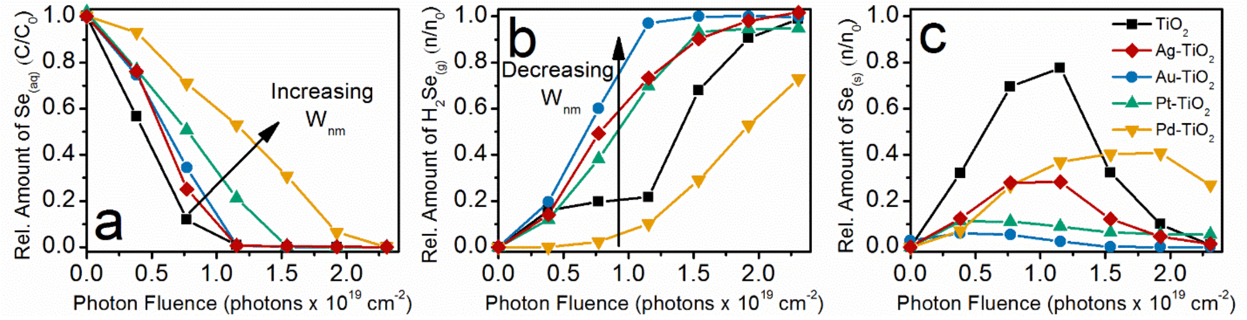

Figure 6-5. Noble metal (Au, Pt, Pd and Ag) deposited TiO_2 catalysts compared to unmodified $nTiO_2$ for the (a) removal of aqueous selenate, (b) production of $H_2Se_{(g)}$ and (c) production of elemental $Se_{(s)}$.

The removal rates of selenate in Figure 6-5a decrease in order of increasing work function with Ag-TiO_2 exhibiting most rapid kinetics and Pd-TiO_2 the slowest. We postulate that the noble metal deposits on the surface of TiO_2 are acting as electron sinks for the photogenerated electrons in the CB of TiO_2. The higher the work function of the noble metal deposit, the further the reduction potential falls when the electrons transfer to the noble metal sink and the more positive is the reduction potential of the elctrons. With a more positive reduction potential, the less likely the photogenerated electrons are able to reduce the Se^{6+}/Se^0 reduction couple ($E^0 = 0.5$ V *vs.* SHE). For instance, Au, Pt and Pd have work functions 0.66 eV, 0.76 eV and 1.06 eV *vs.* SHE respectively, all of which would decrease the rate at which selenate can be reduced by drawing electrons away from the reactive CB of rutile TiO_2 (-0.28 V *vs.* SHE). In addition, the noble metal provides a conductive pathway for the combination of CB e^- from TiO_2 and VB h^+ from Se, as described by the PC-C-PC Z-scheme photocatalyst arrangement. As a result, a competition exists for the available photogenerated electrons to reduce selenate to Se^0 and Se^0 to H_2Se.

The H_2Se gas generation profiles presented in Figure 6-5b follows a similar trend with increased H_2Se generation by noble metal catalysts with smaller work functions, resulting in more negative reduction potentials. All three Au-, Ag- and Pt- TiO_2 catalysts generate H_2Se gas faster than unmodified TiO_2. Thus, it is postulated that photogenerated electrons from TiO_2 and the photogenerated holes from Se are being transferred to the conductive noble metal nanoparticles where they combine, thus preserving the electrons with stronger reducibility in the CB of Se. These preserved electrons are then able to reduce Se^0 to H_2Se at a much greater rate. Pd-TiO_2 demonstrated much slower H_2Se generation when compared to unmodified TiO_2 suggesting that it did not act as a PC-C-PC Z-scheme photocatalyst arrangement, but merely an electron sink with the potential of the Pd-TiO_2 well below the reduction potential of the Se^0/H_2Se redox pair. In addition, it is worth noting that the Ag-TiO_2 sample did not perform as well as predicted, given it has the lowest work function and thus highest reduction potential. A possible explanation for this is its propensity to oxidize to AgO or Ag_2O, altering the electronic properties of the photocatalyst composite.

The solid Se^0 generation profiles presented in Figure 6-5c show that Au- and Pt- are the least solid-generating catalysts, whereas Ag- and Pd-TiO_2 generate a maximum of 30% and 40% solid Se, respectively. This agrees with the slow gas generation of Ag-TiO_2 when compared to Au- or Ag-TiO_2, because the solid Se remains on the catalysts for an extended period of UV exposure.

The selectivity towards solid elemental selenium ($Se^0_{(s)}$) and hydrogen selenide gas ($H_2Se_{(g)}$) are defined according to the following equations:

$$S\left(Se^0_{(s)}\right)_t = \frac{\left[Se^0_{(s)}\right]_t}{\left[SeO_4^{-2}\right]_0 - \left[SeO_4^{-2}\right]_t} \tag{6.3}$$

$$S\left(H_2Se_{(g)}\right)_t = \frac{\left[H_2Se_{(g)}\right]_t}{\left[SeO_4^{-2}\right]_0 - \left[SeO_4^{-2}\right]_t} \tag{6.4}$$

where $[X]_0$ is the initial concentration and $[X]_t$ is the concentration at time = t. Note that $\left[H_2Se_{(g)}\right]_t$ is the theoretical concentration of $H_2Se_{(g)}$ in the reaction chamber for ease of calculation, as a representation for the total $H_2Se_{(g)}$ generated, when in reality the gaseous product is purged out of the chamber with N_2 and bubbled through a $CuSO_4$ scrubber for removal.

The selectivity of Se reaction products during the photocatalytic reduction over various noble metal deposited TiO_2 catalysts is presented in Figure 6-6. Ag-, Au- and Pt-TiO_2 catalysts all have high selectivity for gaseous H_2Se gas generation. Of these three catalysts, Au-TiO_2 has the highest propensity to generate H_2Se gas and is the most effective at transferring photogenerated electrons to Se for photoexcitation and subsequent reduction to H_2Se gas. It has been shown in experiments that the addition of 5nm Au nanoparticles onto TiO_2 can shift the Fermi level by 40 mV (Subramanian et al., 2004), leading to a more reductive potential and higher probability to inject e^- into Se and reduce it to H_2Se gas. Pd-TiO_2 offers a higher selectivity to solid Se^0 generation when compared to unmodified TiO_2. We postulate that this is due to the fact that Pd does not equilibrate charges with the Fermi level of TiO_2 and hence remains at the original Fermi level determined by the work function of Pd. However, Pd acts as a sink for photogenerated electrons in TiO_2, essentially reducing their reduction potential for both redox pairs SeO_4^{2-} / Se^0 and Se^0 / H_2Se.

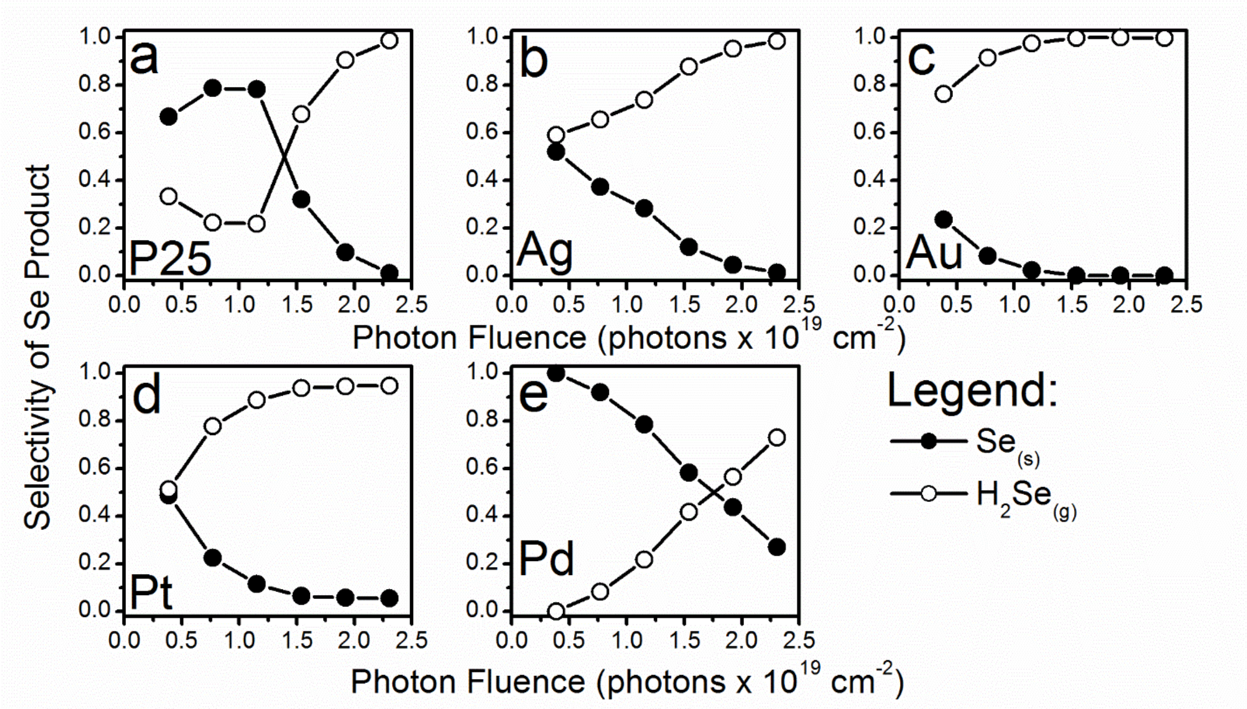

Figure 6-6. Selectivity of Se product, solid elemental Se ($Se_{(s)}$) or gaseous hydrogen selenide ($H_2Se_{(g)}$), from photocatalytic reduction of selenate over (a) unmodified TiO_2, (b) Ag-TiO_2, (c) Au-TiO_2, (d) Pt-TiO_2, and (e) Pd-TiO_2 in the presence of formic acid.

Tan et al. studied the photoreduction of selenate on Ag-TiO_2 and proposed an electron accumulation model to support their findings, similar to that proposed by Kikuchi and Sakamoto (Kikuchi and Sakamoto, 2000; T.T.Y. Tan et al., 2003c). A modified electron transfer theory is proposed in light of the experimental results herein. Unlike bulk films of metals, metal nanoparticles exhibit a property known as quantized double-layer charging effects (D. Scanlon et al., 2015). If such metal particles come in contact with a charged semiconductor nanostructure or nanoparticle, then the Fermi level of the semiconductor and metal nanoparticles equilibrate (Peljo et al., 2017; Raman Chaudhari et al., 2014; Subramanian et al., 2004; Jakob et al., 2003). Upon contact charge equilibration between semiconductor and metal nanoparticles causes the Fermi level to shift close to the conduction-band edge of the semiconductor. Many experiments have demonstrated this increase of Fermi levels in Ag (Peljo et al., 2017; Raman Chaudhari et al., 2014), Au (Jakob et al., 2003; Subramanian et al., 2004), and Pt (D. Scanlon et al., 2015) nanoparticles deposited on TiO_2, to increase closer to the CB of TiO_2. Thus, we postulate that Au, Ag and Pt shift to the Fermi level of TiO_2 and inject CB electrons in Se, overcoming the p-n junction reverse bias between Se and TiO_2.

To investigate the adjusted Fermi levels of the noble-metal deposited TiO_2, the photocatalytic reduction of O_2 was used as a surrogate redox pair (O_2 / $^{\bullet}HO_2$ redox pair -0.015 V *vs.* SHE, see Figure 6-2). Hydroperoxyl ($^{\bullet}HO_2$) generation experiments were conducted in suspensions of the noble-metal deposited TiO_2 catalysts in the presence of 300 mg/L formic acid and dissolved O_2 concentration of 8.7 mg/L. DHE (5×10^{-5} M) was used to quantitatively detect superoxide ($O_2^{\bullet-}$) or hydroperoxyl radicals ($^{\bullet}HO_2$) at pH lower than 4.88, the pKa of superoxide. Figure 6-7 shows the generation rates of hydroperoxyl under the described conditions.

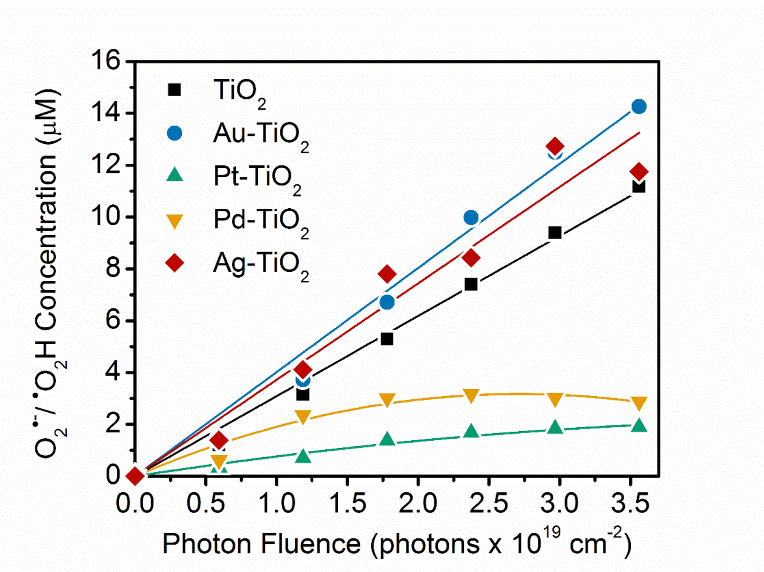

Figure 6-7. Photocatalytic hydroperoxyl ($^{\bullet}O_2H$) radical generation in the presence of oxygen by reduction on TiO_2, Au-, Pt-, Pd- and Ag-TiO_2.

Au- and Ag-TiO_2 generate hydroperoxyl slightly faster than unmodified TiO_2. This suggests that the Fermi levels for these two catalysts after equilibrium are slightly more negative than the potential of the O_2 / $^{\bullet}HO_2$ redox pair ($E_F < -0.015V$). Pt- and Pd-TiO_2 suppress hydroperoxyl generation, suggesting a more positive Fermi level. Presumably, the Fermi equilibrium of Pt-TiO_2 is more positive than the O_2 / $^{\bullet}HO_2$ redox pair (-0.015 V *vs.* SHE) but more negative than the VB of Se (0.24 V *vs.* SHE), thus explaining why Pt-TiO_2 acts similarly to Au-TiO_2 and Ag-TiO_2 during the reduction of selenate and acts similarly to Pd-TiO_2 during the reduction of O_2.

Figure 6-8 illustrates this mechanism schematically, where Figure 6-8a presents the charge carrier separation in Se-noble metal-TiO_2 direct Z-scheme photocatalyst under dark conditions and Figure 6-8b shows the Fermi level increases upon exposure to UV and subsequent charge equilibration between TiO_2 and Au, Ag, and Pt deposits. Since the work function of Pd is too low for equilibration with the Fermi level of TiO_2, the Fermi level within the Pd nanoparticles remain much lower than the VB of Se.

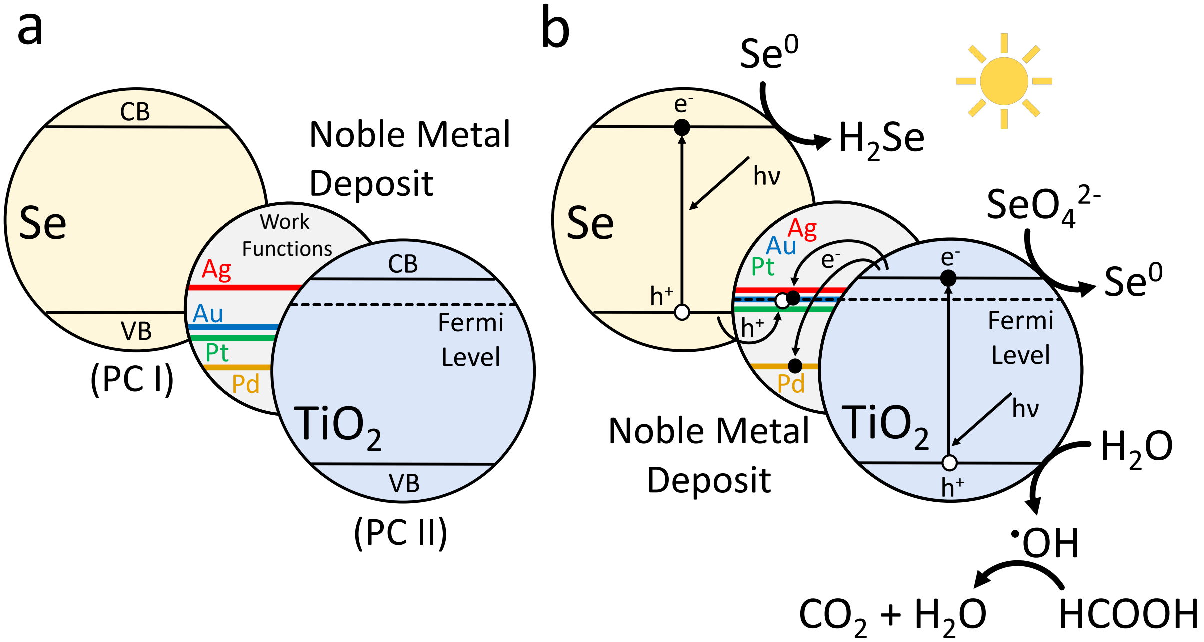

Figure 6-8. Schematic illustration of the mechanism for charge carrier separation in Se-noble metal-TiO_2 direct Z-scheme photocatalyst under (a) dark and (b) UV light conditions after charge equilibration between TiO_2 and noble metal deposits.

As seen in Figure 6-8b, comparing the energy potentials of the CB of Se (-1.71 V *vs.* SHE) and TiO_2 (-0.28 V *vs.* SHE), only Se is more negative than the standard potential of the Se^0/Se^{2-} redox couple (-0.6 V *vs.* SHE), while comparing the energy potentials of the VB of Se (0.24 V *vs.* SHE) and TiO_2 (3.32 V *vs.* SHE), only TiO_2 is more positive than the standard potential of the $OH^{\bullet}/H_2O$ redox couple (2.7 V *vs.* SHE). In this regard, the reduction of Se^0 to H_2Se is likely occurring at the CB of Se while the oxidation of the electron hole scavenger, formic acid, would occur at the VB of TiO_2.

6.5 Conclusions

Noble metal deposited (Ag, Au, Pt and Pd)-TiO_2 catalysts were synthesized and used in a photocatalytic system to reduce selenate in solution with the use of formic acid as an electron hole scavenger. The Se-NM-TiO_2 photocatalytic system is a PC-C-PC direct Z-scheme heterogeneous photocatalyst arrangement which allows for spatial separation of photogenerated charge carriers and preserves the strong reducibility of CB electrons in Se and the strong oxidizability of VB holes of TiO_2 to react with selenate and formate, respectively. Selectivity of the final Se products (Se^0 vs. H_2Se) is tunable based on the varying work functions of the noble metals which can behave as photogenerated electron conductors or sinks and so enables generation of either gaseous H_2Se or solid Se final products from the photoreduction of selenate. Au-, Ag- and Pt-TiO_2 catalysts experience a shift in the metal Fermi levels towards the conduction band edge of the semiconductor, facilitating the transport of photogenerated electrons through the noble metal deposit from TiO_2 to Se and driving an increase in H_2Se generation. Pd-TiO_2 catalysts inhibit H_2Se generation due to the high work function of Pd which does not allow for charge equilibration with the TiO_2 Fermi level. Thus, Pd acts as a sink for electrons from the TiO_2 CB, diverting the flow of electrons into Se^0 and restricting the generation of H_2Se.

7 Conclusions and Perspectives

7.1 Synthesis of major findings

In Chapter 1, the potential of using nanomaterials for selenate removal from water was presented, highlighting the various gaps in conventional Se removal techniques that nanomaterials can address. Several classes of nanomaterials such as nanoscale adsorbents, catalysts and reactants, show promise for the removal of Se in a wide range of oxidation states. A summary of current Se removal technologies and the gaps in current technologies was presented with the focus on emerging nanomaterials capable of removing Se oxyanions from wastewater to ultra-low µg/L limits, namely photocatalysts. These Se removal approaches involve the modification of different nanomaterials in order to achieve high surface adsorbing activity, high reactivity, selectivity and sustainable treatment capability of removing selenium oxyanions.

Chapter 2 & 3 were concerned with photocatalytic selenate reduction in real-world industrial wastewaters, such as flue gas desulphurization wastewater (FGDW) and mine-impacted water (MIW). The potential of photocatalysis on TiO_2 was demonstrated and the simultaneous generation of elemental selenium (Se^0) and hydrogen selenide (H_2Se) through two consecutive first-order reductions was reported under a direct Z-scheme photocatalyst arrangement between photodeposited Se and TiO_2. Selenate was reduced to a concentration of < 1 µg/L as Se in both MIW and FGDW in situations where the concentrations of many competing co-existing ions were more than 2,500 times that of selenate. The kinetics of reduction was thoroughly investigated. The following key reactor parameters were identified to optimize the rate of reduction of selenate: low pH (< pH 5), high temperature (between 20-60 °C), low sulfate concentration, use of formic acid as electron donor, TiO_2 catalyst dose of 0.5 g/L and low dissolved oxygen concentration (< 3 mg/L).

MIW can contain varying concentrations of dissolved species such as sulfate, carbonate, nitrate, selenate, organic matter and many dissolved metals. Due to the reduction potentials of selenate and nitrate, bacteria will favor nitrate over selenate during conventional Se biological reduction process, leading to difficulties in removing Se. The development of a treatment process capable of removing selenate prior to the biological denitrification process is desired due to the numerous advantages a two-stage treatment would provide. Selective photocatalytic reduction of selenate from >500 μg/L to < 1 μg/L was shown to be possible in the presence of the more energetically favourable nitrate electron acceptor (~250x molar concentration of selenate) and at high concentrations of sulfate (~2,000x molar concentration of selenate) given optimal reactor conditions and operating parameters. Selective photocatalysis is highly desired in complex water sources that contain a variety of dissolved species in addition to the target species for efficient use of the UV energy supplied to the reactor.

In Chapter 4, the selectivity of the reduction process achieved through photocatalytic treatment of selenate was examined and the electron transfer mechanism responsible for such selective selenate reduction was elucidated. Sulfate primarily affects the initial adsorption of selenate, inhibiting the reduction of selenate to Se^0 by TiO_2 conduction band electrons, whereas nitrate affects the further reduction of Se^0 to H_2Se by scavenging of carbon dioxide radicals ($CO_2^{\bullet -}$) and Se conduction band electrons. The competitive adsorption and reduction of selenate on TiO_2 in the presence of sulfate, chloride, carbonate and nitrate were thoroughly investigated, using formic acid as an electron hole scavenger.

In Chapter 5, the photocatalytic treatment capabilities were expanded to higher TDS synthetic mine-impacted brines (SMIB) and the tunability of the final Se reduction product ($Se^0_{(s)}$ vs. $H_2Se_{(g)}$) was demonstrated. This is a crucial factor in designing a recoverable Se stream from the water treatment process. This photocatalytic reduction can effectively remove Se from SMIB to < 2 μg/L from an initial Se concentration of > 3,300 μg/L. An increase in solution temperature led to a marked enhancement in selenate removal kinetics and an increase in selectivity towards $H_2Se_{(g)}$, while increasing the concentration of formic acid led to an increase in selenate removal kinetics and an increase in the selectivity towards $Se^0_{(s)}$. A bivariate response surface analysis was used to elucidate the mechanism behind the production of >99% gaseous H_2Se or >85% solid Se^0 under a range of reaction conditions. Finally, a two-pronged electron transfer model was proposed to explain the selectivity towards $Se^0_{(s)}$ vs. $H_2Se_{(g)}$: (i) $Se^0_{(s)}$ is produced through direct reduction of selenate by TiO_2 conduction band electrons and (ii) H_2Se gas is produced by electrons transferred to Se^0 and reduction of Se^0 to H_2Se or through a direct reduction by $CO_2^{\bullet -}$. Finally, the tunable nature of selenate reduction allows for control of the final Se reduction product and suggests the possibility of producing recoverable Se by-products from photocatalytic treatment processes.

Finally, in Chapter 6, the tunability of Se reduction products was also shown to be controllable through a materials engineering approach. Heterogenous nanoscale photocatalysts were synthesized by depositing noble metal nanoparticles (Au, Ag, Pt and Pd) onto TiO_2, which demonstrated work-function dependent bimodal selectivity of final products during the photocatalytic reduction of selenate to Se^0 or H_2Se. The Se-noble metal-TiO_2 (Se-NM-TiO_2) photocatalytic system is structured in a direct Z-scheme arrangement, when Au, Ag or Pt are used, allowing for high selectivity towards H_2Se. In contrast, Pd acted as an electron sink which decreased the reducibility of the photogenerated electrons, ultimately causing a higher selectivity towards Se^0. Au-TiO_2 offers the highest H_2Se selectivity of all catalysts tested, while Pd-TiO_2 (highest work function) offers the highest selectivity for solid Se^0.

7.2 Research perspectives

7.2.1 Future Se analytical approaches and suggested modifications

Analytical work involving Se has proven to be a very challenging task. In addition to the identification of Se species in aqueous samples, measurement of Se species in solid and gaseous phase presents its own array of unique analytical challenges. Commonly, digestion and sample preparation protocols must be followed in order to dissolve solid or gaseous Se in order to analyse with well-established ICP or IC analytical techniques. However, during the digestion or extraction phase the state of Se is altered from its original form and some Se may be lost during the sample processing. The very fact that Se is a redox-sensitive element allows treatment techniques to remove it from the water source by reducing its oxidation state. However, this sensitivity adds to the challenges of Se analysis when Se can exist in all three states of matter. The following are two new analytical approaches that should be considered when better trying to understand the process:

1. Thoroughly identify and characterize the immobilized Se reduction product. To date, this has been determined indirectly by the difference between total Se concentration (unfiltered and acid digested) and dissolved Se concentration (filtered and acid digested) which enables an indirect measurement of the amount of Se that is on the catalyst at the time of sampling. This has been assumed to be solid elemental Se (Se^0) deposited on the catalyst as a result of visual observations (the catalyst turns a bright orange colour as a result of element Se deposition) and reports from the literature. Many researchers performing photocatalytic reduction of selenate over TiO_2 have identified this as solid elemental Se as well (Kikuchi and Sakamoto, 2000; Nguyen et al., 2005a; Tan et al., 2002; T.T.Y. Tan et al., 2003a). Se K-edge X-ray absorption near edge structure (XANES) spectra can characterize valence states of immobilized Se throughout the treatment. In order to properly directly identify the immobilized Se on the surface of the catalyst to confirm the presence of Se^0, XANES should be completed to differentiate deposited Se^0 and Se(-II) as well as adsorbed Se(IV) and Se(VI) species (Shan et al., 2018).
2. Thoroughly identify and characterize the gaseous Se reduction product. To date, gaseous Se was determined by the difference of total Se concentration in the initial water sample and the total Se concentration after treatment. Again, this is an indirect measurement of Se lost through the gaseous phase during the reaction. The reactor is purged with N_2 gas

to remove any volatile species during the reaction and the exiting gas is bubbled through a series of chemical scrubbers designed to react with the gaseous Se reduction products. The gaseous Se has been assumed to be H_2Se as a result of (1) the recovery of CuSe from the $CuSO_4$ scrubber and (2) from thermodynamic reduction potentials of Se (Kikuchi and Sakamoto, 2000). The formation of CuSe in the $CuSO_4$ scrubber is more evident when simple DI systems are treated, but less clear in industrially sourced wastewater. The reason for this deviation could be due to other gaseous species being generated in the complex wastewater that is inhibiting the precipitation reaction between Se(-II) and Cu(II). The direct analysis of gas phase Se species should be done through the use of a cold trap prior to a full speciation of Se by anion exchange chromatography with inductively coupled plasma dynamic reaction cell mass spectrometry (AEC-ICP-DRC-MS) and electrospray tandem mass spectroscopy (ES-MS/MS) (LeBlanc et al., 2016; LeBlanc and Wallschläger, 2016).

7.2.2 Future catalyst design perspectives

In Chapters 2 through 5, the great potential for effective selenate removal through photocatalytic reduction with a common photocatalyst (Degussa P25 TiO_2) was highlighted. nanoparticles. In Chapter 6 & 7, some examples of engineered materials which can optimize the selenate photocatalytic processes were examined either to tune the selectivity of the Se reduction by-product or to enhance the recyclability of the catalyst. These are only a few modification and material design solutions towards engineering a better photocatalytic material. Numerous approaches exist to enhance photocatalytic activity by improving adsorption and reduction kinetics from a materials design approach. The following are promising material design approaches that should be investigated towards designing a better selenate reducing photocatalyst:

1. Designing a composite nanomaterial structured material capable of enhancing adsorption of selenate and increasing the concentration of selenate in the active area around the photocatalyst with graphene. The Langmuir-Hinshelwood analysis in Chapter 2 revealed that adsorption of selenate onto the TiO_2 surface may be rate limiting. Graphene support structures, containing immobilized TiO_2 have been shown to increase adsorption properties and electron conduction and hence increase e^-- h^+ separation (Chen et al., 2018; Hafeez et al., 2018; Trapalis et al., 2016; Fu et al., 2014). Reduced graphene oxide (rGO)

is commonly used as the graphene source for photocatalytic materials. The main challenge with rGO is its hydrophobic nature leading to instability and a tendency for aggregation of the composite material. Strategies to improve the stability and dispersibility of a rGO-TiO_2 have been developed (Bhanvase et al., 2017; Zhang et al., 2017) and should be attempted to improve selenate adsorption and reduction.

2. Designing a composite nanomaterial material which incorporates Al-substituted ferrihydrite or basaluminite could enhance adsorption of selenate and increase the concentration of selenate in the active area of the photocatalyst as well. Al-substituted ferrihydrite has been shown to increase the number of inner-sphere complexes between selenate (Carrero et al., 2017; Johnston and Chrysochoou, 2016). Many layered double hydroxides (LDHs) have shown similar affinity for selenate inner-sphere adsorption and may allow for an increased adsorption capacity of the designed composite material (Constantino et al., 2017; Hu et al., 2017).
3. Catalyst modifications towards more effective selenate reduction through mediating photogenerated electron and electron hole mobility. Internal hole scavenging capabilities through catalyst modifications can improve the reduction potential of the catalyst without the need for an externally added hole scavenger (Du et al., 2007). This would allow for effective selenate reduction in the absence of an electron hole scavenger such as formic acid. Chen et al. carried out thermal hydrolysis of $TiCl_4$ in the presence of diethylene glycol (DEG) that resulted in an internal hole-scavenging effect in the catalyst which exhibited superior reduction of Cr(VI) (G. Chen et al., 2017).
4. Hydroxyl-modified TiO_2 has been shown to increase the zeta potential during acid-neutral treatment conditions and allow for faster photocatalytic reduction kinetics at higher pH (Li et al., 2017). This may allow for faster kinetics at near neutral treatment conditions.

7.2.3 Developing the next generation real-time Se sensing platform

Quick and accurate detection of Se in environmental samples is greatly desired. Currently, the amount of Se in water samples is determined by detection and quantification either through inductively coupled plasma (ICP), atomic absorption spectroscopy or atomic fluorescence spectroscopy. These methods are powerful and able to detect selenium at low ppb or even ppt concentrations, but the main disadvantages of these techniques include: high cost of operation, long analysis time, extensive sample preparation and requirement for advanced operator personnel.

Few existing techniques have been able to offer an on-site analysis of Se content in environmental samples. Real-time Se concentration information would be extremely valuable to water treatment system operators to adjust and optimize treatment conditions due to fluctuating influent conditions. The following is a promising Se sensing approach that should be evaluated further:

1. Gold nanoparticle (Au-NPs) based colourimetric assays are promising due to a unique phenomenon known as surface plasmon resonance (SPR). Since the colour change is sensitive to the shape, size and aggregation state of the Au-NPs, molecular events can be detected through a simple colour change visible to the naked eye. Cao et al. demonstrated that combining a hydride generating apparatus (using $NaBH_4$ as the reducing agent) with a solution of AuNPs allowed for the detection of Se(IV) with a method detection limit (MDL) of 3.9 µg/L Se (Cao et al., 2017). The H_2Se generated in the hydride generation module reacted with the AuNPs and induced aggregation, which led to a colour change of the sensor to detect Se in water samples. One main disadvantage of this technique is its inability to detect Se(VI), the more prevalent Se species in industrial wastewaters. Thus, the hydride generation module could be replaced by a photocatalytic system in order to generate H_2Se, allowing for Se(VI) detection as well. Modifications of the Au-NP detection system could improve sensitivity of the treatment system. Cao et al. used pre-synthesized Au-NPs which would aggregate and cause a colour change for Se detection. The in-situ growth of Au-NPs near H_2Se seed sites may also provide a greater detection range.

7.2.4 Path forward to full-scale industrial application

Industrial wastewater and impacted water treatment are challenging due to the diverse range of dissolved species, some of which need distinct treatment approaches to remove. The incorporation of a photocatalytic reactor into an integrated flow sheet to conduct a number of process operations is required to take an influent industrial water to a treated effluent sufficient for discharge to the environment. For example, during FGDW treatment the raw water must go through a physical-chemical solids removal pre-treatment process including lime addition, settling, pH adjustment, organo-sulfide addition, ferric chloride addition, flocculant polymer addition, settling and sand filtration, prior to the photocatalytic treatment system. This is followed by a temperature and pH adjustment, dissolved oxygen removal, catalyst and electron donor addition before entering the photocatalytic reactor. After the photocatalytic reactor, the product gas must be handled by a stripping and scrubbing column, a solid-liquid separation unit for catalyst recovery and heat recovery. The flowsheet development for this integrated treatment system will allow for an initial economic analysis of total treatment costs associated with a full-scale photocatalytic selenate reduction treatment plant. This information is crucial in designing and planning a scaling-up process. The following are recommended next steps towards developing a pilot scale reactor capable of treating industrially relevant volumes:

1. Integration of Se photocatalytic removal with biological nitrate reduction is desired. In Chapter 3 & 4, photocatalytic reduction was shown to have the unique ability to selectively remove selenate in the presence of common anions such as sulfate, bicarbonate and nitrate. This unique ability allows for the removal of selenate prior to the denitrification process. Numerous advantages to removing Se prior to biological nitrate removal exist: (1) elimination of Se contamination in the bioreactor sludge; (2) biological step can be designed for denitrification only; (3) generation of a recoverable, concentrated Se-containing residual; and (4) compatible electron donors can be used for both photocatalytic and biological processes. Investigation is needed to confirm the biological nitrate reduction process can accept the effluent from the photocatalytic reactor. Excess electron hole scavengers such as formic acid, remains in the wastewater and can be used for electron donation in the biological process, given the proper acclimation period for the microbes (Bill et al., 2009; Doudrick et al., 2012; Li et al., 2015; Nishimura et al., 1980; R. H. Gerber, 1986; Strong et al., 2011; T.T.Y. Tan et al., 2003a). Experimental investigation of the use of formic acid as an electron donor for biological nitrate reduction should be done to confirm this hypothesis.
2. Transition from batch treatment to continuous flow condition is desired to allow for scale-up. While this thesis has focused on batch treatments on a laboratory scale, the transition to a larger-scale continuous flow reactor is necessary to allow for industrially relevant flowrates (1000's of m^3/day). Reactor geometry, arrangement of lamp array, power of UV lamps, internal mixing conditions, UV transmission of treatment suspension all play complex inter-related roles in the successful treatment of selenate in a photocatalytic reactor. Ideally, the reactor will be designed for plug flow conditions to achieve optimal first-order kinetics and multiple orders of magnitude of Se reduction under continuous treatment conditions. The performance of large-scale continuous UV reactors can be

modelled using computational fluid dynamics (CFD), which has been proven in many reactor design applications to predict the performance of a reactor at scales beyond those practical to test, provided appropriate relations and kinetic data can be determined at the bench scale. Most importantly, the relationship between UV exposure surface area and treatment volume (SA/V) and the relationship between UV energy input and treatment volume (E/V) which can be tested in a modelling environment to understand more about how these critical metrics effect Se removal.

3. Se recovery from the generation of a Se reduction product is desired. The two modes of selenate reduction result in either solid Se^0 deposited on the catalyst or gaseous H_2Se generated. The different avenues of recovery of the Se depending on its form have their own advantages and disadvantages. Firstly, deposition of Se^0 onto TiO_2 catalyst leaves Se in the most inert and safe state, although the Se^0 has to be removed from the catalyst surface. Methods for thermal, chemical, photochemical and physical removal from the catalyst should be investigated to produce the most useful form of Se by-product to offset treatment costs and make Se (a valuable rare element) available for reuse. Potential industries interested in the reuse of Se could range from dietary supplements and fertilizers to electronics, photovoltaics and imaging (Yarlagadda V. Nancharaiah and Lens, 2015). Secondly, the production of gaseous H_2Se would enable an easily recyclable catalyst, free of catalyst and directly recyclable for subsequent treatment cycles. However, the production of H_2Se gas, a toxic gaseous substance, would have to be evaluated with a proper gas handling system and robust safety operating protocols.

References

Abreu, I.A., Cabelli, D.E., 2010. Superoxide dismutases-a review of the metal-associated mechanistic variations. Biochim. Biophys. Acta 1804, 263–274. https://doi.org/10.1016/j.bbapap.2009.11.005

Al-Abed, S.R., Jegadeesan, G., Scheckel, K.G., Tolaymat, T., 2008. Speciation, Characterization, and Mobility of As, Se, and Hg in Flue Gas Desulphurization Residues. Environ. Sci. Technol. 42, 1693–1698. https://doi.org/10.1021/es702479n

Ali, I., 2012. New Generation Adsorbents for Water Treatment. Chem. Rev. 112, 5073–5091. https://doi.org/10.1021/cr300133d

Aman, N., Mishra, T., Hait, J., Jana, R.K., 2011. Simultaneous photoreductive removal of copper (II) and selenium (IV) under visible light over spherical binary oxide photocatalyst. Journal of Hazardous Materials 186, 360–366. https://doi.org/10.1016/j.jhazmat.2010.11.001

Anderson, J.A., 2012. Simultaneous photocatalytic degradation of nitrate and oxalic acid over gold promoted titania. Catalysis Today, Frigyes Solymosi's special issue Planar Model System and Heterogeneous Catalysis 181, 171–176. https://doi.org/10.1016/j.cattod.2011.05.027

Anderson, J.A., 2011. Photocatalytic nitrate reduction over Au/TiO2. Catalysis Today, The 6th International Conference on Environmental Catalysis (6th ICEC) Beijing, China, September 12-15, 2010 175, 316–321. https://doi.org/10.1016/j.cattod.2011.04.009

Arakawa, H., Sayama, K., 2000. Solar hydrogen production. Significant effect of Na2CO3 addition on water splitting using simple oxide semiconductor photocatalysts. Catalysis Surveys from Asia 4, 75–80. https://doi.org/10.1023/A:1019096323694

Argyle, M.D., Bartholomew, C.H., 2015. Heterogeneous Catalyst Deactivation and Regeneration: A Review. Catalysts 5, 145–269. https://doi.org/10.3390/catal5010145

Asghar, A., Abdul Raman, A.A., Wan Daud, W.M.A., 2015. Advanced oxidation processes for in-situ production of hydrogen peroxide/hydroxyl radical for textile wastewater treatment: a review. Journal of Cleaner Production 87, 826–838. https://doi.org/10.1016/j.jclepro.2014.09.010

Awual, M.R., Hasan, M.M., Khaleque, M.A., 2015a. Efficient selenium(IV) detection and removal from water by tailor-made novel conjugate adsorbent. Sensors and Actuators B: Chemical 209, 194–202. https://doi.org/10.1016/j.snb.2014.11.010

Awual, M.R., Yaita, T., Suzuki, S., Shiwaku, H., 2015b. Ultimate selenium(IV) monitoring and removal from water using a new class of organic ligand based composite adsorbent. Journal of Hazardous Materials 291, 111–119. https://doi.org/10.1016/j.jhazmat.2015.02.066

Awual, R., Hasan, M., Ihara, T., Yaita, T., 2014. Mesoporous silica based novel conjugate adsorbent for efficient selenium(IV) detection and removal from water. Microporous and Mesoporous Materials 197, 331–338. https://doi.org/10.1016/j.micromeso.2014.07.005

Baga, A.N., Johnson, G.R.A., Nazhat, N.B., Saadalla-Nazhat, R.A., 1988. A simple spectrophotometric determination of hydrogen peroxide at low concentrations in aqueous solution. Analytica Chimica Acta 204, 349–353. https://doi.org/10.1016/S0003-2670(00)86374-6

Bakather, O.Y., Atieh, M.A., 2015. Titanium-impregnated carbon nanotubes for selenium removal. US Pat., US20150136703 A1.

Balistrieri, L.S., Chao, T.T., 1990. Adsorption of selenium by amorphous iron oxyhydroxide and manganese dioxide. Geochimica et Cosmochimica Acta 54, 739–751. https://doi.org/10.1016/0016-7037(90)90369-V

Barcarella, A.L., Grunwald, E., Marshall, H.P., Purlee, E.L., 1955. The Potentiometric measurement of acid dissociation constants and pH in the system methanol-water. pKa values for carboxylic acids and anilinium ions. J. Org. Chem. 20, 747–762. https://doi.org/10.1021/jo01124a007

Bard, A.J., Stratmann, M., Licht, S., 2002. Encyclopedia of electrochemistry. Vol. 6. Semiconductor electrodes and photoelectrochemistry. Germany.

Benkhedir, M.L., Aida, M.S., Adriaenssens, G.J., 2004. Defect levels in the band gap of amorphous selenium. Journal of Non-Crystalline Solids 344, 193–198. https://doi.org/10.1016/j.jnoncrysol.2004.08.062

Bhanvase, B.A., Shende, T.P., Sonawane, S.H., 2017. A review on graphene–TiO2 and doped graphene–TiO2 nanocomposite photocatalyst for water and wastewater treatment. Environmental Technology Reviews 6, 1–14. https://doi.org/10.1080/21622515.2016.1264489

Bill, K.A., Bott, C.B., Murthy, S.N., 2009. Evaluation of alternative electron donors for denitrifying moving bed biofilm reactors (MBBRs). Water Sci. Technol. 60, 2647–2657. https://doi.org/10.2166/wst.2009.622

Bleiman, N., Mishael, Y.G., 2010. Selenium removal from drinking water by adsorption to chitosan–clay composites and oxides: Batch and columns tests. Journal of Hazardous Materials 183, 590–595. https://doi.org/10.1016/j.jhazmat.2010.07.065

Bowman, W.D., Demas, J.N., 1976. Ferrioxalate actinometry. A warning on its correct use. J. Phys. Chem. 80, 2434–2435. https://doi.org/10.1021/j100562a025

Burau, R.G., 1985. Environmental chemistry of selenium. Calif. Agr. 39, 16–18.

Cao, G., Xu, F., Wang, S., Xu, K., Hou, X., Wu, P., 2017. Gold Nanoparticle-Based Colorimetric Assay for Selenium Detection via Hydride Generation. Anal. Chem. 89, 4695–4700. https://doi.org/10.1021/acs.analchem.7b00337

Carrero, S., Fernandez-Martinez, A., Pérez-López, R., Poulain, A., Salas-Colera, E., Nieto, J.M., 2017. Arsenate and Selenate Scavenging by Basaluminite: Insights into the Reactivity of Aluminum Phases in Acid Mine Drainage. Environ. Sci. Technol. 51, 28–37. https://doi.org/10.1021/acs.est.6b03315

Catal, T., Bermek, H., Liu, H., 2009. Removal of selenite from wastewater using microbial fuel cells. Biotechnol Lett 31, 1211–1216. https://doi.org/10.1007/s10529-009-9990-8

Celis, R., Adelino, M.A., Hermosín, M.C., Cornejo, J., 2012. Montmorillonite–chitosan bionanocomposites as adsorbents of the herbicide clopyralid in aqueous solution and soil/water suspensions. Journal of Hazardous Materials 209–210, 67–76. https://doi.org/10.1016/j.jhazmat.2011.12.074

Chan, S.C., Barteau, M.A., 2005. Preparation of Highly Uniform Ag/TiO2 and Au/TiO2 Supported Nanoparticle Catalysts by Photodeposition. Langmuir 21, 5588–5595. https://doi.org/10.1021/la046887k

Chan, Y.T., Kuan, W.H., Chen, T.Y., Wang, M.K., 2009. Adsorption mechanism of selenate and selenite on the binary oxide systems. Water Res. 43, 4412–4420. https://doi.org/10.1016/j.watres.2009.06.056

Chen, G., Feng, J., Wang, W., Yin, Y., Liu, H., 2017. Photocatalytic removal of hexavalent chromium by newly designed and highly reductive TiO2 nanocrystals. Water Research 108, 383–390. https://doi.org/10.1016/j.watres.2016.11.013

Chen, J., Rogers, S.C., Kavdia, M., 2013. Analysis of kinetics of dihydroethidium fluorescence with superoxide using xanthine oxidase and hypoxanthine assay. Ann Biomed Eng 41, 327–337. https://doi.org/10.1007/s10439-012-0653-x

Chen, J.-W., Yuan, B., Shi, J.-W., Yang, J.-C.E., Fu, M.-L., 2018. Reduced graphene oxide and titania nanosheet cowrapped coal fly ash microspheres alternately as a novel photocatalyst for water treatment. Catalysis Today, Graphitic materials in photo(electro)catalysis 315, 247–254. https://doi.org/10.1016/j.cattod.2018.02.044

Chen, M.-L., An, M.-I., 2012. Selenium adsorption and speciation with Mg–FeCO3 layered double hydroxides loaded cellulose fibre. Talanta 95, 31–35. https://doi.org/10.1016/j.talanta.2012.03.038

Chen, Y., Wang, Y., Li, W., Yang, Q., Hou, Q., Wei, L., Liu, L., Huang, F., Ju, M., 2017. Enhancement of photocatalytic performance with the use of noble-metal-decorated TiO2 nanocrystals as highly active catalysts for aerobic oxidation under visible-light irradiation. Applied Catalysis B: Environmental 210, 352–367. https://doi.org/10.1016/j.apcatb.2017.03.077

Choi, J., Lee, H., Choi, Y., Kim, S., Lee, Seokheon, Lee, Seunghak, Choi, W., Lee, J., 2014. Heterogeneous photocatalytic treatment of pharmaceutical micropollutants: Effects of wastewater effluent matrix and catalyst modifications. Applied Catalysis B: Environmental 147, 8–16. https://doi.org/10.1016/j.apcatb.2013.08.032

Choi, Y., Koo, M.S., Bokare, A.D., Kim, D., Bahnemann, D.W., Choi, W., 2017. Sequential Process Combination of Photocatalytic Oxidation and Dark Reduction for the Removal of Organic Pollutants and Cr(VI) using Ag/TiO2. Environ. Sci. Technol. 51, 3973–3981. https://doi.org/10.1021/acs.est.6b06303

Christensen, B.T., Bertelsen, F., Gissel-Nielsen, G., 1989. Selenite fixation by soil particle-size separates. Journal of Soil Science 40, 641–647. https://doi.org/10.1111/j.1365-2389.1989.tb01305.x

Chubar, N., 2014. EXAFS and FTIR studies of selenite and selenate sorption by alkoxide-free sol–gel generated Mg–Al–CO3 layered double hydroxide with very labile interlayer anions. J. Mater. Chem. A 2, 15995–16007. https://doi.org/10.1039/C4TA03463E

Chubar, N., Gerda, V., Megantari, O., Mičušík, M., Omastova, M., Heister, K., Man, P., Fraissard, J., 2013. Applications versus properties of Mg–Al layered double hydroxides provided by their syntheses methods: Alkoxide and alkoxide-free sol–gel syntheses and hydrothermal precipitation. Chemical Engineering Journal 234, 284–299. https://doi.org/10.1016/j.cej.2013.08.097

Conde, J.E., Sanz Alaejos, M., 1997. Selenium Concentrations in Natural and Environmental Waters. Chem. Rev. 97, 1979–2004. https://doi.org/10.1021/cr960100g

Constantino, L.V., Quirino, J.N., Monteiro, A.M., Abrão, T., Parreira, P.S., Urbano, A., Santos, M.J., 2017. Sorption-desorption of selenite and selenate on Mg-Al layered double hydroxide in competition with nitrate, sulfate and phosphate. Chemosphere 181, 627–634. https://doi.org/10.1016/j.chemosphere.2017.04.071

Cordoba, P., Staicu, L.C., 2018. Flue gas desulfurization effluents: An unexploited selenium resource. Fuel 223, 268–276. https://doi.org/10.1016/j.fuel.2018.03.052

Curtin, M.A., Taub, I.A., Kustin, K., Sao, N., Duvall, J.R., Davies, K.I., Doona, C.J., Ross, E.W., 2004. Ascorbate-induced oxidation of formate by peroxodisulfate: product yields, kinetics and mechanism. Research on Chemical Intermediates 30, 647–661. https://doi.org/10.1163/1568567041570384

Dalven, R., 1990. Chapter 2: The semiconductor p–n junction. Introduction to applied solid state physics. Plenum Press, New York and London, pp. 27–80.

Das, J., Das, D., Dash, G.P., Parida, K.M., 2002. Studies on Mg/Fe Hydrotalcite-Like-Compound (HTlc): I. Removal of Inorganic Selenite (SeO32−) from Aqueous Medium. Journal of Colloid and Interface Science 251, 26–32. https://doi.org/10.1006/jcis.2002.8319

Das, J., Sairam Patra, B., Baliarsingh, N., Parida, K.M., 2007. Calcined Mg–Fe–CO3 LDH as an adsorbent for the removal of selenite. Journal of Colloid and Interface Science 316, 216–223. https://doi.org/10.1016/j.jcis.2007.07.082

Dean, J.A., 1985. Lange's Handbook of Chemistry, 13th edition. ed. McGraw-Hill Book Co., New York, NY.

Degabriel, T., Colaço, E., Domingos, R.F., Kirat, K.E., Brouri, D., Casale, S., Landoulsi, J., Spadavecchia, J., 2018. Factors impacting the aggregation/agglomeration and photocatalytic activity of highly crystalline spheroid- and rod-shaped TiO2 nanoparticles in aqueous solutions. Phys. Chem. Chem. Phys. 20, 12898–12907. https://doi.org/10.1039/C7CP08054A

Di Valentin, C., Fittipaldi, D., 2013. Hole Scavenging by Organic Adsorbates on the TiO2 Surface: A DFT Model Study. J. Phys. Chem. Lett. 4, 1901–1906. https://doi.org/10.1021/jz400624w

Doudrick, K., Monzon, O., Mangonon, A., Hristovski, K., Westerhoff, P., 2012. Nitrate Reduction in Water Using Commercial Titanium Dioxide Photocatalysts (P25, P90, and Hombikat UV100). Journal of Environmental Engineering 138, 852–861. https://doi.org/10.1061/(ASCE)EE.1943-7870.0000529

Doudrick, K., Yang, T., Hristovski, K., Westerhoff, P., 2013. Photocatalytic nitrate reduction in water: Managing the hole scavenger and reaction by-product selectivity. Applied Catalysis B: Environmental 136, 40–47. https://doi.org/10.1016/j.apcatb.2013.01.042

D. Scanlon, M., Peljo, P., A. Méndez, M., Smirnov, E., H. Girault, H., 2015. Charging and discharging at the nanoscale: Fermi level equilibration of metallic nanoparticles. Chemical Science 6, 2705–2720. https://doi.org/10.1039/C5SC00461F

Du, M.-H., Feng, J., Zhang, S.B., 2007. Photo-oxidation of polyhydroxyl molecules on TiO2 surfaces: from hole scavenging to light-induced self-assembly of TiO2-cyclodextrin wires. Phys. Rev. Lett. 98, 066102. https://doi.org/10.1103/PhysRevLett.98.066102

Dweydari, A.W., Mee, C.H.B., 1975. Work function measurements on (100) and (110) surfaces of silver. phys. stat. sol. (a) 27, 223–230. https://doi.org/10.1002/pssa.2210270126

Eastman, D.E., 1970. Photoelectric Work Functions of Transition, Rare-Earth, and Noble Metals. Phys. Rev. B 2, 1–2. https://doi.org/10.1103/PhysRevB.2.1

El-Ramady, H., Abdalla, N., Alshaal, T., Domokos-Szabolcsy, É., Elhawat, N., Prokisch, J., Sztrik, A., Fári, M., El-Marsafawy, S., Shams, M.S., 2015. Selenium in soils under climate change, implication for human health. Environ Chem Lett 13, 1–19. https://doi.org/10.1007/s10311-014-0480-4

Ervens, B., Gligorovski, S., Herrmann, H., 2003. Temperature-dependent rate constants for hydroxyl radical reactions with organic compounds in aqueous solutions. Physical Chemistry Chemical Physics 5, 1811–1824. https://doi.org/10.1039/B300072A

Espinosa-Ortiz, E.J., Gonzalez-Gil, G., Saikaly, P.E., van Hullebusch, E.D., Lens, P.N.L., 2015. Effects of selenium oxyanions on the white-rot fungus Phanerochaete chrysosporium. Appl. Microbiol. Biotechnol. 99, 2405–2418. https://doi.org/10.1007/s00253-014-6127-3

Fan, J., Wang, R., Hu, H., Huo, G., Fu, Q., Zhu, J., 2015. Transformation and Bioavailability of Selenate and Selenite Added to a Nicotiana tabacum L. Planting Soil. Communications in Soil Science and Plant Analysis 46, 1362–1375. https://doi.org/10.1080/00103624.2015.1033544

Fink, B., Laude, K., McCann, L., Doughan, A., Harrison, D.G., Dikalov, S., 2004. Detection of intracellular superoxide formation in endothelial cells and intact tissues using dihydroethidium and an HPLC-based assay. Am. J. Physiol., Cell Physiol. 287, C895-902. https://doi.org/10.1152/ajpcell.00028.2004

Fordyce, F.M., 2013. Selenium Deficiency and Toxicity in the Environment, in: Selinus, O. (Ed.), Essentials of Medical Geology: Revised Edition. Springer Netherlands, Dordrecht, pp. 375–416. https://doi.org/10.1007/978-94-007-4375-5_16

Fotiou, T., Triantis, T.M., Kaloudis, T., Hiskia, A., 2015. Evaluation of the photocatalytic activity of TiO2 based catalysts for the degradation and mineralization of cyanobacterial toxins and water off-odor compounds under UV-A, solar and visible light. Chemical Engineering Journal, Photocatalysis for disinfection and removal of contaminants of emerging concern 261, 17–26. https://doi.org/10.1016/j.cej.2014.03.095

Frankenberger Jr., W.T., Amrhein, C., Fan, T.W.M., Flaschi, D., Glater, J., Jr, E.K., Kovac, K., Lee, E., Ohlendorf, H.M., Owens, L., Terry, N., Toto, A., 2004. Advanced Treatment Technologies in the Remediation of Seleniferous Drainage Waters and Sediments. Irrigation and Drainage Systems 18, 19–42. https://doi.org/10.1023/B:IRRI.0000019422.68706.59

Fu, J., Zhang, X., Qian, S., Zhang, L., 2012. Preconcentration and speciation of ultra-trace Se (IV) and Se (VI) in environmental water samples with nano-sized TiO2 colloid and determination by HG-AFS. Talanta 94, 167–171. https://doi.org/10.1016/j.talanta.2012.03.012

Fu, Y., Wang, J., Liu, Q., Zeng, H., 2014. Water-dispersible magnetic nanoparticle–graphene oxide composites for selenium removal. Carbon 77, 710–721. https://doi.org/10.1016/j.carbon.2014.05.076

Gao, S., Tanji, K.K., Peters, D.W., Herbel, M.J., 2000. Water selenium speciation and sediment fractionation in a California flow-through wetland system. J. Environ. Qual. 29, 1275–1283.

Ghosh-Mukerji, S., Haick, H., Paz, Y., 2003. Controlled mass transport as a means for obtaining selective photocatalysis. Journal of Photochemistry and Photobiology A: Chemistry, Proceedings of the Catalysis Research Center International Symposium on Photochemistry at interfaces, held at Hokkaido University, Sapporo, Japan, 9-11 August 2002. 160, 77–85. https://doi.org/10.1016/S1010-6030(03)00224-7

Giam, X., Olden, J.D., Simberloff, D., 2018. Impact of coal mining on stream biodiversity in the US and its regulatory implications. Nature Sustainability 1, 176. https://doi.org/10.1038/s41893-018-0048-6

Giannakas, A.E., Antonopoulou, M., Papavasiliou, J., Deligiannakis, Y., Konstantinou, I., 2017. Photocatalytic performance of Pt-TiO2, Pt-N-TiO2 and Pt-N/F-TiO2 towards simultaneous Cr(VI) reduction/benzoic acid oxidation: Insights into photogenerated charge carrier dynamics and catalyst properties. Journal of Photochemistry and Photobiology A: Chemistry 349, 25–35. https://doi.org/10.1016/j.jphotochem.2017.08.066

Gissel-Nielsen, G., Gupta, U.C., Lamand, M., Westermarck, T., 1984. Selenium in soils and plants and its importance in livestock and human nutrition. Adv. Agron. 37, 397–460.

Goh, K.-H., Lim, T.-T., Dong, Z., 2008. Application of layered double hydroxides for removal of oxyanions: A review. Water Research 42, 1343–1368. https://doi.org/10.1016/j.watres.2007.10.043

Gong, X.-Q., Selloni, A., Vittadini, A., 2006. Density Functional Theory Study of Formic Acid Adsorption on Anatase TiO2(001): Geometries, Energetics, and Effects of Coverage, Hydration, and Reconstruction. J. Phys. Chem. B 110, 2804–2811. https://doi.org/10.1021/jp056572t

Gonzalez, C.M., Hernandez, J., Parsons, J.G., Gardea-Torresdey, J.L., 2011. Adsorption of Selenite and Selenate by a High- and Low-Pressure Aged Manganese Oxide Nanomaterial. Instrumentation Science & Technology 39, 1–19. https://doi.org/10.1080/10739149.2010.537721

Gonzalez, C.M., Hernandez, J., Parsons, J.G., Gardea-Torresdey, J.L., 2010. A study of the removal of selenite and selenate from aqueous solutions using a magnetic iron/manganese oxide nanomaterial and ICP-MS. Microchemical Journal, Polar Chemistry 96, 324–329. https://doi.org/10.1016/j.microc.2010.05.005

Gonzalez, C.M., Hernandez, J., Peralta-Videa, J.R., Botez, C.E., Parsons, J.G., Gardea-Torresdey, J.L., 2012. Sorption kinetic study of selenite and selenate onto a high and low pressure aged iron oxide nanomaterial. Journal of Hazardous Materials, Nanotechnologies for the Treatment of Water, Air and Soil 211–212, 138–145. https://doi.org/10.1016/j.jhazmat.2011.08.023

Gui, M., Papp, J.K., Colburn, A.S., Meeks, N.D., Weaver, B., Wilf, I., Bhattacharyya, D., 2015. Engineered iron/iron oxide functionalized membranes for selenium and other toxic metal removal from power plant scrubber water. Journal of Membrane Science 488, 79–91. https://doi.org/10.1016/j.memsci.2015.03.089

Hafeez, H.Y., Lakhera, S.K., Karthik, P., Anpo, M., Neppolian, B., 2018. Facile construction of ternary CuFe2O4-TiO2 nanocomposite supported reduced graphene oxide (rGO) photocatalysts for the efficient hydrogen production. Applied Surface Science, 4th International Conference on Nanoscience and Nanotechnology 449, 772–779. https://doi.org/10.1016/j.apsusc.2018.01.282

Hageman, S.P.W., van der Weijden, R.D., Stams, A.J.M., van Cappellen, P., Buisman, C.J.N., 2017. Microbial selenium sulfide reduction for selenium recovery from wastewater. Journal of Hazardous Materials 329, 110–119. https://doi.org/10.1016/j.jhazmat.2016.12.061

Hamilton, S.J., 2004. Review of selenium toxicity in the aquatic food chain. Science of The Total Environment 326, 1–31. https://doi.org/10.1016/j.scitotenv.2004.01.019

Hatchard, C.G., Parker, C.A., 1956. A New Sensitive Chemical Actinometer. II. Potassium Ferrioxalate as a Standard Chemical Actinometer. Proceedings of the Royal Society of London. Series A, Mathematical and Physical Sciences 235, 518–536.

Hayyan, M., Hashim, M.A., AlNashef, I.M., 2016. Superoxide Ion: Generation and Chemical Implications. Chem. Rev. 116, 3029–3085. https://doi.org/10.1021/acs.chemrev.5b00407

Hérissan, A., Meichtry, J.M., Remita, H., Colbeau-Justin, C., Litter, M.I., 2017. Reduction of nitrate by heterogeneous photocatalysis over pure and radiolytically modified TiO2 samples in the presence of formic acid. Catalysis Today, Heterogeneous Photocatalyis from fundamentals to possible applications 281, 101–108. https://doi.org/10.1016/j.cattod.2016.05.044

Hernández-Ramírez, E., Wang, J.A., Chen, L.F., Valenzuela, M.A., Dalai, A.K., 2017. Partial oxidation of methanol catalyzed with Au/TiO2, Au/ZrO2 and Au/ZrO2-TiO2 catalysts. Applied Surface Science 399, 77–85. https://doi.org/10.1016/j.apsusc.2016.12.068

Higgins, T.E., Sandy, A.T., Givens, S.W., 2009. Flue Gas Desulfurization Wastewater Treatment Primer. Power (New York) 153.

Holmes, A.B., Gu, F.X., 2016. Emerging nanomaterials for the application of selenium removal for wastewater treatment. Environ. Sci.: Nano 3, 982–996. https://doi.org/10.1039/C6EN00144K

Hopkins, R.L., Altier, B.M., Haselman, D., Merry, A.D., White, J.J., 2013. Exploring the legacy effects of surface coal mining on stream chemistry. Hydrobiologia 713, 87–95. https://doi.org/10.1007/s10750-013-1494-9

Horányi, G., 2003. Investigation of the specific adsorption of sulfate ions on powdered TiO2. J Colloid Interface Sci 261, 580–583. https://doi.org/10.1016/S0021-9797(03)00084-5

Hotze, E.M., Phenrat, T., Lowry, G.V., 2010. Nanoparticle aggregation: challenges to understanding transport and reactivity in the environment. J. Environ. Qual. 39, 1909–1924.

Hu, B., Ye, F., Jin, C., Ma, X., Huang, C., Sheng, G., Ma, J., Wang, X., Huang, Y., 2017. The enhancement roles of layered double hydroxide on the reductive immobilization of selenate by nanoscale zero valent iron: Macroscopic and microscopic approaches. Chemosphere 184, 408–416. https://doi.org/10.1016/j.chemosphere.2017.05.179

Hu, C., Chen, Q., Chen, G., Liu, H., Qu, J., 2015. Removal of Se(IV) and Se(VI) from drinking water by coagulation. Separation and Purification Technology 142, 65–70. https://doi.org/10.1016/j.seppur.2014.12.028

Hu, Q., Liu, B., Zhang, Z., Song, M., Zhao, X., 2010. Temperature effect on the photocatalytic degradation of methyl orange under UV-vis light irradiation. J. Wuhan Univ. Technol.-Mat. Sci. Edit. 25, 210–213. https://doi.org/10.1007/s11595-010-2210-5

Huang, Y.H., Peddi, P.K., Tang, C., Zeng, H., Teng, X., 2013. Hybrid zero-valent iron process for removing heavy metals and nitrate from flue-gas-desulfurization wastewater. Separation and Purification Technology 118, 690–698. https://doi.org/10.1016/j.seppur.2013.07.009

Husen, A., Siddiqi, K.S., 2014. Plants and microbes assisted selenium nanoparticles: characterization and application. Journal of Nanobiotechnology 12, 28. https://doi.org/10.1186/s12951-014-0028-6

Ippolito, J.A., Scheckel, K.G., Barbarick, K.A., 2009. Selenium adsorption to aluminum-based water treatment residuals. J Colloid Interface Sci 338, 48–55. https://doi.org/10.1016/j.jcis.2009.06.023

Jain, R., Jordan, N., Weiss, S., Foerstendorf, H., Heim, K., Kacker, R., Hübner, R., Kramer, H., van Hullebusch, E.D., Farges, F., Lens, P.N.L., 2015. Extracellular Polymeric Substances

Govern the Surface Charge of Biogenic Elemental Selenium Nanoparticles. Environ. Sci. Technol. 49, 1713–1720. https://doi.org/10.1021/es5043063

Jakob, M., Levanon, H., Kamat, P.V., 2003. Charge Distribution between UV-Irradiated TiO2 and Gold Nanoparticles: Determination of Shift in the Fermi Level. Nano Lett. 3, 353–358. https://doi.org/10.1021/nl0340071

Jia, Y., Ye, L., Kang, X., You, H., Wang, S., Yao, J., 2016. Photoelectrocatalytic reduction of perchlorate in aqueous solutions over Ag doped TiO2 nanotube arrays. Journal of Photochemistry and Photobiology A: Chemistry 328, 225–232. https://doi.org/10.1016/j.jphotochem.2016.05.023

Jiang, J., Oberdörster, G., Biswas, P., 2008. Characterization of size, surface charge, and agglomeration state of nanoparticle dispersions for toxicological studies. J Nanopart Res 11, 77–89. https://doi.org/10.1007/s11051-008-9446-4

Johnston, C.P., Chrysochoou, M., 2016. Mechanisms of Chromate, Selenate, and Sulfate Adsorption on Al-Substituted Ferrihydrite: Implications for Ferrihydrite Surface Structure and Reactivity. Environ. Sci. Technol. 50, 3589–3596. https://doi.org/10.1021/acs.est.5b05529

Jordan, N., Foerstendorf, H., Weiß, S., Heim, K., Schild, D., Brendler, V., 2011. Sorption of selenium(VI) onto anatase: Macroscopic and microscopic characterization. Geochimica et Cosmochimica Acta 75, 1519–1530. https://doi.org/10.1016/j.gca.2011.01.012

Jordan, N., Ritter, A., Foerstendorf, H., Scheinost, A.C., Weiß, S., Heim, K., Grenzer, J., Mücklich, A., Reuther, H., 2013. Adsorption mechanism of selenium(VI) onto maghemite. Geochimica et Cosmochimica Acta 103, 63–75. https://doi.org/10.1016/j.gca.2012.09.048

Kagami, T., Narita, T., Kuroda, M., Notaguchi, E., Yamashita, M., Sei, K., Soda, S., Ike, M., 2013. Effective selenium volatilization under aerobic conditions and recovery from the aqueous phase by Pseudomonas stutzeri NT-I. Water Research 47, 1361–1368. https://doi.org/10.1016/j.watres.2012.12.001

Kai, T., Zhou, M., Johnson, S., Ahn, H.S., Bard, A.J., 2018. Direct Observation of C2O4•– and CO2•– by Oxidation of Oxalate within Nanogap of Scanning Electrochemical Microscope. J. Am. Chem. Soc. 140, 16178–16183. https://doi.org/10.1021/jacs.8b08900

Kameda, T., Kondo, E., Yoshioka, T., 2015. Equilibrium and kinetics studies on As(V) and Sb(V) removal by Fe2+-doped Mg–Al layered double hydroxides. Journal of Environmental Management 151, 303–309. https://doi.org/10.1016/j.jenvman.2014.12.050

Kameda, T., Kondo, E., Yoshioka, T., 2014. Preparation of Mg–Al layered double hydroxide doped with Fe2+ and its application to Cr(VI) removal. Separation and Purification Technology 122, 12–16. https://doi.org/10.1016/j.seppur.2013.10.033

Kasap, S., Koughia, C., Berashevich, J., Johanson, R., Reznik, A., 2015. Charge transport in pure and stabilized amorphous selenium: re-examination of the density of states distribution in the mobility gap and the role of defects. J Mater Sci: Mater Electron 26, 4644–4658. https://doi.org/10.1007/s10854-015-3069-1

Kersten, M., Vlasova, N., 2013. The influence of temperature on selenate adsorption by goethite. Radiochimica Acta International journal for chemical aspects of nuclear science and technology 101, 413–420. https://doi.org/10.1524/ract.2013.2041

Khan, H., Berk, D., 2015. Selenium modified oxalate chelated titania: Characterization, mechanistic and photocatalytic studies. Applied Catalysis A: General 505, 285–301. https://doi.org/10.1016/j.apcata.2015.05.030

Kikuchi, E., Sakamoto, H., 2000. Kinetics of the Reduction Reaction of Selenate Ions by TiO2 Photocatalyst. J. Electrochem. Soc. 147, 4589–4593. https://doi.org/10.1149/1.1394106

Kosaka, K., Yamada, H., Matsui, S., Echigo, S., Shishida, K., 1998. Comparison among the Methods for Hydrogen Peroxide Measurements To Evaluate Advanced Oxidation Processes: Application of a Spectrophotometric Method Using Copper(II) Ion and 2,9-Dimethyl-1,10-phenanthroline. Environ. Sci. Technol. 32, 3821–3824. https://doi.org/10.1021/es9800784

Kot, A., Namiesńik, J., 2000. The role of speciation in analytical chemistry. TrAC Trends in Analytical Chemistry 19, 69–79. https://doi.org/10.1016/S0165-9936(99)00195-8

Kou, J., Lu, C., Wang, J., Chen, Y., Xu, Z., Varma, R.S., 2017. Selectivity Enhancement in Heterogeneous Photocatalytic Transformations. Chem. Rev. 117, 1445–1514. https://doi.org/10.1021/acs.chemrev.6b00396

Kumar, S.G., Rao, K.S.R.K., 2017. Comparison of modification strategies towards enhanced charge carrier separation and photocatalytic degradation activity of metal oxide semiconductors (TiO2, WO3 and ZnO). Applied Surface Science, 2nd International Symposium on Energy and Environmental Photocatalytic Materials 391, 124–148. https://doi.org/10.1016/j.apsusc.2016.07.081

Kuroda, M., Notaguchi, E., Sato, A., Yoshioka, M., Hasegawa, A., Kagami, T., Narita, T., Yamashita, M., Sei, K., Soda, S., Ike, M., 2011. Characterization of Pseudomonas stutzeri NT-I capable of removing soluble selenium from the aqueous phase under aerobic conditions. Journal of Bioscience and Bioengineering 112, 259–264. https://doi.org/10.1016/j.jbiosc.2011.05.012

Kwon, T., Tsigdinos, G.A., Pinnavaia, T.J., 1988. Pillaring of Layered Double Hydroxides (LDH's) by Polyoxometalate Anions. Chemical Society 110. https://doi.org/10.1021%2Fja00219a048

Labaran, B.A., Vohra, M.S., 2014. Photocatalytic removal of selenite and selenate species: effect of EDTA and other process variables. Environmental Technology 35, 1091–1100. https://doi.org/10.1080/09593330.2013.861857

Lai, C.-Y., Yang, X., Tang, Y., Rittmann, B.E., Zhao, H.-P., 2014. Nitrate Shaped the Selenate-Reducing Microbial Community in a Hydrogen-Based Biofilm Reactor. Environ. Sci. Technol. 48, 3395–3402. https://doi.org/10.1021/es4053939

Laurindo, F.R.M., Fernandes, D.C., Santos, C.X.C., 2008. Assessment of superoxide production and NADPH oxidase activity by HPLC analysis of dihydroethidium oxidation products. Meth. Enzymol. 441, 237–260. https://doi.org/10.1016/S0076-6879(08)01213-5

LeBlanc, K.L., Ruzicka, J., Wallschläger, D., 2016. Identification of trace levels of selenomethionine and related organic selenium species in high-ionic-strength waters. Anal Bioanal Chem 408, 1033–1042. https://doi.org/10.1007/s00216-015-9124-1

LeBlanc, K.L., Wallschläger, D., 2016. Production and Release of Selenomethionine and Related Organic Selenium Species by Microorganisms in Natural and Industrial Waters. Environ. Sci. Technol. 50, 6164–6171. https://doi.org/10.1021/acs.est.5b05315

Lei, Y., Chen, F., Luo, Y., Zhang, L., 2014. Synthesis of three-dimensional graphene oxide foam for the removal of heavy metal ions. Chemical Physics Letters 593, 122–127. https://doi.org/10.1016/j.cplett.2013.12.066

Lenz, M., Hullebusch, E.D.V., Hommes, G., Corvini, P.F.X., Lens, P.N.L., 2008. Selenate removal in methanogenic and sulfate-reducing upflow anaerobic sludge bed reactors. Water Research 42, 2184–2194. https://doi.org/10.1016/j.watres.2007.11.031

Lenz, M., Lens, P.N.L., 2009. The essential toxin: The changing perception of selenium in environmental sciences. Science of The Total Environment, Thematic Issue - BioMicroWorld Conference 407, 3620–3633. https://doi.org/10.1016/j.scitotenv.2008.07.056

Leshuk, T., B. Holmes, A., Ranatunga, D., Z. Chen, P., Jiang, Y., Gu, F., 2018. Magnetic flocculation for nanoparticle separation and catalyst recycling. Environmental Science: Nano 5, 509–519. https://doi.org/10.1039/C7EN00827A

Li, C., Cao, J., Ren, H., Li, Y., Tang, S., 2015. Comparison on kinetics and microbial community among denitrification process fed by different kinds of volatile fatty acids. Process Biochemistry 50, 447–455. https://doi.org/10.1016/j.procbio.2015.01.005

Li, Y., Bian, Y., Qin, H., Zhang, Y., Bian, Z., 2017. Photocatalytic reduction behavior of hexavalent chromium on hydroxyl modified titanium dioxide. Applied Catalysis B: Environmental 206, 293–299. https://doi.org/10.1016/j.apcatb.2017.01.044

Liang, L., Sun, W., Guan, X., Huang, Y., Choi, W., Bao, H., Li, L., Jiang, Z., 2014. Weak magnetic field significantly enhances selenite removal kinetics by zero valent iron. Water Research 49, 371–380. https://doi.org/10.1016/j.watres.2013.10.026

Lin, Z.-Q., Terry, N., 2003. Selenium Removal by Constructed Wetlands: Quantitative Importance of Biological Volatilization in the Treatment of Selenium-Laden Agricultural Drainage Water. Environ. Sci. Technol. 37, 606–615. https://doi.org/10.1021/es0260216

Ling, L., Pan, B., Zhang, W., 2015. Removal of selenium from water with nanoscale zero-valent iron: Mechanisms of intraparticle reduction of Se(IV). Water Research 71, 274–281. https://doi.org/10.1016/j.watres.2015.01.002

Liu, X., Iocozzia, J., Wang, Y., Cui, X., Chen, Y., Zhao, S., Li, Z., Lin, Z., 2017. Noble metal–metal oxide nanohybrids with tailored nanostructures for efficient solar energy conversion, photocatalysis and environmental remediation. Energy & Environmental Science 10, 402–434. https://doi.org/10.1039/C6EE02265K

Lottermoser, B., 2007. Mine Wastes: Characterization, Treatment and Environmental Impacts. Springer Science & Business Media.

Lou, Z., Fujitsuka, M., Majima, T., 2017. Two-Dimensional Au-Nanoprism/Reduced Graphene Oxide/Pt-Nanoframe as Plasmonic Photocatalysts with Multiplasmon Modes Boosting Hot Electron Transfer for Hydrogen Generation. J. Phys. Chem. Lett. 8, 844–849. https://doi.org/10.1021/acs.jpclett.6b03045

Low, J., Jiang, C., Cheng, B., Wageh, S., Al-Ghamdi, A.A., Yu, J., 2017. A Review of Direct Z-Scheme Photocatalysts. Small Methods 1, 1700080. https://doi.org/10.1002/smtd.201700080

Luek, A., Brock, C., Rowan, D.J., Rasmussen, J.B., 2014. A Simplified Anaerobic Bioreactor for the Treatment of Selenium-Laden Discharges from Non-acidic, End-Pit Lakes. Mine Water Environ 33, 295–306. https://doi.org/10.1007/s10230-014-0296-2

Luiz, D. de B., Andersen, S.L.F., Berger, C., José, H.J., Moreira, R. de F.P.M., 2012. Photocatalytic reduction of nitrate ions in water over metal-modified TiO2. Journal of Photochemistry and Photobiology A: Chemistry 246, 36–44. https://doi.org/10.1016/j.jphotochem.2012.07.011

Mal, J., Nancharaiah, Y.V., van Hullebusch, E.D., Lens, P.N.L., 2017. Biological removal of selenate and ammonium by activated sludge in a sequencing batch reactor. Bioresource Technology 229, 11–19. https://doi.org/10.1016/j.biortech.2016.12.112

Mal, J., Nancharaiah, Y.V., van Hullebusch, E.D., Lens, P.N.L., 2016. Effect of heavy metal co-contaminants on selenite bioreduction by anaerobic granular sludge. Bioresource Technology 206, 1–8. https://doi.org/10.1016/j.biortech.2016.01.064

Manning, B.A., Burau, R.G., 1995. Selenium Immobilization in Evaporation Pond Sediments by in Situ Precipitation of Ferric Oxyhydroxide. Environ. Sci. Technol. 29, 2639–2646. https://doi.org/10.1021/es00010a028

Marks, R., Yang, T., Westerhoff, P., Doudrick, K., 2016. Comparative analysis of the photocatalytic reduction of drinking water oxoanions using titanium dioxide. Water Research 104, 11–19. https://doi.org/10.1016/j.watres.2016.07.052

Marshall, W.L., Jones, E.V., 1966. Second Dissociation Constant of Sulfuric Acid from 25 to 350° Evaluated from Solubilities of Calcium Sulfate in Sulfuric Acid Solutions1,2. J. Phys. Chem. 70, 4028–4040. https://doi.org/10.1021/j100884a045

Martin, A.J., Fraser, C., Simpson, S., Belzile, N., Chen, Y.-W., London, J., Wallschläger, D., 2018. Hydrological and biogeochemical controls governing the speciation and accumulation of selenium in a wetland influenced by mine drainage. Environmental Toxicology and Chemistry 37, 1824–1838. https://doi.org/10.1002/etc.4123

Mavrov, V., Stamenov, S., Todorova, E., Chmiel, H., Erwe, T., 2006. New hybrid electrocoagulation membrane process for removing selenium from industrial wastewater. Desalination 201, 290–296. https://doi.org/10.1016/j.desal.2006.06.005

McNamee, C.E., Tsujii, Y., Matsumoto, M., 2005. Physicochemical Characterization of an Anatase TiO2 Surface and the Adsorption of a Nonionic Surfactant: An Atomic Force Microscopy Study. Langmuir 21, 11283–11288. https://doi.org/10.1021/la0517890

Meng, X., Bang, S., Korfiatis, G.P., 2002. Removal of selenocyanate from water using elemental iron. Water Research 36, 3867–3873. https://doi.org/10.1016/S0043-1354(02)00086-6

Mogal, S.I., Gandhi, V.G., Mishra, M., Tripathi, S., Shripathi, T., Joshi, P.A., Shah, D.O., 2014. Single-Step Synthesis of Silver-Doped Titanium Dioxide: Influence of Silver on Structural, Textural, and Photocatalytic Properties. Ind. Eng. Chem. Res. 53, 5749–5758. https://doi.org/10.1021/ie404230q

Mooney, F.D., Murray-Gulde, C., 2008. Constructed treatment wetlands for flue gas desulfurization waters: Full-scale design, construction issues, and performance. Environmental Geosciences 15, 131–141. https://doi.org/10.1306/eg.09200707011

Morrison, S.J., Metzler, D.R., Dwyer, B.P., 2002. Removal of As, Mn, Mo, Se, U, V and Zn from groundwater by zero-valent iron in a passive treatment cell: reaction progress modeling. Journal of Contaminant Hydrology 56, 99–116. https://doi.org/10.1016/S0169-7722(01)00205-4

Mueller, N.C., Nowack, B., 2008. Exposure Modeling of Engineered Nanoparticles in the Environment. Environ. Sci. Technol. 42, 4447–4453. https://doi.org/10.1021/es7029637

Muggli, D.S., Backes, M.J., 2002. Two Active Sites for Photocatalytic Oxidation of Formic Acid on TiO2: Effects of H2O and Temperature. Journal of Catalysis 209, 105–113. https://doi.org/10.1006/jcat.2002.3640

Myneni, S.C.B., Tokunaga, T.K., Brown, G.E., 1997. Abiotic Selenium Redox Transformations in the Presence of Fe(II,III) Oxides. Science 278, 1106–1109. https://doi.org/10.1126/science.278.5340.1106

Nakajima, T., Kamito, R., Takanashi, H., Ohki, A., 2013. Reduction of Selenate from Simulated Wet Flue Gas Desulfurization Wastewater Using Photocatalyst and Microorganism. J. of Wat. & Envir. Tech. 11, 419–427. https://doi.org/10.2965/jwet.2013.419

Nakajima, T., Yamada, K., Idehara, H., Takanashi, H., Ohki, A., 2011. Removal of Selenium (VI) from Simulated Wet Flue Gas Desulfurization Wastewater Using Photocatalytic Reduction. J. of Wat. & Envir. Tech. 9, 13–19. https://doi.org/10.2965/jwet.2011.13

Nancharaiah, Yarlagadda V., Lens, P.N.L., 2015. Selenium biomineralization for biotechnological applications. Trends in Biotechnology 33, 323–330. https://doi.org/10.1016/j.tibtech.2015.03.004

Nancharaiah, Y. V., Lens, P.N.L., 2015. Ecology and Biotechnology of Selenium-Respiring Bacteria. Microbiol. Mol. Biol. Rev. 79, 61–80. https://doi.org/10.1128/MMBR.00037-14

Nguyen, V.N.H., Amal, R., Beydoun, D., 2005a. Photocatalytic reduction of selenium ions using different TiO2 photocatalysts. Chemical Engineering Science 60, 5759–5769. https://doi.org/10.1016/j.ces.2005.04.085

Nguyen, V.N.H., Beydoun, D., Amal, R., 2005b. Photocatalytic reduction of selenite and selenate using TiO2 photocatalyst. Journal of Photochemistry and Photobiology A: Chemistry 171, 113–120. https://doi.org/10.1016/j.jphotochem.2004.09.015

Ni, M., Leung, M.K.H., Leung, D.Y.C., Sumathy, K., 2007. A review and recent developments in photocatalytic water-splitting using TiO2 for hydrogen production. Renewable and Sustainable Energy Reviews 11, 401–425. https://doi.org/10.1016/j.rser.2005.01.009

Nishimura, T., Hashimoto, H., Nakayama, M., 2007. Removal of Selenium(VI) from Aqueous Solution with Polyamine-type Weakly Basic Ion Exchange Resin. Separation Science and Technology 42, 3155–3167. https://doi.org/10.1080/01496390701513107

Nishimura, Y., Kamihara, T., Fukui, S., 1980. Diverse effects of formate on the dissimilatory metabolism of nitrate in Pseudomonas denitrificans ATCC 13867: Growth, nitrite accumulation in culture, cellular activities of nitrate and nitrite reductases. Arch. Microbiol. 124, 191–195. https://doi.org/10.1007/BF00427726

Nordstrom, D.K., Blowes, D.W., Ptacek, C.J., 2015. Hydrogeochemistry and microbiology of mine drainage: An update. Applied Geochemistry, Environmental Geochemistry of Modern Mining 57, 3–16. https://doi.org/10.1016/j.apgeochem.2015.02.008

Nosaka, Y., Nosaka, A., 2016a. Understanding Hydroxyl Radical (•OH) Generation Processes in Photocatalysis. ACS Energy Lett. 1, 356–359. https://doi.org/10.1021/acsenergylett.6b00174

Nosaka, Y., Nosaka, A.Y., 2016b. Reconsideration of Intrinsic Band Alignments within Anatase and Rutile TiO2. J. Phys. Chem. Lett. 7, 431–434. https://doi.org/10.1021/acs.jpclett.5b02804

Nowack, B., Bucheli, T.D., 2007. Occurrence, behavior and effects of nanoparticles in the environment. Environmental Pollution 150, 5–22. https://doi.org/10.1016/j.envpol.2007.06.006

Nowotny, J., Bak, T., Nowotny, M.K., Sheppard, L.R., 2006. TiO2 Surface Active Sites for Water Splitting. J. Phys. Chem. B 110, 18492–18495. https://doi.org/10.1021/jp063699p

NSMP Working Group, 2007. Identification and Assessment of Selenium and Nitrogen Treatment Technologies and Best Management Practices. NSMP Working Group.

Nu Hoai Nguyen, V., Amal, R., Beydoun, D., 2005. Photocatalytic reduction of selenium ions using different TiO2 photocatalysts. Chemical Engineering Science 60, 5759–5769. https://doi.org/10.1016/j.ces.2005.04.085

Nurlaela, E., Shinagawa, T., Qureshi, M., Dhawale, D.S., Takanabe, K., 2016. Temperature Dependence of Electrocatalytic and Photocatalytic Oxygen Evolution Reaction Rates Using NiFe Oxide. ACS Catal. 6, 1713–1722. https://doi.org/10.1021/acscatal.5b02804

Olegario, J.T., Yee, N., Miller, M., Sczepaniak, J., Manning, B., 2009. Reduction of Se(VI) to Se(-II) by zerovalent iron nanoparticle suspensions. J Nanopart Res 12, 2057–2068. https://doi.org/10.1007/s11051-009-9764-1

Oremland, R.S., Herbel, M.J., Blum, J.S., Langley, S., Beveridge, T.J., Ajayan, P.M., Sutto, T., Ellis, A.V., Curran, S., 2004. Structural and Spectral Features of Selenium Nanospheres Produced by Se-Respiring Bacteria. Appl Environ Microbiol 70, 52–60. https://doi.org/10.1128/AEM.70.1.52-60.2004

Pabby, A.K., Rizvi, S.S.H., Requena, A.M.S., 2008. Handbook of Membrane Separations: Chemical, Pharmaceutical, Food, and Biotechnological Applications. CRC Press.

Pan, Bingjun, Xiao, L., Nie, G., Pan, Bingcai, Wu, J., Lv, L., Zhang, W., Zheng, S., 2010. Adsorptive selenite removal from water using a nano-hydrated ferric oxides (HFOs)/polymer hybrid adsorbent. J Environ Monit 12, 305–310. https://doi.org/10.1039/b913827g

Papp, J., Shen, H.S., Kershaw, R., Dwight, K., Wold, A., 1993. Titanium(IV) oxide photocatalysts with palladium. Chem. Mater. 5, 284–288. https://doi.org/10.1021/cm00027a009

Papp, L.V., Lu, J., Holmgren, A., Khanna, K.K., 2007. From Selenium to Selenoproteins: Synthesis, Identity, and Their Role in Human Health. Antioxidants & Redox Signaling 9, 775–806. https://doi.org/10.1089/ars.2007.1528

Parida, K.M., Gorai, B., Das, N.N., Rao, S.B., 1997. Studies on Ferric Oxide Hydroxides: III. Adsorption of Selenite (SeO2−3) on Different Forms of Iron Oxyhydroxides. Journal of Colloid and Interface Science 185, 355–362. https://doi.org/10.1006/jcis.1996.4522

Paul, S., Ghosh, S., Barman, D., De, S.K., 2017. Maximization of photocatalytic activity of Bi2S3/TiO2/Au ternary heterostructures by proper epitaxy formation and plasmonic sensitization. Applied Catalysis B: Environmental 219, 287–300. https://doi.org/10.1016/j.apcatb.2017.07.057

Peiró, A.M., Colombo, C., Doyle, G., Nelson, J., Mills, A., Durrant, J.R., 2006. Photochemical Reduction of Oxygen Adsorbed to Nanocrystalline TiO2 Films: A Transient Absorption and Oxygen Scavenging Study of Different TiO2 Preparations. J. Phys. Chem. B 110, 23255–23263. https://doi.org/10.1021/jp064591c

Peljo, P., Manzanares, J.A., Girault, H.H., 2017. Variation of the Fermi level and the electrostatic force of a metallic nanoparticle upon colliding with an electrode. Chem. Sci. 8, 4795–4803. https://doi.org/10.1039/C7SC00848A

Peng, H., Zhang, N., He, M., Chen, B., Hu, B., 2015. Simultaneous speciation analysis of inorganic arsenic, chromium and selenium in environmental waters by 3-(2-aminoethylamino) propyltrimethoxysilane modified multi-wall carbon nanotubes packed microcolumn solid phase extraction and ICP-MS. Talanta 131, 266–272. https://doi.org/10.1016/j.talanta.2014.07.054

Pérez-Corona, T., Madrid, Y., Cámara, C., 1997. Evaluation of selective uptake of selenium (Se(IV) and Se(VI)) and antimony (Sb(III) and Sb(V)) species by baker's yeast cells (Saccharomyces cerevisiae). Analytica Chimica Acta 345, 249–255. https://doi.org/10.1016/S0003-2670(96)00633-2

Perissinotti, L.L., Brusa, M.A., Grela, M.A., 2001. Yield of Carboxyl Anion Radicals in the Photocatalytic Degradation of Formate over TiO2 Particles. Langmuir 17, 8422–8427. https://doi.org/10.1021/la0155348

Peshavariya, H.M., Dusting, G.J., Selemidis, S., 2007. Analysis of dihydroethidium fluorescence for the detection of intracellular and extracellular superoxide produced by NADPH oxidase. Free Radic. Res. 41, 699–712. https://doi.org/10.1080/10715760701297354

Petty, J.T., Fulton, J.B., Strager, M.P., Merovich, G.T., Stiles, J.M., Ziemkiewicz, P.F., 2010. Landscape indicators and thresholds of stream ecological impairment in an intensively mined Appalachian watershed. Journal of the North American Benthological Society 29, 1292–1309. https://doi.org/10.1899/09-149.1

Pisanic II, T.R., Blackwell, J.D., Shubayev, V.I., Fiñones, R.R., Jin, S., 2007. Nanotoxicity of iron oxide nanoparticle internalization in growing neurons. Biomaterials 28, 2572–2581. https://doi.org/10.1016/j.biomaterials.2007.01.043

Qu, X., Alvarez, P.J.J., Li, Q., 2013. Applications of nanotechnology in water and wastewater treatment. Water Research, Nanotechnology for Water and Wastewater Treatment 47, 3931–3946. https://doi.org/10.1016/j.watres.2012.09.058

Quamme, M., Almeelbi, T., Bezbaruah, A., 2012. Selenium Removal from Surface Waters: Exploratory Research with Iron Nanoparticles, in: World Environmental and Water Resources Congress 2012. American Society of Civil Engineers, pp. 146–150.

R. H. Gerber, A., 1986. The effect of acetate and other short-chain carbon compounds on the kinetics of biological nutrient removal. Water SA 12, 7–12.

Raman Chaudhari, V., A. Hassan, P., Krishna Haram, S., 2014. Size-dependent quantized double layer charging of monolayer-protected silver nanoparticles. New Journal of Chemistry 38, 1761–1767. https://doi.org/10.1039/C3NJ01077E

Ramaswamy, N., Mukerjee, S., 2011. Influence of Inner- and Outer-Sphere Electron Transfer Mechanisms during Electrocatalysis of Oxygen Reduction in Alkaline Media. J. Phys. Chem. C 115, 18015–18026. https://doi.org/10.1021/jp204680p

Rayman, M.P., 2000. The importance of selenium to human health. The Lancet 356, 233–241. https://doi.org/10.1016/S0140-6736(00)02490-9

Richards, L.A., Richards, B.S., Schäfer, A.I., 2011. Renewable energy powered membrane technology: Salt and inorganic contaminant removal by nanofiltration/reverse osmosis. Journal of Membrane Science 369, 188–195. https://doi.org/10.1016/j.memsci.2010.11.069

Rioja, N., Zorita, S., Peñas, F.J., 2016. Effect of water matrix on photocatalytic degradation and general kinetic modeling. Applied Catalysis B: Environmental 180, 330–335. https://doi.org/10.1016/j.apcatb.2015.06.038

Robinson, R.A., 1936. The dissociation constant of hydrochloric acid. Trans. Faraday Soc. 32, 743–744. https://doi.org/10.1039/TF9363200743

Rockafellow, E.M., Haywood, J.M., Witte, T., Houk, R.S., Jenks, W.S., 2010. Selenium-Modified TiO2 and Its Impact on Photocatalysis. Langmuir 26, 19052–19059. https://doi.org/10.1021/la1026569

Rodrigues, A.C., Boroski, M., Shimada, N.S., Garcia, J.C., Nozaki, J., Hioka, N., 2008. Treatment of paper pulp and paper mill wastewater by coagulation–flocculation followed by heterogeneous photocatalysis. Journal of Photochemistry and Photobiology A: Chemistry 194, 1–10. https://doi.org/10.1016/j.jphotochem.2007.07.007

Rosengrant, L., 1990. Final Best Demonstrated Available Technology (BDAT) Background Document for... Characteristic Selenium Wastes (D010). U.S. EPA, Washington, D.C.

Rossini, M., Garrido, J.G., Galluzzo, M., 1999. Optimization of the coagulation–flocculation treatment: influence of rapid mix parameters. Water Research 33, 1817–1826. https://doi.org/10.1016/S0043-1354(98)00367-4

Rovira, M., Giménez, J., Martínez, M., Martínez-Lladó, X., de Pablo, J., Martí, V., Duro, L., 2008. Sorption of selenium(IV) and selenium(VI) onto natural iron oxides: Goethite and hematite. Journal of Hazardous Materials 150, 279–284. https://doi.org/10.1016/j.jhazmat.2007.04.098

Santos, S., Ungureanu, G., Boaventura, R., Botelho, C., 2015. Selenium contaminated waters: An overview of analytical methods, treatment options and recent advances in sorption methods. Science of The Total Environment 521–522, 246–260. https://doi.org/10.1016/j.scitotenv.2015.03.107

Sanuki, S., Arai, K., Kojima, T., Nagaoka, S., Majima, H., 1999. Photocatalytic reduction of selenate and selenite solutions using TiO2 powders. Metall and Materi Trans B 30, 15–20. https://doi.org/10.1007/s11663-999-0002-0

Savory, D.M., McQuillan, A.J., 2013. Influence of Formate Adsorption and Protons on Shallow Trap Infrared Absorption (STIRA) of Anatase TiO2 During Photocatalysis. J. Phys. Chem. C 117, 23645–23656. https://doi.org/10.1021/jp404321f

Schiavon, M., Pilon-Smits, E.A.H., 2017. Selenium Biofortification and Phytoremediation Phytotechnologies: A Review. Journal of Environmental Quality 46, 10–19. https://doi.org/10.2134/jeq2016.09.0342

Schneider, J., Matsuoka, M., Takeuchi, M., Zhang, J., Horiuchi, Y., Anpo, M., Bahnemann, D.W., 2014. Understanding TiO2 Photocatalysis: Mechanisms and Materials. Chem. Rev. 114, 9919–9986. https://doi.org/10.1021/cr5001892

Séby, F., Potin-Gautier, M., Giffaut, E., Borge, G., Donard, O.F.X., 2001. A critical review of thermodynamic data for selenium species at 25°C. Chemical Geology 171, 173–194. https://doi.org/10.1016/S0009-2541(00)00246-1

Shaban, Y.A., El Maradny, A.A., Al Farawati, R.K., 2016. Photocatalytic reduction of nitrate in seawater using C/TiO2 nanoparticles. Journal of Photochemistry and Photobiology A: Chemistry 328, 114–121. https://doi.org/10.1016/j.jphotochem.2016.05.018

Shan, C., Chen, J., Yang, Z., Jia, H., Guan, X., Zhang, W., Pan, B., 2018. Enhanced removal of Se(VI) from water via pre-corrosion of zero-valent iron using H2O2/HCl: Effect of solution chemistry and mechanism investigation. Water Research 133, 173–181. https://doi.org/10.1016/j.watres.2018.01.038

Sharmasarkar, S., Vance, G.F., 2002. Selenite–selenate sorption in surface coal mine environment. Advances in Environmental Research 7, 87–95. https://doi.org/10.1016/S1093-0191(01)00110-1

Sheng, H., Li, Q., Ma, W., Ji, H., Chen, C., Zhao, J., 2013. Photocatalytic degradation of organic pollutants on surface anionized TiO2: Common effect of anions for high hole-availability by water. Applied Catalysis B: Environmental 138–139, 212–218. https://doi.org/10.1016/j.apcatb.2013.03.001

Sheng, Y., Abreu, I.A., Cabelli, D.E., Maroney, M.J., Miller, A.-F., Teixeira, M., Valentine, J.S., 2014. Superoxide Dismutases and Superoxide Reductases. Chem. Rev. 114, 3854–3918. https://doi.org/10.1021/cr4005296

Shih, Y., Zhuang, C., Peng, Y.-H., Lin, C., Tseng, Y., 2012. The effect of inorganic ions on the aggregation kinetics of lab-made TiO2 nanoparticles in water. Science of The Total Environment 435–436, 446–452. https://doi.org/10.1016/j.scitotenv.2012.06.076

Sors, T.G., Ellis, D.R., Salt, D.E., 2005. Selenium uptake, translocation, assimilation and metabolic fate in plants. Photosynth Res 86, 373–389. https://doi.org/10.1007/s11120-005-5222-9

Souza, M.P. de, Chu, D., Zhao, M., Zayed, A.M., Ruzin, S.E., Schichnes, D., Terry, N., 1999. Rhizosphere Bacteria Enhance Selenium Accumulation and Volatilization by Indian Mustard. Plant Physiol. 119, 565–574. https://doi.org/10.1104/pp.119.2.565

Sowmya, A., Meenakshi, S., 2015. Photocatalytic reduction of nitrate over Ag–TiO2 in the presence of oxalic acid. Journal of Water Process Engineering 8, e23–e30. https://doi.org/10.1016/j.jwpe.2014.11.004

Spycher, N., Pruess, K., 2005. CO2-H2O mixtures in the geological sequestration of CO2. II. Partitioning in chloride brines at 12–100°C and up to 600 bar. Geochimica et Cosmochimica Acta 69, 3309–3320. https://doi.org/10.1016/j.gca.2005.01.015

Staicu, L.C., van Hullebusch, E.D., Lens, P.N.L., 2015a. Production, recovery and reuse of biogenic elemental selenium. Environ Chem Lett 13, 89–96. https://doi.org/10.1007/s10311-015-0492-8

Staicu, L.C., van Hullebusch, E.D., Oturan, M.A., Ackerson, C.J., Lens, P.N.L., 2015b. Removal of colloidal biogenic selenium from wastewater. Chemosphere 125, 130–138. https://doi.org/10.1016/j.chemosphere.2014.12.018

Stolz, J.F., Oremland, R.S., 1999. Bacterial respiration of arsenic and selenium. FEMS Microbiology Reviews 23, 615–627. https://doi.org/10.1111/j.1574-6976.1999.tb00416.x

Strong, P.J., McDonald, B., Gapes, D.J., 2011. Enhancing denitrification using a carbon supplement generated from the wet oxidation of waste activated sludge. Bioresource Technology, Special Issue on Challenges in Environmental Science and Engineering, CESE-2010: Technological Advances in Waste Treatment for a Sustainable Future 102, 5533–5540. https://doi.org/10.1016/j.biortech.2010.12.025

Subramanian, V., Wolf, E.E., Kamat, P.V., 2004. Catalysis with TiO2/Gold Nanocomposites. Effect of Metal Particle Size on the Fermi Level Equilibration. J. Am. Chem. Soc. 126, 4943–4950. https://doi.org/10.1021/ja0315199

Sun, D., Yang, W., Zhou, L., Sun, W., Li, Q., Shang, J.K., 2016. The selective deposition of silver nanoparticles onto {101} facets of TiO2 nanocrystals with co-exposed {001}/{101} facets, and their enhanced photocatalytic reduction of aqueous nitrate under simulated solar illumination. Applied Catalysis B: Environmental 182, 85–93. https://doi.org/10.1016/j.apcatb.2015.09.005

Sun, W., Pan, W., Wang, F., Xu, N., 2015. Removal of Se(IV) and Se(VI) by MFe2O4 nanoparticles from aqueous solution. Chemical Engineering Journal 273, 353–362. https://doi.org/10.1016/j.cej.2015.03.061

Suttiponparnit, K., Jiang, J., Sahu, M., Suvachittanont, S., Charinpanitkul, T., Biswas, P., 2010. Role of Surface Area, Primary Particle Size, and Crystal Phase on Titanium Dioxide Nanoparticle Dispersion Properties. Nanoscale Res Lett 6, 27. https://doi.org/10.1007/s11671-010-9772-1

Szlachta, M., Chubar, N., 2013. The application of Fe–Mn hydrous oxides based adsorbent for removing selenium species from water. Chemical Engineering Journal 217, 159–168. https://doi.org/10.1016/j.cej.2012.11.100

T. Tan, D.B., 2003. Effect of organic hole scavengers on the photocatalytic reduction of selenium ions. Journal of Photochemistry and Photobiology A: Chemistry 159, 273–280. https://doi.org/10.1016/S1010-6030(03)00171-0

Tan, L.C., Nancharaiah, Y.V., van Hullebusch, E.D., Lens, P.N., 2018. Selenium: environmental significance, pollution, and biological treatment technologies, in: Anaerobic Treatment of Mine Wastewater for the Removal of Selenate and Its Co-Contaminants. CRC Press, pp. 9–71.

Tan, L.C., Nancharaiah, Y.V., van Hullebusch, E.D., Lens, P.N.L., 2016. Selenium: environmental significance, pollution, and biological treatment technologies. Biotechnology Advances 34, 886–907. https://doi.org/10.1016/j.biotechadv.2016.05.005

Tan, L.-L., Ong, W.-J., Chai, S.-P., Mohamed, A.R., 2015. Noble metal modified reduced graphene oxide/TiO2 ternary nanostructures for efficient visible-light-driven photoreduction of carbon dioxide into methane. Applied Catalysis B: Environmental 166–167, 251–259. https://doi.org/10.1016/j.apcatb.2014.11.035

Tan, T.H., Wong, R.J., Scott, J., Ng, Y.H., Taylor, R.A., Aguey-Zinsou, K.-F., Amal, R., 2018. Multipronged Validation of Oxalate C–C Bond Cleavage Driven by Au-TiO2 Interfacial Charge Transfer Using Operando DRIFTS. ACS Catal. 8, 7158–7163. https://doi.org/10.1021/acscatal.8b01903

Tan, T.T.Y., Beydoun, D., Amal, R., 2003a. Effects of organic hole scavengers on the photocatalytic reduction of selenium anions. Journal of Photochemistry and Photobiology A: Chemistry 159, 273–280. https://doi.org/10.1016/S1010-6030(03)00171-0

Tan, T.T.Y., Beydoun, D., Amal, R., 2003b. Photocatalytic reduction of Se(VI) in aqueous solutions in UV/TiO2 system: importance of optimum ratio of reactants on TiO2 surface. Journal of Molecular Catalysis A: Chemical 202, 73–85. https://doi.org/10.1016/S1381-1169(03)00205-X

Tan, T. T. Y., Beydoun, D., Amal, R., 2003. Photocatalytic Reduction of Se(VI) in Aqueous Solutions in UV/TiO2 System: Kinetic Modeling and Reaction Mechanism. J. Phys. Chem. B 107, 4296–4303. https://doi.org/10.1021/jp026149+

Tan, T.T.Y., Yip, C.K., Beydoun, D., Amal, R., 2003c. Effects of nano-Ag particles loading on TiO2 photocatalytic reduction of selenate ions. Chemical Engineering Journal 95, 179–186. https://doi.org/10.1016/S1385-8947(03)00103-7

Tan, T.T.Y., Zaw, M., Beydoun, D., Amal, R., 2002. The Formation of Nano-sized Selenium–titanium Dioxide Composite Semiconductors by Photocatalysis. Journal of Nanoparticle Research 4, 541–552. https://doi.org/10.1023/A:1022858409731

Tang, C., Huang, Y., Zhang, Z., Chen, J., Zeng, H., Huang, Y.H., 2016. Rapid removal of selenate in a zero-valent iron/Fe3O4/Fe2+ synergetic system. Applied Catalysis B: Environmental 184, 320–327. https://doi.org/10.1016/j.apcatb.2015.11.045

Tanuma, S., Powell, C.J., Penn, D.R., 2011. Calculations of electron inelastic mean free paths. IX. Data for 41 elemental solids over the 50 eV to 30 keV range. Surface and Interface Analysis 43, 689–713. https://doi.org/10.1002/sia.3522

Thabet, S., Simonet, F., Lemaire, M., Guillard, C., Cotton, P., 2014. Impact of photocatalysis on fungal cells: depiction of cellular and molecular effects on Saccharomyces cerevisiae. Appl. Environ. Microbiol. 80, 7527–7535. https://doi.org/10.1128/AEM.02416-14

Trapalis, A., Todorova, N., Giannakopoulou, T., Boukos, N., Speliotis, T., Dimotikali, D., Yu, J., 2016. TiO2/graphene composite photocatalysts for NOx removal: A comparison of surfactant-stabilized graphene and reduced graphene oxide. Applied Catalysis B: Environmental 180, 637–647. https://doi.org/10.1016/j.apcatb.2015.07.009

Turolla, A., Piazzoli, A., Farner Budarz, J., Wiesner, M.R., Antonelli, M., 2015. Experimental measurement and modelling of reactive species generation in TiO2 nanoparticle photocatalysis. Chemical Engineering Journal 271, 260–268. https://doi.org/10.1016/j.cej.2015.03.004

Twidwell, L.G., McCloskey, J., Miranda, P., Gale, M., 1999. Technologies and potential technologies for removing selenium from process and mine wastewater. Proceedings of the TMS Fall Extraction and Processing Conference 2, 1645–56.

Uden, P.C., 2002. Modern trends in the speciation of selenium by hyphenated techniques. Anal Bioanal Chem 373, 422–431. https://doi.org/10.1007/s00216-002-1405-9

U.S. EPA, 2014. National Primary Drinking Water Regulations - List of Contaminants and their MCLs [WWW Document]. National Primary Drinking Water Regulations - List of Contaminants and their MCLs. URL http://www.epa.gov/your-drinking-water/table-regulated-drinking-water-contaminants#Inorganic (accessed 5.17.16).

U.S. EPA, 2011. The Effects of Mountaintop Mines and Valley Fills on Aquatic Ecosystems of the Central Appalachian Coalfields (2011 Final).

U.S. EPA, 1996. EPA Method 3050B: Acid Digestion of Sediments, Sludges, and Soils.

U.S. EPA Office of Water, 2016. Aquatic Life Ambient Water Quality Criterion for Selenium - Freshwater 2016 (No. EPA 822-R-16-006). U.S. EPA, Washington, D.C.

U.S. EPA, Office of Water, 2015. Draft Aquatic Life Ambient Water Quality Criterion for Selenium - Freshwater. U.S. EPA, Washington, D.C.

Vaiano, V., Iervolino, G., Sannino, D., Murcia, J.J., Hidalgo, M.C., Ciambelli, P., Navío, J.A., 2016. Photocatalytic removal of patent blue V dye on Au-TiO2 and Pt-TiO2 catalysts. Applied Catalysis B: Environmental 188, 134–146. https://doi.org/10.1016/j.apcatb.2016.02.001

Valari, M., Antoniadis, A., Mantzavinos, D., Poulios, I., 2015. Photocatalytic reduction of Cr(VI) over titania suspensions. Catalysis Today, 8th European Meeting on Solar Chemistry and Photocatalysis: Environmental Applications 252, 190–194. https://doi.org/10.1016/j.cattod.2014.10.014

Vittadini, A., Selloni, A., Rotzinger, F.P., Grätzel, M., 2000. Formic Acid Adsorption on Dry and Hydrated TiO2 Anatase (101) Surfaces by DFT Calculations. J. Phys. Chem. B 104, 1300–1306. https://doi.org/10.1021/jp993583b

Wang, X., Liu, J., Leong, S., Lin, X., Wei, J., Kong, B., Xu, Y., Low, Z.-X., Yao, J., Wang, H., 2016. Rapid Construction of ZnO@ZIF-8 Heterostructures with Size-Selective Photocatalysis Properties. ACS Appl. Mater. Interfaces 8, 9080–9087. https://doi.org/10.1021/acsami.6b00028

Watson, R.J., Butler, E.C.V., Clementson, L.A., Berry, K.M., 2005. Flow-injection analysis with fluorescence detection for the determination of trace levels of ammonium in seawater. J. Environ. Monit. 7, 37–42. https://doi.org/10.1039/B405924G

Wei, X., Bhojappa, S., Lin, L.-S., Viadero, R.C., 2011. Performance of Nano-Magnetite for Removal of Selenium from Aqueous Solutions. Environmental Engineering Science 29, 526–532. https://doi.org/10.1089/ees.2011.0383

World Health Organization, 2011. Guidelines for Drinking-water Quality, Fourth Edition. WHO Press, Geneva, Switzerland.

Wu, L., Li, F., Xu, Y., Zhang, J.W., Zhang, D., Li, G., Li, H., 2015. Plasmon-induced photoelectrocatalytic activity of Au nanoparticles enhanced TiO2 nanotube arrays electrodes for environmental remediation. Applied Catalysis B: Environmental 164, 217–224. https://doi.org/10.1016/j.apcatb.2014.09.029

Wu, W., He, Q., Jiang, C., 2008. Magnetic Iron Oxide Nanoparticles: Synthesis and Surface Functionalization Strategies. Nanoscale Res Lett 3, 397–415. https://doi.org/10.1007/s11671-008-9174-9

Xiang, Q., Yu, J., Jaroniec, M., 2011. Tunable photocatalytic selectivity of TiO2 films consisted of flower-like microspheres with exposed {001} facets. Chem. Commun. 47, 4532–4534. https://doi.org/10.1039/C1CC10501A

Xiao, Q., Yu, S., Li, L., Wang, T., Liao, X., Ye, Y., 2017. An overview of advanced reduction processes for bromate removal from drinking water: Reducing agents, activation methods, applications and mechanisms. Journal of Hazardous Materials 324, 230–240. https://doi.org/10.1016/j.jhazmat.2016.10.053

Xu, Q., Zhang, L., Yu, J., Wageh, S., Al-Ghamdi, A.A., Jaroniec, M., 2018. Direct Z-scheme photocatalysts: Principles, synthesis, and applications. Materials Today. https://doi.org/10.1016/j.mattod.2018.04.008

Yamani, J.S., Lounsbury, A.W., Zimmerman, J.B., 2014. Adsorption of selenite and selenate by nanocrystalline aluminum oxide, neat and impregnated in chitosan beads. Water Research 50, 373–381. https://doi.org/10.1016/j.watres.2013.10.054

Yang, G.Q., Wang, S.Z., Zhou, R.H., Sun, S.Z., 1983. Endemic selenium intoxication of humans in China. Am J Clin Nutr 37, 872–881.

Yang, J., Liu, B., Xie, H., Zhao, X., Terashima, C., Fujishima, A., Nakata, K., 2015. In Situ Photoconductivity Kinetic Study of Nano-TiO2 during the Photocatalytic Oxidation of Formic Acid: Effects of New Recombination and Current Doubling. J. Phys. Chem. C 119, 21711–21722. https://doi.org/10.1021/acs.jpcc.5b06534

Yang, L., Shahrivari, Z., Liu, P.K.T., Sahimi, M., Tsotsis, T.T., 2005. Removal of Trace Levels of Arsenic and Selenium from Aqueous Solutions by Calcined and Uncalcined Layered Double Hydroxides (LDH). Ind. Eng. Chem. Res. 44, 6804–6815. https://doi.org/10.1021/ie049060u

Yang, T., Doudrick, K., Westerhoff, P., 2013. Photocatalytic reduction of nitrate using titanium dioxide for regeneration of ion exchange brine. Water Res. 47, 1299–1307. https://doi.org/10.1016/j.watres.2012.11.047

Yang, W., Gao, Y., Wu, L., Hou, X., Zheng, C., Zhu, X., 2013. Preconcentration and in-situ photoreduction of trace selenium using TiO2 nanoparticles, followed by its determination by slurry photochemical vapor generation atomic fluorescence spectrometry. Microchim Acta 181, 197–204. https://doi.org/10.1007/s00604-013-1101-9

Ye, L., Chu, K.H., Wang, B., Wu, D., Xie, H., Huang, G., Yip, H.Y., Wong, P.K., 2016. Noble-metal loading reverses temperature dependent photocatalytic hydrogen generation in methanol–water solutions. Chem. Commun. 52, 11657–11660. https://doi.org/10.1039/C6CC05689J

Yoon, I.-H., Bang, S., Kim, K.-W., Kim, M.G., Park, S.Y., Choi, W.-K., 2015. Selenate removal by zero-valent iron in oxic condition: the role of Fe(II) and selenate removal mechanism. Environ Sci Pollut Res 23, 1081–1090. https://doi.org/10.1007/s11356-015-4578-4

You, Y., Vance, G.F., Zhao, H., 2001. Selenium adsorption on Mg–Al and Zn–Al layered double hydroxides. Applied Clay Science 20, 13–25. https://doi.org/10.1016/S0169-1317(00)00043-0

Yu, A.Y.-C., Spicer, W.E., 1968. Photoemission and Optical Studies of the Electronic Structure of Palladium. Phys. Rev. 169, 497–507. https://doi.org/10.1103/PhysRev.169.497

Zanella, R., Giorgio, S., Henry, C.R., Louis, C., 2002. Alternative Methods for the Preparation of Gold Nanoparticles Supported on TiO2. J. Phys. Chem. B 106, 7634–7642. https://doi.org/10.1021/jp0144810

Zawislanski, P.T., Benson, S.M., TerBerg, R., Borglin, S.E., 2003. Selenium Speciation, Solubility, and Mobility in Land-Disposed Dredged Sediments. Environ. Sci. Technol. 37, 2415–2420. https://doi.org/10.1021/es020977z

Zelmanov, G., Semiat, R., 2013. Selenium removal from water and its recovery using iron (Fe3+) oxide/hydroxide-based nanoparticles sol (NanoFe) as an adsorbent. Separation and Purification Technology 103, 167–172. https://doi.org/10.1016/j.seppur.2012.10.037

Zeng, X., Wang, Z., Meng, N., McCarthy, D.T., Deletic, A., Pan, J., Zhang, X., 2017. Highly dispersed TiO2 nanocrystals and carbon dots on reduced graphene oxide: Ternary nanocomposites for accelerated photocatalytic water disinfection. Applied Catalysis B: Environmental 202, 33–41. https://doi.org/10.1016/j.apcatb.2016.09.014

Zhang, F., Jin, R., Chen, J., Shao, C., Gao, W., Li, L., Guan, N., 2005. High photocatalytic activity and selectivity for nitrogen in nitrate reduction on Ag/TiO2 catalyst with fine silver clusters. Journal of Catalysis 232, 424–431. https://doi.org/10.1016/j.jcat.2005.04.014

Zhang, L., Liu, N., Yang, L., Lin, Q., 2009. Sorption behavior of nano-TiO2 for the removal of selenium ions from aqueous solution. Journal of Hazardous Materials 170, 1197–1203. https://doi.org/10.1016/j.jhazmat.2009.05.098

Zhang, S., Xu, J., Hu, J., Cui, C., Liu, H., 2017. Interfacial Growth of TiO2-rGO Composite by Pickering Emulsion for Photocatalytic Degradation. Langmuir 33, 5015–5024. https://doi.org/10.1021/acs.langmuir.7b00719

Zhang, Y., Wang, J., Amrhein, C., Frankenberger, W.T., 2005. Removal of selenate from water by zerovalent iron. J. Environ. Qual. 34, 487–495.

Zhang, Z., Adedeji, I., Chen, G., Tang, Y., 2018. Chemical-Free Recovery of Elemental Selenium from Selenate-Contaminated Water by a System Combining a Biological Reactor, a Bacterium–Nanoparticle Separator, and a Tangential Flow Filter. Environ. Sci. Technol. https://doi.org/10.1021/acs.est.8b04544

Zhao, H., Kalivendi, S., Zhang, H., Joseph, J., Nithipatikom, K., Vásquez-Vivar, J., Kalyanaraman, B., 2003. Superoxide reacts with hydroethidine but forms a fluorescent product that is distinctly different from ethidium: potential implications in intracellular fluorescence detection of superoxide. Free Radic. Biol. Med. 34, 1359–1368.

Zheng, L., Hu, K., Teng, F., Fang, X., 2017. Novel UV–Visible Photodetector in Photovoltaic Mode with Fast Response and Ultrahigh Photosensitivity Employing Se/TiO2 Nanotubes Heterojunction. Small 13, 1602448. https://doi.org/10.1002/smll.201602448

Zhu, X., Jin, C., Li, X.-S., Liu, J.-L., Sun, Z.-G., Shi, C., Li, X., Zhu, A.-M., 2017. Photocatalytic Formaldehyde Oxidation over Plasmonic Au/TiO2 under Visible Light: Moisture Indispensability and Light Enhancement. ACS Catal. 7, 6514–6524. https://doi.org/10.1021/acscatal.7b01658

Zielonka, J., Zhao, H., Xu, Y., Kalyanaraman, B., 2005. Mechanistic similarities between oxidation of hydroethidine by Fremy's salt and superoxide: stopped-flow optical and EPR studies. Free Radic. Biol. Med. 39, 853–863. https://doi.org/10.1016/j.freeradbiomed.2005.05.001

Appendices

Appendix A – Supplementary Information for Chapter 2

A1. FGDW Characterization

Table A-1. Water quality characteristics of FGDW from a coal-fired power plant in the southeastern United States. The FGDW was sampled after coagulation and flocculation physico-chemical pre-treatment.

Physical Tests (Water)			
Parameter	Lowest Detection Limit	Units	FGDW Industry Wastewater
Total Suspended Solids	2.0	mg/L	5.1
Total Dissolved Solids	20	mg/L	4620
Turbidity	0.10	NTU	1.94

Anions and Nutrients (Water)			
Parameter	Lowest Detection Limit	Units	FGDW Industry Wastewater
Alkalinity, Total (as CaCO3)	10	mg/L	57
Bromide (Br)	1.0	mg/L	44.1
Chloride (Cl)	5.0	mg/L	1070
Fluoride (F)	0.20	mg/L	6.99
Nitrate (as N)	0.20	mg/L	3.48
Nitrite (as N)	0.10	mg/L	0.16
Sulfate (SO4)	3.0	mg/L	1670

Organic / Inorganic Carbon (Water)			
Parameter	Lowest Detection Limit	Units	FGDW Industry Wastewater
Total Organic Carbon	1.0	mg/L	9.2

Total Metals (Water)				Dissolved Metals (Water)			
Parameter	Lowest Detection Limit	Units	FGDW Industry Wastewater	Parameter	Lowest Detection Limit	Units	FGDW Industry Wastewater
Aluminum (Al)-Total	1.0	mg/L	<1.0	Aluminum (Al)-Dissolved	0.50	mg/L	<0.50
Antimony (Sb)-Total	0.010	mg/L	<0.010	Antimony (Sb)-Dissolved	0.010	mg/L	<0.010
Arsenic (As)-Total	0.010	mg/L	<0.010	Arsenic (As)-Dissolved	0.010	mg/L	<0.010
Barium (Ba)-Total	0.020	mg/L	0.078	Barium (Ba)-Dissolved	0.010	mg/L	0.078

Beryllium (Be)-Total	0.010	mg/L	<0.010	Beryllium (Be)-Dissolved	0.010	mg/L	<0.010
Bismuth (Bi)-Total	0.0050	mg/L	<0.0050	Bismuth (Bi)-Dissolved	0.0050	mg/L	<0.0050
Boron (B)-Total	1.0	mg/L	13.9	Boron (B)-Dissolved	1.0	mg/L	14.1
Cadmium (Cd)-Total	0.0010	mg/L	<0.0010	Cadmium (Cd)-Dissolved	0.0010	mg/L	<0.0010
Calcium (Ca)-Total	50	mg/L	808	Calcium (Ca)-Dissolved	5.0	mg/L	831
Cesium (Cs)-Total	0.0010	mg/L	<0.0010	Cesium (Cs)-Dissolved	0.0010	mg/L	<0.0010
Chromium (Cr)-Total	0.050	mg/L	<0.050	Chromium (Cr)-Dissolved	0.050	mg/L	<0.050
Cobalt (Co)-Total	0.010	mg/L	<0.010	Cobalt (Co)-Dissolved	0.010	mg/L	<0.010
Copper (Cu)-Total	0.10	mg/L	0.21	Copper (Cu)-Dissolved	0.020	mg/L	0.058
Iron (Fe)-Total	5.0	mg/L	<5.0	Iron (Fe)- Dissolved	1.0	mg/L	<1.0
Lead (Pb)-Total	0.0050	mg/L	<0.0050	Lead (Pb)-Dissolved	0.0050	mg/L	<0.0050
Lithium (Li)-Total	0.10	mg/L	0.31	Lithium (Li)-Dissolved	0.10	mg/L	0.33
Magnesium (Mg)-Total	5.0	mg/L	185	Magnesium (Mg)-Dissolved	5.0	mg/L	190
Manganese (Mn)-Total	0.050	mg/L	1.36	Manganese (Mn)-Dissolved	0.050	mg/L	1.32
Molybdenum (Mo)-Total	0.0050	mg/L	0.0442	Molybdenum (Mo)-Dissolved	0.0050	mg/L	0.0451
Nickel (Ni)-Total	0.050	mg/L	<0.050	Nickel (Ni)-Dissolved	0.050	mg/L	<0.050
Phosphorus (P)-Total	5.0	mg/L	<5.0	Phosphorus (P)-Dissolved	5.0	mg/L	<5.0
Potassium (K)-Total	5.0	mg/L	21.3	Potassium (K)-Dissolved	5.0	mg/L	21.5
Rubidium (Rb)-Total	0.020	mg/L	0.039	Rubidium (Rb)-Dissolved	0.020	mg/L	0.039
Selenium (Se)-Total	0.0050	mg/L	0.256	Selenium (Se)-Dissolved	0.0050	mg/L	0.249
Silicon (Si)-Total	10	mg/L	<10	Silicon (Si)-Dissolved	5.0	mg/L	<5.0
Silver (Ag)-Total	0.0050	mg/L	<0.0050	Silver (Ag)-Dissolved	0.0050	mg/L	<0.0050
Sodium (Na)-Total	50	mg/L	149	Sodium (Na)-Dissolved	50	mg/L	158
Strontium (Sr)-Total	0.10	mg/L	3.54	Strontium (Sr)-Dissolved	0.10	mg/L	3.62
Sulfur (S)-Total	50	mg/L	552	Sulfur (S)-Dissolved	50	mg/L	558
Tellurium (Te)-Total	0.020	mg/L	<0.020	Tellurium (Te)-Dissolved	0.020	mg/L	<0.020
Thallium (Tl)-Total	0.0010	mg/L	<0.0010	Thallium (Tl)-Dissolved	0.0010	mg/L	<0.0010

A2. Effect of Coagulation-Flocculation pretreatment of FGDW on selenate photoreduction

The effect of CF pretreatment on the rate of PC Se removal was investigated in FGDW samples. The CF pretreatment of the FGDW was responsible for removing 27% of total Se in the FGDW. More specifically, this removed both solid elemental selenium and SeO_3^{2-} adsorbed onto solids from the FGDW. The majority of the remaining soluble selenium is fully oxidized SeO_4^{2-}, which is consistent with literature (Hu et al., 2015). CF pretreatment employs a cationic metal as a coagulant agent which promotes water hydrolysis and formation of hydroxide compounds available for adsorption of metals and other contaminants. Coagulation effectiveness relies heavily on the interaction of colloidal materials through charge neutralization or adsorption (Rodrigues et al., 2008). In this case, due to very low adsorptive capacity of SeO_4^{2-}onto hydroxide materials, SeO_4^{2-} is not effectively removed through CF pretreatment.

Removing suspended solids with a glass microfiber filter proved as effective as CF pretreatment prior to PC reduction shown in Figure A-1. The main factor for PC reduction in these experiments is the UV transmittance through the FGDW sample. Any SeO_3^{2-} remaining in the non-CF treated samples is reduced, at a faster rate than SeO_4^{2-} in the CF pretreated FGDW, allowing for improved reaction kinetics of total Se removal. Apparent first-order kinetics were observed for each sample, with pseudo-first-order rate constants of 0.493 ± 0.081 hr^{-1} and 0.465 ± 0.069 hr^{-1} measured for filtered FGDW CF treated and non-CF treated, respectively. Removal of suspended solids contributing to high turbidity and inorganic co-contaminants competing for adsorption sites on the photocatalyst proves a crucial pre-treatment step for PC Se removal techniques. In high flowrate industrial wastewater treatment systems, CF is an indispensable solids removal method (Rossini et al., 1999). Throughout the manuscript FGDW simply refers to filtered, CF pretreated FGDW.

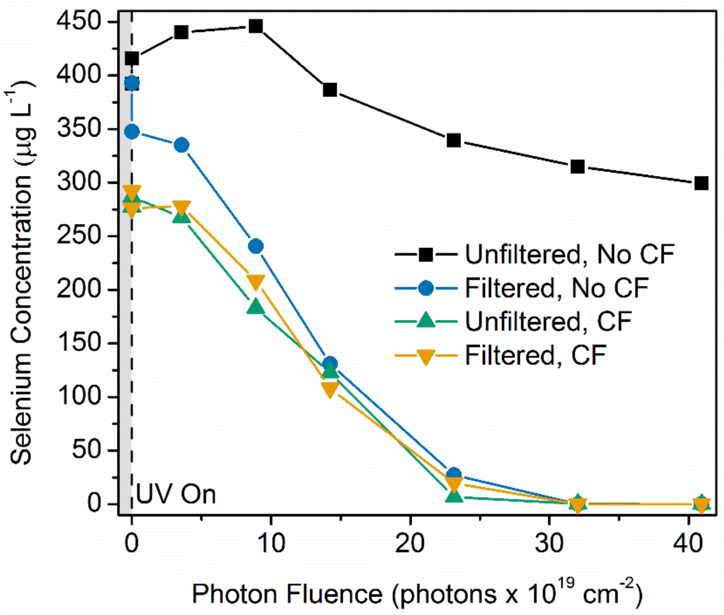

Figure A-1. Effect of coagulation-flocculation (CF) physico-chemical solids removal pretreatment of FGDW prior to PC treatment.

A3. Photocatalytic experimental set-up

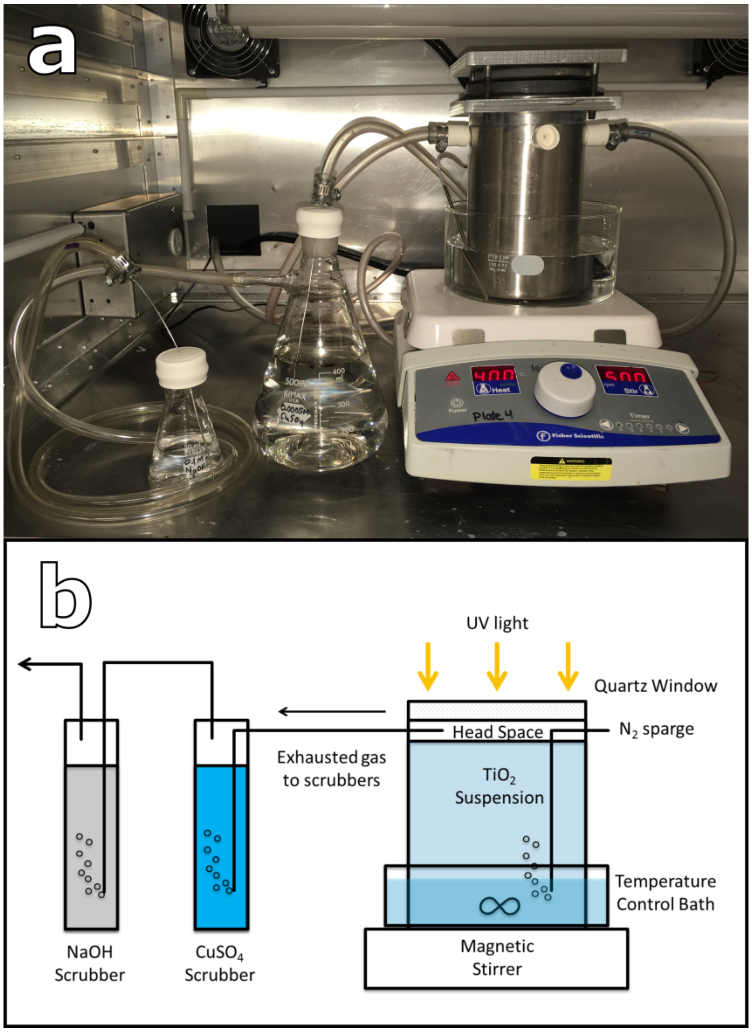

Figure A-2**.** (a) Photograph and (b) schematic image of the batch photocatalytic reaction set-up for the reduction of selenium oxyanions in synthetic and real industrial FGDW.

A4. Reaction Modelling

The following are the photocatalytic reduction reactions governing the chemical and physical state of selenium in the reaction system:

$$SeO_4{}^{2-}{}_{(aq)} + 8H^+ + 6e^- \overset{k_1}{\rightarrow} Se^0{}_{(s)} + 4H_2O \tag{A-1}$$

$$Se^0{}_{(s)} + 4H^+ + 2e^- \overset{k_2}{\rightarrow} H_2Se_{(g)} \tag{A-2}$$

Or these reactions can be simplified to focus on the selenium species in the following reaction:

$$SeO_4{}^{2-}{}_{(aq)} \overset{k_1}{\rightarrow} Se^0{}_{(s)} \overset{k_2}{\rightarrow} H_2Se_{(g)} \tag{A-3}$$

Now, we can write the reaction rates of the selenium species as follows:

$$\frac{d\left[SeO_4{}^{2-}{}_{(aq)}\right]}{dt} = -k_1\left[SeO_4{}^{2-}{}_{(aq)}\right] \tag{A-4}$$

$$\frac{d\left[Se^0{}_{(s)}\right]}{dt} = k_1\left[SeO_4{}^{2-}{}_{(aq)}\right] - k_2\left[Se^0{}_{(s)}\right] \tag{A-5}$$

$$\frac{d\left[H_2Se_{(g)}\right]}{dt} = k_2\left[Se^0{}_{(s)}\right] \tag{A-6}$$

Integrating with respect to t leads to:

$$\left[SeO_4{}^{2-}{}_{(aq)}\right] = \left[SeO_4{}^{2-}{}_{(aq)}\right]_0 e^{-k_1 t} \tag{A-7}$$

Similarly, the concentration of solid Se can be written as:

$$\left[Se^0{}_{(s)}\right] = \frac{k_1\left[SeO_4{}^{2-}{}_{(aq)}\right]_0}{k_2-k_1}\left(e^{-k_1 t} - e^{-k_2 t}\right) \tag{A-8}$$

Then, solving for $[H_2Se_{(g)}]$, we find that:

$$\left[H_2Se_{(g)}\right] = \left[SeO_4{}^{2-}{}_{(aq)}\right]_0\left[1 + \frac{1}{k_1-k_2}\left(k_2 e^{-k_1 t} - k_1 e^{-k_2 t}\right)\right] \tag{A-9}$$

Using the least squares curve fitting method, the equations were fit to the data to obtain the reaction rate constants, $k_1 = 0.657\ cm^2/10^{20}\ photons$ and $k_2 = 1.397\ cm^2/10^{20}\ photons$.

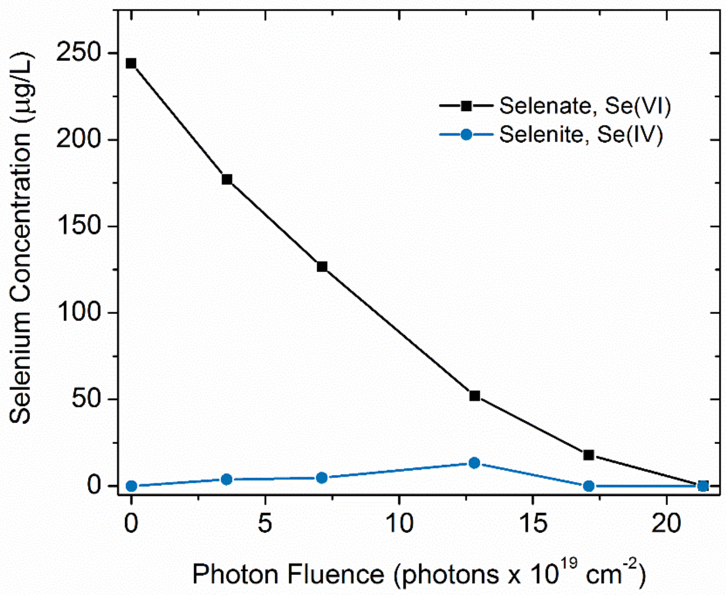

Figure A-3. Dissolved selenium speciation during photocatalytic reduction of selenate in FGDW.

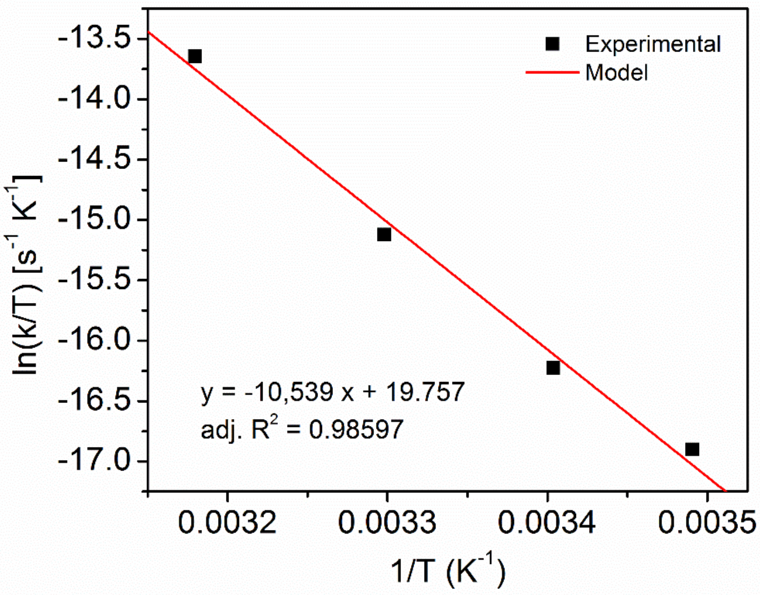

Figure A-4**.** Eyring plot ln(k/T) vs (1/T) for the determination of enthalpy and entropy of activation of the photodegradation of Se in FGDW.

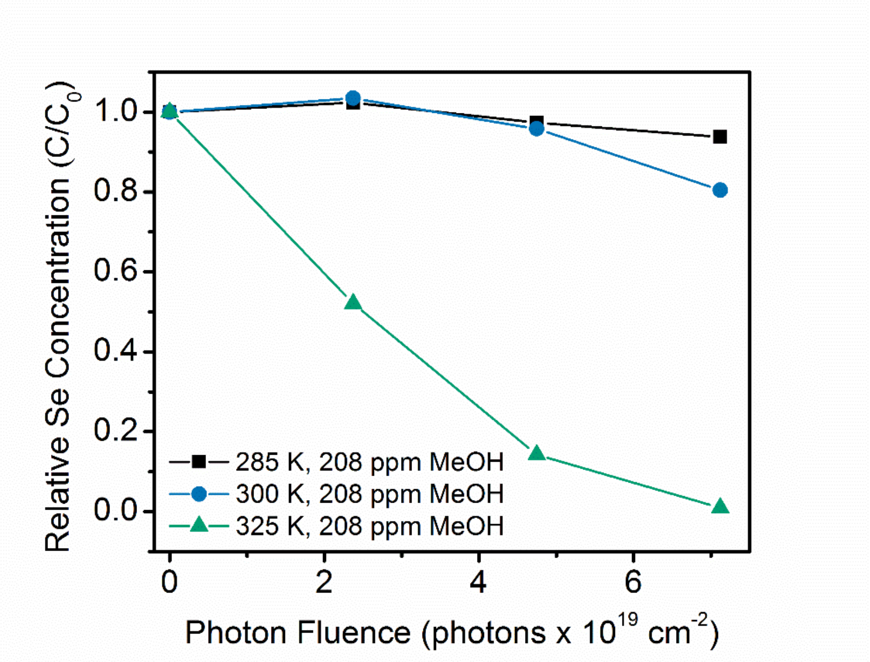

Figure A-5. Photocatalytic removal of Se from FGDW using methanol as the electron hole scavenger under varying temperatures.

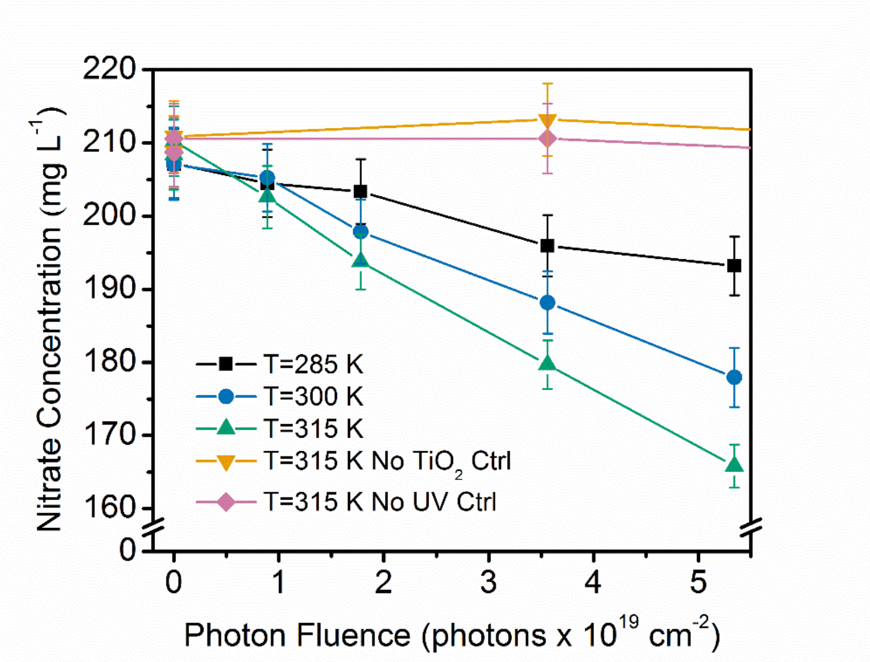

Figure A-6**.** Photocatalytic removal of nitrates under varying temperatures.

A5. Response Surface

Table A-2**.** Central composite design, experimental results, fitted values and residuals for the response surface study with 3 center point replicates. Factor and level coding corresponds to Table 2 in the main manuscript.

Run	Factor Levels					First Order Apparent Rate Constant, $k_{app,1}$ ($cm^2/10^{20}$ photons)	Fitted Values, $\hat{k}_{app,1}$ ($cm^2/10^{20}$ photons)	Residuals, e_i ($cm^2/10^{20}$ photons)	Standardized Residual, d_i
	x_1	x_2	${x_1}^2$	${x_2}^2$	x_1x_2				
1	-1	-1	1	1	1	0.087365	0.093109	-0.00574	-0.0240
2	1	-1	1	1	-1	2.289132	1.740735	0.548397	2.2914
3	-1	1	1	1	-1	0.26364	-0.02878	0.292416	1.2218
4	1	1	1	1	1	6.007533	5.160976	0.846557	3.5373
5	-1	0	1	0	0	0.229997	0.235057	-0.00506	-0.0211
6	1.414	0	2	0	0	3.58234	4.389736	-0.8074	-3.3737
7	0	-1.414	0	2	0	0.134769	0.344435	-0.20967	-0.8761
8	0	1.414	0	2	0	2.044981	2.676373	-0.63139	-2.6382
9	0	0	0	0	0	1.766261	1.916061	-0.1498	-0.6259
10	0	0	0	0	0	1.718099	1.916061	-0.19796	-0.8272
11	0	0	0	0	0	1.932257	1.916061	0.016197	0.0677
12	0	0	0	0	0	2.247626	1.916061	0.331565	1.3854

Table A-3. Analysis of variance for the response surface study (Type III partial sum of squares). Factor coding corresponds to Table 2 in the main manuscript.

Source of Variation	Sum of Squares	Degrees of Freedom	Mean Squares	F-Value	p-Value
Regression	29.618	5	5.924	14.997	0.002
x_1	20.574	1	20.574	52.089	0.000
x_2	5.478	1	5.478	13.870	0.010
${x_1}^2$	0.070	1	0.070	0.176	0.689
${x_2}^2$	0.347	1	0.347	0.879	0.385
$x_1 x_2$	3.176	1	3.176	8.042	0.030
Residual	2.370	6	0.395		
Lack of Fit	2.198	4	0.550	1.391	0.140
Pure Error	0.172	2	0.086		
Total	31.895	11	2.900		

Coefficients of multiple determination: $R^2 = 0.9286$, $R^2_{adj} = 0.9215$

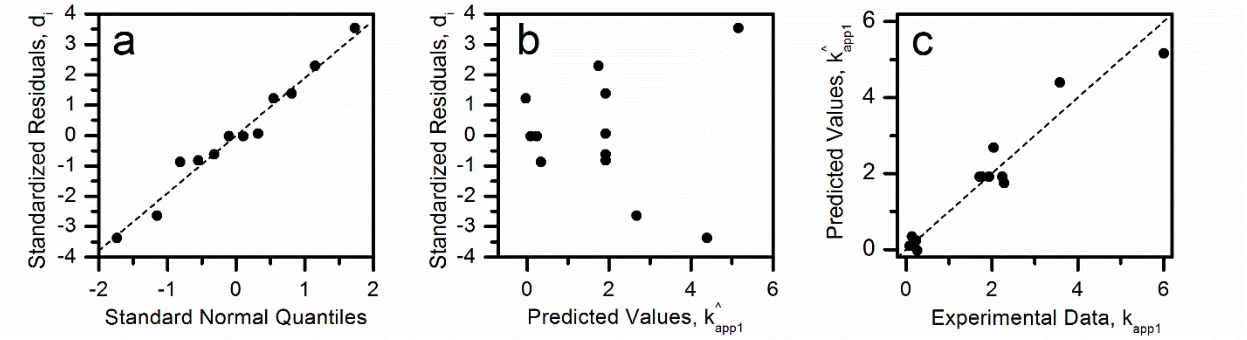

Figure A-7. (a) Half-normal probability plot of residuals, (b) residual plot and (c) predicted vs actual apparent first-order rate constants for the response surface regression.

A6. Radical Experiments

Radical experiments were conducted in order to elucidate the mechanistic pathway of degradation in the presence of oxygen during the photocatalytic reaction. Dihydroethidium (DHE) at a concentration of 5×10^{-5} M was used to quantitatively detect superoxide radical ($O_2^{\bullet-}$) generated by the TiO_2 photoreduction system. Unless otherwise stated, a 0.08 M DHE stock solution in DMSO was used and stored in the dark at –20°C for at most 2 days. Superoxide concentrations were indirectly determined by monitoring the increase in fluorescence intensity at 580 nm (ex. 480 nm), attributed to the formation of the superoxide-specific product 2-hydroxyethidium, at set time intervals (Chen et al., 2013; Fink et al., 2004; Peshavariya et al., 2007; Zhao et al., 2003). When superoxide dismutase (SOD) was used, it was added prior to the dark adsorption period and the aforementioned DHE procedure was conducted without further modifications. Fluorescence spectra were recorded on a Photon Technology International QM-4SE fluorimeter and were smoothed using Origin Pro by removing Fourier components with frequencies higher than a particular cut-off frequency prior to integration of the area under the emission peak. A calibration curve for 2-hydroxyethidium was generated by reacting known amounts of DHE with potassium nitrosodisulfonate (Fremy's Salt), which has been demonstrated to yield the same superoxide-specific oxidation product (Laurindo et al., 2008; Zielonka et al., 2005). The previously mentioned procedure for photoreduction experiments was adapted for this probe molecule, with DHE replacing selenium. Contrary to previous investigations where DHE was added immediately after stoping illumination (Thabet et al., 2014), it was necessary to have DHE present during illumination because the half-life of superoxide and disproportionation of hydroperoxyl are significantly lower at low pH compared to alkaline conditions (Hayyan et al., 2016).

In order to investigate the role of H_2O_2 in the system, a spectrophotometric method was employed based on the reduction of Cu(II) by H_2O_2 in the presence of excess 2,9-dimethyl-1,10-phenanthroline (DMP) (Baga et al., 1988; Kosaka et al., 1998; Zeng et al., 2017). At set time intervals, samples were taken from the solution volume, filtered with a 0.2 μM pore size, and 1 mL of the supernatant was added to 250 μL of Cu/DMP reagent (a 50/50 v/v solution of 0.01 M $CuSO_4$ and 10 $g\cdot L^{-1}$ DMP). Hydrogen peroxide concentrations were determined by monitoring the peak absorbance at 454 nm of the resulting $Cu(DMP)_2^+$ complex (Baga et al., 1988), with the limit of detection of approximately 2 μM. UV-Vis measurements were conducted in a BioTek Epoch spectrophotometer and the spectra were imported into Excel and used without further processing. It is important to note that reacted samples were stored in the dark for 24 h prior to analysis, because at pH values below 4, the absorbance increased for approximately 1 day to the quantitative value, as reported previously (Baga et al., 1988).

Appendix B – Supplementary Information for Chapter 3

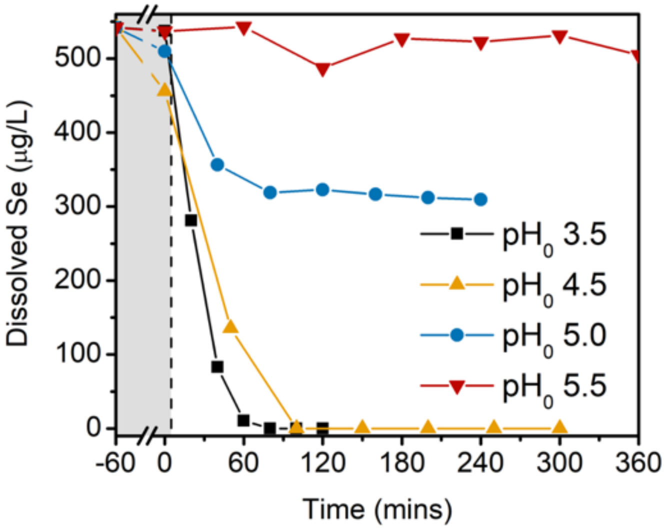

Figure B-1. pH effects of MIW photocatalytic selenate reduction kinetics under varying initial pH conditions - pH was not controlled during these experiments.

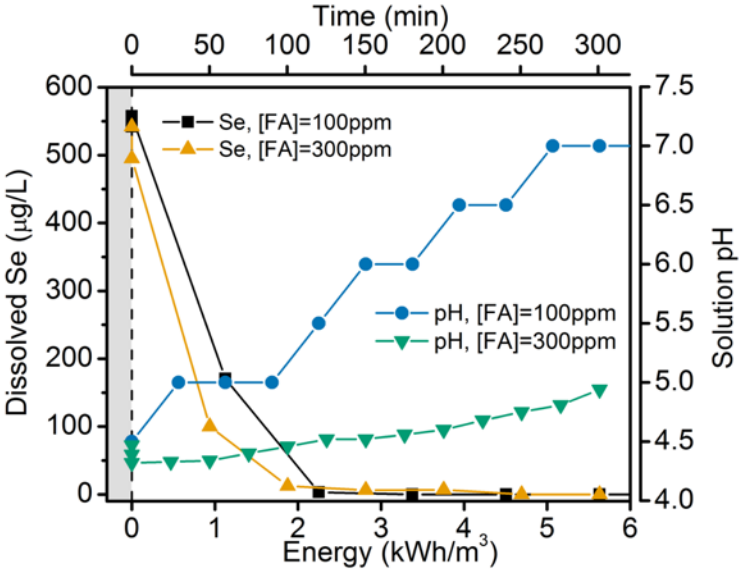

Figure B-2. pH increases throughout MIW photocatalytic reduction over TiO_2 treatment with the use of formic acid.

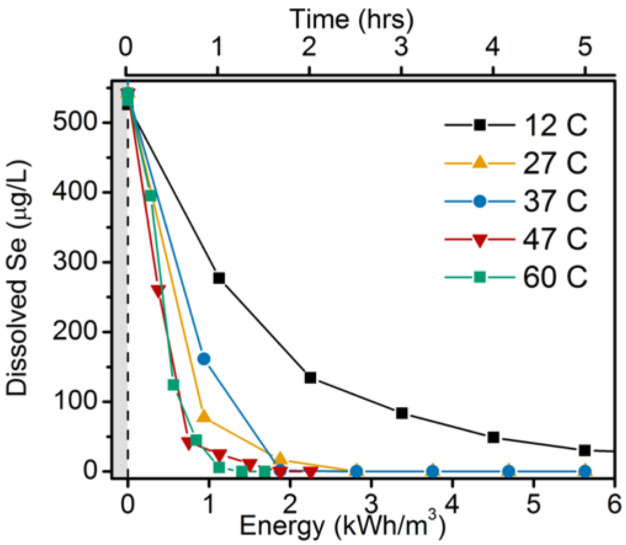

Figure B-3. Effect of temperature on photocatalytic reduction of selenate for the removal of dissolved Se from MIW.

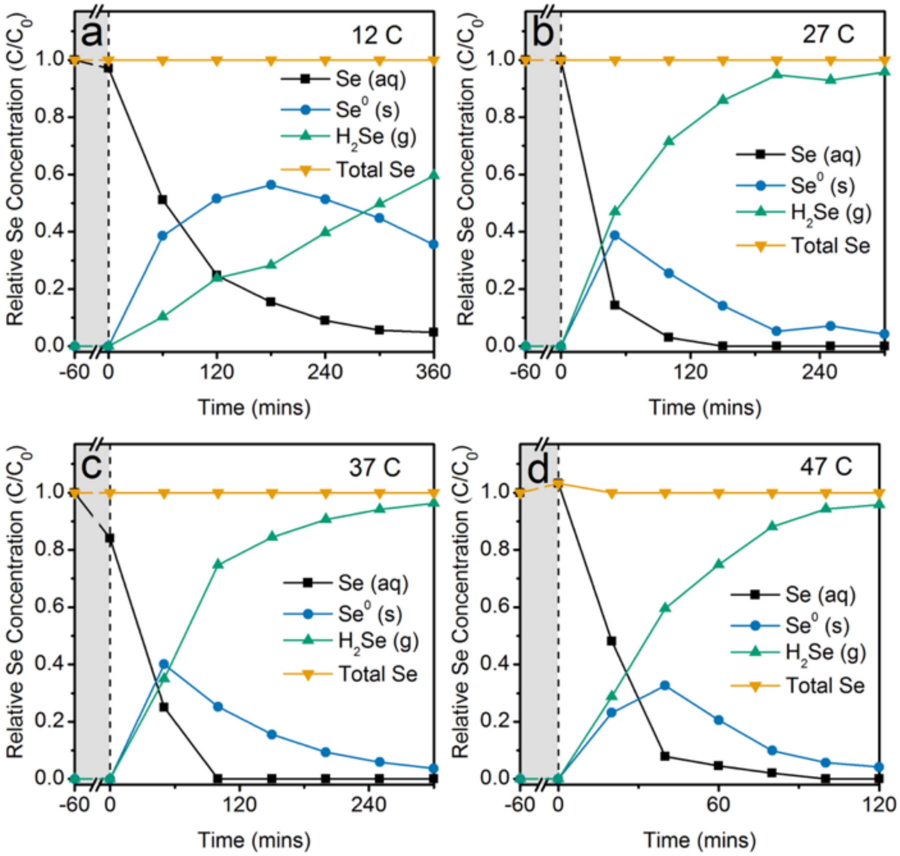

Figure B-4. Effects of temperature on the selectivity of solid element Se vs gaseous H_2Se during the photocatalytic reduction of selenate over TiO_2 in MIW.

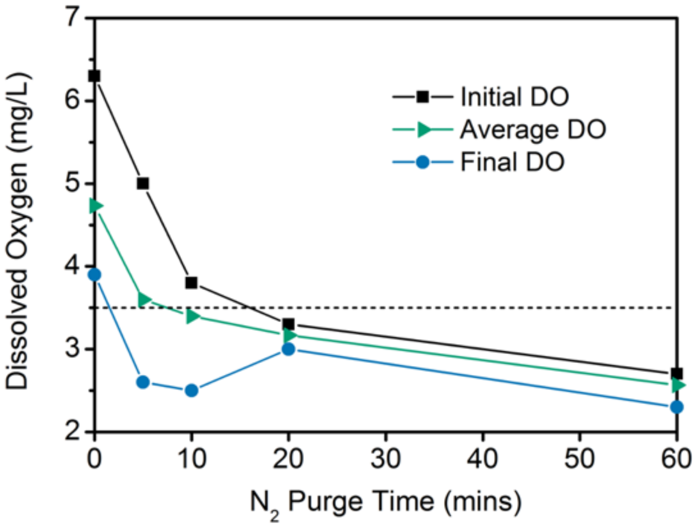

Figure B-5. Dissolved oxygen (DO) content of MIW during N_2 purge of varying times.

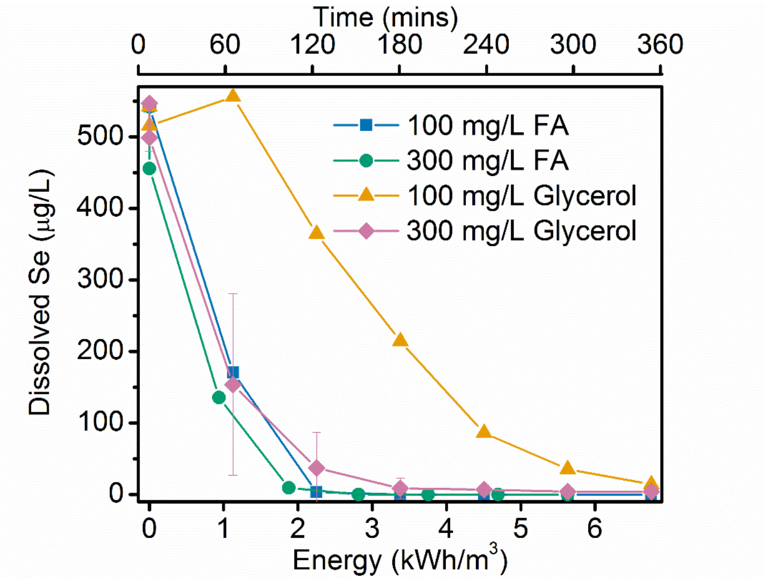

Figure B-6. Selenate reduction in MIW while using formic acid or glycerol as electron hole scavengers and either 100 or 300 mg L^{-1}.

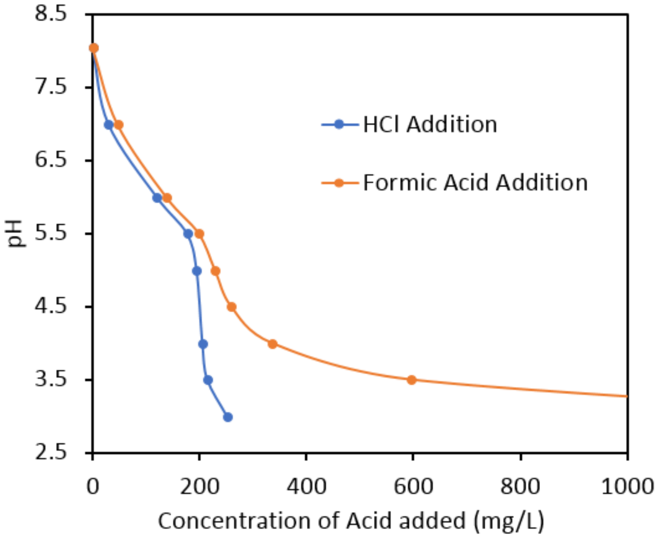

Figure B-7. Titration curve for hydrochloric acid and formic acid addition to MIW.

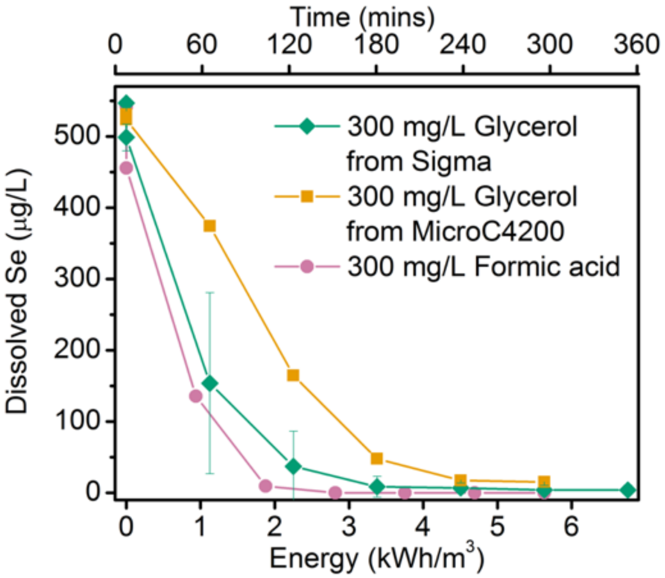

Figure B-8**.** Comparison of lab grade glycerol from Sigma-Aldrich, glycerol from a common electron donor for denitrification, MicroC4200, and formic acid used as electron hole scavengers during the photocatalytic reduction of selenate in MIW.

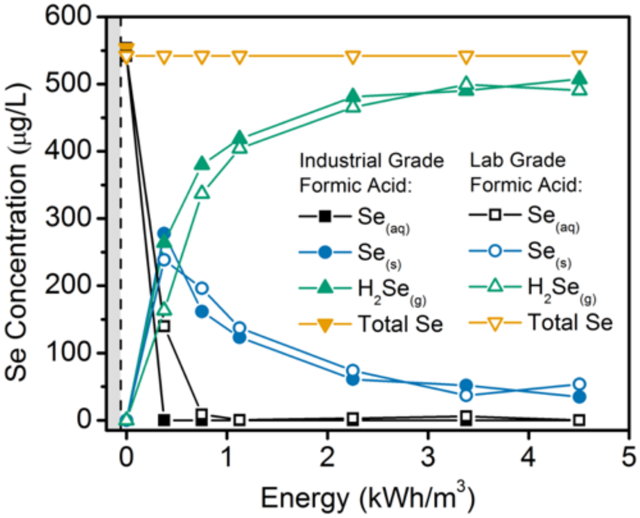

Figure B-9**.** Comparison of Se speciation while using lab grade formic acid from Sigma-Aldrich vs. industrial grade formic acid sourced from Quadra Chemicals used as electron hole scavengers during the photocatalytic reduction of selenate in MIW.

Appendix C – Supplementary Information for Chapter 5

Table C-1. Treatability results from SMIB A, B and C including the apparent first-order reaction rate constant and the average selectivity to $Se^0_{(s)}$ for the photocatalytic reduction of selenate in synthetic brine under reaction conditions of 0.2 g L^{-1} TiO_2, pH 4.5, 300 mg L^{-1} formic acid and 37°C.

Parameter	Units	SMIB A		SMIB B		SMIB C	
		Raw	Treated (2.1x10^{20} photons cm^{-2})	Raw	Treated (2.1x10^{20} photons cm^{-2})	Raw	Treated (2.1x10^{20} photons cm^{-2})
Photocatalytic Kinetic Data							
$k_{app,1}$	$cm^2/10^{20}$ photons	1.299 ± 0.043		1.206 ± 0.046		2.139 ± 0.066	
Average selectivity to $Se^0_{(s)}$	-	0.468		0.311		0.328	
Physical Tests (Water)							
Total Dissolved Solids	mg/L	6250	5700	5900	5730	5810	5670
Hardness (as CaCO3)	mg/L	2120	2130	2030	2020	1930	1920
pH	pH	8.16	4.89	7.81	5.2	7.54	4.94
ORP	mV	390	291	377	332	387	242
Anions and Nutrients (Water)							
Alkalinity, Total (as CaCO3)	mg/L	200	22.1	34	28.9	19.7	18.8
Ammonia (as N)	mg/L	0.0429	1.36	0.0265	1.41	0.0246	2.38
Nitrate (as N)	mg/L	556	528	546	528	535	510
Nitrite (as N)	mg/L	<0.0050	0.142	<0.0050	0.154	<0.0050	0.157
Chloride (Cl)	mg/L	58.8	135	58.7	126	799	846
Sulfate (SO4)	mg/L	1720	1680	1700	1680	723	690
Organic / Inorganic Carbon (Water)							
Total Inorganic Carbon	mg/L	39.3	<0.50	3.64	<0.50	2.4	<0.50
Total Organic Carbon	mg/L	1.92	67.8	1.8	68	1.35	64.5
Total Metals (Water)							
Calcium (Ca)-Total	mg/L	485	480	454	459	418	410
Magnesium (Mg)-Total	mg/L	235	226	221	215	230	218
Selenium (Se)-Total	ug/L	3280	165	3350	191	2720	32
Sodium (Na)-Total	mg/L	826	863	859	971	865	947
Titanium (Ti)-Total	mg/L	<0.010	<0.010	<0.010	<0.010	<0.010	<0.010

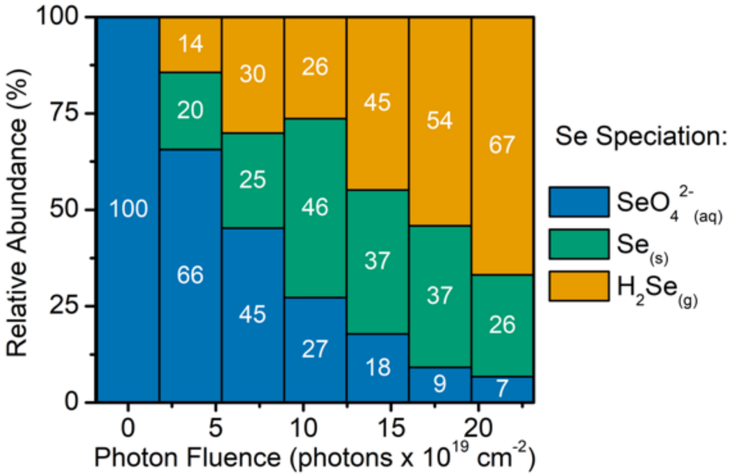

Figure C-1. Relative Se speciation during photocatalytic reduction of selenate in SMIB A under 37°C, 300 mg/L formic acid, 0.5 g/L TiO_2, pH 4.5 reaction conditions.

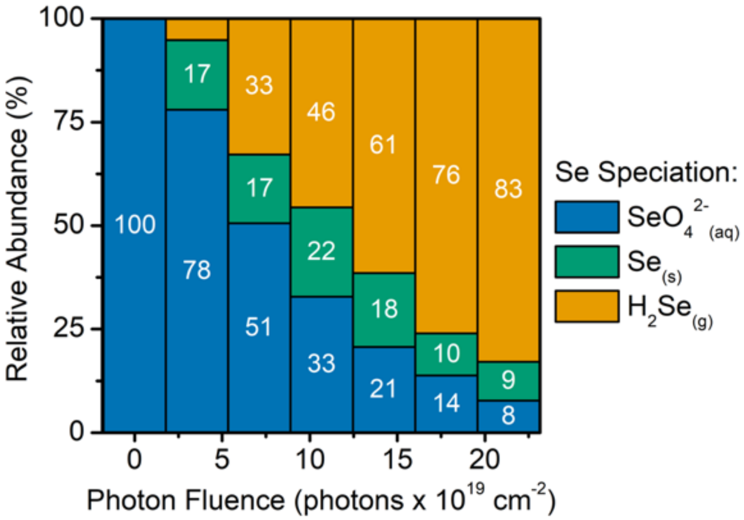

Figure C-2. Relative Se speciation during photocatalytic reduction of selenate in SMIB B under 37°C, 300 mg/L formic acid, 0.5 g/L TiO_2, pH 4.5 reaction conditions.

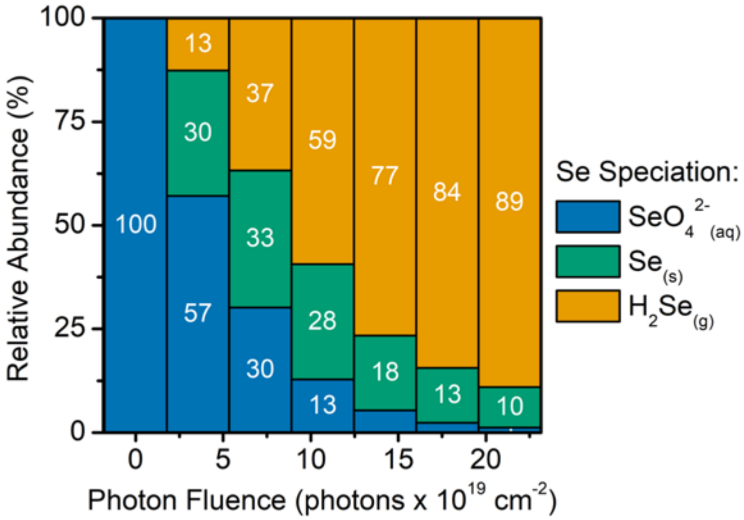

Figure C-3. Relative Se speciation during photocatalytic reduction of selenate in SMIB C under 37°C, 300 mg/L formic acid, 0.5 g/L TiO₂, pH 4.5 reaction conditions.

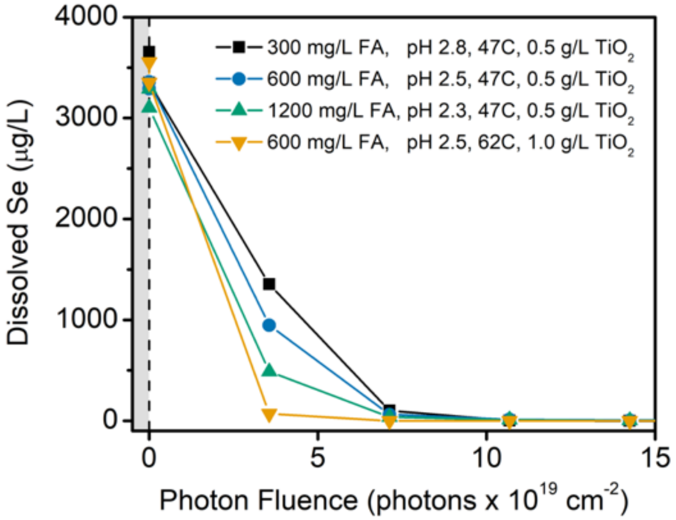

Figure C-4. Selenate removal curves through the photocatalytic reduction of selenate in SMIB at varying reaction conditions.

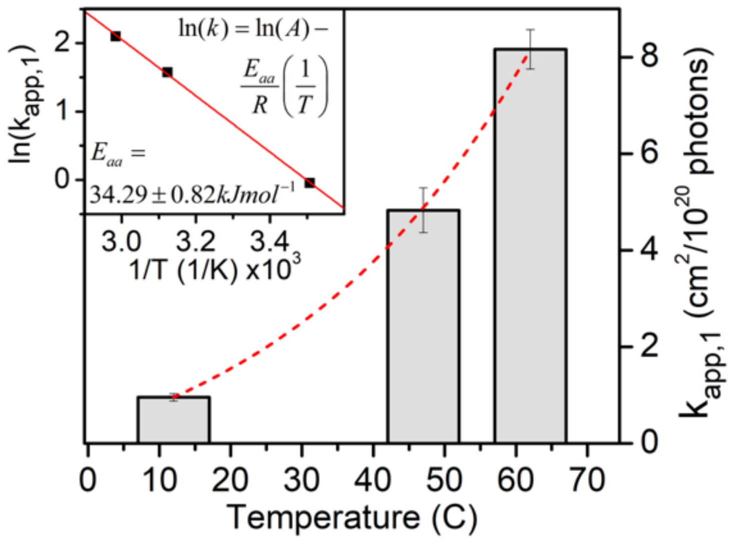

Figure C-5. Apparent first-order rate constant as a function of reaction temperature for the photocatalytic reduction of selenate in SMIB with inset Arrhenius plot.

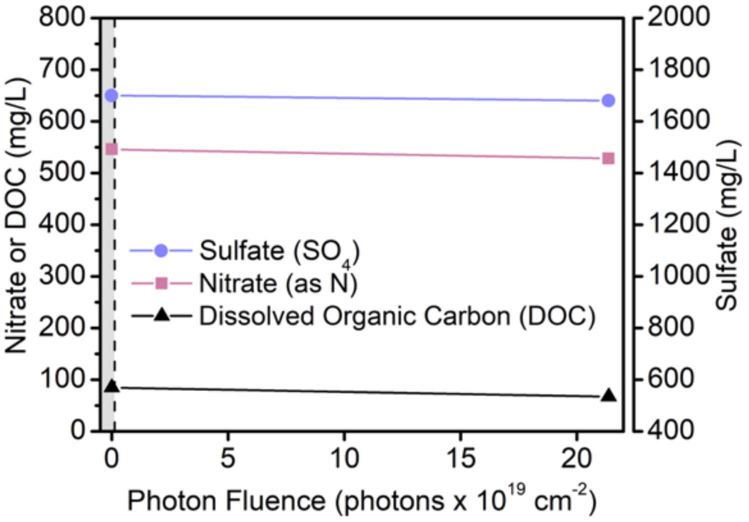

Figure C-6**.** Nitrate, sulfate and dissolved organic carbon concentrations during the photocatalytic reduction of selenate in SMIB. Reaction conditions: 0.2 g L^{-1} TiO_2, pH 4.5, 300 mg L^{-1} formic acid and 37°C.

Response Surface Analysis

Table C-2**.** Central composite design, experimental results, fitted values and residuals for the response surface study of the apparent first-order reaction rate constant with 4 center point replicates. Factor and level coding corresponds to **Table 5-1** in the main manuscript.

Run	Factor Levels					First Order Apparent Rate Constant, $k_{app,1}$ (cm^2/10^{20} photons)	Fitted Values, $\hat{k}_{app,1}$ (cm^2/10^{20} photons)	Residuals, e_i (cm^2/10^{20} photons)	Standardized Residual, d_i
	x_1	x_2	${x_1}^2$	${x_2}^2$	x_1x_2				
1	-1	-1	1	1	1	0.991	0.746	0.245	0.120
2	1	-1	1	1	-1	5.179	4.844	0.336	0.164
3	-1	1	1	1	-1	1.575	1.341	0.234	0.114
4	1	1	1	1	1	7.004	6.680	0.324	0.159
5	-1.389	0	1.929	0	0	0.957	2.204	-1.247	-0.611
6	1.389	0	1.929	0	0	7.457	7.822	-0.365	-0.179
7	0	-1.413	0	1.996	0	1.173	1.461	-0.288	-0.141
8	0	1.413	0	1.996	0	2.906	3.179	-0.273	-0.134
9	0	0	0	0	0	4.890	4.641	0.250	0.122
10	0	0	0	0	0	7.422	4.641	2.782	1.363
11	0	0	0	0	0	3.356	4.641	-1.285	-0.630
12	0	0	0	0	0	2.895	4.641	-1.746	-0.855

Table C-3**.** Analysis of variance for the response surface study of the apparent first-order reaction rate constant (Type III partial sum of squares). Factor coding corresponds to **Table 5-1** in the main manuscript.

Source of Variation	Sum of Squares	Degrees of Freedom	Mean Squares	F-Value	p-Value
Regression	55.830	5	11.166	5.091	**0.0362***
x_1	51.865	1	51.865	23.649	**0.0028***
x_2	11.092	1	11.092	5.058	0.0655
${x_1}^2$	7.208	1	7.208	3.287	0.1198
${x_2}^2$	8.983	1	8.983	4.096	0.0894
$x_1 x_2$	8.526	1	8.526	3.887	0.0961
Residual	13.159	6	2.193		
Lack of Fit	0.658	4	0.164	0.075	0.9872
Pure Error	12.501	2	6.251		
Total	69.488	11	6.317		

*Statistically significant ($p < 0.05$)

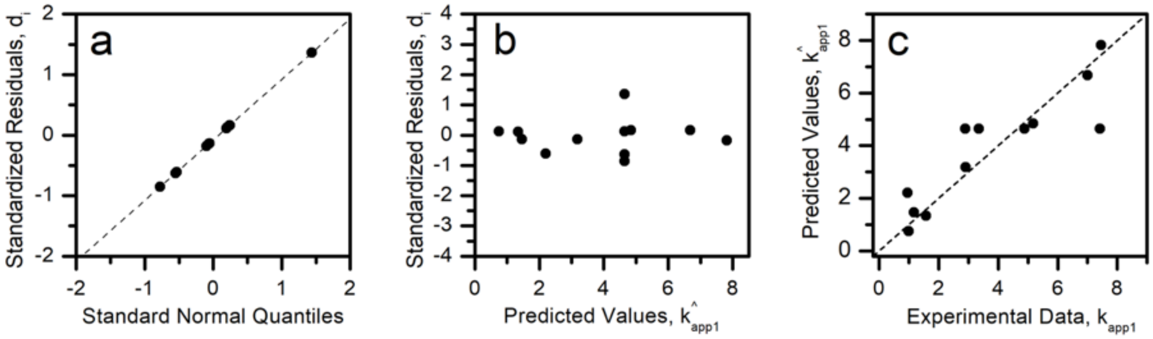

Figure C-7. (a) Half-normal probability plot of residuals, (b) residual plot and (c) predicted vs actual apparent first-order rate constants for the response surface regression.

Table C-4. Central composite design, experimental results, fitted values and residuals for the response surface study of the solid elemental Se selectivity with 4 center point replicates. Factor and level coding corresponds to **Table 5-1** in the main manuscript.

Run	Factor Levels					Selectivity to $Se^0_{(s)}$ @ 2.1×10^{20} $photons\ cm^{-2}$, $S(Se^0_{(s)})$ (no units)	Fitted Values, $\hat{S}(Se^0_{(s)})$ (no units)	Residuals, e_i (no units)	Standardized Residual, d_i
	x_1	x_2	$x_1{}^2$	$x_2{}^2$	x_1x_2				
1	-1	-1	1	1	1	0.832	0.883	-0.051	-0.438
2	1	-1	1	1	-1	0.069	0.050	0.019	0.163
3	-1	1	1	1	-1	0.966	0.894	0.071	0.611
4	1	1	1	1	1	0.913	0.771	0.142	1.212
5	-1.389	0	1.929	0	0	0.781	0.777	0.004	0.038
6	1.389	0	1.929	0	0	0.018	0.113	-0.095	-0.812
7	0	-1.413	0	1.996	0	0.641	0.600	0.041	0.354
8	0	1.413	0	1.996	0	0.985	1.117	-0.132	-1.129
9	0	0	0	0	0	0.436	0.574	-0.137	-1.174
10	0	0	0	0	0	0.610	0.574	0.037	0.314
11	0	0	0	0	0	0.713	0.574	0.139	1.189
12	0	0	0	0	0	0.535	0.574	-0.038	-0.329

Table C-5**.** Analysis of variance for the response surface study of the solid elemental Se selectivity (Type III partial sum of squares). Factor coding corresponds to **Table 5-1** in the main manuscript.

Source of Variation	Sum of Squares	Degrees of Freedom	Mean Squares	F-Value	p-Value
Regression	1.029	5	0.206	0.018	**0.0038***
x_1	0.480	1	0.480	0.041	**0.0016***
x_2	0.300	1	0.300	0.026	**0.0051***
${x_1}^2$	0.137	1	0.137	0.012	**0.0272***
${x_2}^2$	0.158	1	0.158	0.014	**0.0204***
x_1x_2	0.158	1	0.158	0.014	**0.0206***
Residual	0.097	6	0.016		
Lack of Fit	0.056	4	0.014	0.001	0.5337
Pure Error	0.041	2	0.020		
Total	1.125	11	0.102		

*Statistically significant ($p < 0.05$)

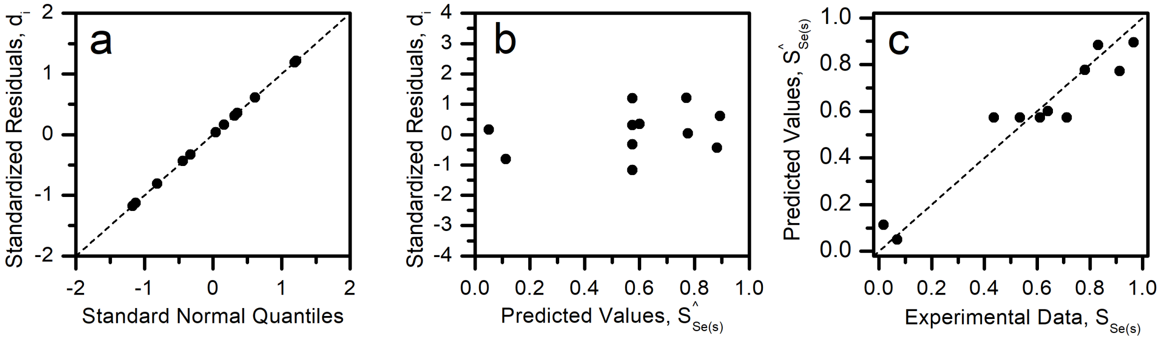

Figure C-8. (a) Half-normal probability plot of residuals, (b) residual plot and (c) predicted vs actual solid elemental Se selectivity for the response surface regression.

Appendix D – Supplementary Information for Chapter 6

Modified from the supporting information in:

Holmes, A.B., Daid, K., Livera, D., and Gu, F. (in submission). Modifying Se-TiO_2 photocatalytic reduction of selenate in water using noble metal deposits (Ag, Au, Pt and Pd) to tune final Se product selectivity. *Environment Science: Nano*.

D1. Photocatalytic experimental set-up

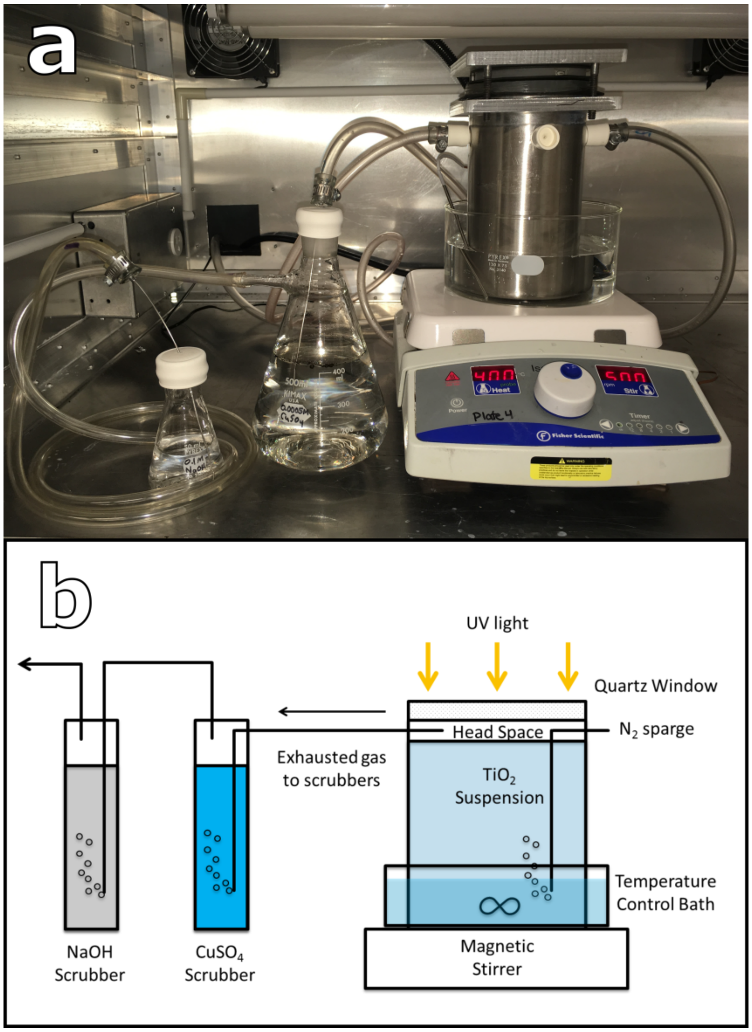

Figure D-1. (a) Photograph and (b) schematic image of the batch photocatalytic reaction set-up for the reduction of selenium oxyanions in synthetic and real industrial FGDW.

D2. Noble metal deposited TiO_2

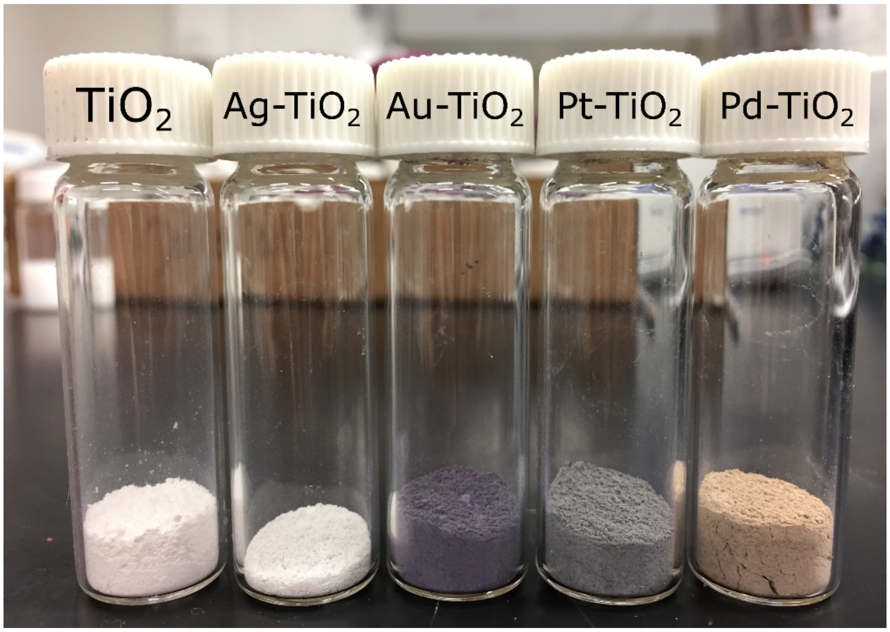

Figure D-2. Photograph presenting the various colours of the final noble metal deposited TiO_2 photocatalysts. From left to right: TiO_2, Ag-TiO_2, Au-TiO_2, Pt-TiO_2 and Pd-TiO_2.

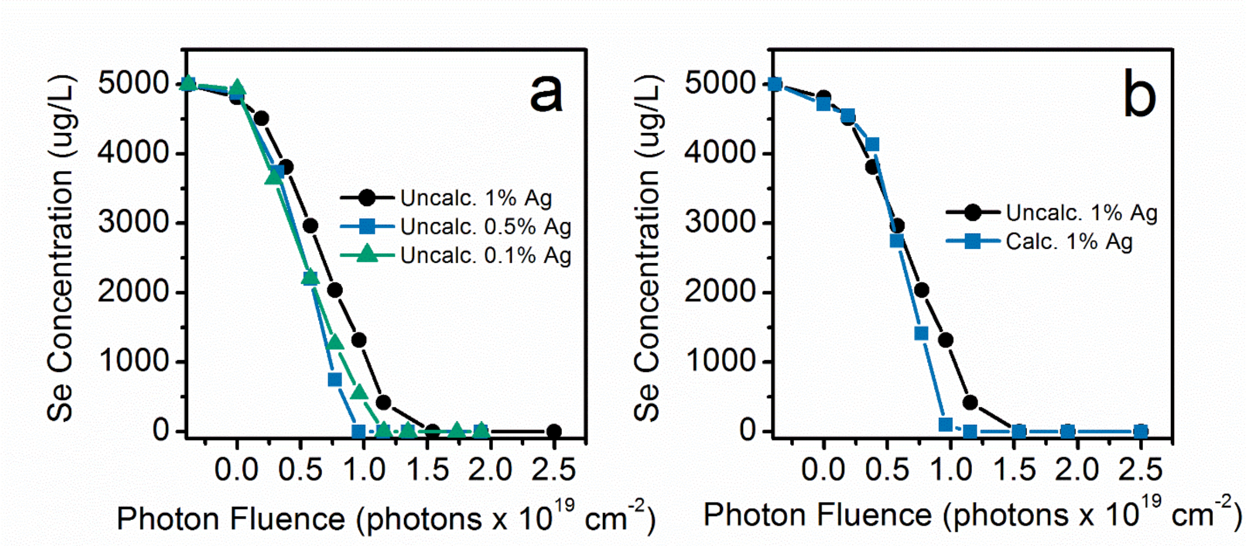

Figure D-3. (a) Photocatalytic reduction of 5 mg/L (as Se) sodium selenate in MilliQ over varying concentrations of silver deposited on TiO_2 and (b) Photocatalytic reduction of 5 mg/L (as Se) sodium selenate in MilliQ over calcined and uncalcined samples of 1 wt% Ag-TiO_2.

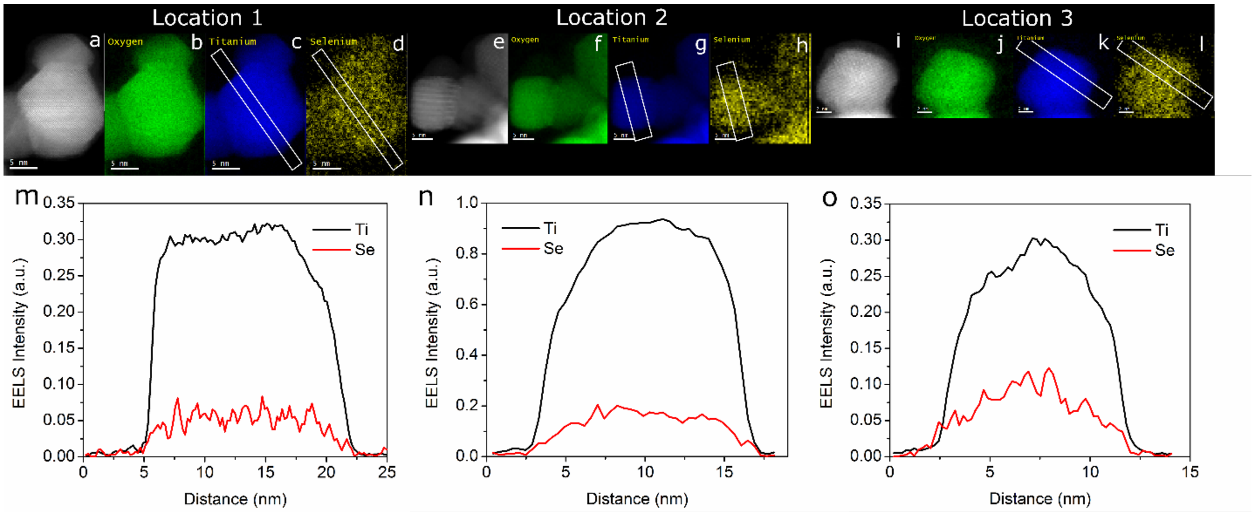

Figure D-4. High resolution transmission electron microscopy (HR-TEM) with electron energy loss spectroscopy (EELS) for three separate locations on the TEM grid prepared with Se deposited onto TiO_2 after 1.0 photons × 10^{19} cm^{-2} of UV exposure. (a-d, e-h, i-l) HR-TEM, EELS O imaging, EELS Ti Imaging, EELS Se imaging, for location 1, 2 and 3 respectively and (m-o) EELS line scans for location 1, 2 and 3 respectively.

D3. $O_2^{\bullet-}$ / $^{\bullet}HO_2$ Radical Experiments

Experiments were conducted to reveal the variations in hydroperoxyl generation rate with the varying noble metal deposited TiO_2 samples. Dihydroethidium (DHE) at a concentration of 5×10^{-5} M was used to quantitatively detect superoxide (and consequently hydroperoxyl) radical ($O_2^{\bullet-}$ / $^{\bullet}HO_2$) generated by the TiO_2 photoreduction system. Unless otherwise stated, a 0.08 M DHE stock solution in DMSO was used and stored in the dark at –20°C for at most 2 days. Superoxide concentrations were indirectly determined by monitoring the increase in fluorescence intensity at 580 nm (ex. 480 nm), attributed to the formation of the superoxide-specific product 2-hydroxyethidium, at set time intervals (Chen et al., 2013; Fink et al., 2004; Peshavariya et al., 2007; Zhao et al., 2003). When superoxide dismutase (SOD) was used, it was added prior to the dark adsorption period and the aforementioned DHE procedure was conducted without further modifications. Fluorescence spectra were recorded on a Photon Technology International QM-4SE fluorimeter and were smoothed using Origin Pro by removing Fourier components with frequencies higher than a particular cut-off frequency prior to integration of the area under the emission peak. A calibration curve for 2-hydroxyethidium was generated by reacting known amounts of DHE with potassium nitrosodisulfonate (Fremy’s Salt), which has been demonstrated to yield the same superoxide-specific oxidation product (Laurindo et al., 2008; Zielonka et al., 2005). The previously mentioned procedure for photoreduction experiments was adapted for this probe molecule, with DHE replacing selenium. Contrary to previous investigations where DHE was added immediately after stopping illumination (Thabet et al., 2014), it was necessary to have DHE present during illumination because the half-life of superoxide and disproportionation of hydroperoxyl are significantly lower at low pH compared to alkaline conditions (Hayyan et al., 2016).